A new vision for fuel cells: application in cancer biomarker screening

Liliana Patrícia Teixeira Carneiro

Dissertation presented for the Doctor degree in Chemical and Biological Engineering

This thesis is supervised by Doctor Maria Goreti Ferreira Sales, Departamento de Engenharia Química, Faculdade de Ciências e Tecnologia da Universidade de Coimbra and Co-supervised by Doctor Alexandra Maria Pinheiro da Silva Ferreira Rodrigues Pinto, Departamento de Engenharia Química, Faculdade de Engenharia da Universidade do Porto

Departamento de Engenharia Química

Faculdade de Engenharia

Universidade do Porto

Porto, January 2023

Acknowledgments

Like a brilliant mind once said, *"…. Be curious. And however difficult life may seem, there is always something you can do and succeed at. It matters that you don't just give up. Unleash your imagination. Shape the future".* (Stephen Hawking, in Brief Answers to the Big Questions). This thesis is the outcome of a very challenging work and it would not be possible without the contribution of all the important persons who are present in my life and that I would like to acknowledge.

First of all, I want to acknowledge my supervisor Prof. Goreti Sales, for all the encouragement and for believing in me, it was really important and fundamental to me to keep the motivation and inspiration, and continue working each day without giving up. Thanks for the supervision, guidance, counseling, and friendship. It was an honor and a pleasure to work with an amazing scientist that inspires everyone surrounding, with an enormous knowledge, enthusiasm, and a magical capability to find solutions for every problem. I also want to acknowledge Prof. Alexandra Pinto for sharing her scientific knowledge, which has a crucial input at the beginning of this thesis work. Thanks for the support and supervision through this work.

To all BioMark team (Porto and Coimbra), that also contributes positively to this work, in special to Nádia Ferreira for the friendship, support, and for lessening my "crazy thinking"; Raquel Vaz for her advice, kindness, and patience; Margarida Piloto for making me laugh when I need it, for the support, and enthusiastic scientific talks.

To my friends that also support me and lessen my frustrations; especially Gisela Borges that even the distance has found time to motivate me when is necessary.

To my parents for their unconditional support in all the moments, being always present for me when I needed, and for always believing in my capabilities and success.

To my dear Carlos, since the first day we meet, helped me to find the scientist in me, been my constant support throughout my research life. I wouldn't be here without you, that's for sure! Your presence in my life, encouragement, motivation, patient, support, and science passion have inspired me to be the best scientist possible.

And finally, my reason to continue this journey, my daughters Inês and Leonor, who every day inspire me to achieve my golds; in the end part of this PhD journey a new reason appears in my life (Maria Francisca) that despite only arriving in this world in March- 2023 has already part of this story.

I would like to acknowledge the financial support from Fundação para a Ciência e Tecnologia (FCT) for conceding me the grants: SFRH/BD/122954/2016 and COVID/BD/151738/2021, making this thesis possible.

Resumo

O cancro é a uma das principais causas de morte no mundo, e a sua deteção precoce aumenta as hipóteses de cura, o que reforça a necessidade de desenvolver dispositivos capazes de detetar precocemente biomarcadores de cancro que circulam no organismo. Quando a deteção do cancro é demorada, as possibilidades de sucesso do tratamento e de sobrevivência diminuem, além de acarretar maiores custos para os sistemas de saúde. Apesar da aplicação de exames de imagem e biópsia no diagnóstico do cancro, ainda faltam métodos mais rápidos, simples e que possam ser realizados fora de um laboratório para deteção do cancro. A deteção de biomarcadores específicos do cancro em programas de rastreio no ponto de atendimento (POC) sem a necessidade de equipamentos de alto custo e análises laboratoriais continua a ser um desafio.

Para este efeito, o presente plano aborda o desenvolvimento de dispositivos biossensores autónomos, baseados em células de combustível, que oferecem resposta rápida, simples, confiável e de baixo custo, com a capacidade de detetar biomarcadores do cancro diferentes, numa abordagem não invasiva. Para além disso, esses dispositivos biossensores baseados em células de combustível são totalmente independentes eletricamente, o que permite o seu uso em qualquer lugar, não exigindo um ambiente laboratorial ou técnicos especializados para a sua operação. Neste âmbito, apresenta-se o desenvolvimento de camadas de bio-reconhecimento, integradas no ânodo (elétrodo) de diferentes configurações de células de combustível de metanol que operam em modo passivo. A combinação de duas tecnologias poderosas, como células de combustível e técnicas de impressão molecular, permite a criação de dispositivos biossensores compactos que integram uma função de bio-reconhecimento seletiva acoplada a um elemento transdutor autónomo, o que dispensa o uso de baterias externas e respetivos componentes eletrónicos associados. Durante o desenvolvimento da configuração da célula de combustível de metanol passiva contendo o biossensor, o papel foi introduzido como uma nova alternativa às configurações convencionais das células de combustível, que normalmente envolvem diferentes peças plásticas/metálicas. O papel foi utilizado como suporte contendo todos os componentes fundamentais de uma célula de combustível de metanol, permitindo a criação de uma de célula de combustível em forma de tira de camada única, com possibilidade de ser acoplada a uma célula eletroquímica, também desenvolvida em papel, tornando possível a incorporação da propriedade de auto-sinalização. A combinação destas

tecnologias permitiu o desenvolvimento de diferentes plataformas do conjunto biossensor/célula de combustível para detetar três biomarcadores do cancro com relevância clínica. No geral, espera-se que os resultados obtidos neste trabalho possam contribuir no futuro para abrir novos horizontes, permitindo a disseminação de biossensores em programas de rastreio do cancro, mesmo em locais com escassez de energia.

Termos-chave: *Biossensor eletroquímico autónomo; Células de combustível de metanol; Polímero de impressão molecular; Biomarcadores do cancro; Deteção no ponto de cuidado; Células de combustível à base de papel.*

Abstract

Cancer is a leading cause of death worldwide, and its early detection increases the healing chances, which stresses the need to develop devices capable of detecting cancer biomarkers that circulate early in the body. When cancer detection is delayed, the chances of successful treatment and survival decrease, leading later to higher costs for the healthcare systems.
Despite the application of imaging tests and biopsy in cancer diagnosis, faster, simple and laboratory-free methods for cancer detection are still lacking. The detection of specific cancer biomarkers in point-of-care (POC) screening programs without requiring high-cost equipment and laboratory analysis remains a challenge.
Thus, to overpass this limitation, the present plan addresses the development of rapid, simple, reliable, and low-cost autonomous fuel cell-based biosensor devices, with the capability of detecting different cancer biomarkers in a non-invasive approach. Besides, these fuel cell-based biosensor devices are fully electrical independent which allows their use anywhere, not requiring a laboratory environment or expert technicians to its operation. Under this scope, the development of sensitive biosensing layers integrated into the anode electrode of different passive methanol fuel cell configurations is presented. The combination of two powerful technologies, as fuel cells and molecular imprinting strategy, allows the creation of compact biosensor devices that integrates a highly selective biorecognition function coupled with an autonomous transducer element, eliminating the use of external batteries and their associated electronics. During the development of the passive methanol fuel cell biosensor assembly, paper was introduced as a novel alternative to the conventional fuel cell setups, which typically involves different plastic/metallic moving parts. Paper was used as support for all the important components of a methanol fuel cell, which allows the creation of a simple single layer fuel cell strip with the possibility to be coupled to an electrochemical cell, also paper-based, turning possible the incorporation of the self-signalling propriety. This technology merging allowed the development of two different biosensor/fuel cell sensing platforms for screening three different cancer biomarkers with clinical relevance.

Overall, it is expected that the outcomes provided by this work can contribute in the future to open new horizons for biosensors dissemination in POC cancer screening programs, even in places with energy shortages.

Key-words: *Autonomous electrochemical biosensor; Methanol fuel cells; Molecular imprinting polymer; Cancer biomarkers; Point-of-care sensing; Paper-based fuel cells.*

Table of Contents

Chapter 1 - Framework 31

1.1 Motivation 31

1.2 Objectives 32

1.3 Thesis outline 33

1.4 List of publications 35

1.4.1 Papers published in international scientific journals 35

1.4.2 Book chapter 36

1.4.3 Communications presented in national and international scientific conferences 37

Chapter 2 - Introduction 38

2. Introduction 38

2.1 Cancer disease 38

2.2 Cancer biomarkers 40

2.2.1 Carcinoembryonic antigen (CEA) 41

2.2.2 Sarcosine 43

2.2.3 Recombinant human L1CAM protein 44

2.3 Biosensors 46

2.3.1 Recognition element 47

2.3.1.1 Biological recognition elements and aptamers 47

2.3.1.2 Synthetic recognition elements - MIPs 48

2.3.2 Signal transducer 51

2.4 Electrochemical biosensors 54

2.4.1 Electrochemical cell configurations 55

2.4.2 Electrodes composition 56

2.4.3 Electrochemical techniques 58

2.4.3.1 Cyclic Voltammetry 59

2.4.3.2 Electrochemical Impedance Spectroscopy 62
2.5 Fuel cells 63
2.5.1 Fuel cells overview 63
2.5.2 Direct methanol fuel cells 67
2.5.3. Fuel cell electrodes: carbon support, metal catalysts, and ionomer 71
2.5.4 Conductive nano-inks for fuel cell application 75
2.5.5 Passive DMFCs 78
2.5.6 Applications of Direct methanol fuel cells 80

Chapter 3 - A passive direct methanol fuel cell as transducer of an electrochemical sensor, applied to the detection of carcinoembryonic antigen 83

3.1 Introduction 84
3.2 Experimental section 86
3.2.1 Reagents and solutions 86
3.2.2 Preparation of the sensing unit 86
3.2.3 Fuel cell unit 88
3.2.4 Apparatus and integrated device set-up 91
3.2.5 Electrochemical assays 91
3.3 Results and discussion 92
3.3.1 Normal operation of the passive fuel cell 92
3.3.2 Setting the integrated device 93
3.3.3 Response to CEA in buffer 98
3.3.4 Response to CEA in synthetic fluid model and human serum 100
3.3.5 Comparison to previous CEA (bio)sensors 103
3.4 Conclusions 105

Chapter 4 - An all-in-one approach for self-powered sensing: A methanol fuel cell modified with a molecularly imprinted polymer for cancer biomarker detection 106

4.1 Introduction 107

4.2 Experimental section 108

4.2.1 Reagents and solutions 108

4.2.2 Fuel cell assembly 109

4.2.3 Preparation of the biosensing element 111

4.2.4 Electrochemical assays and equipment 112

4.3 Results and discussion 113

4.3.1 Production of the sensing anode electrode 113

4.3.1.1 Assembly of the sensing film on Carbon Cloth-Pt/Ru supports 113

4.3.1.2 Chemical characterization 114

4.3.1.3 Morphological characterization 117

4.3.2 Integration of the anode sensing electrode on the DMFC 117

4.3.3 Selection of ideal MeOH concentration for biosensor DMFC operation 120

4.3.4 Calibrations of the biosensor DMFC 124

4.3.5 Device operation with an alternative fuel: Ethanol 129

4.4 Conclusions 130

Chapter 5 - Development of an innovative flexible paper-based methanol fuel cell (PB-DMFC) sensing platform – Application to sarcosine detection 131

5.1 Introduction 132

5.2 Experimental section 134

5.2.1 Reagents and solutions 134

5.2.2 Apparatus and equipment 135

5.2.3 Electrochemical assays 136

5.2.4 Paper based fuel cell assembly 137

5.2.5 Biosensor element preparation 139
5.3 Results and discussion 140
5.3.1 Assembly of the paper-based fuel cell device 140
5.3.1.1 Configuration 140
5.3.1.2 Selection of ideal MeOH concentration 143
5.3.2 PB-DMFC device characterization 147
5.3.3 Integration of the sensing area on the PB-DMFC 152
5.3.3.1 Imprinted film layer development 152
5.3.3.2 Impact of the imprinted film in the PB-DMFC 156
5.3.4 Calibrations of the PB-DMFC/biosensor 157
5.3.5 Selectivity studies 162
5.4 Conclusions 164

Chapter 6 - Portable and autonomous PEDOT modified flexible paper-based methanol fuel cell sensing platform applied to L1CAM recombinant protein detection 165

6.1 Introduction 166
6.2 Experimental and methods 169
6.2.1 Reagents and solutions 169
6.2.2 Equipment and apparatus 171
6.2.3 PEDOT Paper Based Fuel Cell (PEDOT/PB-DMFC) assembly 172
6.2.4 PEDOT biosensor element preparation 177
6.2.5 Electrochromic cell (EC) preparation 178
6.2.6 Electrochemical and electrochromic assays 180
6.3 Results and discussion 181
6.3.1 PEDOT/PB-DMFC device 181
6.3.1.1 Set-up assembly configuration and characterization 181
6.3.1.2 Sensory layer development and characterization 185
6.3.2 Calibrations of the PEDOT/PB-DMFC biosensor (single cell configuration) 188

6.3.3 EC assembly and characterization 193
6.3.4 Assembly of the portable system – PEDOT/PB-DMFC/biosensor-stack interfaced with the EC 196
6.4 Conclusions..... 198

Chapter 7 - Conclusions and Future Perspectives 199

List of figures

Figure 2.1 – Graphic representation of all new cancer cases (A) and mortality associated to cancer disease (B), for both genders and ages in the 2020 year. Figure adapted from GLOBOCAN 2020 - https://gco.iarc.fr/today/data/factsheets/cancers/39-All-cancers-fact-sheet.pdf. 39

Figure 2.2 – Schematic illustration of different types of cancer biomarkers and their role in the five main areas of controlling cancer disease: diagnosis, therapy follow-up, risk evaluation, screening and prognosis. 41

Figure 2.3 – Schematic representation of CEA structure (A) displaying insertion of CEA into the plasma membrane (down arrow) (adapted from [19]) and (B) 3D structure of the N-terminal domain of CEA (adapted from [20]). 42

Figure 2.4 – Chemical structure of glycine and the derived amino acid sarcosine..... 43

Figure 2.5 – General schematic topology of human L1CAM, evidencing the fibronectin domains as green squares, the Ig-like domains as blue circles and the potential N-glycosylation site. Adapted from [49]. 45

Figure 2.6 – General scheme of a biosensor and common recognition elements and transducers 47

Figure 2.7 – Schematic representation of the synthesis of molecularly imprinted polymers. 49

Figure 2.8 -A)- Representative monomers applied for the electrosynthesis of MIPs, B) with some examples of monomers that can polymerize to developed conductive films. 51

Figure 2.9 - Types of biosensors with basis on the transducer operation 52

Figure 2.10 – Schematic view of the 2 (A) and 3 electrodes configuration (B), with an example of application of each system. 56

Figure 2.11– Schematic cyclic voltammogram obtained for a reversible system, including the peak cathodic potential (Ep_c), peak anodic potential (Ep_a), cathodic current (i_{pc}), and anodic current (i_{pa}). Adapted from [113]. 60

Figure 2.12– Schematic simulation of a reversible (blue curve) and irreversible (red curve) electrochemical processes, evidencing the effect of increasing the scan rate to restore reversibility (dashed arrow). 61

Figure 2.13– Schematic representation of a Nyquist plot. 63

Figure 2.14– General scheme of a fuel cell assembly including typical reactions in different types of fuel cells, including proton exchange membrane fuel cells (PEMFCs), alkaline fuel cells (AFCs), phosphoric acid fuel cells (PAFCs), solid oxide fuel cells (SOFCs), and molten carbonate fuel cells (MCFCs). Reactions expected in each electrode depend on the type of cell, as identified for each electrode. 64

Figure 2.15– General scheme illustrating the working principle of a typical DMFC fuel cell. 67

Figure 2.16– Polarization curve evidencing the electric losses found in a DMFC operation. 68

Figure 2.17– General scheme illustrating the membrane electrode assembly (MEA) scheme, complemented with a real image of the assembly. 70

Figure 2.18– Principal components of a general proton exchange membrane fuel cell, including the flow field plates (FFPs), gas diffusion layer (GDL), microporous layer (MPL), catalyst layer (CL) and proton exchange membrane (PEM). (A) Basic and common catalyst nano-ink components for application fuel cell electrodes. (B) Structure and transport processes of components forming CLs: Transmission electron microscopy image of a CL. (1) Scheme of distribution of ink components and transport processes of oxygen molecules between carbon aggregates. (2) General scheme considering transport processes of oxygen through ionomer layer to Pt catalyst surface (C). ((A), reproduced with permission from [128] and (C) with permission of [129]). 71

Figure 2.19– Schematically representation of the most common carbon supports employed in fuel cell electrodes development, complemented with real SEM images of their structure. 73

Figure 2.20– Schematically representation of the triple-phase boundary between the carbon support/metal catalyst/ionomer, displaying also the Nafion binder chemical structure. 74

Figure 2.21 – Direct Methanol Fuel Cell portable prototypes, including a methanol fuel cell mobile phone launched by ©Toshiba (A), a portable laptop powered by a methanol fuel cell launched by ©Ultracell (B), a methanol fuel cell MP3 player launched by ©Toshiba (C), and a hybrid fuel cell system integrating a DMFC and a Li-ion battery launched by ©Sony (D). 81

Figure 2.22 – Total publications search using keywords of all types of alcohol fuel cells found from 2010 to 2020. Adapted from [160]. 81

Figure 3.1- Schematic representation of the constituents of the final biosensor device, including (A) the different steps for the sensing layer development (B) the methanol fuel cell device and membrane electrode assembly (MEA) (B) integrated DMFC/Sensor electrically coupled (C). 87

Figure 3.2 - Designed passive DMF device: (A) Anode side of the fuel cell, which contains a reservoir for the methanol solution insertion into the system; (B) Cathode side of the fuel cell, with a grid open to the atmosphere, in order to allow that the O_2 present in the atmospheric air reaches the electrode. 88

Figure 3.3 - Technical drawings of the DMFCs used in this work. 89

Figure 3.4 - Power curves obtained during an experimental assay: for the DMFC alone, for the DMFC/Biosensor without the target protein (after buffer incubation) and for the DMFC/Biosensor with the target protein (after incubation of a CEA standard with concentration of 100 mg/mL). 90

Figure 3.5 - Electrochemical data of the passive DMFC in the form of (A) polarization and (B) power density curves of the passive DMFC device operating with different MeOH concentrations; Electrochemical data of the passive DMFC device using different reading times (30s – 180s) in each potential, using 2.0 M MeOH concentration, plotted as (C) polarization curves and (D) power curves. 92

Figure 3.6 - Polarization curves and power curves obtained for different potential reading times: (A) 30 s, (B), 60 s and (C) 120 s, using 2.0 M of MeOH. Each plot contains 3 consecutive measurements. 94

Figure 3.7 - Polarization curves and power curves obtained for different potential reading times: (A) 30 s, (B), 60 s and (C) 120 s, using 2.0 M of MeOH. Each plot contains 3 consecutive measurements. 95

Figure 3.8 - Integrated set-up assembly including a (A) Schematic diagram representation of the DMFC functioning with the chemical species involved in methanol oxidation-reduction process and real image of the set-up of DMFC/Sensor. Electrochemical results of the polarization and power densities obtained: (A) before (dark line) and after (blue line) the coupling of the sensor with the fuel cell; (B) stability of the DMFC/Sensor assembly in two consecutive assays. 96

Figure 3.9 - Scheme of the different setups tested for the (MIP/FTO-glass) electrode integration in the external circuit of the DMFC and electrochemical results obtained with the different assemblies..... 97

Figure 3.10 - Typical Power-Current Density curves of the DMFC/Sensor device towards CEA increasing concentrations in the range of 0.10 ng/mL to 100.0 μg/mL in buffer. Results show: (A) a calibration curve obtained during calibrations of crescent concentrations of CEA standards; (B) the average value of the maximum power density obtained in each CEA concentration..... 99

Figure 3.11 - Selectivity tests results performed with different possible interferents (glucose, urea, ascorbic acid) and similar potential interfering proteins (CA15-3 and CA125) obtained in parallel, using independent sensing units integrated in the DMFC device. 100

Figure 3.12 - Typical Power-Current Density curves of the DMFC/Sensor device towards CEA increasing concentrations in the range of 0.10 ng/mL to 100.0 μg/mL in physiological medium. Results show: (A) a calibration curve obtained during calibrations of crescent concentrations of CEA standards in a synthetic fluid model and (B) the average value of the maximum power density obtained in each CEA concentration. (C) A calibration curve obtained during calibrations of crescent concentrations of CEA standards in Cormay® serum and (D) the average value of the maximum power density obtained in each CEA concentration..... 101

Figure 3.13 - Maximum power density in function of log CEA concentrations for a calibration with standard solutions prepared in Cormay® serum, and an independent signal of similar standards (red dots) obtained simultaneously from another independent calibration (using a different DMFC and sensor unit). 102

Figure 4.1 - Schematic representation of the components of the DMFC sensing device, including (A) the MeOH fuel cell device and the membrane electrode assembly (MEA) and (B) the various steps in the development of the sensing layer on the anode, which is sensitive to CEA and is obtained by a surface electropolymerization process using EDOT/PPy monomers; (C) Schematic representation of the soot surface with an anchored MIP polymer film showing the cavities (binding sites) and the different pathways limiting the access of MeOH molecules. 109

Figure 4.2 - Opened fuel cell set-up showing all the constituent components, including the MEA (Nafion membrane and carbon cloth electrode). 110

Figure 4.3 - Cyclic voltammograms obtained in a 3-electrode system in a PBS buffer solution, for the different steps involved in the assembly of the sensing polymers on CC-Pt/Ru electrodes. (A) Highlights the results of the MIP (CC-Pt/Ru-CEA-MIP) and NIP (CC-Pt/Ru-NIP) electrodes, as well as MIP electrodes after removal of the CEA template (CC-Pt/Ru-MIP). (B) Zooms in the voltammograms of-CC-Pt/Ru-MIP and CC-Pt/Ru-NIP electrodes. 114

Figure 4.4 - Characterization results obtained by (A) Raman analysis of the different electrodes (Carbon Cloth supported EDOT/PPy, untreated Carbon Cloth-Pt/Ru and Carbon Cloth-Pt/Ru- MIP/NIP) and the corresponding confocal images; scanning electron microscopy analysis (SEM) of different electrodes including a (B) Carbon Cloth-Pt/Ru-MIP electrode, (C) Carbon Cloth-Pt/Ru-NIP electrode, (D) unmodified Carbon Cloth-Pt/Ru (control) with the corresponding elemental assignment of Pt, Ru and other chemical elements and (E) Carbon Cloth-Pt/Ru-MIP electrode with the corresponding elemental assignment of Pt, Ru and other chemical elements evidencing the S peak derivate for the presence of EDOT co-polymer. 115

Figure 4.5 - Electrochemical data obtained with 2 M MeOH for the passive DMFCs assemblies integrating different anodes in terms of (A) OCV start-up for control, MIP and NIP anodes and (B) respective EIS analysis; (C) current and power curve of a DMFC assembly including a control anode (without polymer) and (D) current and power curves obtained with MIP and NIP anode electrodes. 118

Figure 4.6 - Power curves of a biosensor DMFC obtained in a calibration experiment with consecutive incubations of CEA standards using 2 M of a MeOH solution for the readings. 121

Figure 4.7 - Power curves of a biosensor DMFC after a complete calibration, first with a solution of 0.5 M of MeOH until stabilization (dashed line) and later in the absence of the MeOH solution (empty container) in consecutively readings. 121

Figure 4.8 - Polarization and power curves of the passive DMFC assemblies using different MeOH concentrations for a DMFC with (A) an unmodified anode as a control and (B) a MIP-assisted anode and (C) the effect on the power in both the DMFC and the biosensor DMFC with different MeOH concentrations; (D) simplest scheme representing and

visually explaining the Pt-block by the polymeric layer which conditionate the MeOH oxidation and thus the power output recorded for both systems.……...…….121

Figure 4.9 - Polarization and power curves of a passive DMFC assembly with a MIP supported anode using (A) 0.5 M and (B) 0.05 M of MeOH feed solution until electric signal stabilization. 123

Figure 4.10 - Power curves of a biosensor DMFC obtained in a calibration experiment with consecutive incubations of CEA standards using 0.5 M of MeOH for the readings. 124

Figure 4.11 - Power curves obtained in electric signal stabilization after incubations of (A) buffer and (B) Cormay® serum. After 2 incubations of buffer the variation in the power signal is 0.05% which agrees with the normally variation observed with buffer before calibrations (0.05-1%). After 3 incubations of Cormay® serum the variation in the power signal is 1.4% which is in agreement to the variation observed in the system before calibrations (1-1.5%)..... 125

Figure 4.12 - Power-Current Density curves and the corresponding calibration curves obtained after incubation of CEA-increasing standards in the range of 30–30000 ng/mL prepared in (A) buffer and (B) Cormay® serum. Calibration curves for the MIP and NIP anode electrodes were traced using the average of the maximum power density obtained at each CEA concentration. 126

Figure 4.13 - Selectivity assays results (average of 3 different MIP-anodes with the respective standard deviation as error bars) performed with different possible interferents (CA15-3, glucose, urea) obtained in parallel, using different DMFC assemblies. 128

Figure 4.14 - Power-Current Density curves obtained with (A) the fuel cell stack (MIP anode) fed with ethanol solution (2 M and 0.05 M) and a (B) calibration test of a MIP-DMFC with the 0.05 M ethanol solution (including the corresponding calibration curve, inset) against increasing CEA concentrations in the rangeof 30–30000 ng/mL, prepared in buffer..... 129

Figure 5.1 – Overview of the PB-DMFC/Biosensor developed in this work with an example of the power curves obtained during a calibration against sarcosine (buffer).. 134

Figure 5.2 – Schematic representation of the various steps required to obtain an (A) PB-DMFC assembly on the paper substrates, which includes: the incorporation of the

electrolyte, the deposition of the anode/cathode inks, the paraffin impermeabilization and the silver ink current collectors; after the fabrication of the PB-DMFC platform and the evaluation of the electrochemical reaction (B) a sarcosine-sensitive MIP layer was obtained by electropolymerization on the anode side using EDOT/PPy monomers, and later the sarcosine template is removed under acidic conditions. 137

Figure 5.3 - Paper based methanol fuel cell prototypes tested during this work until meet the appropriate prototype n° 4..... 140

Figure 5.4 - Electrochemical data of PB-DMFCs in terms of polarization (empty symbols) and power curves (full symbols) obtained under different test conditions: (A) the Nafion® electrolyte incorporated into the paper matrix; (B) the paraffin amount used as an impermeabilizing agent; (C) operation of the device using various methanol concentrations in the range of 0.5–2.0 M; and (D) electrochemical impedance spectroscopy measurements under open-circuit conditions (OCV) using 0.5 and 2.0 M methanol concentrations. ... 142

Figure 5.5 - Polarization and power curves obtained in consecutive electrochemical readings of two PB-DMFCs assemblies using (A) 0.5 M of MeOH and (B) 2 M of MeOH. 145

Figure 5.6 - Polarization and power curves obtained in consecutive electrochemical readings of two PB-DMFCs assemblies using (A) 0.5 M of MeOH and (B) 2 M of MeOH. 146

Figure 5.7 - Characterization results of the paper fuel cells developed in this work: SEM Cross-sectional images of a (A) control cell PB-DMFC and a (B) polymer modified PB-DMFC /MIP; (C) overview of the anode layer of PB-DMFC and (D) PB-DMFC /MIP showing differences in the structure of the catalytic layer; topography analysis of (E) PB-DMFC and (F) PB-DMFC /MIP showing different roughness. Raman analysis at 532 nm for a control sample PB-DMFC, PB-DMFC /MIP and a sample with EDOT carbon support for comparison; confocal images of a PB-DMFC and PB-DMFC /MIP assemblies highlighting the color difference (blue) (G). TGA and DTG curves of different paper fuel cell units (PB-DMFC, PB-DMFC /MIP, PB-DMFC / NIP) in an inert atmosphere (nitrogen, 20 mL min^{-1}, heating rate 30 °C/min) (H). Overview of a PB-DMFC strip showing the chemical reactions responsible for the dual function (power and sensor) of the developed platform (I). 148

Figure 5.8- SEM images of the polymer modified PB-DMFC/NIP in: (A-B) cross-section and (C) topography surface analysis. EDS analysis of a (D) non-modified PB-DMFC assembly and a (E)) PB-DMFC/MIP configuration, evidencing the sulphur percentage detected in the sample. 149

Figure 5.9 - TGA thermograms of a control PB-DMFC in comparison with a paper impregnated with Nafion® electrolyte (Paper + Nafion®) and a paper impregnated with the paraffin hydrophobic agent (Paper + Paraffin) performed in an inert atmosphere (nitrogen, 20 mL min^{-1}, heating rate 30 °C/min). 151

Figure 5.10 - Analysis of the behavior of the different fuel cell platforms with respect to (A) general scheme complemented with surface SEM images evidencing the possible different methanol pathways in the fuel cell anode electrode and showing the blocking effect of the catalytic Pt active sites in the polymer modified fuel cells (PB-DMFC/Biosensor and PB-DMFC/NIP). The CB-PtRu is covered by a sarcosine imprinted film in the PB-DMFC/Biosensor, shown in blue color, or a control film without printed sites in the PB-DMFC/NIP, shown in gray color. The voids in the anode of the PB-DMFC/Biosensor allow a faster and more efficient reaction of the methanol fuel on the surface of the Pt catalysts compared to the polymer layer of the control (without voids), which acts as a barrier for the reaction of the methanol molecules. Comparison of the measured polarization and power curves recorded for the different paper fuel cell systems (PB-DMFC, PB-DMFC/Biosensor, PB-DMFC/NIP) (B) and evaluation of the EIS analysis of a PB-DMFC before, after polymerization and at the end of a calibration (C). 153

Figure 5.11 - Cyclic voltammograms obtained in a 3-electrode system in a PBS buffer solution (10 cycles, −0.3 V to 1.2 V, 25 mV/s), for the assembly of the PEDOT/PPy sensing polymer on the anode layer of PB-DMFCs (MIP and NIP) and corresponding removal step in sulfuric acid solution. 155

Figure 5.12 - EIS data and equivalent electric circuits (inlet) of a PB-DMFC before polymerization protocol (A), after polymerization (B) and after calibration (C). Measurements conducted under open-circuit conditions (OCV) using 0.5 M methanol concentrations. 157

Figure 5.13 - Power curves obtained in consecutive electrochemical readings using independent PB-DMFCs assemblies after stabilization and prior incubation with MES

buffer (A), human urine 10x times diluted (B) and human urine 100x times diluted (C) using 0.5 M of MeOH solution for the readings. 158

Figure 5.14 - Power-current density curves obtained during calibration after incubation of sarcosine standards of increasing concentrations prepared in buffer (A), with the respective calibration curve compared with a control experiment (NIP) in the range $1.0 \times 10^{-7} - 1.0 \times 10^{-3}$ mol/L (B); Power-current density curves obtained during calibration with sarcosine standard solutions prepared in healthy human urine in the same concentration range used in buffer (C), with the respective calibration curve compared with the NIP sample (D). All calibration curves were traced using the average of the maximum power density obtained at each sarcosine concentration. 160

Figure 5.15 - Selectivity assays in buffer using independent PB-DMFCs after incubation of a sarcosine standard solution (1.0×10^{-5} M) and sarcosine spiked with interfering compounds [urea (U), uric acid (UA), creatinine (C), glutamic acid and histidine (H)], recording of the respective power curves (A) and the respective interference analysis in normalized values (B). 163

Figure 6.1 – PEDOT/PB-DMFC/biosensor strips assembled in a 5-stack configuration to produce a voltage of ~1.5 V, to allow the color change of the paper based PEDOT:PSS electrochromic cell. 168

Figure 6.2 – Pre-treatment steps of the human serum (Cormay®) for L1CAM standards preparation: (1) – add $AgNO_3$ to the pure Cormay serum; (2)- stir in a stirring plate for 30 minutes until a yellow/white turve solution is formed; (3) – centrifugation at 10000 rpm during 10 minutes until the solution appears light yellow with a white precipitate in the bottom of the flask, indicating the removing of the chloride ions present in the initial serum; (0.1 M of Cl^- present in the initial serum) (4) – Cormay serum pre-treated is compatible for incubation in the anode side of the PEDOT/PB-DMFC with a 100x MES buffer dilution; (5)- example of a stabilization protocol using the diluted pre-treated serum in a PEDOT/PB-DMFC assembly containing the MIP sensor, evidencing a stable system after 4/5 incubations. 170

Figure 6.3 – Steps involved in the PEDOT/PB-DMFC development which includes (1) – the Nafion® electrolyte incorporation in the Whatman paper, (2) inks deposition (anode/cathode) in both sides of the electrolyte, (3) paraffin impermeabilization in the surrounding area of the electrodes (50/50 paraffin/IPA), and (4) electrical connector's

integration on the top edges with silver ink.; (5) this final assembly is isolated with glue tape to avoid leaking of the methanol solution and avoid short circuit; (6) the final PEDOT/PB-DMFC operates with a solution of methanol (0.5 M – 1 M) which is adsorbed in a square of adsorbent paper and with the cathode exposed to the atmospheric O_2; (7) a typical polarization and power curve are graphically represented for a PEDOT/PB-DMFC containing a MIP sensor to L1CAM detection after signal activation and stabilization. 173

Figure 6.4 - Schematic representation of the preparation of the anode/cathode inks for the PB-DMFC assembly using a high-speed ultrasound with microtip: the anode ink is composed by a mediated ultrasound synthetized nanocomposite of PEDOT/MWCNT-COOH/CB-PtRu dispersed in IPA in the presence of Nafion®, and the cathode ink is obtained by ultrasonication of a solution of CB-Pt, Nafion® and IPA(A). Polymerization tests using two different substrates (Whatman paper and FTO glass) to drop-cast two ultrasonicated solutions: Nafion®/EDOT/IPA and EDOT/IPA, evidencing the formation of a blue color in the sonicated solution containing Nafion® compound, both at room temperature and at 60 ˚C (with temperature the coloration was more intense) In the absence of Nafion® no coloration was observed in any substrate (at least in the 30 min of the experience duration) (B). General scheme of a typical PB-DMFC evidencing the Whatman paper impregnated with the Nafion® electrolyte which separates the anode and cathode electrodes, applied in both sides of Whatman/Nafion® electrolyte using the airbrush method; the chemical reactions that occurred in anode and cathode electrodes were also represented (C). Maximum power density recorded using different PB-DMFCs assemblies in relation to the addiction of different amounts of MWCNTs (0-10 mg) in the anode ink formulation (D); SEM image evidencing the topography of the anode layer of a PB-DMFC containing the composite PEDOT/MWCNT-COOH/CB-PtRu, revealing the nanotubes dispersed in the catalyst matrix (E)..... 174

Figure 6.5 - Schematic representation of the different steps involved in the development of the EC and characterization results obtained in the follow up of the final assembly. The steps involved consist: of PDMS spreading in the paper surface by spin coating (1500 rpm, 60 s) and curing at 60 ˚C (A) to obtain a hydrophobic paper/PDMS compared to the untreated paper (B). Adhesion promotor (MPTMS) anchoring in the paper/PDMS to improve binding of gold and PEDOT/PSS (C); gold electrical connections obtained after sputtering using a glass made mold protected in the center area (D); a plasma treatment (inclusion of hydroxide groups) was applied in the EC surface to decrease hydrophobicity

of the support, essential to bind PEDOT/PSS electrochromic compound (E). Differences observed in the presence and absence of MPTMS, after an electrochemical reading in terms of gold stability (F). FTIR-ATR analysis was used to follow the chemical modifications observed in the untreated paper, paper + PDMS, and paper + PDMS + MPTMS (G). Contact angle determination was also used to follow the water wettability and stability of the untreated paper and modified treated papers (H). 179

Figure 6.6 - Electrochemical data of PB-DMFCs in terms of polarization (empty symbols) and power curves (full symbols) obtained with different (nano)-ink formulations combining: hydrophobic components- layer of paraffin and PTFE (A) and the EDOT monomer in the ink formulations before applying ultrasonication in different concentrations (B), doped with different amounts of TiO_2 (C) and doped with different amounts of MWCNTs-COOH (D); Characterization results by FTIR-ATR spectra of the PEDOT-CB-PtRu powder nanocomposite obtained by ultrasonication in comparison with EDOT monomer and commercial CB-PtRu powder (E). Thermogravimetric analysis of the different steps involved in the anode nano-ink preparation: commercial CB-PtRu powder (unmodified), CB-PtRu-MWNTs-EDOT ultrasonicated in IPA until gelification of the sample (30 s), and CB-PtRu-MWNTs-EDOT-Nafion® upon ultrasonication during 15s (F). 182

Figure 6.7 - Steps involved in the development of a PEDOT/PB-DMFC/biosensor by electropolymerization, evidencing the interactions of the PEDOT based anode with the EDOT solution in the MIP formulation (A) and characterization results obtained by Raman analysis at 532 nm of the different PEDOT/PB-DMFC assemblies (PEDOT/PB-DMFC/MIP and PEDOT/PB-DMFC/NIP) with the corresponding I_D/I_G calculated ratios (inset) (B); Scanning electron microscopy analysis (SEM) images in cross-section and topography of a PEDOT/PB-DMFC (C), and electropolymerized samples to obtain the biosensor function (PEDOT/PB-DMFC/MIP) (D) and the control (PEDOT/PB-DMFC/NIP) (E). 186

Figure 6.8 - Cyclic voltammograms obtained in a 3-electrode system in a PBS buffer solution (5 cycles, −0.3 V to 1.2 V, 50 mV/s), for the assembly of the PEDOT sensing polymer on the anode layer of PEDOT/PB-DMFC- MIP in comparison with the control PEDOT/PB-DMFC- NIP and corresponding removal step in sulfuric acid solution. 187

Figure 6.9 - Power curves obtained in consecutive electrochemical readings using independent PEDOT/PB-DMFCs assemblies after stabilization and prior incubation with

MES buffer (A), pre-treated diluted (100x) Cormay® serum (B) using 0.5 M of MeOH solution for the readings..... 189

Figure 6.10 - Power-current density curves obtained during a calibration after incubation of L1CAM standards of increasing concentrations prepared in buffer (A), with the respective calibration curve compared with a control experiment (PEDOT/PB-DMFC/NIP) in the range 1.0×10^{-12} – 1.0×10^{-8} M (B); Comparison of the recorded power-current density curves of a pair of PEDOT/PB-DMFC/biosensor/ PEDOT/PB-DMFC/NIP obtained in the same batch, showing the effect of the polymer cavities in the power produced by the two different set-ups (C). Power-current density curves obtained during a calibration with L1CAM standard solutions prepared in cormay serum® in the same concentration range used in buffer (D), with the respective calibration curve compared with the control PEDOT/PB-DMFC/NIP sample (E). All calibration curves were drawn using the average of the maximum power density obtained at each L1CAM concentration. Selectivity assays results (buffer) obtained using independent PEDOT/PB-DMFC/biosensor strips after incubation of a L1CAM standard solution (1×10^{-10} M) and L1CAM spiked with interfering compounds [carcinoembryonic antigen (CEA), glucose (GLU) and urea] with the respective interference analysis presented in normalized values (F)..... 191

Figure 6.11 - Analysis of the PEDOT/PB-DMFC/biosensor strips assembled in a 5-stack configuration to produce a voltage of ~1.5 V (recorded with a multimeter) (A), connected to the EC cell (B) to promote the color change of PEDOT:PSS polymer (C) from light to dark blue (inversion of polarization) (D). Color variation of PEDOT:PSS polymer obtained in three electrodes system (E) and the respective voltammogram in the range of -2V to +2V (F). Calibration of PEDOT/PB-DMFC/biosensor-EC showing the RGB color coordinates extracted from image J software (using blue coordinates) in three different spots (G). Schematic representation of the PEDOT/PB-DMFC/biosensor and EC evidencing the flexibility of each component and the overall properties suitable for wearable devices (H). Example of the pictures recorded during a calibration protocol after L1CAM incubation in the range of 1x10-12-1x10-8 M (I). 195

Figure 6.12 - Different images of the PEDOT/PB-DMFC-stack evidencing the electrical set-up (A), and the anode sensing anodes (B) electrical connected to the cathode electrodes (C). 196

List of tables

Table 3.1- Previous works reporting molecularly-imprinted polymers for CEA detection in the literature. 104

Table 4.1- Calculated I_D/I_G ratio obtained from Raman Spectra for Carbon Cloth-Pt/Ru (control), MIP and NIP Carbon Cloth polymerized samples. 116

Table 5.1- Calculated I_D/I_G ratio obtained from Raman Spectra for the PB-DMFC and polymerized PB-DMFC/MIP samples 150

Table 6.1- Summary of the electrochemical characterization of the different PB-DMFCs assemblies produced in this work and comparison with prototype 1. 176

List of Abbreviations

AFCs	Alkaline fuel cells
CB	Carbon Black
CEA	Carcinoembryonic antigen
CE	Counter electrode
CEL	Chemiluminescence immunoassay
CC	Carbon cloth
CC-PtRu	Carbon cloth with platinum ruthenium
CL	Catalyst layer
CNFs	Carbon nanofibers
CV	Cyclic voltammetry
DMFC	Direct methanol fuel cell
DMSO	Dimethyl sulfoxide
DNA	Deoxyribonucleic acid
DSSC	Dye-sensitized solar cells
DPV	Differential pulse voltammetry
EC	Electrochromic cell
ECL	Electrochemiluminescent immunoassay
EIS	Electrochemical impedance spectroscopy
ELISA	Enzyme-Linked Immunosorbent Assay
FFPs	Flow field plates
FTO	Fluorine doped Tin Oxide
FTIR-ATR	Fourier transform infrared spectroscopy-Attenuated total reflectance
GDL	Gas diffusion layer
GLOBOCAN	Global Cancer Observatory
LOD	Limit of detection
MC	Mesoporous carbon
MCFCs	Molten carbonate fuel cells
MEA	Membrane electrode assembly
MES	2-(N-morpholino) ethanesulfonic acid
MIP	Molecularly imprinted polymer

MPL	Microporous layer
MWCNTs	Multiwalled carbon nanotubes
MWCNT-COOH	Multi-walled carbon nanotube, carboxylic acid functionalized
MPTMS	Mercaptopropylmethyldimethoxysilane
NIP	Non-imprinted polymer
OCV	Open circuit voltage
PAFCs	Phosphoric acid fuel cells
PANI	Polyaniline
PBS	Phosphate buffered saline
PDMS	Polydimethylsiloxane
PEDOT	Poly(3,4-ethylenedioxythiophene
PEM	Polymer electrolyte membrane
PEMFCs	Polymer electrolyte membrane fuel cells
PEDOT/PSS	Poly(3,4-ethylenedioxythiophene)-poly(styrenesulfonate)
PFSA	Perfluorosulfonic acid
PL	Photoluminescence
POC	Point of care
PPy	Polypyrrole
PTFE	Polytetrafluoroethylene
PTh	Polythiophene
Py	Pyrrole
QCM	Quartz crystal microbalance
RE	Reference electrode
RNA	Ribonucleic acid
RT-PCR	Real-time polymerase chain reaction
SARC	Sarcosine
SARDH	Sarcosine dehydrogenase
SEM	Scanning electron microscope
SERS	Surface-enhanced Raman scattering
SOFCs	Solid oxide fuel cells
SPE	Screen-printed electrodes
SPR	Surface plasmon resonance
SWV	Square wave voltammetry
TBP	4-tertbutylpyridine

TEM	Transmission electron microscopy
TGA	Thermogravimetry analysis
WE	Working electrode
WHO	World Health Organization

Symbols

E	Applied potential
E_{pc}	Peak cathodic potential
E_{pa}	Peak anodic potential
f	Excitation frequency
i_{pc}	Cathodic current
i_{pa}	Anodic current
R_{act}	Activation resistance
R_{mt}	Mass transfer resistance
R_{ohm}	Ohmic resistance
R_s	Solution resistance
t	Time
U	Sinusoidal potential
W	Warburg impedance
Z	Impedance
w	Angular frequency
ΔE	Electromotive force
ΔG	Free energy

Chapter 1

Framework

1.1 Motivation

According to the most recent World Health Organization (WHO) data (WHO, 2023), one in five people worldwide develops cancer during their lifetime. This upsetting statistic turns the prevention and early cancer diagnosis into one of the most significant public health challenges. In developed countries, this disease is the leading cause of death nevertheless cancer mortality can be diminished through the early detection of tumours. In the last 3 years, the diagnosis and treatment of cancer were adversely affected by the coronavirus disease (COVID-19) pandemic, and this delay may be responsible for increasing substantially cancer mortality worldwide. In this context, arises the need of developing cancer biomarkers screening devices that could allow a simple, faster, and *in loco* diagnostic, contributing to an increase in the number of individuals tested in the screening programs. Despite all the research efforts that have been made in the last decades, simple and quick diagnostic tools for cancer screening that can be used and provide results "*on time*" are still lacking.

The main motivation of the present work was the development of portable electrical independent electrochemical biosensors, for targeting important cancer markers involved in different types of cancer diagnosis and progression. The electrical autonomy is accomplished by integrating a sensing layer into the anode of a direct methanol fuel cell (DMFC), which allows the construction of a simple, and portable DMFC/biosensor where it is possible to correlate the electrical signal measured with the concentration of the cancer biomarker from patient fluids. Furthermore, to accomplish a configuration that is suitable for everywhere usage, a novel flexible paper-based fuel cell strip was developed enabling it to improve the portability, miniaturization, sensitivity, and faster

results obtained with the first developed DMFC/biosensor prototype. Moreover, these paper fuel cell strips can be assembled in a stack, to increase the voltage produced allowing the connection to a user-friendly paper electrochromic cell, that acts as a signalling device. This simple user-friendly configuration colour readout, works with few microliters of a methanol solution and with oxygen from atmospheric air, being equipment-free and enabling quick and low-cost readings that are appropriate for POC testing.

1.2 Objectives

The development of the biosensor devices results mostly from the work carried out at BioMark@ISEP (Polytechnic Institute of Porto, Portugal) in collaboration with CEFT (Department of Chemical Engineering, Faculty of Engineering, University of Porto, Portugal) for the design of the first developed fuel cell prototype. The final part of this work, which consists in the development of an electrochromic cell, was developed in collaboration with LEPABE (Laboratory for Process Engineering, Environment, Biotechnology and Energy, Faculty of Engineering, University of Porto).

This work aims to develop an autonomous electrochemical fuel cell biosensor assembly for targeting cancer protein markers related to different important types of cancer. Achieving this general objective requires fulfilling the following objectives:

- Development and characterization of suitable fuel cell assemblies operating in passive mode; optimization of the best conditions for a passive DMFC system considering the best conditions for sensor layer integration.

- Selection of the cancer biomarkers that are most relevant in cancer diseases;

- Design and integration of bio-recognition layers, especially obtained by molecular imprinting technology, which are sensitive to the selected cancer biomarkers;

- Analysis of the rebinding response of the bio-recognition layers produced, using suitable electrochemical techniques to fuel cells characterization; integration

(inside/outside) of the most promising bio-recognition layers developed into the passive fuel devices and analysis of the corresponding performance.

- Calibrations of the developed assemblies containing the fuel cell/biosensor to evaluate the performance of the combination of the bio-recognition layer and the transducer; different media should be tested (buffer and serum medium) as also real samples (such as urine) to assess the selectivity of the response of the final devices.

- And ultimately, the fabrication of a sensing platform, completely electrical independent and self-signalled, incorporating a stack of fuel cell paper strips, suitable for application in POC.

1.3 Thesis outline

This thesis is organized in seven chapters, starting with this chapter, **Chapter 1** which includes the motivation and main goals of this PhD work. The description of the structure of the thesis is also presented. A list of publications and communications (oral and poster) in the context of this PhD thesis is as well presented.

Chapter 2 includes a general introduction, providing fundamental background about the different topics involved in this work. The principle and design of biosensor devices and their importance in the screening of cancer biomarkers are presented. A brief state-of-the-art related to the selected cancer biomarkers is also given. A description of the fuel cell technology as power source is made, emphasizing the DMFCs which are relevant to this work. An overview of the most commonly used nanomaterials with application as fuel cell components to achieve the best fuel cell performance and their main applications is also addressed.

Chapter 3 presents the main results obtained in the development, characterization, and application of a biomimetic plastic antibody film produced by polymer imprinting technology, for the detection of carcinoembryonic antigen (CEA, an important biomarker

involved in different types of cancer). This biosensing film was integrated into the electrical circuit of a DMFC, working in passive mode and used as power supply and signal transducer. The results obtained evidenced the possibility of using a DMFC as a transducing element in an electrochemical sensor, confirming the sensitive and selective readings of the (bio)sensing imprinted film. This configuration can be improved by integrating the sensor inside the fuel cell, to obtain a simpler self-powered configuration compatible with POC analysis.

To overcome this limitation and obtain a simpler configuration, **Chapter 4** describes an all-in-one approach that involves a hybrid methanol fuel cell operating simultaneously as biosensor and power source in a single device. The molecularly-imprinted polymer (MIP) previously tailored for CEA detection was adapted to be obtained *in situ* directly in the anode electrode of the fuel cell. The overall power of this hybrid system is CEA concentration dependent, operating in a simple and effective concept, and is closer to meeting POC requirements. Thus, the levels of CEA detection were better in the configuration consisting of the biosensor unit externally connected to the fuel cell, since methanol molecules keep adsorbed during the stabilization/calibration experiments, acting as a background memory signal.

To further improve the response of the hybrid fuel cell/biosensor device, **Chapter 5** describes the development and characterization of a completely novel fuel cell platform paper strip, with an easy and effective method of adding/removing the methanol fuel solution and also incubating the patient sample. Besides the novelty of developing a flexible paper-based methanol fuel cell, this platform has the advantage of the simplest set-up configuration, containing all the components of the fuel cell and the biosensor layer in a small square of paper. This novel hand-made methanol fuel cell designed on a paper substrate, consists of a miniaturized system, which turns it completely compatible with the POC environment since it does not require any toll for its operation. Thus, this self-powered paper strip PB-DMFC/biosensor can be used for screening and monitoring sarcosine biomarkers, herein used as a proof-of-concept. Further improvements of this first PB-DMFC/biosensor prototype can be made, mostly in terms of materials and fabrication procedures to obtain a higher voltage and sensitivity.

To enhance both the power produced and sensitivity of the previous approach, a new approach was developed and presented in **Chapter 6**. Herein, the incorporation of poly(3,4-ethylenedioxythiophene) (PEDOT) in the anode ink formulation allowed the

replacement of the hydrophobic paraffin as impermeabilization agent, and since this compound is a semi-conductor polymer, the power, voltage and stability of the paper strips was improved. In addition, the presence of PEDOT through the anode electrode enabled the creation of a sensing layer whit higher specificity to the final target selected for this work - L1CAM recombinant protein. This improved power/sensitivity paper fuel cell configuration can operate in two different modes: single-cell device and five-stack cell device. The five-stack cell device allowed the connection to a developed electrochromic cell (EC) also paper-based containing PEDOT as a colour change substance. This final system remains completely flexible and with a simple set-up, acting as a fully autonomous and self-signalled sensing system with higher potential and suitable for POC applications.

Finally, **Chapter 7** summarizes the main conclusions of the present work, highlighting the potential applications and future work.

1.4 List of publications

1.4.1 Papers published in international scientific journals

- ✓ Liliana P. T. Carneiro, Alexandra Pinto, Dzmitry Ivanou, Adélio M. Mendes, M. Goreti F. Sales, "Portable PEDOT modified flexible paper-based methanol fuel cell (PEDOT/PB-DMFC) sensing platform applied to L1CAM recombinant protein detection", accepted in Applied polymers materials (19-02-2024).

- ✓ Nádia S. Ferreira, Liliana P.T. Carneiro1, Alexandra M.F.R. Pinto, M. Goreti F. Sales, "Fuel cells operating as an immunosensor for cancer biomarker screening", Biosensors and Bioelectronics: X (2023), 14, 100344.

- ✓ Carolina S. Hora, Ana P. M Tavares, Liliana P. T Carneiro, Dzmitry Ivanou, Adélio M Mendes, M Goreti F Sales, "New autonomous and self-signaling biosensing device for sarcosine detection", Talanta (2023), 257, 124340.

- ✓ Liliana P. T. Carneiro, Alexandra M. F. R. Pinto, M. Goreti F. Sales, "Development of an innovative flexible paper-based methanol fuel cell (PB-

DMFC) sensing platform – Application to sarcosine detection", Chemical Engineering Journal (2023), 452, 139563.

- ✓ Nádia S. Ferreira, Liliana P. T. Carneiro, Christian Viezzer, Maria J. T. Almeida, Ana C. Marques, Alexandra M. F. R. Pinto, Elvira Fortunato, M. Goreti F. Sales, "Passive direct methanol fuel cells acting as fully autonomous electrochemical biosensors: Application to sarcosine detection", Journal of Electroanalytical Chemistry, (2022), 922, 116710.

- ✓ Liliana P. T. Carneiro, Alexandra M. F. R. Pinto, Adélio Mendes, M. Goreti F. Sales, "An all-in-one approach for self-powered sensing: A methanol fuel cell modified with a molecularly imprinted polymer for cancer biomarker detection", Journal of Electroanalytical Chemistry, (2022), 906, 116009.

- ✓ Ana R. Cardoso, Liliana P. T. Carneiro, Gustavo Cabral-Miranda, Martin F. Bachmannde M. Goreti F. Sales "Employing bacteria machinery for antibiotic detection: Using DNA gyrase for ciprofloxacin detection", Chemical Engineering Journal, (2021), 409, 128135.

- ✓ Liliana P.T. Carneiro, Nádia S. Ferreira, Ana P. M. Tavares, Alexandra M. F. R. Pinto, Adélio Mendes, M. Goreti F. Sales "A passive direct methanol fuel cell as transducer of an electrochemical sensor, applied to the detection of carcinoembryonic antigen", Biosensors and Bioelectronics, (2021), 175, 112877.

- ✓ Ana P. M. Tavares, Liliana A. A. N. A. Truta, Felismina T. C. Moreira, Liliana P. T. Carneiro, M. Goreti F. Sales, "Self-powered and self-signalled autonomous electrochemical biosensor applied to carcinoembryonic antigen determination", Biosensors and Bioelectronics, (2019), 175, 112877.

1.4.2 Book chapter

- ✓ Liliana P.T. Carneiro, Nadia S. Ferreira, Alexandra M.F.R. Pinto and M. Goreti F. Sales, "Nano-inks for fuel cells application" – Chapter 13, SMART

MULTIFUNCTIONAL NANO-INKS - Fundamentals and Emerging Applications, Elsevier, (2023), 333, ISBN: 978-0-323-91145-0.

1.4.3 Communications presented in national and international scientific conferences

- ✓ Liliana P. T. Carneiro; Maria Goreti Ferreira Sales; Alexandra Ferreira Rodrigues Pinto. "A new vision for fuel cells: application in cancer biomarker screening", Encontro Ciência 21, Lisboa (Portugal), June 2021, (poster presentation).

- ✓ L.P.T. Carneiro, A.M.F.R. Pinto, M.G.F. Sales, "A passive direct methanol fuel cell acting as electrochemical biosensor, applied to the detection of carcinoembryonic antigen", Biosensors 2021 – online, September 2021, (poster presentation).

- ✓ L. P. T. Carneiro, N. S. Ferreira, A. P. M. Tavares, M. G. F. Sales, " Biosensor for carcinoembryonic antigen determination powered by passive methanol fuel cell", GSS MIP 2019, Berlim (Germany), 29 August 2019, (oral presentation).

- ✓ L.P.T. Carneiro, M.G.F. Sales, L.R. Brandão, "Fuel cell transduced biosensor for myoglobin screening", Biosensors 2018, 12-15 June 2018, Miami, USA, (poster presentation).

Chapter 2

2. Introduction

This chapter presents a brief background, mainly regarding the fundamental principles related to the two important areas approached in this thesis: fuel cells power source technology and electrochemical biosensors. The importance and application of methanol fuel cells in the achievement of lightweight and portable devices with potential applications as point-of-care medical devices were discussed. The biosensor element principle and design are presented and related to the possibility of screening some important cancer biomarkers with special relevance to the present thesis. An overview concerning the selected cancer biomarkers is also performed. In addition, different fuel cell assemblies were explored as simple, low-cost, user-friendly, and electrical independent sensing platforms by conjugation with an electrochromic cell.

2.1 Cancer disease

According to the World Health Organization (WHO), cancer is the term given to a vast group of diseases that can affect practically any organ or tissue in the body, characterized by an uncontrolled development of abnormal cells, which can also spread into the surrounding organs/tissues [1]. This disease was globally responsible for a higher number of cases in the 2020 year (Total: 19 292 789 cases) with almost 10.0 million cancer deaths (Total: 9 958 153 deaths) according to the data available in *GLOBOCAN 2020*, which are adapted and schematically represented in Figure 2.1 [2]. The most commonly diagnosed types of cancer are presented in Figure 2.1-A, with breast cancer appearing as the most common, followed by lung, colorectal, prostate, and stomach cancers. Figure 2.1-B shows the mortality of the different cancer types, with lung cancer leading the recorded mortality (18% of the overall cancer deaths), followed by colorectal, liver, stomach, and breast cancer.

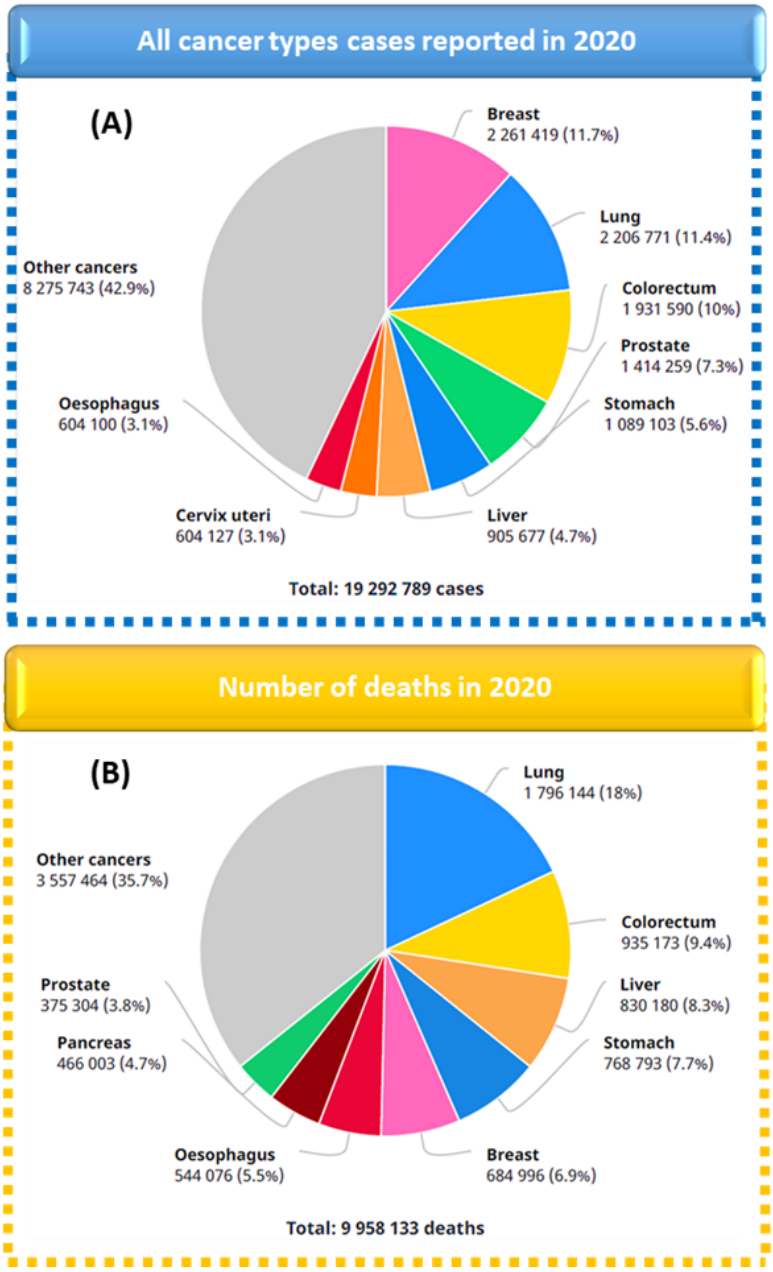

Figure 2.1 – Graphic representation of all new cancer cases (A) and mortality associated to cancer disease (B), for both genders and ages in the 2020 year. Figure adapted from GLOBOCAN 2020 - https://gco.iarc.fr/today/data/factsheets/cancers/39-All-cancers-fact-sheet.pdf.

In the case of men, the lung cancer is the most commonly diagnosed cancer, and the leading cause of cancer obits in these individuals, followed by prostate and colorectal cancer for incidence and liver and colorectal cancer in terms of mortality; in women, breast cancer appears as the most frequently diagnosed cancer and also the leading cause of cancer death in the female individuals, followed by colorectal and lung cancer in terms of incidence, and inversely in terms of mortality [3].

The cancer incidence seems to be related to several factors, including lifestyle (high body mass index, lack of physical activity, tobacco and alcohol) and also population growth and ageing [4–6]. One in five persons will be diagnosed with cancer in their lifetime [7]. This upsetting statistic turns cancer disease a leading cause of concern worldwide, as it is a barrier of increasing life expectancy and life quality, for both men and women. Cancer mortality can be sustainably reduced if the disease is detected and treated at early stages. As such, early detection is a crucial tool to organize the appropriate treatment plan to improve the chances of survival [8]. With the COVID-19 pandemic, a decline in cancer screening was observed, due to the overwhelming of the health care systems allied to the goal of reducing the risk of spreading COVID-19 in healthcare settings. The precise effects at long term of this late cancer screening are difficult to predict, but the importance of developing simple, fast and sensitive detection strategies is clear, as they increase healing chances while decreasing costs of healthcare systems.

2.2 Cancer biomarkers

The detection of cancer at its early stages is a fundamental tool to increase the cancer survival rate, with the cancer-specific biomarkers playing a fundamental role in this field. Cancer biomarkers are specific biological molecules which are released in tumour tissues or biological fluids during the first stages of cancer disease in levels not found in healthy individuals [9]. Cancer biomarkers may also be tumour specific, thereby crucial to identify the cancer type, phase and follow-up clinical treatment [10]. Several types of biomarkers were identified in the last years, linked to different cancer diseases. Cancer biomarkers can include proteins (e.g. enzymes or receptors), nucleic acids (e.g. microRNA, DNA), antibodies and peptides, amongst other categories (Figure 2.2); they can be found in the circulation system (blood, serum or plasma) or secretions (urine, saliva, or nipple discharge) [11]. The main goal of the cancer biomarker field is the development of simple, low-cost, reliable and sensitive detection and monitoring approaches, for early disease screening, tumour identification, cancer risk assessment and evaluation of the disease progression, regression and recurrence [12].

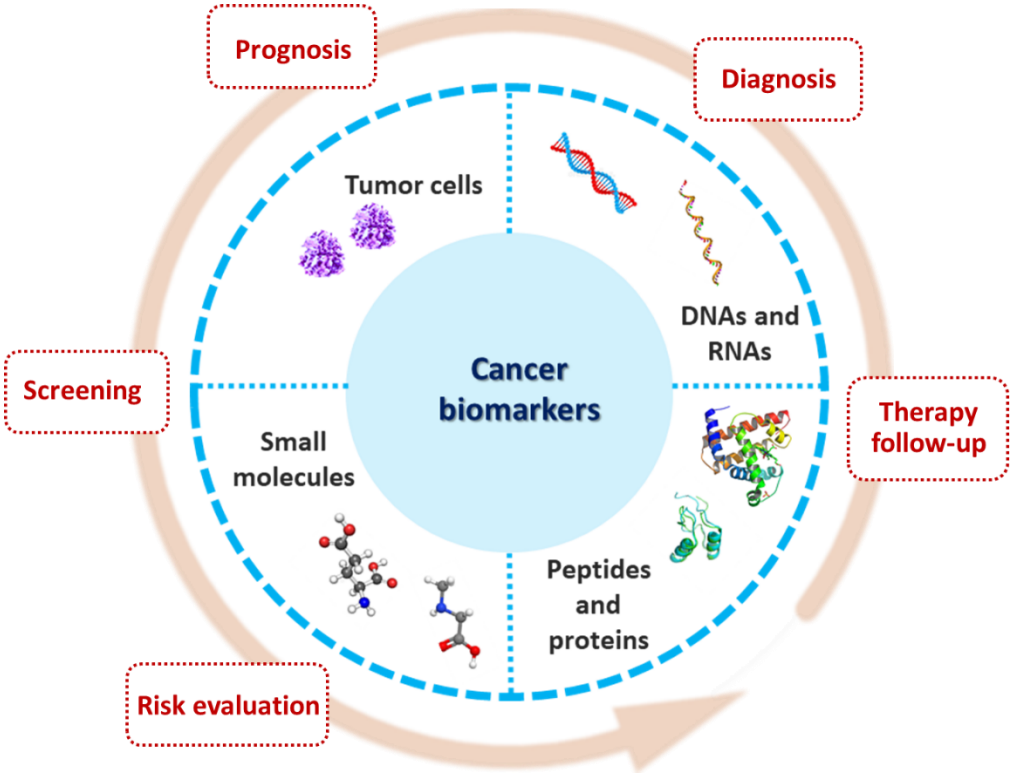

Figure 2.2 – Schematic illustration of different types of cancer biomarkers and their role in the five main areas of controlling cancer disease: diagnosis, therapy follow-up, risk evaluation, screening and prognosis.

This PhD thesis involves the detection of different cancer biomarkers, for which specific bio-recognition layers were developed. The selected biomarkers were carcinoembryonic antigen (CEA), sarcosine aminoacid and recombinant human L1CAM protein. These molecules are involved in the screening of different cancer diseases, and alterations in their values of reference may be a strong indication of the presence of cancer disease. Each of these molecules has a particular importance and role in cancer disease detection and follow-up.

2.2.1 Carcinoembryonic antigen (CEA)

CEA is a complex glycoprotein with approximately 150–180 kDa that was identified as the first human cancer-associated antigen in the colon rectal cancer in 1965 by Gold and Freedman [13,14]. CEA protein is not found in significant amounts after birth, therefore higher levels may indicate pathologic events, especially colon and rectal

cancer [15]. CEA is also a tumour marker and CEA levels >10 ng/mL are frequently associated with malignant conditions; CEA levels >20 ng/mL may be suspicious for metastatic disease [15].

CEA can be measured in serum and has been one of the most extensively used clinical tumour biomarkers for colorectal and some other cancer diseases due to the restricted expression in healthy individuals and expression at high levels in positive tumour, being considered a broad-spectrum cancer biomarker [16]. Hence, the CEA level can be measured before and after surgery, to monitor the level of surgical success and predict recovery. In addition, CEA levels can be measured during chemotherapy treatment to follow-up the disease progression [17]. Thus, detecting CEA has great importance in diagnosis, as well as in monitoring and therapeutic adjustments made throughout the cancer treatment [17].

CEA structure consists of a polypeptide chain with variable carbohydrate components and high degree of glycosylation. It can attach to the cell membrane, modulating the intercellular adhesion and also playing a role in intracellular signalling (Figure 2.3-A/B)[18].

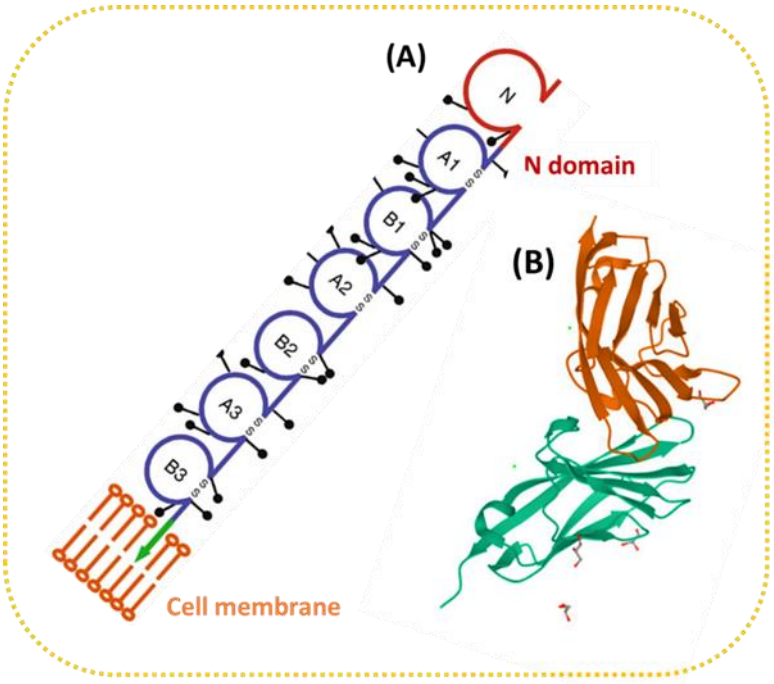

Figure 2.3 – Schematic representation of CEA structure (A) displaying insertion of CEA into the plasma membrane (down arrow) (adapted from [19]) and (B) 3D structure of the N-terminal domain of CEA (adapted from [20]).

Currently, immunological assays are the fundamental tool to target CEA in the field of clinical diagnoses and biochemical studies. Several detection methods are developed in the last years, such as, enzyme-linked immunosorbent assay (ELISA) [21], electrochemiluminescent immunoassay (ECL) [22], chemiluminescence immunoassay (CEL) [23] and the radiation immunological assay [24]. These methods are usually linked to sensitive and selective results, due to the high affinity of antigen/antibody interactions. However, most of these methods are not so simple, involving pre-treatment of the samples, highly qualified personnel to operate sophisticated and expensive instrumentation, long assay times, higher volume samples and the high price of the reactants used [25].

Recently, the research in electrochemical biosensors for targeting CEA has attracted widespread attention, due to their simple architecture, non-invasive, low cost, rapid response and high sensitivity. Several research works can be found in literature concerning the development of electrochemical biosensors to detect CEA biomarker making use of different bio-recognition entities, such as antigens or antibodies [26,27], aptamers [17] and MIPs [28,29]. The extensive efforts devoted to CEA detection endure the importance of this biomarker in cancer disease [30].

2.2.2 Sarcosine

Sarcosine (SARC), also known as N-methyglycine, is a derivative of the amino acid glycine and was identified as a potentially important biomarker related to prostate cancer progression and aggressivity [31]. The presence of SARC in the human urine was also suggested as a promising biomarker for prostate cancer diagnostics [32]. SARC occurs in the body as a product of the metabolism of glycine by the glycine N-methyltransferase (GMT) and is metabolized by sarcosine dehydrogenase (SARDH) enzyme (Figure 2.4) [33].

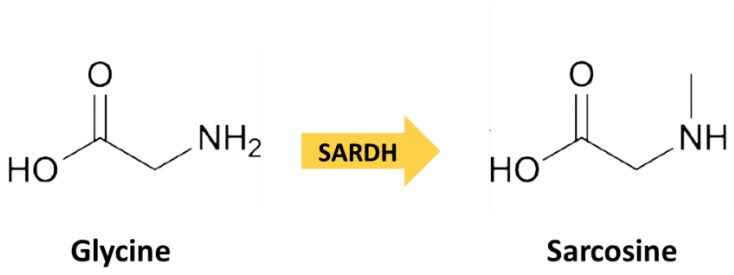

Figure 2.4 – Chemical structure of glycine and the derived amino acid sarcosine.

SARC can be found in human body in the skeletal muscles and prostate. In the laboratory environment, the analytical techniques commonly employed for the determination of SARC include chromatography [34–36] and mass spectrometry [37,38]. Therefore, these techniques require specific and high-cost equipment, specialized personnel to operate the equipment and also a complex pre-treatment of the samples to analyze. As an alternative, SARC can be quantified indirectly, using colorimetry, fluorimetry and electrochemical biosensors. These methods involve the same principle which is related to the reaction between SARC and SARC oxidase (SOX) enzyme [39]. The enzyme SOX catalyzes the oxidative demethylation of SARC into glycine, formaldehyde and hydrogen peroxide [40]. While the use of SOX enzyme in analytical systems may offer advantages in terms of selectivity, the chemical modification employed for its immobilization is critical, as it may cause enzyme denaturation or conformational changes affecting reproducibility and sensitivity [41].

The role of SARC in cancer diagnosis and prognosis has been extensively discussed in different works and some contradicting studies can be found reporting that this metabolite should not be used as a diagnostic marker [42,43]. Therefore, the overexpression of SARC observed in patients with prostate cancer and also the association of SARC with other potential metabolites in the patient's urine may be useful in improving the diagnostic values, helping in the identification of cancer-related metabolic abnormalities [44,45]. In addition, SARC has an important role in controlling immunity, acting as cell marker and being recognized by a high number of receptors [46], which increases the importance of SARC detection and quantification in clinical trials.

2.2.3 Recombinant human L1CAM protein

The recombinant human protein (L1CAM) is a cell adhesion molecule that belongs to the immunoglobulin superfamily of cell adhesion molecules (IgCAM) and was initially identified on the neuronal system [47]. Later, its overexpression of L1CAM in various types of cancer was reported, mainly in advanced stages of tumours and metastases [48]. This relation with cancer progression makes L1CAM an important target to be considered. A general schematic topology of L1CAM is represented in Figure 2.5. The extracellular portion is subject to membrane cleavage generating a soluble L1CAM with a molecular weight in the range of [200- 220 kDa] [49]. The extracellular region is

composed of six immunoglobulin-like domains and five fibronectin domains and an N-glycosylation site located at the first fibronectin domain [50]. The L1CAM cleavage and release of the soluble molecule is involved in the promotion of migration, invasion and protection from apoptosis of cancer cells [51].

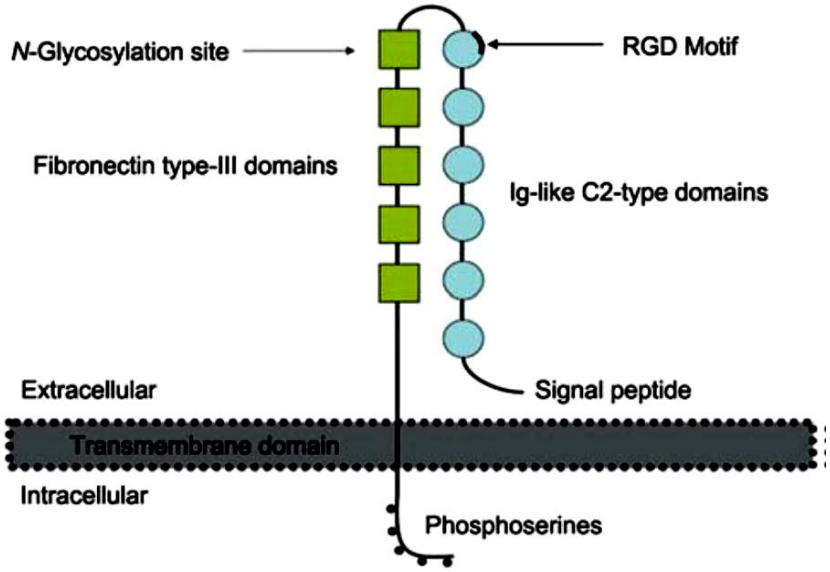

Figure 2.5 – General schematic topology of human L1CAM, evidencing the fibronectin domains as green squares, the Ig-like domains as blue circles and the potential N-glycosylation site. Adapted from [50].

The L1CAM molecule can be found in serum and the most commonly employed approaches for its detection are the enzyme-linked immunosorbent assay (ELISA), radioimmunoassay and real-time polymerase chain reaction (RT-PCR) [52,53]. Recently, the role of L1CAM outside the nervous system has been extensively investigated and has been reported that this molecule is a key factor during the progression of human cancers [54]. L1CAM molecule has many advantages as a valuable target, since it is important for tumour progression and promotes cell invasion and metastatic formation, being overexpressed in several cancer types, such as ovarian and pancreatic carcinomas [54]. For these reasons, LCAM is considered an important and suitable biomarker for diagnostic/prognostic protocols and also an attractive target for cancer therapy [55].

2.3 Biosensors

Biosensors are analytical devices that integrate a recognition element coupled to a physicochemical transducer, with the ability of converting a biological response into a detectable signal. Their development has started in 1960 with the invention of the first enzymatic biosensor, by Clark and Lyons, for detection of glucose from blood samples [56], in response to the limitations of the conventional methods involved in routine analytical testing procedures. Conventional methods are, in general, of high complexity (specialized technicians are required, as well as complex equipment) and time consuming, requiring also high sample volume. In contrast, biosensors offer the possibility of performing clinical analysis outside the laboratory with a simple, quick, and relatively inexpensive procedure. The combination of different materials (biologic entities, synthetic polymers, electronic components) has further opened new horizons into the development of biosensors with exceptional analytical features, and wide range of applications. Biosensors can today be applied to a wide range of targets, from small to large molecules (including body fluids, food samples and cell cultures).

The signals produced by biosensors are of electronic or optical nature and are proportional to the specific interaction between the analyte and recognition element [57]. Signals are measured and analyzed rapidly and with high sensitivity/selectivity, making biosensors ideal tools for POC applications. Biosensors are also robust and easy to use, enabling in specific conditions portability and real time analysis, being therefore important and suitable tools for detecting cancer biomarkers routinely.

There are various types of biosensors, according to the receptor element and transducer employed [58]. A general scheme of a biosensor is represented in Figure 2.6, concerning the most common sensing layers employed and the different transducer modes. According to the transducer employed, biosensors can be divided into different categories, as electrochemical, optical, thermometric, piezoelectric and magnetic. There are also several groups of compounds that may be used as recognition element. A brief description concerning different transducer modes and recognition elements are presented in the next topics, with special emphasis to electrochemical detection and biomimetic materials, since these are involved in the methodologies adopted in this PhD thesis.

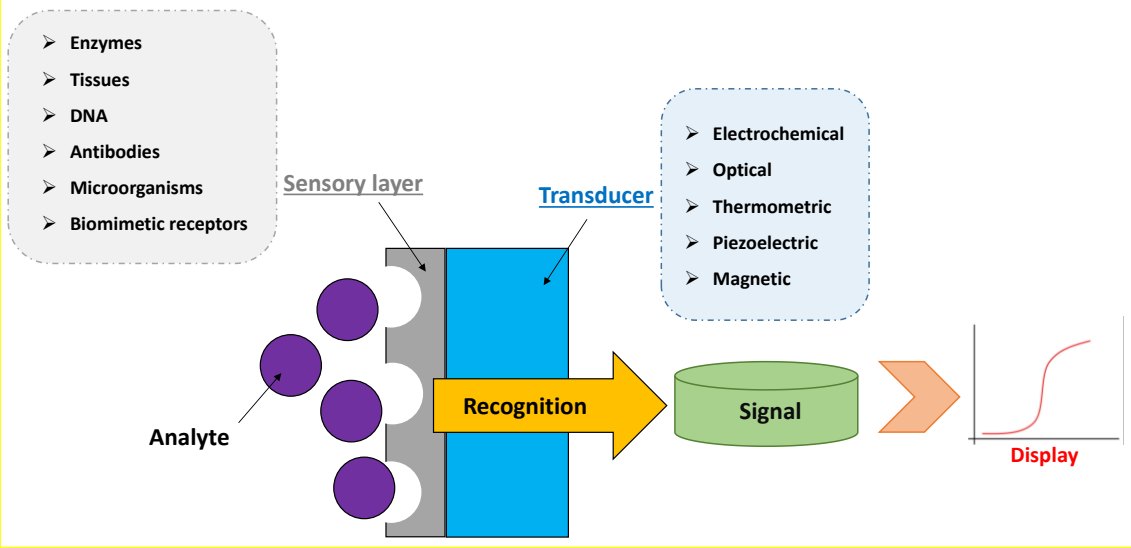

Figure 2.6 – Schematic representation of a biosensor and common recognition elements and transducers employed in this context.

2.3.1 Recognition element

Recognition elements are responsible for the recognition of the target analyte and plays a key role in the performance of the biosensor, as it significantly impacts the selectivity and the sensitivity of the analytical response. The most common ones are enzymes, nucleic acids, antigens or antibodies [59]. Synthetic nanomaterials with artificial recognition sites specifically created to bind to the target analytes may also be used, as biomimetic recognition elements, as MIPs or aptamers [60].

The recognition element of a given biosensor is selected according to the target analyte and other parameters such as cost or storage stability (temperature, pH, oxidizing environments) [59].

2.3.1.1 Biological recognition elements and aptamers

In terms of biomolecules employed as sensing elements, enzymes are widely used because of their high selectivity. As they are involved in catalytic reactions, there are several features that may be monitored and related to concentration. This includes protons, electrons, and heat [61]. However, enzymes have some drawbacks such as the need of high purification levels, great impact from small pH and/or temperature changes, or easy denaturation upon chemical manipulation, such as immobilization [62]. The most

important example of enzyme-based biosensors is the glucose biosensor employing glucose oxidase. This enzyme has been extensively studied and stabilized to ensure a response with good reproducibility and stability.

Nucleic acids are another class of biomolecules suitable for biosensors development because of their chemical stability. The stability and specificity of the binding between DNA or RNA targets and support-bound probe molecules are crucial factors for this based type of biosensors [63]. The sensing of the target analytes occurs through the hybridization of the DNA or RNA recognition element (DNA or RNA probe) due to the high natural affinity between these molecules [62]. The hybridization process occurs only with specific regions of the target DNA sequence due to the complementary DNA base pairing [62].

Synthetic materials of nucleic acids in a given sequence have also been designed and used as recognition elements, known as aptamers. Each aptamer contains a specific sequence of nucleotides that organizes itself in a given tertiary structure that favours binding to an intended target compound. Aptamers are primarily generated using the so-called SELEX procedure, an iterative in vitro selection in which aptamers are isolated from a random library using a targeted in vitro evolution. This in vitro selection process determines the sequence of the aptamers that best binds the target analyte. Once their sequence is established, aptamers can be easily and inexpensively synthesized and reproduced [64]. In a biosensor application, their performance is evaluated in terms of selectivity and sensitivity against an intended target compound [65].

2.3.1.2 Synthetic recognition elements - MIPs

MIPs are polymeric materials that contain imprinted sites, formed when the polymer is growing in the presence of a given compound that is later extracted from the polymeric network. This technology allows the generation of biomimetic polymeric recognition sites or ‘‘plastic antibodies/receptors’’ with tailor-made binding sites complementary to a selected template molecule [66]. These polymer materials can mimic the natural antibody/antigen and enzyme/substrate systems, overpassing the stability problems of using natural bio-receptors in non-physiological conditions with high selectivity and specificity [67]. MIP technology is viewed today as a highly promising technology with rapidly attracting interest to improve the conventional bio-recognition

methodologies, due to their beneficial features, including high surface area, low price and easy preparation and handling.

The typical steps involved in the production of MIPs are schematically represented in Figure 2.7. This involves suitable functional monomers and cross-linking agents which are polymerized in the presence of a target analyte (the imprint molecule), considered as a molecular template. Firstly, the functional monomers form a complex with the template, in order to self-organize their functional groups, forming a pre-polymerization complex. Then polymerization proceeds immobilizing this complex into a cross-linked polymer matrix. Subsequent removal of the imprint molecule reveals binding sites that are complementary in size, shape and orientation to the target analyte [68]. In other words, a molecular memory is introduced into the polymer, conferring the ability to selectively recognize the target molecule.

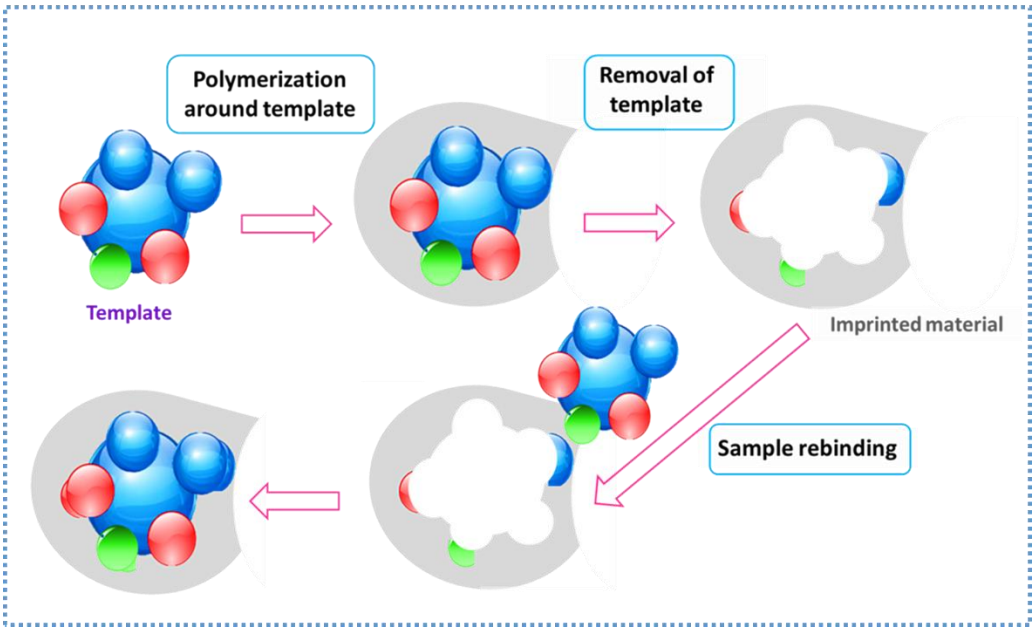

Figure 2.7 – Schematic representation of the synthesis of molecularly imprinted polymers.

A wide variety of polymerization approaches can be employed to synthesize MIPs. They are generally obtained by radical polymerization, which includes initiation by electrical, chemical or optical stimulus. The polymer growth may occur in different modes, with the final polymer being produced by precipitation [69]. Using biosensors, MIPs may be assembled in-situ, directly on the substrate that composes the biosensor by undergoing electropolymerization.

Electropolymerization has attracted increasing attention from the scientific community mainly because it enables the generation of ultrathin polymer films, in situ on different surfaces, by controlled application of an electrical stimulus to the system. The advantages of this methodology over the other methods are the high control of the layer thickness and the possibility of direct grafting onto the electrode surface, resulting in a rapid, homogeneous, and highly reproducible method to obtain coated surfaces with MIP layers [70]. This method enables the tuning of a polymer film thickness and morphology by varying the electrical parameters and deposition protocol mode, allowing the production of coatings in the order of micro and nano-structure sizes [70].

Electropolymerization was used through all the works contained in this thesis to produce the MIPs, since it is the best approach to obtain polymeric films directly on the electrodes surface. Although electropolymerization may have a limited choice of electro-active monomers and a low degree of cross-linking, it can be performed in an aqueous electrolyte, which is compatible when proteins are used as templates. Yet, many variables have to be studied to obtain the appropriate optimal conditions for the production of a MIP by electropolymerization, such as temperature, pH, solvent, monomers, cross-linking elements, the interaction between monomer and template, and the template removal protocol, as well as the electrochemical variables by which the polymer chain grows and reticulates. Each ingredient added or conditions alteration within the polymerization process has its particular influence over the properties and performances of the final MIP [71].

In general, two approaches for MIP development are commonly employed in an electropolymerization process, concerning the template interaction with the working electrode. The template can be added within the polymerization mixture (bulk imprinting) or added before to the surface of the working electrode where the polymerization takes place (surface imprinting). Both strategies allow the development of a polymer matrix with selective recognition sites and have advantages and disadvantages. When working electrodes have high surface areas (as those used in the works contained in this PhD thesis) and the template to be imprinted is expensive, the use of surface imprinting allows using less volume of template, which reduces the cost of MIP electrodes production.

Electropolymerization of monomers on conducting substrates can lead to the formation of conducting/non-conducting polymer films depending on the selection of the monomers and experimental conditions [72]. Some examples of representative monomers

employed in the electrosynthesis of MIPs are represented in Figure 2.8-A/B, evidencing in Figure 2.8-B the monomers that can polymerize into conductive films. The electrically conducting polymers can be grown in thicker and highly controlled films, which is beneficial to the design of nanostructured MIPs, contrasting with the insulating polymer films that are self-limited in terms of thickness, since the insulating polymer layer affects the electron transfer between the electrode and the monomer [72].

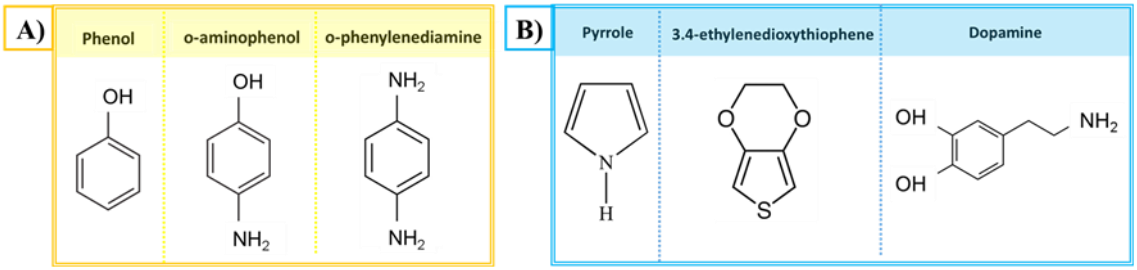

Figure 2.8 -A)- Representative monomers applied for the electrosynthesis of MIPs, B) with some examples of monomers that can polymerize to developed conductive films.

Generally, MIPs do not own signal output ability, meaning that they need to be coupled to an appropriate transducer technology to translate the rebinding event into a readable signal. Different works have demonstrated the successful integration of the polymers with several readout technologies, including, but not limited to, the heat-transfer method (HTM) [73], quartz crystal microbalance (QCM) [74], surface plasmon resonance (SPR) [75], surface-enhanced Raman scattering (SERS) [76], and various electrochemical and optical transducers [77].

Owing to their unique properties of structure predictability and recognition selectively, MIPs found application in a wide range of fields, including chemistry analysis (purification and separation), biosensing, drug delivery and catalysis. The long-term chemical and physical stability allied to the easy and low-cost synthesis procedure turn MIPs into an attractive technology with the ability to detect from small to large molecules, such as proteins [78].

2.3.2 Signal transducer

Biosensors can also be classified according to the type of transducer mechanism selected. Thus, based on the detection method and transducer system, biosensors can be

divided into four categories: electrochemical, optical, piezoelectric and thermometric [79] as schematized in Figure 2.9.

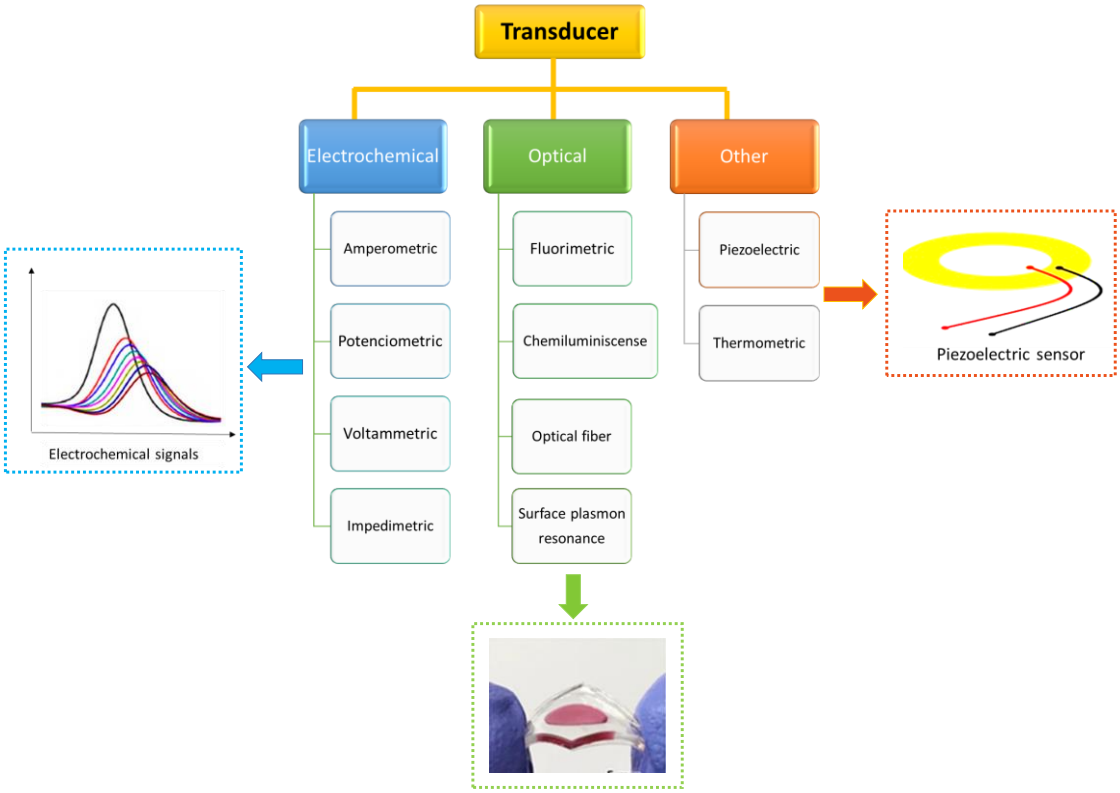

Figure 2.9 - Types of biosensors with basis on the transducer operation.

The optical transduced biosensors are based on light emission or light–matter interaction, such as fluorescence, absorbance, or photoluminescence (PL) of an appropriate indicator and changes in the refractive index. The fundamental idea of optical biosensors is to produce a signal proportional in frequency or intensity to the concentration of a specific target to which the biosensor element was conceived [79]. The main advantages of these systems include a direct, faster and real-time visual response related to the presence of the target analyte [80]. In addition, these systems have high selectivity, sensitivity, reliability and potential to be miniaturized and integrated on a single chip [81]. A wide variety of non-invasive optical detections have been developed, from absorption, fluorescence, Surface-Enhanced Raman Scattering (SERS) and SPR (surface plasmon resonance) [81]. These different optical configurations have different working principles, features, and properties and can be applied in diverse fields such as clinical diagnostics, environmental monitoring, food quality control, and drug discovery

[82]. Some optical based biosensors have been introduced into the market, but most research is necessary to obtain mechanically stable, reproducible, low-cost and user-friendly optical devices [82].

Other transducers include piezoelectric or thermometric configurations. Piezoelectric transducers are mass-sensitive sensors mostly represented by a quartz crystal microbalance, which consists of a thin circular quartz plate with metallic electrodes placed on the opposite side [83]. In the biosensors field, the electrodes employed are typically made of gold. Their working principle is based on an alternating potential that produces a standing wave in a crystal at a defined frequency, with the thickness of the quartz plate defining the basic resonance frequency [83]. This frequency is very sensitive and can be related to the surface properties of a crystal; if the crystal was modified with a bio-recognition element, the binding of the target analyte to the sensory element will produce a variation in the resonant frequency [84]. A variety of materials exert a piezoelectric effect, such as inorganic, and organic and even some biomolecules like nucleic acid can provide piezoelectricity [84]. Piezoelectric transduced biosensors can work in different modes, in direct and real-time interaction with the analyte which provides a simple, reliable and low-cost piezoelectric platform. In addition, antibodies and antigens can be employed as promising biomolecules with high compatibility with piezoelectric sensors [85]. Thus, piezoelectric biosensors are suitable devices for the determination of a wide variety of analytes, such as proteins, nucleic acids, viruses and bacteria [85–87]; they can also be employed in the detection of small molecules such as drugs, hormones and pesticides [88,89]. The simple manufacture of these biosensor devices, without the application of any further reagents, turns them economically attractive approaches, especially for diagnosis. Furthermore, more research concerning innovation in piezoelectric materials is needed to enhance their potential for routine applications.

Thermometric transduced biosensors are based on the quantification of the absorbance or release of thermal energy during a biochemical reaction. Thermal activity is a fundamental phenomenon of biochemical reactions, thus thermal biosensing founds a broad application [90]. Thermometric biosensors are based on the combination of enzymes with temperature sensors, relating the heat of the enzymatic reaction with the target analyte concentration [90]. These systems allow the analysis of small volumes of sample with higher sensitivity, being especially advantageous when multiple reactions

are involved [91]. Thermometric sensors can include different types of temperature transducers such as thermocouples, thermopiles, thermistors and diodes [92].
The thermistor configuration is the most commonly employed in medical wearable devices and industrial monitoring systems [93]. Thermistors are consisted of resistors with a negative temperature coefficient of resistance and are mainly based on ceramic semiconductors, made by sintering mixtures of metal oxides from different metals (cobalt, copper, iron, manganese, nickel, and uranium) [94]. Currently can be employed in a wide variety of formats, sizes and resistance values using different types of fabrication technologies which make this technology easily accessible [95]. However, thermometric methods play an important role in sensing physical parameters.

Finally, the electrochemical transduced biosensors approach involves the measuring of the variation in current, potential and/or impedance signals allowing to relate these variations with the interactions that occur in the interface of the sensor electrode/ analyzed sample. Currently, the electrochemical biosensors appear as the best suited for point of care applications, since they can be easily miniaturized in portable configurations with fast *in-place* analysis and higher sensitivity responses. These advantages turn electrochemical-based biosensors the most promising approach for the development of autonomous biosensors as intended in this PhD thesis. The electrochemical transduced approach was selected for the development of different self-powered biosensors configurations taking into view their usage in point of care applications for cancer biomarkers determination.

In general, optical and electrochemical systems are the most common transducers in biosensors aiming a biomolecule target, since they represent high sensitivity and easy miniaturization in simple and user-friendly devices. Between these two systems, electrochemical transduction allows a smoother interface with fuel cells for sensing purposes as it operates with electrical-based elements. This justifies the use of electrochemical transduction throughout this thesis and the description of its main principles in the following section.

2.4 Electrochemical biosensors

The principle of electrochemical biosensors is based on the change in the current or voltage of a system when the analyte is recognized by the biorecognition element. The interest in electrochemical biosensors by the scientific community is constantly

increasing, focused on the development of new detection platforms with higher sensitivity, selectivity and reproducibility.

In the last decades, a huge variety of electrochemical (bio)sensors have been successfully developed as promising tools for the detection of multiple compounds, including cancer biomarkers [96], viral/ bacterial infections [97,98], pesticides [99] or antibiotics [100]. The concerns around the development of simple user-friendly electrochemical set-ups with electrical autonomy are currently a great challenge. Great interest and attention in electrochemical wearable devices have been explored for health monitoring, allowing to use of saliva, sweat, tear and even interstitial fluid [101]. In the next sections, the composition of electrochemical biosensors, including electrodes, materials and supports was discussed. The most common electrochemical techniques used to date were also discussed with special emphasis on the more relevant techniques employed in the works contained in this thesis.

2.4.1 Electrochemical cell configurations

The composition of electrochemical biosensors comprises two or three electrodes (working, reference, and counter or auxiliary electrodes) depending on their configuration (Figure 2.10). In a common 3-electrodes system, the working electrode (WE) consists of a chemically stable solid conductive material, such as carbon, platinum, or gold; the reference electrode (RE) has a steady potential (nonpolarizable, meaning that none or little current passes through it), and normally includes a silver metal coated with a layer of silver chloride (Ag/AgCl); and the counter electrode (CE) records the current in the system and normally involves a conductive material such as carbon or platinum [102].

In a 2-electrodes configuration, the system consists of working and counter/reference electrodes combined [102]**.** In this, CE and RE are connected forming one electrode while the WE are connected on the opposite electrode (Figure 2.10-A). This configuration allows measuring the potential across the complete cell system, including contributions of the electrolyte interface. This setup is appropriate when the behaviour of the whole cell is being investigated and is commonly employed in the study of energy conversion devices such as fuel cells, photovoltaic panels and batteries and also in the evaluation of energy storage devices. The 3-electrodes configuration (Figure 2.10-B) is the most common electrochemical setup used in the electrochemistry area, including in

electrochemical biosensors. In this configuration, the current flow between CE and WE and the potential difference is measured and controlled against the RE.

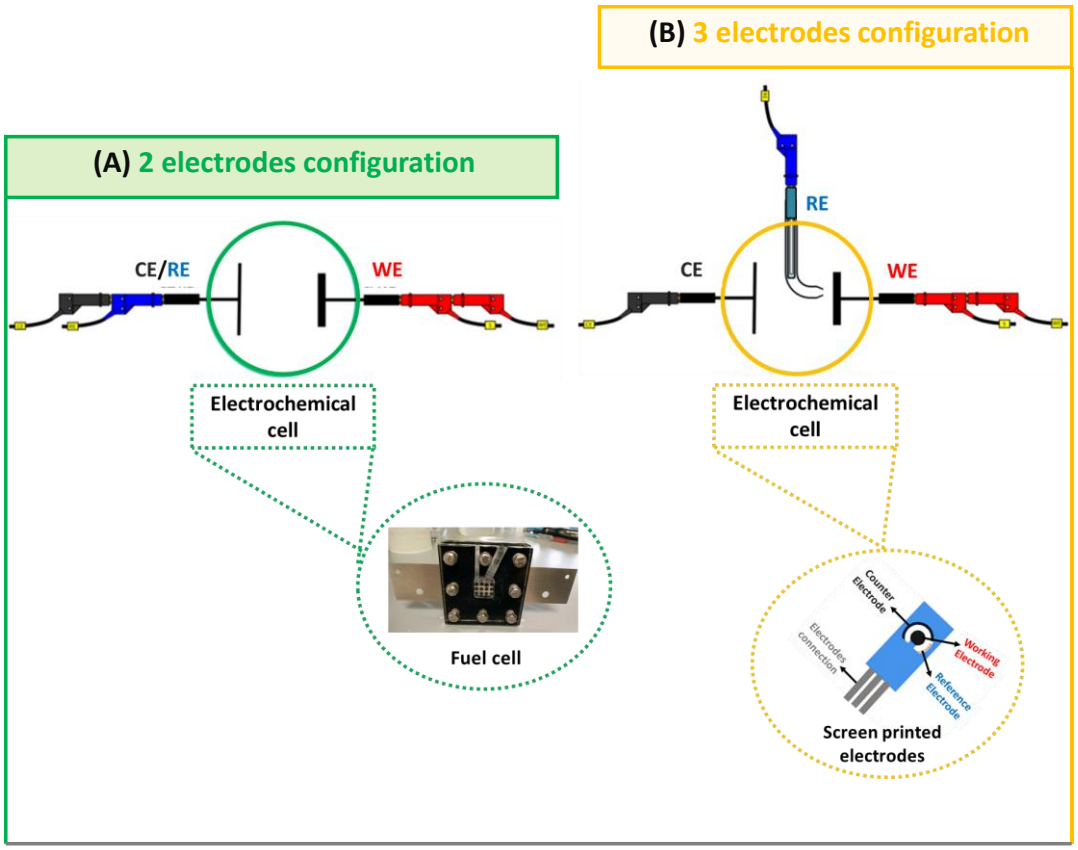

Figure 2.10 – Schematic view of the 2-electrodes (A) and 3-electrodes (B) configuration, with an example of application of each system.

The format of the electrodes is variable. They may present a conventional configuration, as that of the typical pH electrode existing among chemistry laboratories, or they may be designed in a planar format. A common example of the later are the commercial screen-printed electrodes (SPEs), which are widely used to obtain a wide range of electrochemical biosensors. They can be applied in different fields, such as pharmaceutical detection, clinical diagnosis and environmental analysis, being promising tools for a prominent commercialization [103].

2.4.2 Electrodes composition

During the fabrication of electrochemical biosensor platforms, different support and electrode materials can be employed. While RE and CE are displaying common roles

among different electrochemical biosensors, the WE is providing the required selectivity against a given target analyte. Thus, the materials employed to produce WEs should be carefully selected. While gold and mercury were used often in the past, carbon has emerged as an important alternative to these metals, being rather inexpensive and displaying little toxicity.

In terms of electrode materials, carbon nanomaterials are widely used in electrochemistry as support materials in the WE development and the final design can vary according to the specific requirements of the sensing application and technology products (e.g. SPEs, fuel cells) [104]. Recent advances in nanotechnology have evidenced that carbon nanomaterials have the capacity of enhancing the sensing performance of biosensors due to their nanoscale size, which makes them unique for various biosensing applications. In addition, their properties can be tailored to achieve optimal biosensor responses [105].

Nanomaterials possess high surface area, which can enhance the sensitivity and detection range of the fabricated biosensors, allowing for example the immobilization of higher concentrations of enzymes or electroactive compounds [105]. Thus, the high electrocatalytic activity of nanomaterials is crucial for both enzymatic and non-enzymatic biosensors. The selection of the ideal electrode should consider a suitable active nanomaterial and a suitable nanomaterial deposition technique, which are crucial parameters to fabricate a biosensor device. Thus, the discovery of new carbon nanostructures, such as graphene, carbon nanotubes, and carbon nanofibers with unique properties, has contributed largely to the development of innovative electrochemical (bio)sensors with low-cost fabrication methods. Some of the most commonly employed methods in electrochemical biosensors' fabrication include drop casting, dip coating, spin coating and blade coating, due to their simplicity and low cost [106].

In terms of support materials, paper arises as an innovative and low-price alternative to the conventional support materials of synthetic polymers usually employed in the electrode systems. The biocompatibility and renewability of cellulose paper, allied to the chemical and biological inertness, turns cellulose into an attractive option for electrochemical sensing. An important example of this approach is the commercial glucose meter, which may combine paper-based strips with SPEs, where electrodes are directly printed on the paper support [107].

To select a paper substrate, some features should be considered to obtain a sensor with a good sensitivity, and stability. The specific features required for the paper support

depend on the application selected, including the thickness, pore size, permeability, and capillary nature. To this end, the most common paper-based biosensors developed in recent years use Whatman paper filter, which has been a popular choice. Whatman paper filter can be found with different grades, thicknesses, and pre-treatments, with good hydrophilic properties, mechanical strength, and easy degradability.

The properties of cellulose paper can also be tuned by the addition of different compounds, such as polymers and surfactants. Cellulose surface modification can improve the physical and chemical properties of the paper substrate, such as surface area and adsorption capacity [108]. One of the common modifications employed concerns the hydrophobization of cellulose. This is required to avoid electrical short-circuit among the several printed electrodes. This is typically done with hydrophobic polymers, such as wax, PVC, or PDMS [109].

Overall, paper-based analytical devices offer cost-effective solutions for POC diagnostics, providing to the end-users a simple and inexpensive healthcare tool. They can be developed, for example, for the detection of biomarkers related to infectious diseases, as commercial COVID-19 rapid tests, and for monitoring health conditions, as the widespread paper-based glucose strips.

2.4.3 Electrochemical techniques

Electrochemical techniques are suitable for achieving low-cost, simple and miniaturized portable devices for application in a wide range of fields, particularly medical diagnosis and monitoring. To date, various electrochemical techniques, such as cyclic voltammetry (CV), differential pulse voltammetry (DPV), square-wave voltammetry (SWV), and electrochemical impedance spectroscopy (EIS), have been successfully employed in biosensing devices. Furthermore, depending on the type of transducer selected, electrochemical techniques can be divided into amperometric, potentiometric, voltammetric biosensors and impedimetric biosensors [110].

In a simple description, amperometric devices measure currents formed by the reduction or oxidation of electroactive species. The potentiometric devices measure potential variations of an electrochemical cell, operating in open circuit potential (near-zero current conditions). In voltammetric based-biosensors, the current is measured in relation to the oxidation or/and reduction reactions of electroactive species at the

electrode surface. Impedimetric-based devices involve measuring the impedance of the system upon immobilization of sensing layers in the electrode surface [111].

Amperometric based-biosensors attracted great attention due to their widespread application in glucose monitoring. These types of devices are suitable to study the charge transfer between the interfaces of phases, for example, between two electrodes separated by an electrolyte [111]. Commonly, to describe the system of phases and interfacial boundaries the term electrochemical cell is adopted. Two types of processes can conduct current across an electrode/solution boundary: faradaic and non-faradaic processes. The Faradaic processes are governed by Faradays law (which refers that the amount of chemical reaction at an electrode being proportional to the current). A Faradaic process involves a direct transfer of electrons through an oxidation reaction in one electrode and a reduction reaction at the other. The resulting currents are named faradaic currents [112]. The other processes (such as the formation of a double layer) that change the interfacial surface but do not cause charge transfer across the interfacial boundary are called non-Faradaic processes, resulting in non-faradaic currents [111].

Both faradaic and non-faradaic processes can take place at an electrode, and their differences are important since the two processes represent two fundamentally different modes of how an electrode operates and their distinction determines how an electrode (process) can be characterized experimentally [113].

In the next sub-section, two important electrochemical techniques for the work developed in this thesis are discussed. These are CV and EIS. CV was employed to develop the sensing layers directly in the surface of the electrode and EIS was employed in the transducer fuel cell characterization.

2.4.3.1 Cyclic Voltammetry

The most widespread electrochemical technique for developing protein MIPs is CV. CV is a simple, fast and possibly the most straightforward electroanalytical technique for obtaining qualitative and quantitative information about any electroactive species (species that can be oxidized and/or reduced) [114]. This electrochemical method allows monitoring the current variation as a function of the voltage applied on the working electrode, under a fixed scan-rate value. Varying the scan rate and the number of scan cycles, it is possible to control the thickness and compactness of the immobilized polymer

film. Thus, the scan rate must be sufficiently long to let the chemical reactions occur in a significant degree [114].

A voltage is measured between the RE and WE, whereas a current is measured between the WE and CE. A typically obtained voltammogram is represented in Figure 2.11, consisting of a representation of the measured current as a function of the applied potential. The resulting current at the electrode surface is measured at each applied potential.

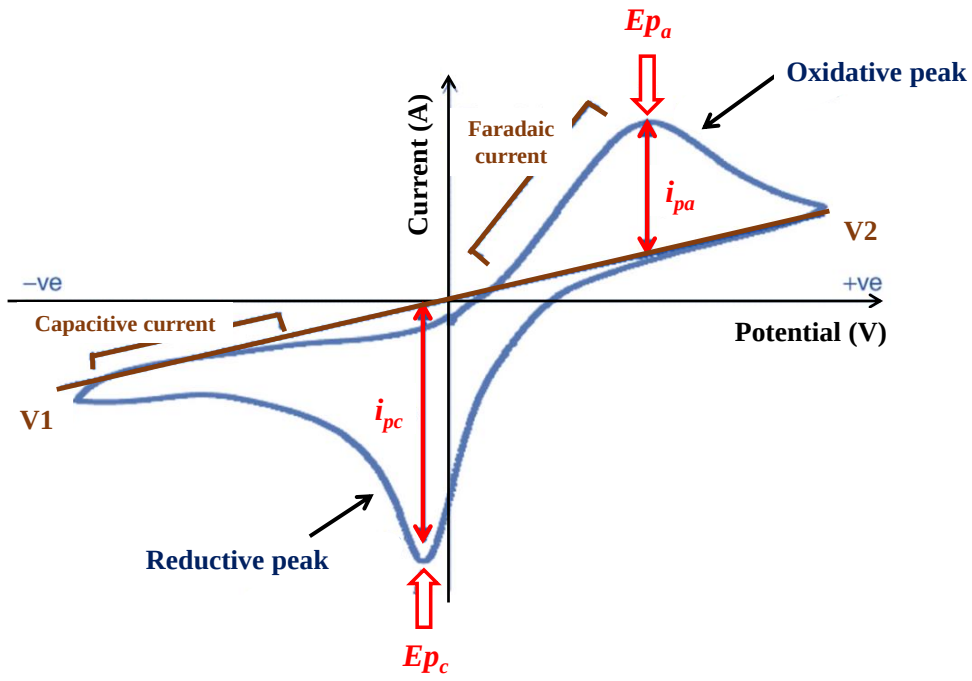

Figure 2.11– Schematic cyclic voltammogram obtained for a reversible system, including the peak cathodic potential (Ep_c), peak anodic potential (Ep_a), cathodic current (i_{pc}), and anodic current (i_{pa}). Adapted from [114].

Normally, the voltammogram includes two peaks: a peak related to the oxidation process and a peak related to the reduction process. As the potential applied increases from V1 to V2, the current increases, resulting in the anodic peak potential (Ep_a). In the reverse cycle, the current decreases and the applied potential goes into the negative direction until reaching the electrochemical reductive potential of the analyte. When the applied potential exceeds this point, a cathodic peak potential (Ep_c) can be measured. The differences between the cathodic and anodic current from the remaining current are called i_{pc} and i_{pa}, respectively [115]. As the reaction proceeds, an approximation of the oxidative

and reductive CV curves is observed, which indicates that the reaction is close to completion.

The reversibility of a redox process is related to the electron transfer kinetics between the electroactive species and the electrode surface. When there is a low barrier to the electron transfer, the Nernstian equilibrium is immediately established upon any change in applied potential. On the opposite, when the barrier to electron transfer is higher, the electron transfer reactions are slow and more negative (positive) potentials are required to observe reduction (oxidation) reactions, causing an electrochemical irreversibility process [116]. The scan rate selected in one experiment controls how fast the applied potential is scanned, which leads to a decrease in the size of the diffusion layer and causes higher currents.

Figure 2.12 represents a comparison between the two electrochemical processes. When the process is irreversible, the concentrations of the oxidized and reduced species do not follow the Nernst equation and the individual peaks appear widely separated and size reduced. Depending on the system, increasing the scan rate can restore reversibility. [116] (as seen in the simulation shown in Figure 2.12, from the red, and green to the blue curve).

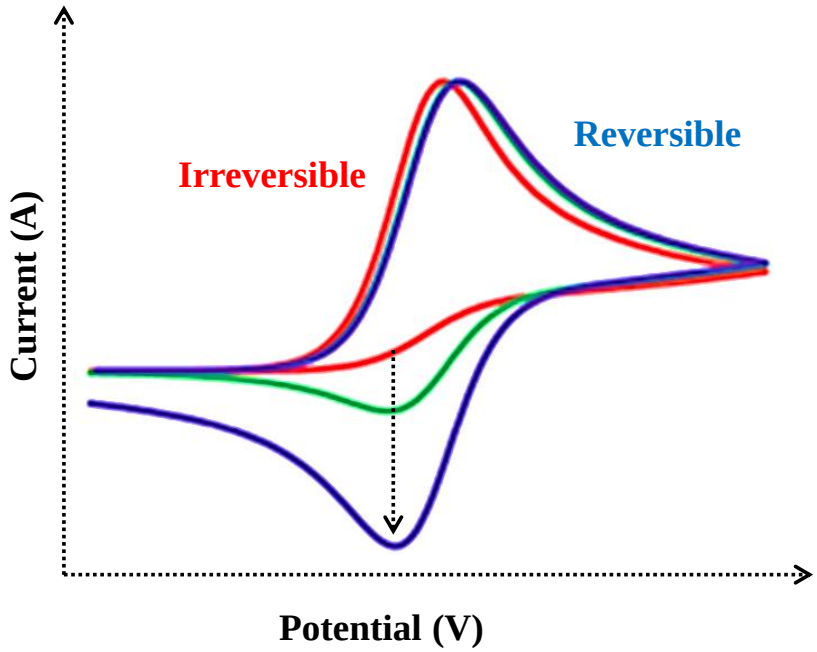

Figure 2.12– Schematic simulation of a reversible (blue curve) and irreversible (red curve) electrochemical processes, evidencing the effect of increasing the scan rate to restore reversibility (dashed arrow).

2.4.3.2 Electrochemical Impedance Spectroscopy

EIS is a powerful technique, increasingly used for the detection of relevant chemical and biological species due to its ability to detect variations in resistance, capacitance, and binding events without causing disturbance in the electrochemical system. EIS undergoes the application of a small sinusoidal potential (*U*) to the WE, while the resulting current response is measured [117]. Varying the excitation frequency (*f)* of the applied potential over a range of frequencies, makes it possible to calculate the impedance which is the sum of the real and imaginary impedance components of the system as a function of the frequency (called angular frequency *w*). Thus, EIS combines the analysis of real and imaginary components of impedance, specifically the electrical resistance and reactance, as shown in Equation 2.1 [118].

$$Z\,(jw) = \frac{U\,(jw)}{I\,(jw)} = Z_r(w) + jZ_i(w): \quad w = 2\pi f \tag{2.1}$$

In electrochemical sensing, EIS techniques are important to follow changes in the electrical properties derived from the bio-recognition events that occur in the electrode surface. The impedance expression is achieved by the "Nyquist plot", the most frequently employed in impedance measurements regarding its simplicity, not requiring additional calculations [119]. An example of a Nyquist plot was schematically represented in Figure 2.13, which consists of the plot of the real part of impedance (Z' or Z_{RE}) on the x-axis and the negative value of the imaginary part of impedance (Z'' or Z_{Im}) on the y-axis.

The different characteristic features of Nyquist plots define the applied equivalent circuit model, which represents any process that occurs in an electrochemical cell. The Nyquist plots are commonly applied to evaluate the performance of electrochemical biosensors, normally by monitoring the dependence of the charge transfer resistance (Rct) of the system on the analyte concentration [119]; the R_{ct} is inversely proportional to the electron transfer kinetic.

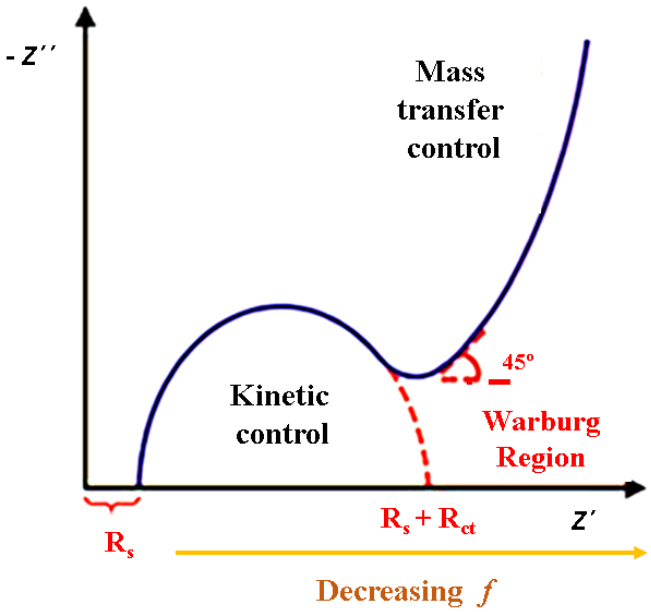

Figure 2.13– Schematic representation of a Nyquist plot.

Other components collected and displayed in the Nyquist plots include the solution resistance (R_s), which depends on the electrode area and ionic concentration, and the Warburg impedance (W) which is related to the diffusion coefficients of molecules or redox species (W may not exist and is frequency dependent). On the Nyquist plot shown in Figure 2.13, the Warburg impedance is displayed as a dotted line with a slope of 45°.

2.5 Fuel cells

The contents presented in this section were partially published in Liliana P.T. Carneiro, Nadia S. Ferreira, Alexandra M.F.R. Pinto, M. Goreti F. Sales, *" Smart Multifunctional Nano-inks: Fundamentals and Emerging Applications ", Elsevier, 1 st Edition - October 26, 2022* – Chapter 13 - Nano-inks for fuel cells application, 333-343. ISBN 978-0-323-91145-0. **doi.org/10.1016/B978-0-323-91145-0.00008-6.**

2.5.1 Fuel cells overview

Fuel cell technology was designed to convert the chemical energy of a fuel directly into electrical energy, operating until the fuel is continuously supplied to the device (not

rechargeable as batteries). The first developed fuel cell operating with hydrogen and oxygen was conceived by Francis Bacon in 1932 [120]. Since then, fuel cell technology has had an important journey of evolution and development.

This technology could be a main electrical energy source in the future. The most important applications for fuel cell technology are related to the transportation sector (e.g., fuel cell vehicles and buses) [121] and power systems (e.g., power plants and residential generation) [122] as a sustainable response to the increased demand for the dependence on fossil fuels. Also, in the portable market sector, fuel cells have received much attention because they can easily be adapted and miniaturized to passive compact microfuel cell configurations [123].

A simplified structure of a fuel cell is represented in Figure 2.14, displaying the two component electrodes (anode and cathode) separated by an electrolyte polymer membrane (permeable to protons and insulant to electrons). The fundamental working principle of different types of fuel cells is similar. Thus, different reactants can be used as fuels involving different chemical reactions occurring in the anode/cathode electrodes.

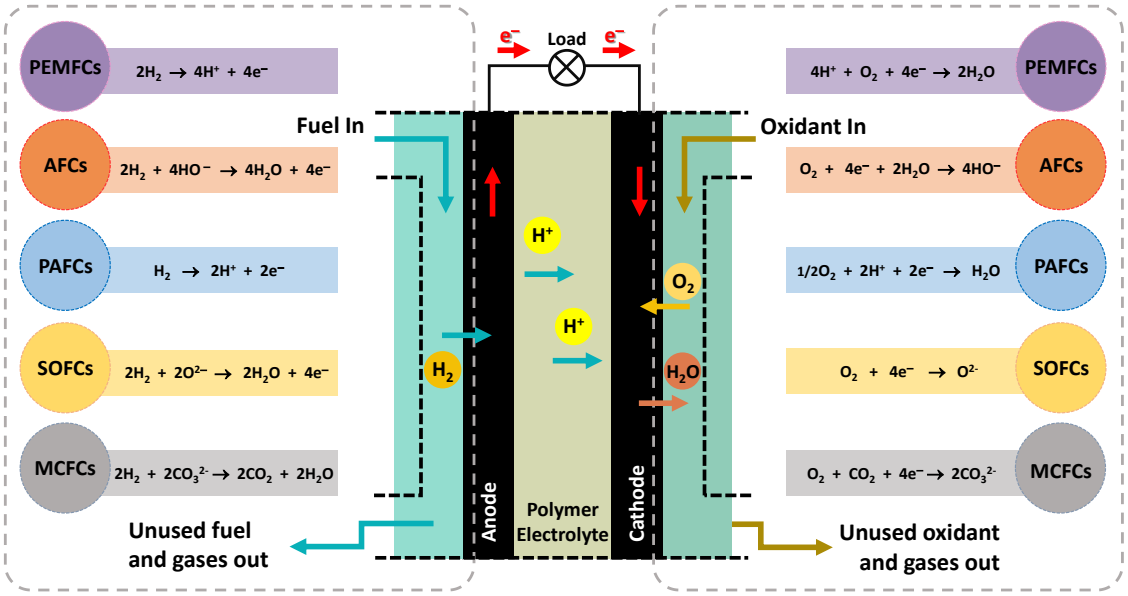

Figure 2.14– General scheme of a fuel cell assembly including typical reactions in different types of fuel cells, including proton exchange membrane fuel cells (PEMFCs), alkaline fuel cells (AFCs), phosphoric acid fuel cells (PAFCs), solid oxide fuel cells (SOFCs), and molten carbonate fuel cells (MCFCs). Reactions expected in each electrode depend on the type of cell, as identified for each electrode.

Typical reactants used in fuel cells are hydrogen and oxygen (in most cases, oxygen comes from atmospheric air, and therefore the cell can also be continuously supplied) that undergo electrochemical reactions at the anode/cathode electrodes, to produce an electric current [124]. At the anode, hydrogen molecules are oxidized, producing protons and electrons. The protons migrate to the cathode side through the electrolyte membrane and electrons flow through an external electrical circuit. The oxygen reduction reaction occurs in the cathode electrode among electrons, protons, and oxygen molecules, generating electricity, heat, and water (fuel cell by-products).

The fuel cell efficiency ranges from 40% to 60%, but it can be improved to higher values (85%) when the released waste heat is captured and used [125]. Besides H_2, other fuels can be used to feed fuel cells, such as methane, butane, and natural gas [126]. Liquid fuels can also be employed, such as alcohol solutions (methanol and ethanol) and nonalcohol compounds such as hydrazine, dimethyl ether, ammonium borane, and sodium borohydride aqueous solutions [127]. These direct liquid fuel cells have advantages regarding hydrogen fuel cells because liquid fuels are easier to transport and do not require high pressure for operation, which are considerable benefits in terms of safety.

Fuel cell technology involves a wide variety of options in terms of operating temperatures, fuels, and nanomaterials. Depending on the type of electrolyte used, they can be classified as proton exchange membrane fuel cells (PEMFCs), alkaline fuel cells (AFCs), solid oxide fuel cells (SOFCs), phosphoric acid fuel cells (PAFCs) and molten carbonate fuel cells (MCFCs) [128].

PEMFCs have attracted increased interest as a promising energy-conversion technology, first with hydrogen fuel cells and later when methanol fuel cells joined the group, because they include a proton exchange membrane (PEM). PEM fuel cells use a solid electrolyte membrane (normally Nafion®) and are considered low temperature fuel cells (below 100 ºC), an operating condition favourable for implementation in the transport and portable sectors. The higher power density and faster start-up are also advantages of this type of fuel cell, but some barriers need to be overcome, namely those related to the catalyst price and device durability. The higher technological innovation and commercial interest of this group of fuel cells make them an important subject of debate. A section part of this chapter will be dedicated to DMFCs devices since is the power source technology selected for the biosensor integration.

Another main innovative fuel cell technology involves the SOFCs group with a much higher operating temperature range (reaching 1000 ºC) and a ceramic electrolyte adapted to this range (normally yttrium-stabilized zirconia (YSZ). Thus, this type of fuel cell requires electrodes composed of extremely resistant materials, which makes this technology expensive [129]. Nevertheless, the higher efficiency and performance make it appropriate for stationary applications compared with PEMFCs. The main disadvantages are the high starting time needed and material degradation due to the high operating temperatures. The development of SOFCs technology is still growing, mainly related with the production of novel materials and deposition methods, to turn this type of fuel cell technology into a suitable candidate for high power applications, such as industrial and large-scale central electricity generating stations.

Other types of fuel cell technologies were developed, such as alkaline fuel cells, PAFCs, and MCFCs. AFCs use an alkaline electrolyte, an aqueous solution of potassium hydroxide (KOH). They can operate between 60 ºC and 250 ºC, depending on the concentration of KOH in the electrolyte. They need pure H_2 and pure oxygen as fuels. The presence of CO_2, even at atmospheric levels, degrades the KOH electrolyte. This intolerance is the main disadvantage, as is the effective decrease in OH^- concentration in the electrolyte with the increase in operating times. Although not economically viable for most terrestrial applications, AFCs have high electrical efficiencies and are mostly used in the aerospace industry. In PAFCs, liquid phosphoric acid electrolyte (pure or highly concentrated) is contained in a thin SiC matrix. Pure hydrogen as fuel and air or oxygen as oxidant are involved in electrochemical reactions similar to those occurring in PEMFCs. Because of the solidification temperature of phosphoric acid (42 ºC), PAFCs must operate above this temperature. Optimal performance occurs at 180-210 ºC (twice the optimal PEMFC temperature range). Compared to PEMFCs, PAFCs have a slightly lower electric efficiency (40%) and a longer start-up time. The electrolyte in the MCFC is a molten carbonate mixture of alkali carbonates immobilized in an $LiOAlO_2$ matrix and the carbonate ion acts as the mobile charge. The relatively high operating temperature (650 ºC) provides fuel flexibility and enables the use of nonnoble metal catalysts (nickel-based materials in the electrodes). They have higher efficiencies, but corrosion of the components is a major limitation. Despite their importance and potential, the difficulties of finding appropriate materials for AFCs, PAFCs, and MCFCs to improve and/or hinder

the poisoning and corrosion phenomena make the development of novel nanomaterials more restricted.

2.5.2 Direct methanol fuel cells

DMFCs are a special form of low-temperature fuel cells based on the PEM technology that generates electricity by direct oxidation of methanol and reduction of oxygen. This type of fuel cells, a particular case of the PEMFC class described in the previous section, uses a solid polymer membrane as electrolyte. The operating principle of a typical DMFC is represented in figure 2.15.

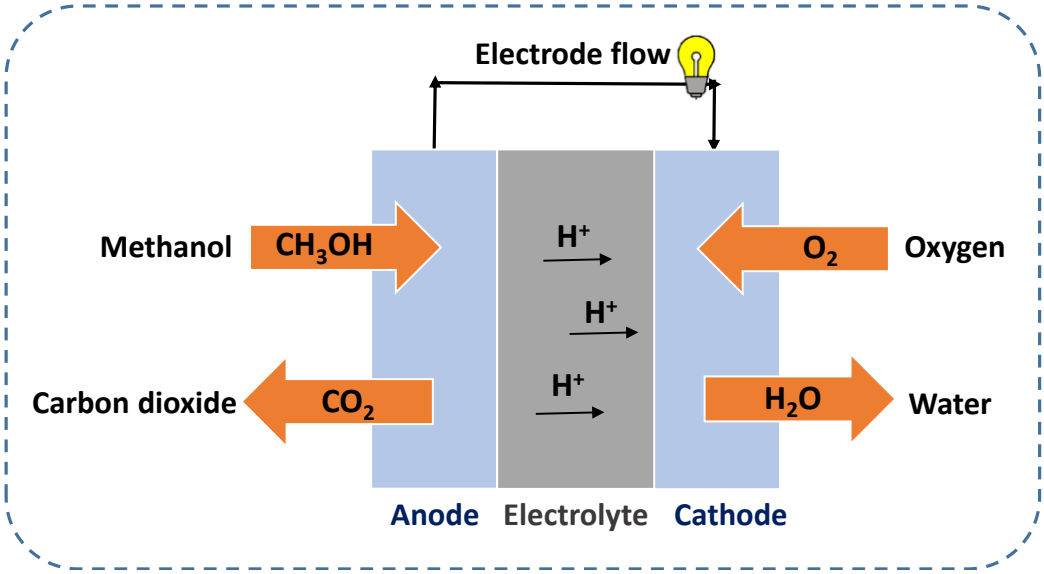

Figure 2.15– General scheme illustrating the working principle of a typical DMFC fuel cell.

An aqueous solution of methanol is oxidized in the anode side of the DMFC producing carbon dioxide, protons and electrons; the protons produced migrate through the polymer electrolyte to the cathode side, where the reduction reaction with oxygen occurs producing water. The produced electrons travel to the cathode through the external circuit, where they can power a device [130].

When compared to the hydrogen oxidation reaction, the methanol electrooxidation reaction is a considerably slower process, since it involves the transfer of six electrons to the electrode for complete oxidation to carbon dioxide. The

electrochemical reactions in direct methanol fuel cells are represented by the following equations [131] :

Anode reaction: $CH_3OH + H_2O \longrightarrow CO_2 + 6\,H^+ + 6\,e^-$ (2.2)

Cathode reaction: $O_2 + 4\,H^+ + 6\,e^- \longrightarrow 2\,H_2O$ (2.3)

Overall reaction: $CH_3OH + 3/2\,O_2 \longrightarrow CO_2 + 2\,H_2O$ (2.4)

The free energy associated with the overall reaction at 25 ºC and 1 atm and the electromotive force are:

$\Delta G = -686$ kJ/mol $\quad\quad \Delta E = 1.21$ V (2.5)

The maximum thermodynamic voltage of a DMFC is approximately 1.21 V at 25 ˚C, thus in practice the real cell voltage is much lower than the theoretical value (0.5 V-0.6 V). This difference is a result of several types of voltage losses, such as the slow kinetic of methanol-oxidation and oxygen-reduction at the anode and cathode, respectively, the occurrence of methanol crossover from the anode to the cathode side together with ohmic and mass transport losses [130]. This information can be extracted by obtaining a polarization curve, which involves simultaneously the measurement of the voltage and current delivered by the fuel cell, generating a voltage-current curve. A typical representation of a polarization curve evidencing the voltage losses found in a DMFC operation is shown in Figure 2.16.

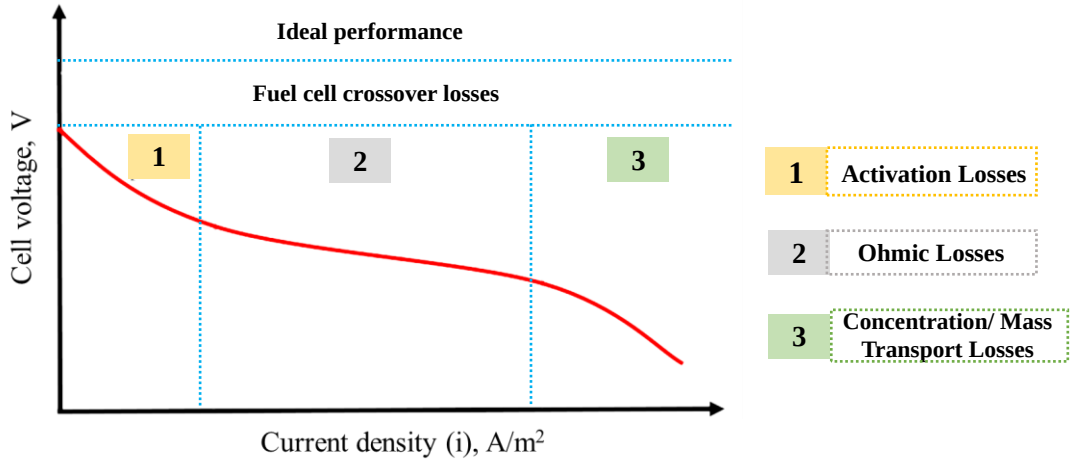

Figure 2.16– Polarization curve evidencing the voltage losses found in a DMFC operation.

The activation region or kinetic control region is governed by the sluggish methanol oxidation kinetics at the anode as well as the oxygen reduction kinetics at the cathode. This phenomenon occurs all over the polarization curve but has a deeper impact for low current density values [132].

The area where the cell voltage decreases near linearly is assessed as the ohmic control region and occurs mainly due to the resistance of the flow of protons through the membrane. This polarization can be minimized by good hydration of the DMFC electrolyte membrane. The linear fit of ohmic law to this region enables the estimation of the fuel cell ohmic resistance [132].

The last part of the curve is referred to as the mass transport control region where either the methanol transport at the anode represents a mass transfer limiting current and the oxygen supply at the cathode becomes a limiting step. This loss is more significant at higher currents when the fuel and oxidant are used at higher rates [132].

The methanol crossover and slow methanol kinetics lead to a decrease in power density which difficult DMFC commercialization, in comparison with hydrogen fuel cells. Methanol oxidation is a more complex anodic reaction that involves the transfer of six electrons, thus the power of a DMFC is three to four times lower compared with the power produced by a hydrogen fuel cell. However, DMFCs present several advantages over their direct competitor H_2-O_2 fuel cells. The main advantage is the use of a liquid fuel, which strongly simplifies handling and storage. In particular, for portable applications, mostly due to the lack of effective miniaturized hydrogen storage technologies, the use of a liquid fuel, requiring less ancillary equipment, is the best option to achieve a high-power density with an attractive cost-to-power ratio [132].

The voltage required to power a portable device is at least 1.5 V, thus for practical applications fuel cells must be connected in a stack, to can deliver enough voltage and power. The fuel cell stack consists of individual cells displayed in a setup that allows electrical contact between the anode and the cathode of one cell to the other. The final stack configuration ensures that the same current is passed throughout the stack. Fuel cells can be developed with different active areas, been the active area of the fuel cell is directly proportional to the power output required.

The reactions of the DMFC take place in the catalyst layers (CL). The core of a DMFC is called the membrane electrode assembly (MEA) which consists of a polymer electrolyte membrane (PEM) sandwiched between an anode and cathode electrode

(Figure 2.17). Generally, a sulphonated fluoropolymer (Nafion®) is employed as an electrolyte membrane; the electrodes are typically made of a random matrix of carbon fibers (carbon cloth or carbon paper), commonly referred to as a porous diffusion layer.

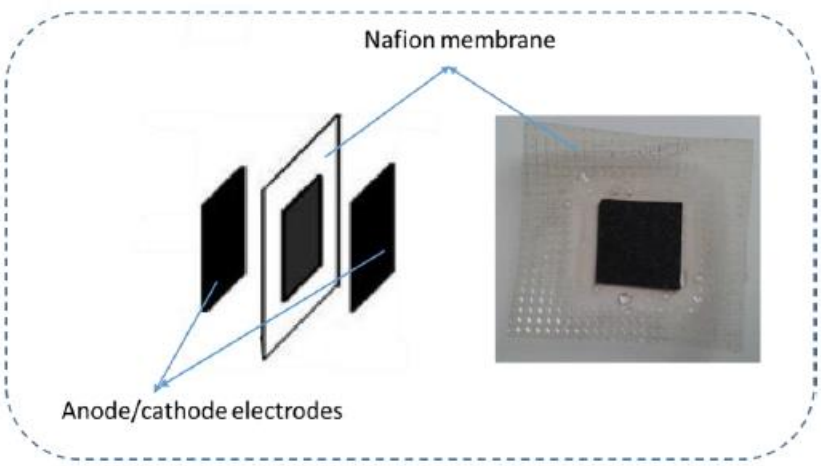

Figure 2.17– General scheme illustrating the membrane electrode assembly (MEA) scheme, complemented with a real image of the assembly.

The catalyst layer includes noble metals such as platinum (Pt) and ruthenium (Ru) as electro-catalysts in the electrodes. The Pt-Ru binary alloy electro-catalyst appears as the most promising formulation for anode incorporation; the Ru combination with Pt forms a binary catalyst, which is fundamental to preventing carbon monoxide poisoning during the methanol oxidation reaction.

Until the current knowledge, the best catalysts for fuel cell electrodes are the PtRu alloy for the anode and the Pt for the cathode; these electrodes normally were supported on carbon black materials; Nafion® is the most used and suitable solid polymer electrolyte. The research in other combinations of carbon supports, metal catalysts, and electrolyte/ionomers is in constant growing, with the target to improve the best materials found so far. In the next section, the development of novel nanomaterials for DMFCs application is approached and explored taking into view the improvement of the performance and widespread dissemination of these power source devices.

2.5.3. Fuel cell electrodes: carbon support, metal catalysts, and ionomer

As referred, the anode/cathode electrodes and electrolyte comprise the membrane electrode assembly (MEA), which is considered the heart of a fuel cell. It hosts electrochemical reactions involved in energy production.

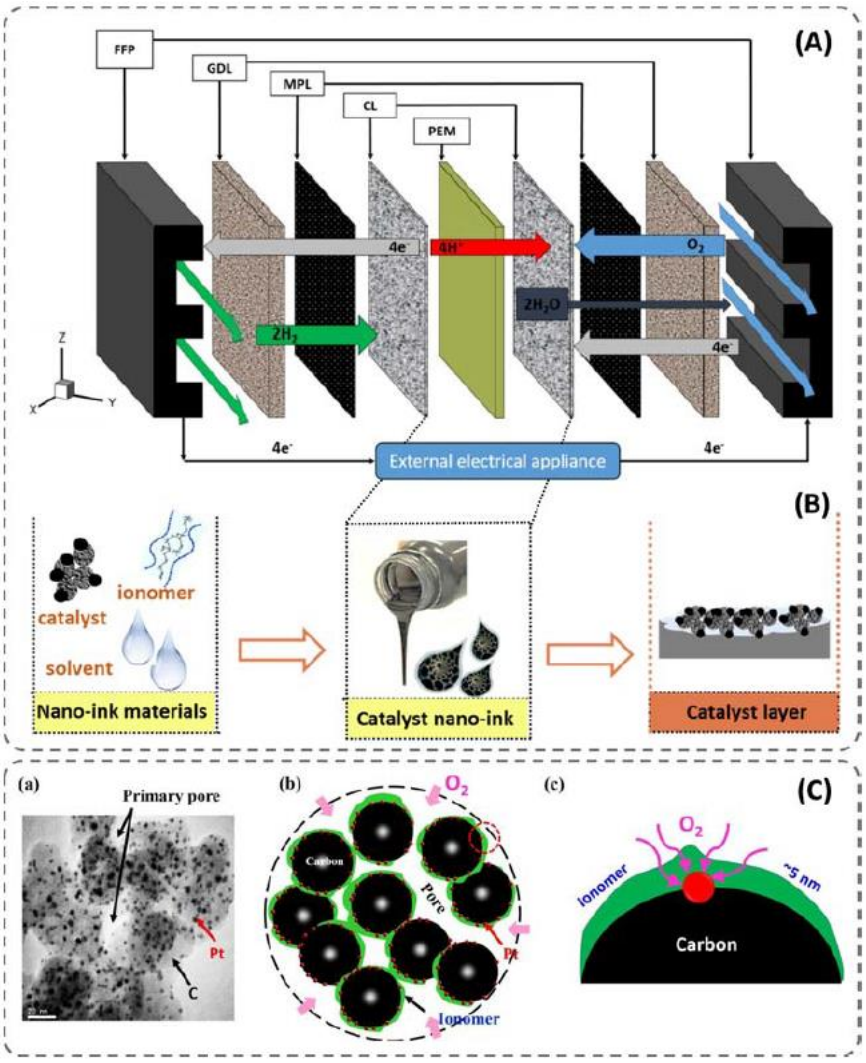

Figure 2.18– Principal components of a general proton exchange membrane fuel cell, including the flow field plates (FFPs), gas diffusion layer (GDL), microporous layer (MPL), catalyst layer (CL) and proton exchange membrane (PEM). (A) Basic and common catalyst nano-ink components for application fuel cell electrodes. (B) Structure and transport processes of components forming CLs: Transmission electron microscopy image of a CL. (1) Scheme of distribution of ink components and transport processes of oxygen molecules between carbon aggregates. (2) General scheme considering transport processes of oxygen through ionomer layer to Pt catalyst surface (C). ((A), reproduced with permission from [133] and (C) with permission of [134]).

The MEA includes a gas diffusion layer (GDL) with a microporous layer (MPL) and an anchored catalyst layer (CL) (Figure 2.18- A/B) that normally include a carbon support, a metallic catalyst, and an ionomer binder (Figure 2.18- C).

The components of the catalyst layer form an ink dispersion which is integrated in the carbon MPL; the inks developed to the fuel cell electrodes can be denominated in the recent research as particle-based nano-ink systems, since are consisted for carbon and carbon-metallic nanostructures dispersed in a solvent medium.

The GDL and MPL are designed to manage heat, water, and electron flow and to ensure the supply of reactants [135]. CLs are involved in transport phenomena and electrocatalytic activity [136]. These fuel cell components are found in all types of fuel cells. Their selection is closely related to the type of fuel and oxidant employed, and to electrolytes and operation temperatures. Different carbon supports, metals and alloys, and ionomers have been used, depending on fuel cell requirements.

The carbon support is a key parameter in fuel cell technology. It has an important role in mass transport and electronic conductivity, improving the access of reactants to catalysts, maximizing catalyst activity, and contributing to avoiding aggregation during fuel cell operation. The performance of catalysts strongly depends on the characteristics of the support. Carbon black (CB) is a material with conductive properties, it is made of spherical aggregated carbon nanoparticles and is the most extensively used support for PEMFC electrodes. Its most common commercial form is Vulcan XC-72R [130], owing to the higher surface area, good electrical properties, great availability, and low price [131]. However, its resistance against corrosion is limited, leading to a limited durability of the electrocatalytic activity of metal catalysts and subsequent fuel cell deterioration [132].

With the advent of nanotechnology, more noble and advanced carbonaceous materials have been explored, such as graphene and its derivatives as carbon nanofibers (cylindrical graphene nanostructures) or carbon nanotubes (rolled sheets of graphene) [133]. Graphene and other related materials attract significant interest for replacing traditional materials and enhancing fuel cell performance when they are used as electrocatalysts and or conductive fillers in protonic membranes [133]. The key features of graphene-based nanomaterials are related to their high surface area, chemical stability, and high electronic conductivity. They are able to enhance the dispersion, catalytic activity, and durability of catalyst nanoparticles [134]. Thus, most graphene-based

nanomaterials require prior modification (chemical or thermal treatments and/or a surfactant combination) to improve solubility and processability as solvent dispersions. To this end, functionalization may be performed, which increases the number and/or diversity of functional active sites on the surface of these nanomaterials [134]. The structure of these described carbon nanomaterials is represented in Figure 2.19.

Carbon nanostructure-based materials are widely applied to support Pt and Pt alloy electrocatalysts in fuel cell electrodes. They can be found in several works employing optimized nano-inks involving these materials [137].

Pt-based catalysts are conventional metal catalysts used in low-temperature fuel cells, mostly because Pt offers an excellent catalytic activity toward methanol decomposition. However, these catalysts are expensive and not widely available.

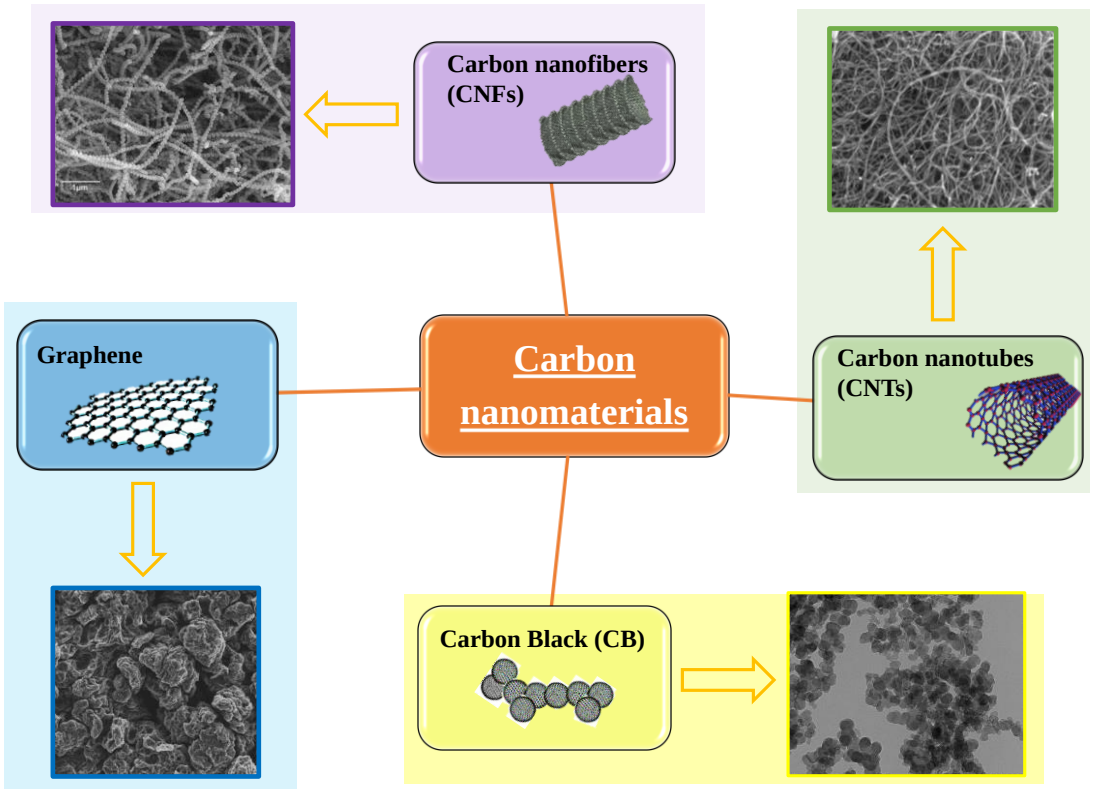

Figure 2.19– Schematically representation of the most common carbon supports employed in fuel cell electrodes development, complemented with real SEM images of their structure.

Therefore, efforts to lower Pt catalyst loading [137] or replace it with other nonprecious metals or metal oxides in both fuel cell electrodes are undertaken by the scientific community, because they may decrease the cost and disseminate fuel cell

technology [138]. Other methods to replace Pt-based catalysts include combining them with conducting polymers, as described in the section 2.5.4.

Carbon-supported metal nanoparticles are mixed with an ionomer that completes the triple-phase boundary between the carbon support/metal catalyst/ionomer (Figure 2.20), which is essential for the mass transport pathway of protons, electrons, and gas reactants [140]. The ionomer has the double function of keeping the CL together and providing pathways for ion mass transport. Ionomers are polymers with the backbone of ionized side-chain groups in their structure. The most common ionomers in DMFCs contain perfluorosulfonic acid (PFSA) group, including different types of backbone structures, such as Nafion® [141].

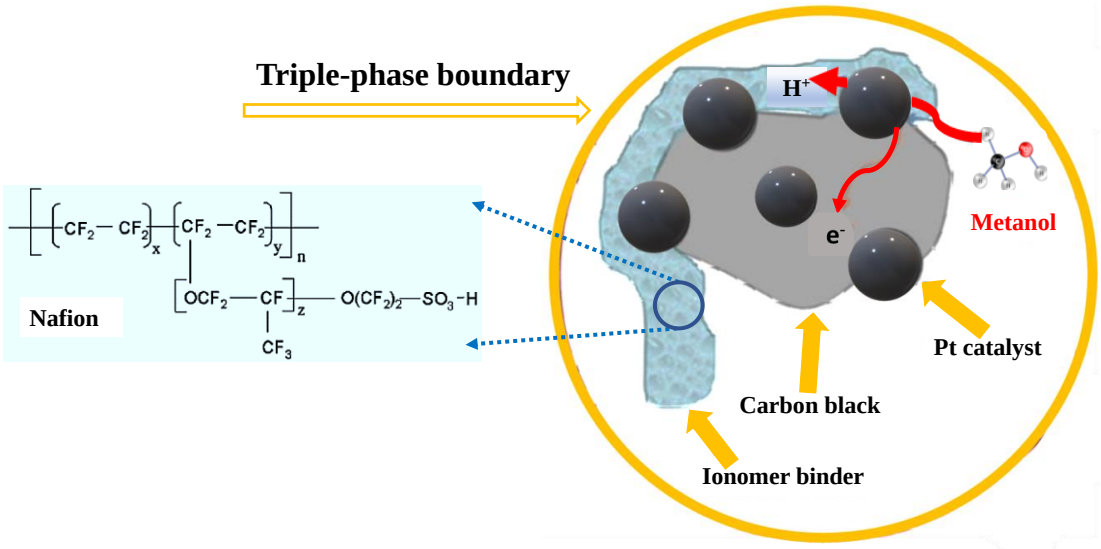

Figure 2.20– Schematically representation of the triple-phase boundary between the carbon support/metal catalyst/ionomer, displaying also the Nafion® binder chemical structure.

Nafion® is extensively used in fuel cell electrodes as an ionomer, but it also acts as a binder for all components in fuel cell inks [142]. Normally, Nafion® ionomer is used to prepare PEMFC electrodes with a mixture of isopropanol and water as solvent. Different ratios of isopropanol and water may be employed because the solvent has an important role in dispersing and agglomerating the ink components [143]. Thus, the commonly used Nafion® still needs improvements, such as dispersion and mass transport limitations, and attempts to modify the intermolecular structure are emerging. This includes, as example, using short-sidechain PFSA ionomers [144] and incorporating

dioxolane homopolymers (2-methylene-4-methyl-1.3-dioxolane) into the PFSA backbone [145].

Modification of these materials composing fuel cell electrodes is essential to reduce the cost and boost the commercialization of this environmentally friendly energy production technology. Novel strategies to improve or replace these materials are described in the next section, highlighting the conducting polymer-based metallic nano-inks, since it is the approach selected to modify the anode electrodes integrated in the DMFCs developed into this work.

2.5.4 Conductive nano-inks for fuel cell application

Electrochemical reactions in fuel cell systems occur in CLs, and their development involves several nano-ink fabrication methods, including the deposition of catalyst inks in different carbonaceous materials. As described in the previous topic, CLs were formed by the set support-metal/alloy-ionomer dispersed in a solvent, originating catalyst conductive inks in suspension forms.

Metallic nanoparticles are widely employed to fabricate conductive nano-inks owing to their unique properties in terms of a low melting point and high conductivity. In addition to metallic nanoparticles, mixed metal oxides can also be employed, and finally the combination with conducting polymers can result in many advantages to enhance the development of fuel cell electrodes.

As described earlier, the catalyst is a fundamental component in any nano-ink formulation for fuel cell electrode applications. Pt-based catalysts are the most common and commercially employed metallic electrocatalysts, because of the higher electrocatalytic activity. Therefore, to widen the commercialization of this power source technology, it is essential to overcome barriers associated with the nearly exclusive use of Pt and Pt-based nano-catalysts in both anode and cathode fuel cell electrodes. In turn, their combination with transition metals forming alloy structures decreases the amount of Pt in ink formulations, improving long-term durability and the stability of the material against intermediate product poisoning while lowering the cost. Combinations with Co [139], Cu [140], Ni [141], Pd [142], Fe [143], and, more commonly, Ru [144] have been investigated. PtRu is the best binary catalyst used to enhance methanol oxidation in direct methanol fuel cells (DMFCs) [145]. Pd is a close alternative to Pt because it is less

expansive and has better resistance by CO poisoning. Nevertheless, it is unstable in acidic media and displays higher activity in alkaline media [146].

Pt nanoparticles are more suitable materials for operating under acidic media. For acid media PEMFC applications, a catalyst ink containing synthetized nanoparticles of PtPd alloy was obtained with higher stability and electrocatalytic activity for electrooxidation reactions of methanol and formic acid fuels. This shows the importance of the cubic shape of metallic nanoparticles [147]. The replacement of Pt in fuel cell electrodes is an interesting research target in fuel cell electrode optimization in the cathode electrode, where less expensive options were found. Composites of transition metal/nitrogen/carbon catalysts (M/N/C) appear to be promising candidates owing to their higher activity, low price, and durability [148]. Among different combinations, composite Fe/N/C-type catalytic inks are promising for Pt replacement. They have similar electrocatalytic performance in reducing oxygen species [149]. The development of other nonprecious metal catalysts of metal/N/C has attracted attention; they are composed of different metallic structures such as Co, Ni, and Mn. However, their implementation remains challenging compared with the performance of commercial Pt/C catalysts [150]. In addition to the electrochemical activity of nonnoble low-cost metals such Fe and Ni, corrosion problems usually affect their practical implementation, with a drop in the stability and durability of anode electrodes. Incorporating Ag [151] and Au [152] noble metals in the Pt structure is a promising approach among the low-cost alternatives, owing to their excellent conductivity and stability. A favorable synergetic effect is observed in PtAg alloy, improving catalytic activity and the stabilization of Pt and decreasing CO poisoning. Incorporation of PtAu electrocatalysts with different atomic Pt/Au ratios in reduced graphene oxide was tested. It produced different metal catalytic inks with higher methanol oxidation currents than pure Pt catalysts and showed that incorporating Au in the Pt core catalyst significantly improves the catalytic properties and CO tolerance of Pt [153].

Furthermore, the design of inexpensive Pt-based and non-Pt-based catalysts is interesting to researchers because of the economic advantages and the limited availability of Pt. Studies on this topic reveal examples of common approaches already developed, in which different metal combinations were tested to reduce or replace Pt nano-catalysts for both the oxidation and reduction of electrochemical reactions. The different combinations tested include also combination with conductive polymers.

Polymer-based materials can be broadly applied in practically all types of fuel cells. Developments in polymer-based conductive inks revealed their relevance for fuel cell applications, owing to their high surface area, high thermal stability, easy manipulation, environmentally friendly, and tunable electrical properties [154]. Conducting polymers have the ability to form nanocomposites with metallic nanoparticles, enabling the production of unique nanomaterials that combine the characteristics of each element [155]. These hybrid catalysts offer numerous pathways for electrocatalyst improvement, because it is possible to obtain multiple composite electrocatalytic active sites, which is promising for fuel cell implementation, and to improve the life cycle of fuel cells. Catalytic inks with conducting polymers containing polypyrrole (PPy), poly(3,4-ethylenedioxythiophene) (PEDOT), polyaniline (PANI), and/or polythiophene (PTh) were investigated as conducting catalyst support materials in different fuel cell types, to integrate the unique electroactive properties and high conductivity of the conducting polymer materials.

In this thesis, the anode electrodes of the DMFCs were combined with the conductive polymers made of PEDOT and PPy. The idea of developing sensing layers making use of the combination of conductive polymers have the goal of developed a biosensor platform with dual function: power source and biosensor unit.

Some works can be found in literature considering the DMFCs electrodes modification by these materials. PPy nano-capsules were developed and used as support material for PtRu catalysts to improve the electrocatalytic activity [156]. Modified composite PtRu electrocatalysts inks were developed (PteRu@PPyeMWNT) by anchoring the PtRu nanoparticles on the surface of the polymer-coated multi walled carbon nanotubes (MWCNT) for DMFCs application. The catalysts obtained were suitable for methanol electro-oxidation, conferring protection to CO poisoning [157]. A cobalt-PPy-MWCNT composite ink was developed and tested as a cathode catalyst in DMFCs, with promising results in terms of the improvement in power density for hydrogen, methanol, and ethanol-based fuel cells. This highlights the importance of none Pt based electrocatalysts as inexpensive and available alternatives [158]. A PPy/graphene oxide (PPy/GO) nanosheet-based composite was developed that showed a high conductivity, thermal stability, and surface area, with potential for use as improved catalyst supports in PEMFCs [159].

PEDOT and PEDOT/poly(styrenesulfonic acid), PEDOT/PSSA were studied as Pt supports in PEMFC electrodes, evidencing an increase in fuel cell performance compared with the Pt supported in Vulcan XC-72R. The presence of PEDOT/PSSA enabled better dispersion of the Pt nanoparticles on the electrodes and facilitated electronic and ionic conduction within the catalyst. Other important findings are related to the reduction of Nafion® loading in PEMFC electrode inks and the reduction of Pt corrosion compared with commercially available CB-Vulcan XC-72R carbon [160].

Compared with the conducting polymer, the employment of conducting polymer-carbon composites appears to improve the overall conductivity. Thus, different nanocomposites involving mesoporous carbon (MC) and conducting polymers were investigated. A nanocomposite of Pt/MC-PEDOT was developed as Pt nanoparticle support in the cathode electrode, which improved stability and durability (resistance to corrosion) compared with commercial Pt/carbon [161]. Conductive inks of Pt/PEDOT/C nanocomposites were prepared with different carbon ratios to understand the influence of the carbon ratio in the performance of developed composites in fuel cell electrodes. The results obtained showed that PEDOT/C materials were promising support materials and that the carbon ratio in the composite material has a key role in the morphology and electrocatalytic activity, affecting the overall PEMFC performance [162].

The polymer-based nano-inks are good candidates to improve or replace the current metal catalysts used in fuel cell electrodes and thus reduce the cost of fuel cell production.

2.5.5 Passive DMFCs

DMFCs can be classified as active, semi-passive, or passive based on the fuel supplying mode. In the active mode, the reactants are fed with the use of pumps, fans, sensors, heaters and humidity components. In this system, the fuel and oxidant supply rates can be controlled having the advantage of obtaining higher performance. Semi-passive DMFCs have a passive anode and active cathode or an active anode and a passive cathode [163].

In a passive mode, no auxiliary components for the supply of methanol and oxygen are used; the reactants are passively transported from the methanol chamber and ambient air to the MEA, by capillary forces, gravity and concentration gradients. Although the passive DMFCs systems displayed lower power than the active version,

they possess a much simpler and compact structure, thus more suitable for miniaturization and portable applications that have low power requirements. Hence, passive DMFCs are suitable for application in devices with low power requirements, such as biosensor platforms devices, whereas the active setups are more suitable for higher power and continuous operation devices such as laptops and cell phones.

The passive DMFCs systems are good candidates to replace the currently used batteries in portable applications, turning electronic devices much lighter due to the higher energy content per unit mass in comparison with conventional batteries [163]. The powered DMFCs systems are smaller, less costly, and environmentally friendly, with fast methanol refuelling. Apart from the fuel refilling, the batteries need to be replaced periodically since the voltage of the battery degrades with a decrease in charge, although the fuel cell system can maintain a constant voltage, as long the fuel is supplied.

The prototype design and fabrication of micro passive DMFCs systems depend on the intended application, since each application has different requirements, such as power, voltage and geometric assembly. Miniaturization is a challenging process and not a simple scaling down of a larger system. Hence, each component of the fuel cell must be readapted and redesigned taking into view the final application and specifications. The most critical challenges to overcome in passive configurations are related to methanol crossover and mass transport of the different species [164].

The methanol crossover rate is related to the use of membranes that have permeability to methanol, along with water. Hence, methanol can pass through the membrane to the cathode side and consequently the voltage of the DMFC decrease and also fuel is wasted, contaminating also de Pt in the cathode electrode. To minimize this problem, small methanol concentrations can be used; thus, the methanol concentration should not be too low, since an insufficient methanol concentration in the anode CL leads to a large mass-transport loss and consequently to a lower cell voltage.

In passive set-ups, additional fans/compressors were not employed, so the primary transport mechanisms for the species delivering in the CLs are diffusion and natural convection. This condition limits the rate of electrode reactions and can be minimized by a suitable fuel cell design and nanomaterials employed, been adapted to improve the reduction of the mass transfer resistance, water management and also CO_2 removal.

As discussed in this section, there are many challenges to the development of passive DMFC systems. The miniaturization also adds more challenging and crucial steps

to obtain a device that fulfills the intended final application. In this thesis, two different passive prototypes were developed and successfully applied to the biosensor application. This field of application is almost not explored, with very few works published considering biosensing application. Therefore, another prototype considering methanol fuel cells were successfully developed and presented in the next section.

2.5.6 Applications of Direct methanol fuel cells

DMFCs have been receiving much attention in recent years as an alternative to fossil fuels-based energy sources, owing to their high efficiencies and very low emissions. There are three main fields of application where fuel cells can be employed, being more specifically divided into stationary, portable and transportation fields. Presently, the most appealing applications for DMFCs are in the portable sector, with the potential to replace everything that uses a battery, such as computers, mobile phones, or personal organizers. Some prototype examples involving the DMFCs technology in portable applications are shown in Figure 2.21.

To date, DMFCs have shown that they can be successfully produced on a commercial scale, as seen in the last presented prototypes. Therefore, the dependence on high-load expensive catalysts, allied to the performance enhancement in terms of fuel crossover limits their dissemination in the commercial market. The research interest by the scientific community in improving the features of this technology is increasing through the last decade as can be seen in Figure 2.22.

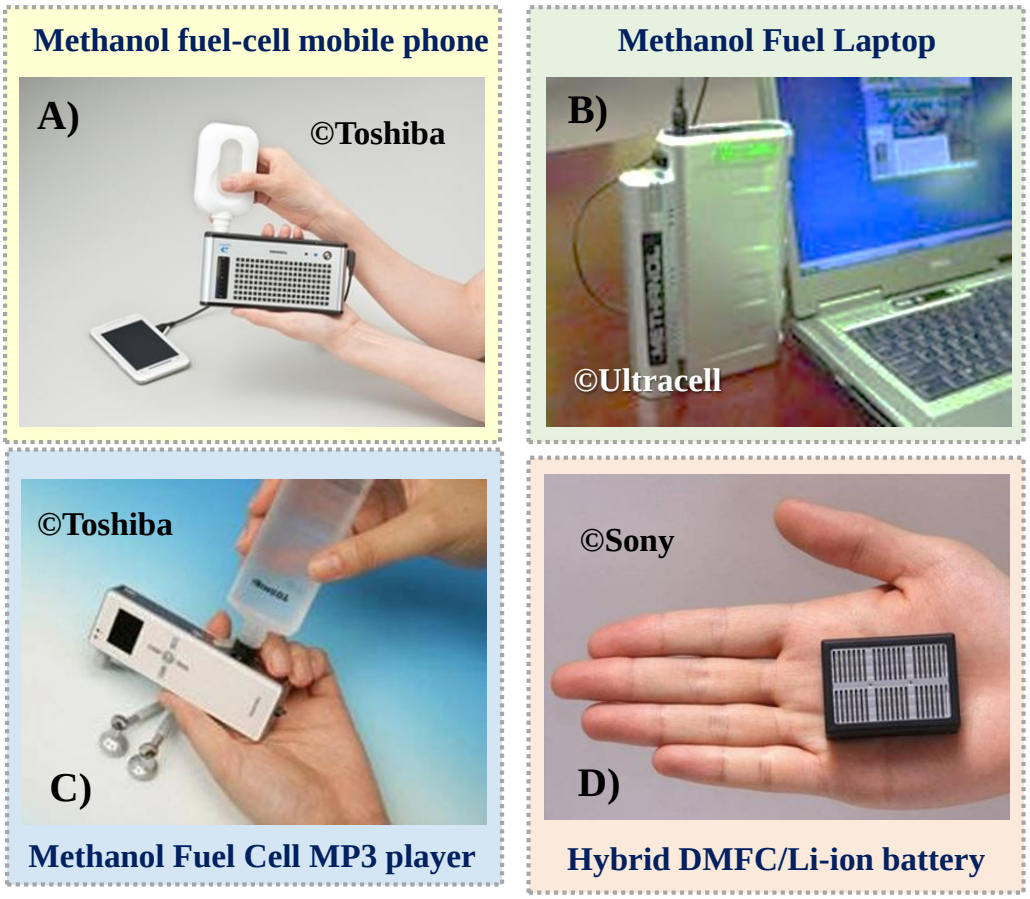

Figure 2.21 – Direct Methanol Fuel Cell portable prototypes, including a methanol fuel cell mobile phone launched by ©Toshiba (A), a portable laptop powered by a methanol fuel cell launched by ©Ultracell (B), a methanol fuel cell MP3 player launched by ©Toshiba (C), and a hybrid fuel cell system integrating a DMFC and a Li-ion battery launched by ©Sony (D).

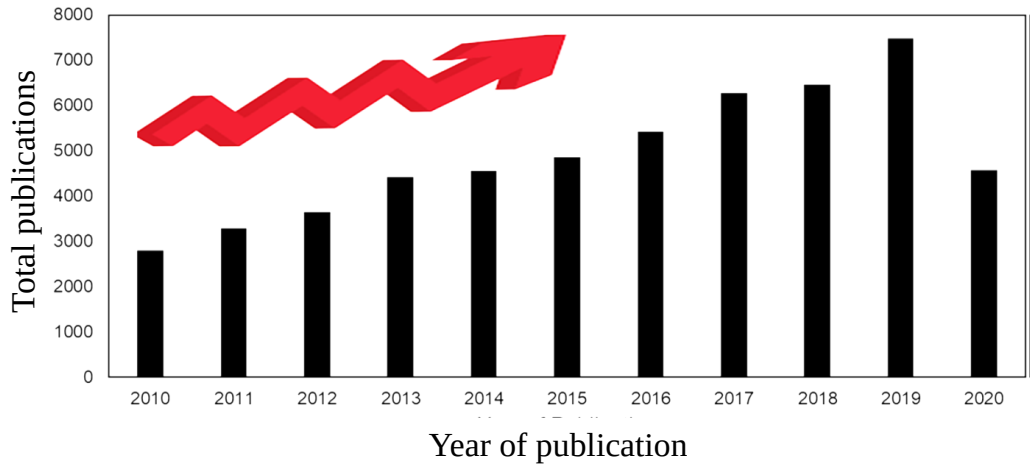

Figure 2.22 – Total publications search using keywords of all types of alcohol fuel cells found from 2010 to 2020. Adapted from [127].

Numerous topics of study have been identified to address some of the problems of the DMFC promising technology, and the development of new catalysts and membranes plays a key role in the enhancement of the performance of these devices. Thus, the development of new and low-cost materials is not the only topic to consider; the commercialization proposes into broad commercial markets brings new challenges in terms of the development of different fuel cell configurations, with the capability to keep the higher efficiency, reliability, with a competitive producing cost. The continuous research and development in this area will certainly contribute to the dissemination of this technology as a powerful power source, contributing to satisfy the worldwide energy demand.

Chapter 3

3. A passive direct methanol fuel cell as transducer of an electrochemical sensor, applied to the detection of carcinoembryonic antigen

The results presented in this chapter were published in Liliana P.T. Carneiro, Nadia S. Ferreira, Ana P.M. Tavares, Alexandra M.F.R. Pinto, Adélio Mendes, M. Goreti F. Sales, *" A passive direct methanol fuel cell as transducer of an electrochemical sensor, applied to the detection of carcinoembryonic antigen* ", *Biosensors and Bioelectronics* (2021), 175, 112877. **doi: https://doi.org/10.1016/j.bios.2020.112877.**

3.1 Introduction

The ability of monitoring cancer biomarkers in biological fluids by means of electrochemical biosensors has emerged as a fundamental tool for disease diagnosis and also for monitoring of the progression of disease [165,166]. Thus, the advantages of biosensors are vast, since they are easy to use and offer fast responses with high sensitivity and selectivity [167,168]. Despite all the advantages of biosensors so far, their autonomy still needs to be improved, in order to promote and disseminate their use among healthcare systems, especially in places where electrical power may not be promptly available or in times of natural disasters or global crises. Considering electrochemical biosensors in particular, this would mean having an electrical power source. To this end, other biosensors have been interfaced with dye-sensitized solar cells (DSSC) as an electrical power source [169,170]. Despite their advantages in terms of environmental impact, DSSC-based biosensors do not operate at night, because they do not integrate a battery as they are of single use.

As an alternative innovative approach, we propose herein the interface of a biosensing unit in the electrical circuit of a passive direct methanol fuel cell (DMFC), in which the DMFC acts as the transducer of the sensing element. The combination of DMFCs and sensors results in off-grid devices, opening new opportunities to the development of autonomous sensors, which are particularly important in times of global crisis.

The sensing element considered for this purpose is a MIP layer, obtained to detect carcinoembryonic antigen, CEA. Suitable monomers and crosslinking agents are selected and polymerized in appropriate conditions, in order to obtain a polymeric layer that displays high and selective affinity for the given target molecule.

Aiming at a simple integration of the sensor on the DMFC electrical circuit, the MIP layer was produced on the transparent conductive oxide (TCO) of FTO-glass, by electropolymerizing in-situ EDOT and Py. When CEA binds to the binding sites formed therein, the electrical resistance of this layer increases. As the number of binding sites occupied by CEA on the MIP film depends of the concentration of CEA in solution, the resistance increase is also concentration dependent. In turn, as this FTO/MIP film is integrated in the electrical circuit of the DMFC, the power of the fuel cell is also concentration dependent. This integrated DMFC/sensing element is therefore a new kind of integrated (bio)sensor.

In this work, the DMFC was set-up with a passive configuration, to allow its use outside the laboratory. In this device, few drops of an aqueous methanol solution were added to the initially dry DMFC anode; at the anode, the added methanol is transported passively by capillarity and concentration gradients [171]. Overall, these passive set-ups are suitable to operate at room temperature, allowing miniaturization and portable applications [172]. The single work published so far employing DMFCs for a similar end was operated in a non-passive environment, which means that the system required constant mechanical feeding of the reagents (methanol and oxygen) [173]. This particular configuration depends of many accessories (pumps, auxiliary tubes and pressure requirement), which makes impossible its future application as an autonomous and portable device. In addition to this, the cell set-up used there required special tools to open and close, because the pressure exerted into the cell needed accurate control to avoid irreproducible data.

Thus, to the best knowledge of the authors, this is the first work reporting a MIP sensing element transduced by a passive DMFC device, and actually allowing its use as portable unit. The selection of CEA as target biomarker was due to the fact that it is a very important biomolecule in cancer disease diagnosis and follow-up, being most especially related to colorectal cancer disease [174,175]. There are several methods described in the literature for CEA determination, but no one of these employs the technical approach proposed herein.

In detail, the integrated device contained the DMFC and the sensor units integrated in the series in a closed electrical circuit. The passive DMFC unit was developed as described in [172] and optimized in the absence of auxiliary components for the supply of methanol and oxygen. The sensor unit contained an imprinted CEA film assembled on a Fluorine doped Tin Oxide (FTO) glass with a layer of PEDOT [170]. This electrode was sandwiched with another FTO-glass with Pt nanoparticles, having electrical contact by means of a suitable electrolyte solution. The final set-up was tested against CEA in different media (buffer, synthetic fluid model, Cormay® serum), transduced by the electrical power of the DMFC.

3.2 Experimental section

3.2.1 Reagents and solutions

All chemicals were of analytical grade and water was ultrapure Milli-Q laboratory grade. MES buffer, 10 mM, pH 6.0, was obtained by dissolving 2-morpholinoethanesulfonic acid buffer grade (obtained from AppliChem). This buffer was used throughout. CEA stock solutions (obtained from MyBiosource) were prepared in the previously prepared MES buffer, and less concentrated standards were obtained by accurate dilution of the previous solution in the same buffer, ranging from 0.1 ng/mL to 100 μg/mL.

The electrolyte solution used in the biosensing unit consisted of 0.05 M iodine (Riedel-de-Häen), 0.1 M lithium iodide (anhydrous, beads, ~10 mesh, 99.999% trace metals basis, Sigma-Aldrich), 0.6 M 1-hexyl3-methylimidazolium iodide (HMII, 98%, Alfa Aesar), and 0.5 M 4-tertbutylpyridine (TBP, >96.0%, from TCI) in acetonitrile, as described in [169]. The monomers used in the synthesis of the MIP film were 3,4-ethylenedioxythiophene (EDOT, 97%, Alfa Aesar) and Py, obtained both from TCI.

For selectivity studies, a physiological Synthetic fluid model and Cormay® serum (PZ Cormay S.A) were used with a dilution of 1000 x. The Synthetic fluid model was prepared using 145 mM sodium chloride (Panreac), 4.5 mM potassium chloride (Merck), 32.5 mM calcium chloride (VWR chemicals), 0.8 mM magnesium chloride (Riedel-de-Häen), 2.5 mM urea (Fagron), and 4.7 mM glucose (Alfa Aesar) as described [176]. These media were spiked with the same biomarker concentrations, as previously described for the buffer.The selectivity study used ascorbic acid (0.02 mg/mL; Riedel-de-Häen), D-Glucose Monohydrate (1.3 mg/mL; Alfa Aesar), Urea (0.2 mg/mL;Fagron), Cancer Antigen 15–3 (150 U/mL; MyBiosource), and Cancer Antigen 125 (150 U/mL; HyTest) were used with the mentioned concentrations (in buffer).

3.2.2 Preparation of the sensing unit

The sensor unit combines two conductive FTO-glass electrodes interfaced in the electrical circuit. One was de anode (Figure 3.1-A) and acted as the sensing unit and the other was the counter electrode, allowing the electrical flow through the overall set-up

and completing the electrical circuit by means of an electrolyte solution between these two electrodes (Figure 3.1-C).

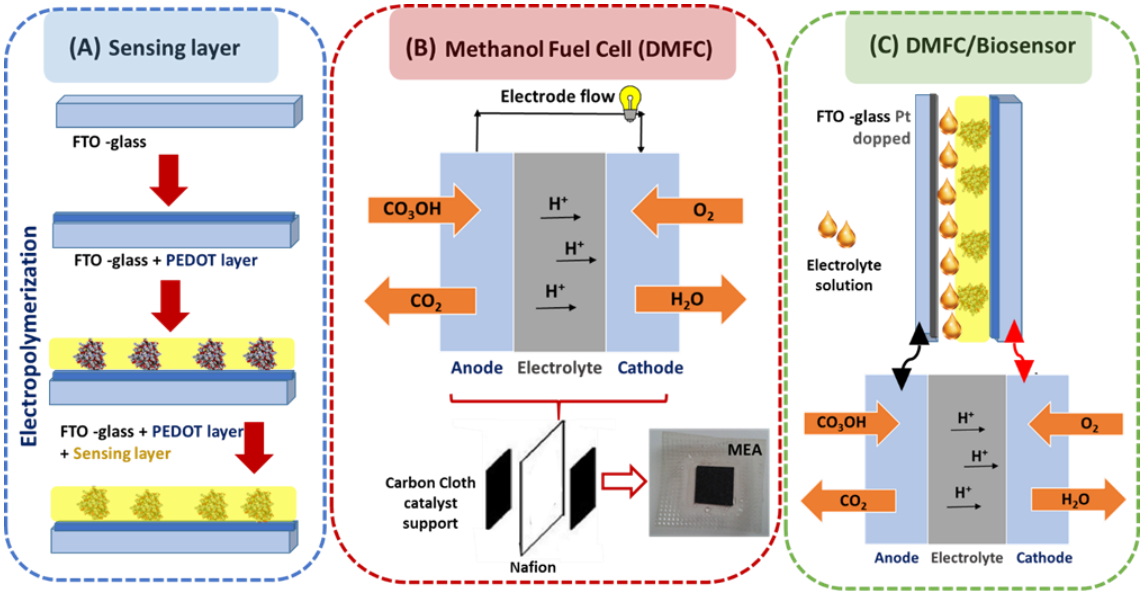

Figure 3.1- Schematic representation of the constituents of the final biosensor device, including (A) the different steps for the sensing layer development (B) the methanol fuel cell device and membrane electrode assembly (MEA) (B) integrated DMFC/Sensor electrically coupled (C).

The counter electrode consisted of a FTO-glass with Pt nanoparticles, deposited by spin-coating and subsequent annealing. It was obtained as described in [169], by coupling gold nanoparticles to Dye-Sensitized Solar Cells, for an increased efficiency. Briefly, the FTO-glass was cleaned in acetone, followed by ethanol and deionized water. The active area of the FTO-glass was covered by a Pt film obtained by a dissolved platinum salt in ethanol, which was deposited by spin coating at 2000 rpm for 20 s. Afterwards, the glass with Pt was annealed in the oven at 450 ˚C for 15 min. To grant a good electrical contact, silver ink was painted on one edge of the glass.

The sensing electrode consisted of a FTO-glass modified with a PEDOT layer was prepared by electropolymerization in-situ of an EDOT solution. The MIP film was assembled on top of the PEDOT by co-electropolymerization of Py and EDOT in the presence of CEA (CV, 10 cycles) [170]. CEA was after removed by incubating the electrode in Proteinase K (500 µg/mL) overnight. A control non-imprinted polymer electrode (NIP) was obtained in parallel, using the same steps, but without CEA.

The MIP sensing electrode was discarded after each respective calibration (single use). The Pt coated counter electrode was reused several times, as it was not modified during the readings of the sensing layer.

3.2.3 Fuel cell unit

The passive DMFC device used herein was set-up as indicated in Figure 3.1-B, according to [172]. The actual set-up may be seen in Figure 3.2 (A and B). It contains two acrylic cover plates, one for each electrode. The anode side is represented in Figure 3.2-A and contains a specific storage deposit for methanol solution refueling, with easy access to allow fast introduction of the fuel into the system. The cathode is represented in Figure 3.2-B and has an "open" grid area for allowing oxygen from atmospheric air to enter the cell.

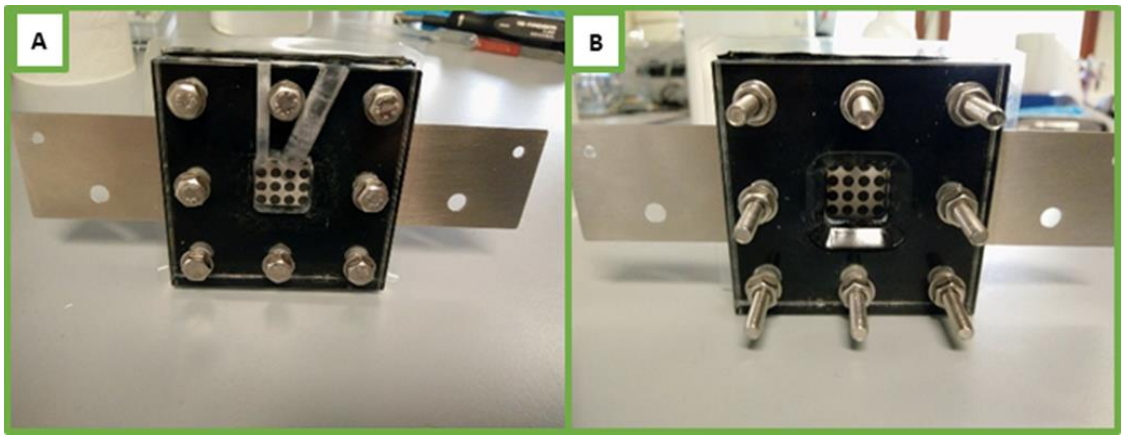

Figure 3.2 - Designed passive DMF device: (A) Anode side of the fuel cell, which contains a reservoir for the methanol solution insertion into the system; (B) Cathode side of the fuel cell, with a grid open to the atmosphere, in order to allow that the O_2 present in the atmospheric air reaches the electrode.

The overall set-up also includes two metallic end plates, working as current collectors, and a rubber gasket, that works as an insulating element, in order to avoid electrical short-circuit (technical drawings showed in Figure 3.3).

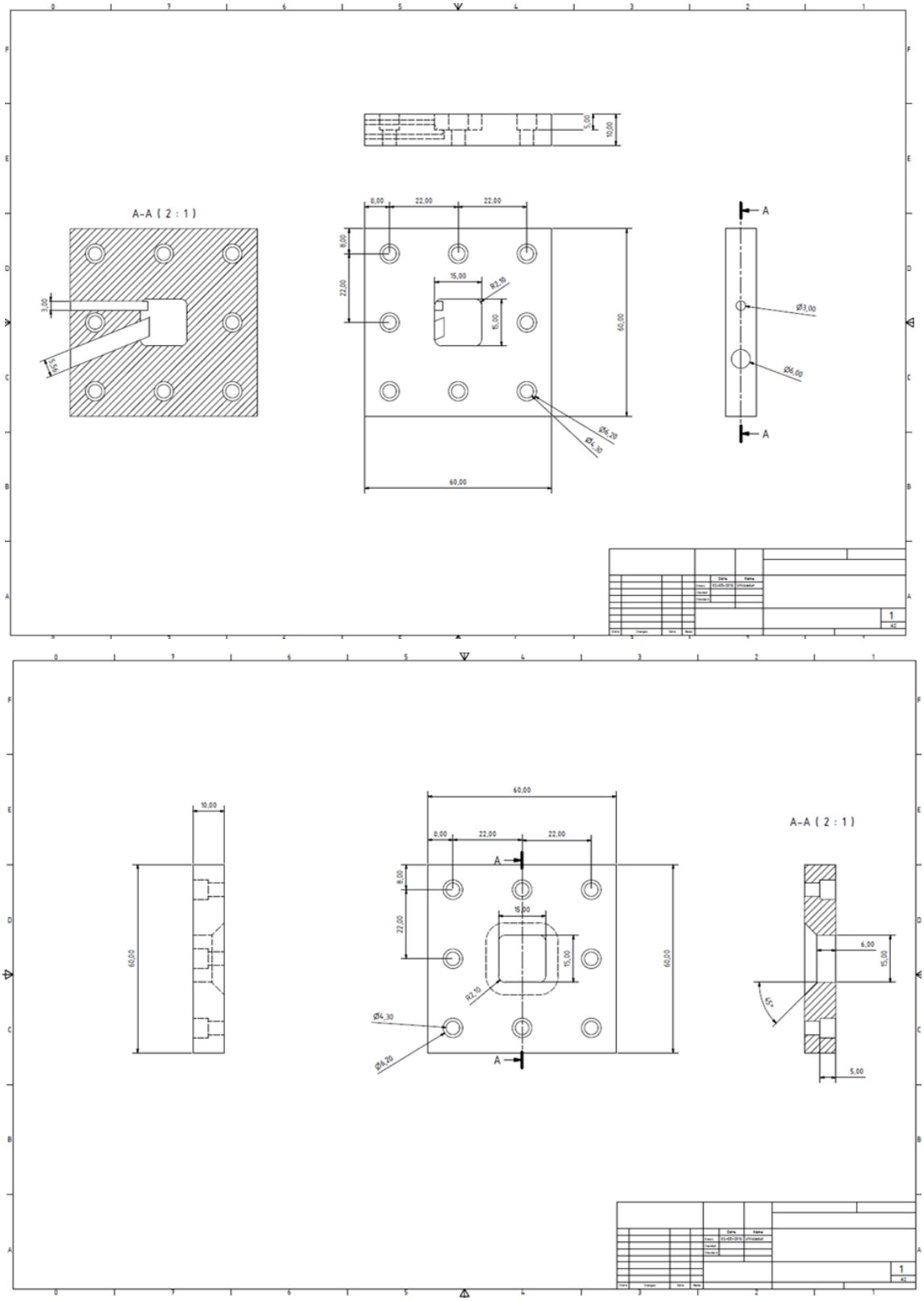

Figure 3.3 - Technical drawings of the DMFCs used in this work**.**

The assembly of this DMFC was made in a single cell, using a passive fuel cell operation mode. It is important to highlight that the added fuel percolates to the anode by

capillarity and diffusivity, without the need of an active pump. These characteristics allied to the compact structure of this device make it suitable for a portable application, such as, power a sensor. Inside the DMFC set-up there is the membrane electrode assembly (MEA), consisting of two commercial carbon cloth electrodes, separated by a solid Nafion® membrane (115). The active area of the MEA was 2.25 cm^2. The cathode consisted of a carbon cloth layer containing 1 mg Pt/cm^2 and the anode was a carbon cloth with 2 mg PtRu/ cm^2 content.

The DMFC cell was operated at room temperature and atmospheric pressure. The anode was feed by a 2 M methanol aqueous solution and the cathode used O_2 from the atmospheric air. Before use, fuel cells were activated by measuring consecutively polarization curves, until OCP values reached 0.63–0.66 V, depending of the DMFC, and current values changed less than 1–2%. After the feeding the DMFC with the fuel and its activation, three different type of polarization curves (Sampled DC technique) were obtained: a) for the DMFC alone; b) for the DMFC/ Sensor without the target protein, in blank assays; c) for the DMFC/Sensor with the target protein (calibrations). Figure 3.4 shows the typical polarization curves obtained throughout the overall process, reflecting the behavior of the DMFC before and after the MIP integration, including the blank assay response (after MES buffer incubation) and protein incubation response.

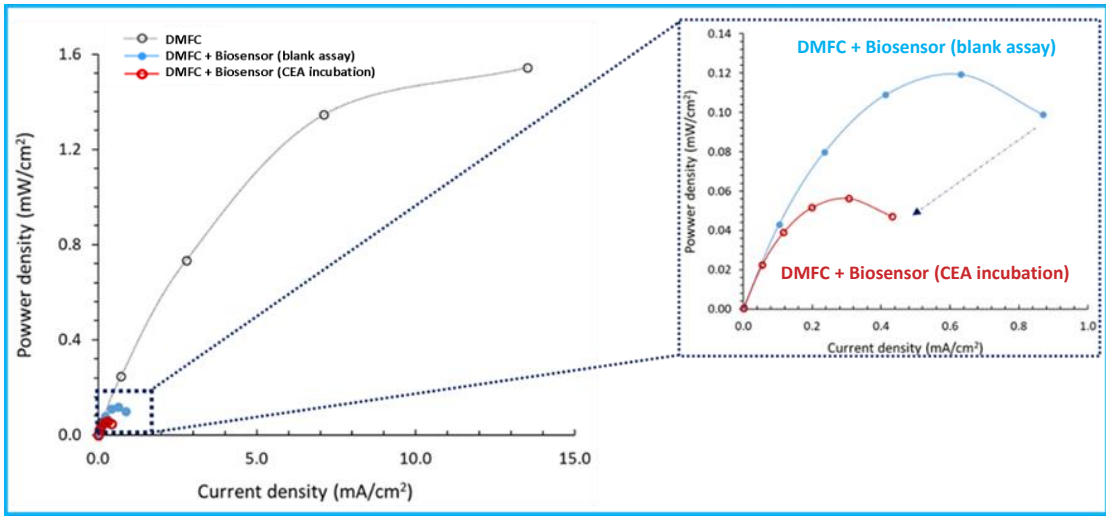

Figure 3.4 - Power curves obtained during an experimental assay: for the DMFC alone, for the DMFC/Biosensor without the target protein (after buffer incubation) and for the DMFC/Biosensor with the target protein (after incubation of a CEA standard with concentration of 100 mg/mL).

The DMFCs used in this work were not directly modified through the sensing analysis, and therefore they may be reused for a long period. Between reutilization, the DMFCs were stored by replacing the methanol solution in the container by water and sealing it with Parafilm®, to avoid evaporation.

3.2.4 Apparatus and integrated device set-up

Electrochemical measurements were conducted in a potentiostat/ galvanostat from Metrohm Autolab and a PGSTAT302N, controlled by Nova software (NOVA 2.1). All electrochemical measurements were performed at room temperature and atmospheric pressure. The set-up of the integrated DMFC/Sensor is shown in Figure 3.1-C. The anode of the DMFC was feed with an aqueous 2 M methanol solution, loaded in the reservoir. The cathode used O_2 from atmospheric air. The sensor element was electrically integrated with the external electrical circuit of the passive DMFC. To this end, the electrical crocodile connectors were used to connect both systems (Figure 3.1-C, bidirectional arrows).

3.2.5 Electrochemical assays

The response of the passive DMFC with the integrated sensor was evaluated by Sampled DC. Before coupling with the sensor, the DMFC was activated running few polarization curves. The calibrations of the integrated system were made by incubating CEA standard solutions of increasing CEA concentrations on the anode sensing electrode, for 20 min; this solution was carefully washed out with Milli-Q water and dried with nitrogen and closed again using the previously described electrolyte. After integrating this biosensing cell in the electrical circuit, the performance of the DMFC integrated system was evaluated. This procedure was repeated for increasing concentrations of CEA, prepared first in MES buffer and after in diluted Cormay® Serum (1000 ×) to assess the ability of the MIP film to discriminate CEA (selectivity).

3.3 Results and discussion

3.3.1 Normal operation of the passive fuel cell

The resolution, the response time and stability of the sensor response are related to the power supply potential and stability [177]. The DMFC was then optimized to provide a stable power at optimized potential by checking essentially the effect of the methanol aqueous concentration, ranging from 0.25 to 2.0 M. The obtained polarization curves and power curves were shown in Figure 3.5-A/B.

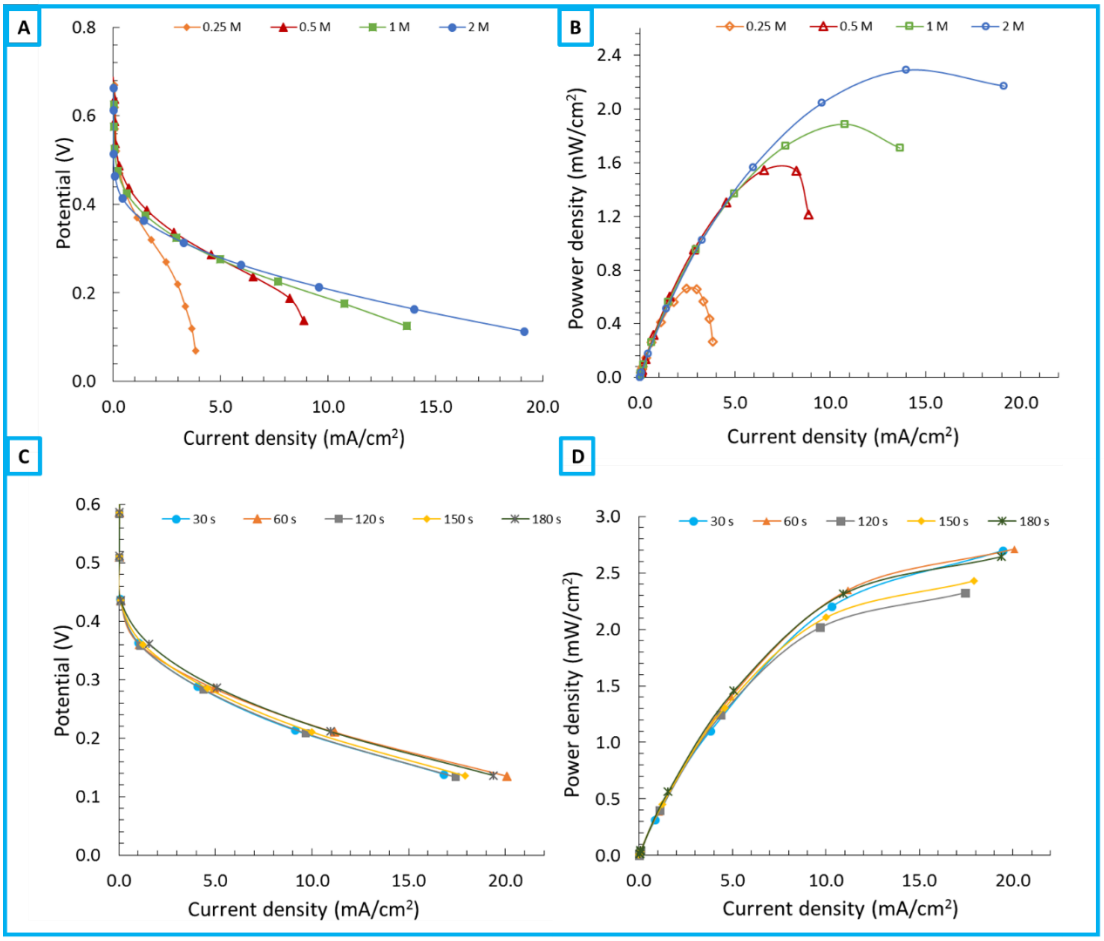

Figure 3.5 - Electrochemical data of the passive DMFC in the form of (A) polarization and (B) power density curves of the passive DMFC device operating with different MeOH concentrations; Electrochemical data of the passive DMFC device using different reading times (30 s – 180 s) in each potential, using 2.0 M MeOH concentration, plotted as (C) polarization curves and (D) power curves.

As expected, results indicated that both current density and power density increased with increasing MeOH concentrations. The highest MeOH concentration yielded a maximum power of 2.5 mW/cm^2 and a maximum potential of 0.66 V (OCP), which are acceptable values for a passive DMFC operating at room temperature [164]. Increasing methanol concentrations were also linked to faster, sharper and stable responses of the sensor unit. Thus, the maximum concentration tested, 2.0 M, was selected for further studies. Although having the risk of some methanol crossover, this condition yielded the best performance of the DMFC, guaranteeing the highest energy possible to the sensor and directly impacting upon the sensitivity of the integrated sensor response.

For obtaining the polarization curve, the time given for each reading was optimized, varying from 30 s to 180 s, with steps of 30 s. The optimal reading time was set to 60 s, compromising the quality of the readings and the time needed for obtaining the overall polarization curve. At least 5 experimental reads were collected per curve. The resulting polarization curves were represented in Figure 3.5-C and the power curves in Figure 3.5-D. When the reading time was set to 30 s and 120 s, the reproducibility of the sensor was inferior. With the exception of the 30 s of reading time, all other potential reading times led to stable power readings, with relative standard deviations ranging from 0.2% to 3.1% (data showed in Figure 3.6).

3.3.2 Setting the integrated device

The electrochemical cell of the sensing unit was composed of two electrodes. One electrode had the MIP film selective to CEA, similar to that developed in [170], and assembled on top of a PEDOT layer on a FTO-glass support. In detail, this MIP film was obtained by co-electropolymerization of EDOT and Py, in the presence of CEA. CEA was later extracted from the polymeric network, to create vacant positions of high affinity for CEA binding (Figure 3.1-A). The electrochemical EIS data of the different steps involved in the construction of the sensing unit was compared with the NIP control, as represented in Figure 3.7.

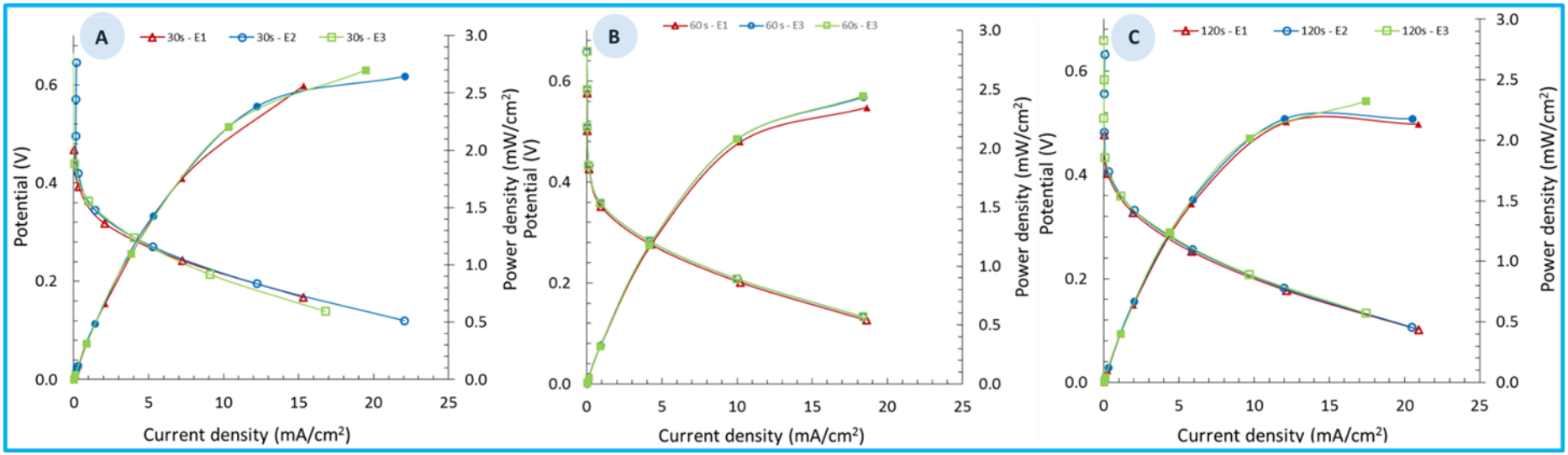

Figure 3.6 - Polarization curves and power curves obtained for different potential reading times: (A) 30 s, (B), 60 s and (C) 120 s, using 2.0 M of MeOH. Each plot contains 3 consecutive measurements.

In general, the PEDOT layer on the FTO-glass was confirmed by confocal microscopy, while being also perceptible to the naked eye (Figure 3.7-A).

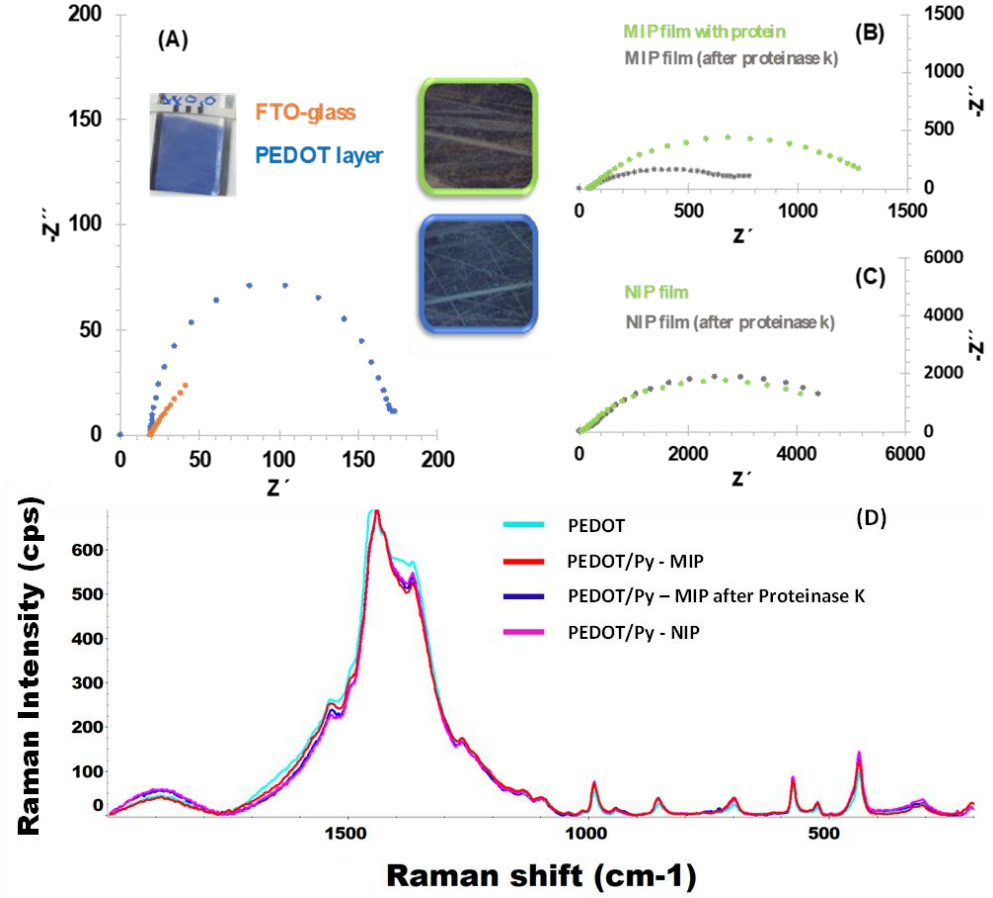

Figure 3.7 - Electrochemical EIS data of the different steps involved in the construction of the different electrodes. (A) FTO-glass with (blue) or without (orange) PEDOT layer and the photography of FTO glass after PEDOT layer and respective confocal image of PEDOT layer before and after polymerization PEDOT/PPy. (B) MIP film with (green) or without CEA (gray). (C) NIP film before (green) or after (gray) proteinase k treatment. (D) Raman Spectra of the different construction steps of MIP and NIP. Data in (A), (B) and (C) used 5.0×10^{-3} M $[Fe(CN)_6]^{3-/4-}$ readings in PBS buffer, pH 7.0.

The formation of the MIP/NIP film on top of this PEDOT layer was evident by EIS studies, in which the charge transfer resistance displayed a significant increase (Figure 3.7–B/C). This increase was more evident on the NIP, because the presence of CEA (on the MIP) by the time the polymer was being formed hindered its growth. The removal of CEA from the polymeric network was confirmed by a decreasing resistance to charge transfer (Figure 3.7–B). The presence of the polymeric MIP/NIP films on the

FTO/PEDOT glass was also confirmed by Raman spectroscopy (Figure 3.7-D), although the observed changes were not significant, because the MIP/NIP films also contained PEDOT. The imprinting factor of the MIP was also calculated as the ratio of the signal produced by the same standard CEA solution (the highest concentration tested) in both MIP and NIP. Considering the corresponding relative values to the blank and subtracting the unitary effect of the blank, this imprinting factor was 2.65, thereby confirming the great ability of the MIP to detect CEA by means of its imprinted positions.

The second electrode of this electrochemical cell was a FTO-glass covered with a layer of Pt nanoparticles generated in-situ. A suitable electrolyte between the MIP and the Pt layer ensured electrical contact between these two electrodes. The integrated DMFC/Sensor is represented in Figure 3.8.

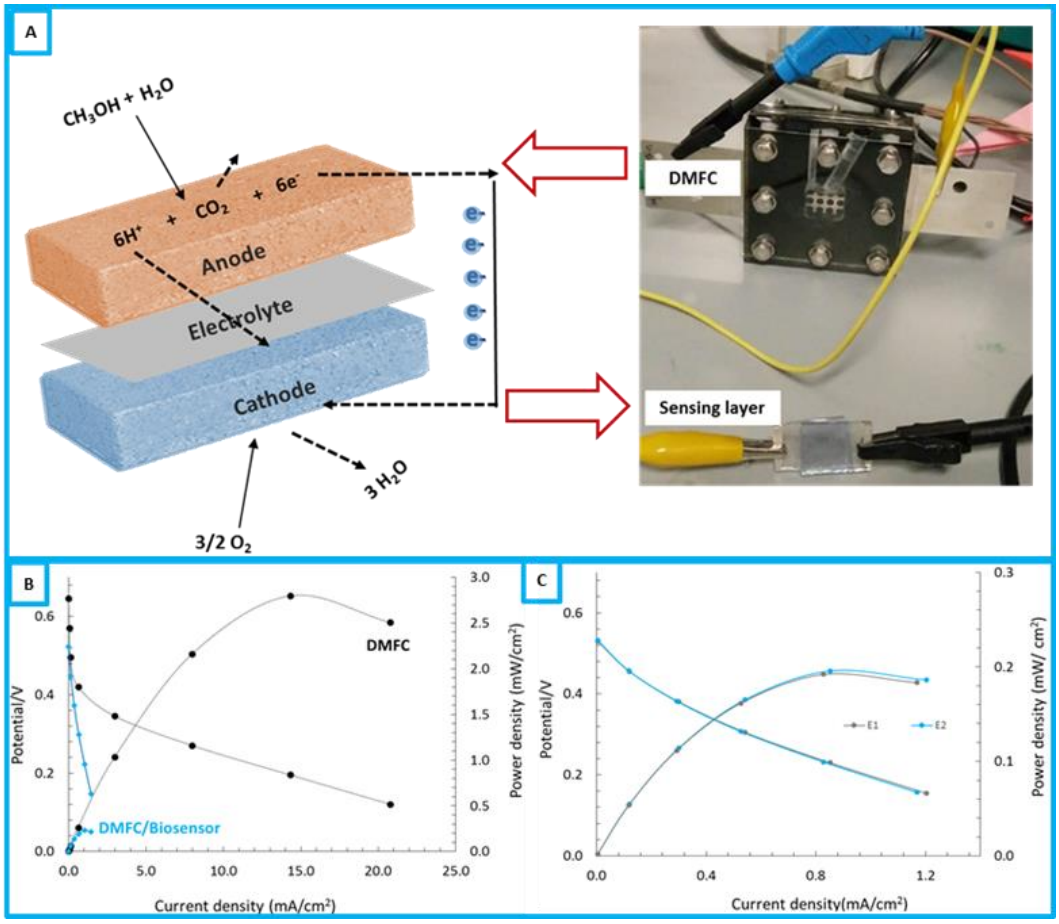

Figure 3.8 - Integrated set-up assembly including a (A) Schematic diagram representation of the DMFC functioning with the chemical species involved in methanol oxidation-reduction process and real image of the set-up of DMFC/Sensor. Electrochemical results of the polarization and power densities obtained: (B) before (dark line) and after (blue line) the coupling of the sensor with the fuel cell; (C) stability of the DMFC/Sensor assembly in two consecutive assays.

This integrated sensor/power supply assembly was never reported before and therefore different configurations had to be tested first to achieve an optimized unit. This includes checking the response of FTO-glass without Pt and loaded with different electrolyte compositions (Figure 3.9), but the conditions described before were the ones promoting the lowest resistance upon the external circuit of the DMFC.

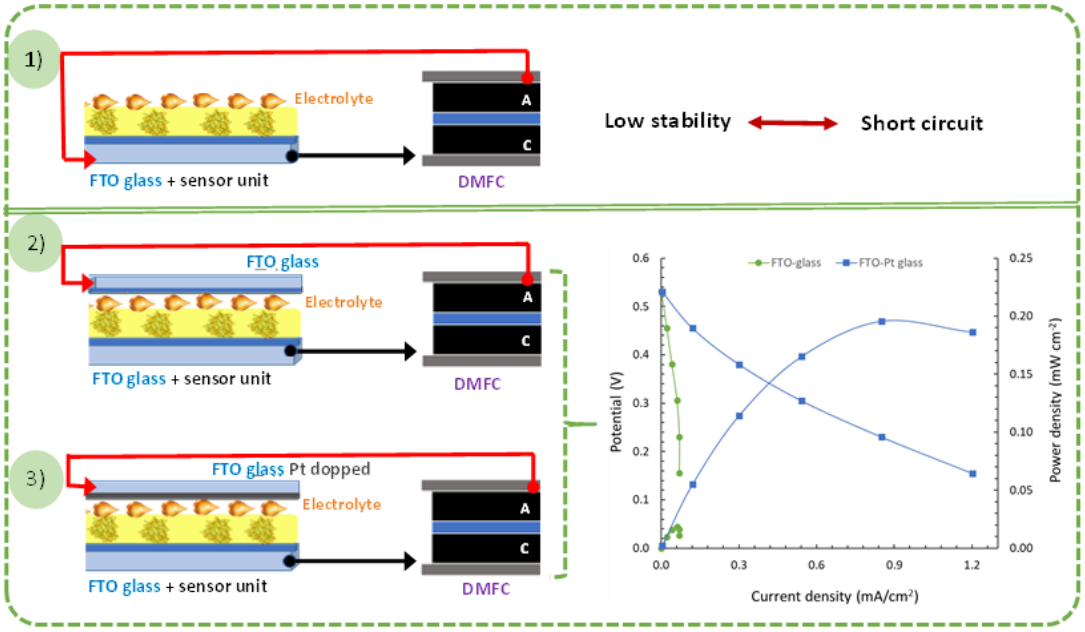

Figure 3.9 - Scheme of the different setups tested for the (MIP/FTO-glass) electrode integration in the external circuit of the DMFC and electrochemical results obtained with the different assemblies.

The integration of a single electrode (MIP/FTO-glass) in the external circuit of the DMFC was also tested (Figure 3.9), because this configuration would facilitate the incubation of the sample. However, the response of the sensor was insensitive to concentration changes, as the electrical conduction through the FTO layer prevailed, or lead to short-circuit when an electrolyte was present and met the electrical connections.

The impact of the external sensor upon the DMFC cell output was evaluated by incubating buffer only and measuring after polarization and power curves. Comparing to the DMFC device, the integrated DMFC/Sensor setup showed lower current and power values (Figure 3.8-B/C). The power density of the integrated device was ~5% of the power density generated by the DMFC alone (Figure 3.8-B). The mean power of the DMFC was 2.50 mW/cm^2 (average of four assays), whereas the mean power of the

integrated system (DMFC + Sensor) was 0.12 mW/cm^2 (average of three assays). These results were as expected, considering that the sensing unit integrated in the external circuit imposed a very significant resistance to the electrical circuit. This resistance affected, in turn, the electron flow along the external circuit. As the electrons migrating through the external circuit were required at the cathode for oxygen reduction (Fig. 3.8-A), this limited electron flow was translated by a breakdown in the final power of the integrated device.

To serve as a transducer, this integrated set-up should be reproducible and generate repeatable data. Thus, four independent units were evaluated for the different media tested herein. This includes buffer and synthetic fluid model. The results obtained indicated mean power values of 0.12 mW/cm^2, with relative standard deviations of ~3%, which confirmed the good reproducibility of the integrated set-up in buffer (Figure 3.8-C). Tests made with the synthetic fluid model incubated in the MIP film yielded mean power values of 0.075 mW/cm^2, with relative standard deviations of ~6%. This indicated that the fluid model could be affecting the inherent performance of the DMFC, but this was likely to happen due to the complex composition of this medium, which would lead to a higher background resistance of the MIP film.

3.3.3 Response to CEA in buffer

The calibrations of the integrated DMFC/Sensor device were made after ensuring a signal stabilization, in which the necessary incubations of MES buffer were made to ensure a repeatable signal output. After this, increasing concentrations of CEA standard solutions ranging from 100 pg/mL to 100 μg/mL were incubated consecutively on the MIP film and the device performance recorded after each concentration. Each standard solution was let stand on the MIP film for 20 min. After this period, the sensing layer was washed with buffer, a few drops of electrolyte were casted on top of it and the cell closed with the FTO-glass/Pt electrodes. This cell was further integrated in the external electrical circuit of the DMFC. After feeding the DMFC unit with 2 M methanol, the performance of the cell was recorded by sampled DC (important to note that this solution could sustain the sensor response for several hours). Several calibrations were made to assess the standard analytical features of operation of this integrated set-up. A typical plot obtained is shown in Figure 3.10-A and the normalized average values of power density and the standard deviation of all curves (error bars) were represented in Figure 3.10-B.

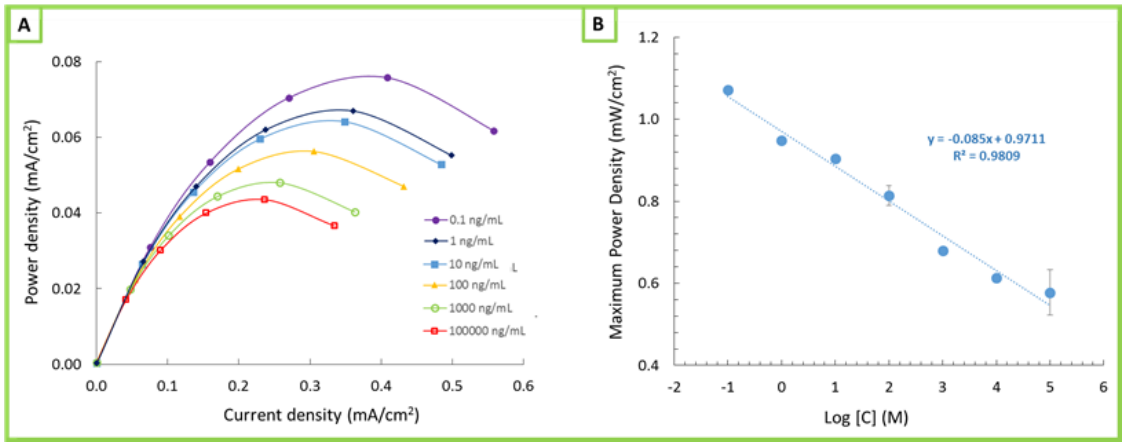

Figure 3.10 - Typical Power-Current Density curves of the DMFC/Sensor device towards CEA increasing concentrations in the range of 0.10 ng/mL to 100.0 µg/mL in buffer. Results show: (A) a calibration curve obtained during calibrations of crescent concentrations of CEA standards; (B) the average value of the maximum power density obtained in each CEA concentration.

In general, the average power density decreases for higher concentrations of the CEA, in a concentration dependent mode. The results shown in Figure 3.10-A show that after the successive incubations with increasing CEA concentrations, the output power of the device also decreased. After an initial value of 0.12 mW/cm^2 for stabilization in MES buffer, the power decreased to 0.044 mW/cm^2 when probing the maximum concentration of CEA. This variation was consistent among the different calibrations performed in buffer, indicating that after completing the calibration, the power was about ~63% smaller than the original for the blank unit. This was consistent with the increasing electrical resistance that the MIP film imposes to the circuit, after binding with increasing concentrations of CEA, thereby imposing an increasing power consumption. The binding of CEA in the MIP layer clearly limits the electronic flow along the external circuit, making the DMFC a transductor of this binding event.

In terms of general performance, the calibration curves displayed a slope of -0.085 mW × cm^{-2}/decade concentration and a squared correlation coefficient of ~0.981. This data is shown in Figure 3.10-B, corresponding to normalized power values ($power_{sample}/power_{blank}$). Overall, the system was highly reproducible, yielding relative standard deviations of each standard reading ranging from 0.26% to 5.5%. The resulting limit of detection was 0.08 ng/mL.

Comparing to the previously published setup for this MIP film [170], it is interesting to note that this new integrated configuration was able to increase by 100 x

the detection capability of the system. The previous work used Electrochemical Impedance Spectroscopy (EIS) to yield a linear response range from 10 ng/mL to 100 µg/mL of CEA standard solutions, while this one used a DMFC power and yielded a linear range from 0.1 ng/mL to 100 µg/mL.

To evaluate the selectivity of the MIP sensor response, selectivity tests were made in buffer solutions against common interfering compounds in serum (glucose, urea, ascorbic acid) or other cancer biomarkers (CA15-3 and CA125). This was done by testing (i) a CEA solution in a sensing unit and (ii) another CEA solution prepared with the same CEA concentration and spiked with different interfering species. The obtained data was shown in Figure 3.11 and confirmed the high preference of the sensor for CEA, with signals changing 6–7%, both in positive and negative directions.

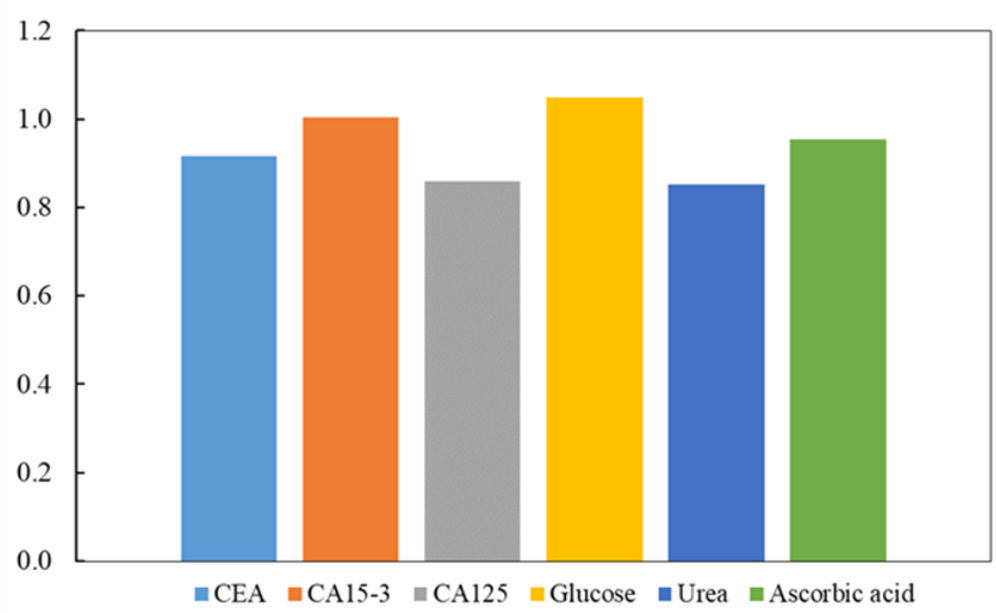

Figure 3.11 - Selectivity tests results performed with different possible interferents (glucose, urea, ascorbic acid) and similar potential interfering proteins (CA15-3 and CA125) obtained in parallel, using independent sensing units integrated in the DMFC device.

3.3.4 Response to CEA in synthetic fluid model and human serum

Further studies of this set-up proceeded by testing it under similar conditions to the biological fluids, considering that the main target of this work was to analyse CEA in serum. To this end, several calibrations were made in standard solutions prepared in a background medium of two different physiological media, to evaluate the sensing

response in a background medium that is similar to real samples, and to determine if there is any influence of interfering substances present in real samples. Figure 3.12 shows the obtained results from both tested media, synthetic fluid model and Cormay® serum, respectively.

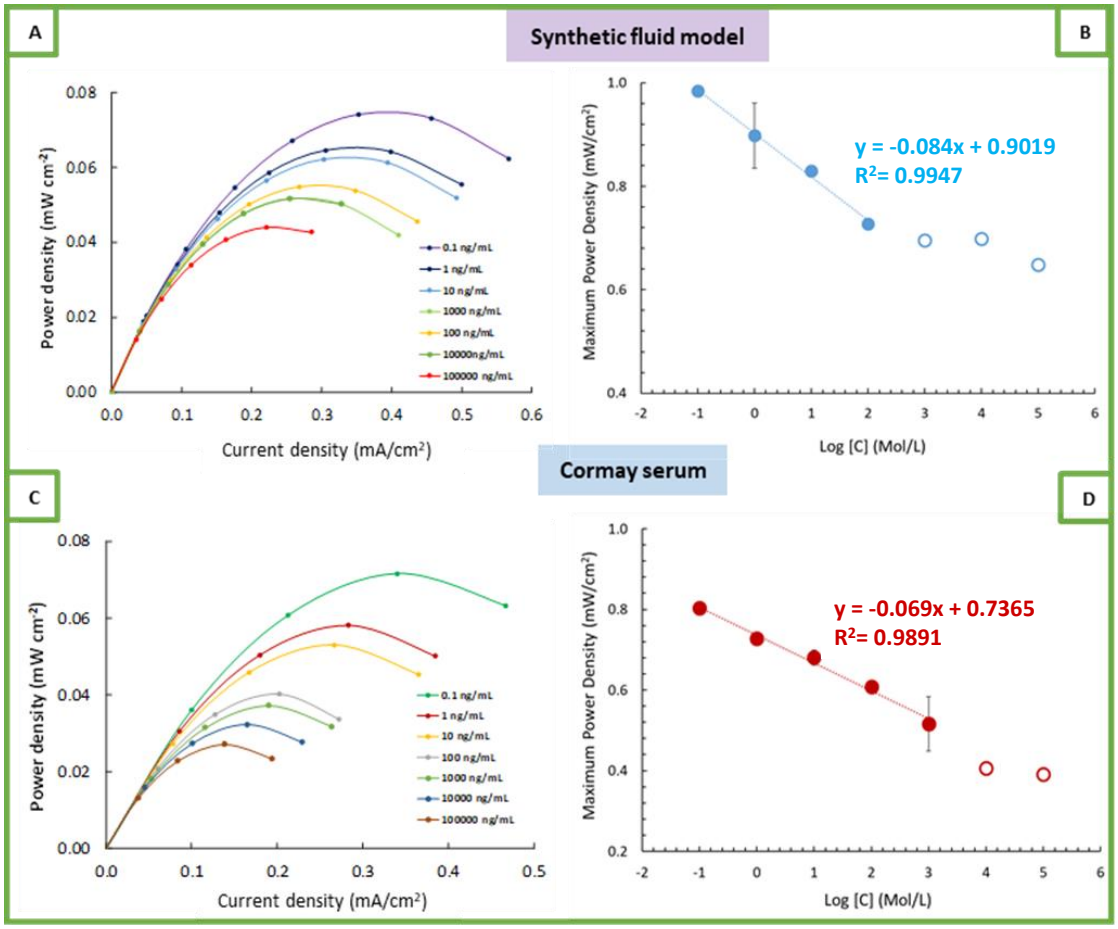

Figure 3.12 - Typical Power-Current Density curves of the DMFC/Sensor device towards CEA increasing concentrations in the range of 0.10 ng/mL to 100.0 µg/mL in physiological medium. Results show: (A) a calibration curve obtained during calibrations of crescent concentrations of CEA standards in a synthetic fluid model and (B) the average value of the maximum power density obtained in each CEA concentration. (C) A calibration curve obtained during calibrations of crescent concentrations of CEA standards in Cormay® serum and (D) the average value of the maximum power density obtained in each CEA concentration.

As shown in Figure 3.12, both media yielded a decreasing power response when incubating increasing concentrations of CEA, evidencing also a concentration dependent behaviour. Comparing to synthetic fluid model, the data obtained with Cormay® serum

presented a wider linear response range for similar squared correlation coefficients. Considering that Cormay® serum has the same composition as real samples, it seems that the developed sensor may provide a selective response for the target molecule (CEA).

In addition, when two independent calibrations with Cormay® serum with two independent devices were tested, the concentrations in the CEA standards generated by one calibration were calculated by means of using the other calibration, without generating significant errors. As an example, Figure 3.13 shows a calibration curve of an integrated set-up generated by standard solutions prepared in Cormay® serum and the signal generated by a CEA standard solutions in Cormay® serum obtained by another independent system (DMFC + MIP sensor) (red dots).

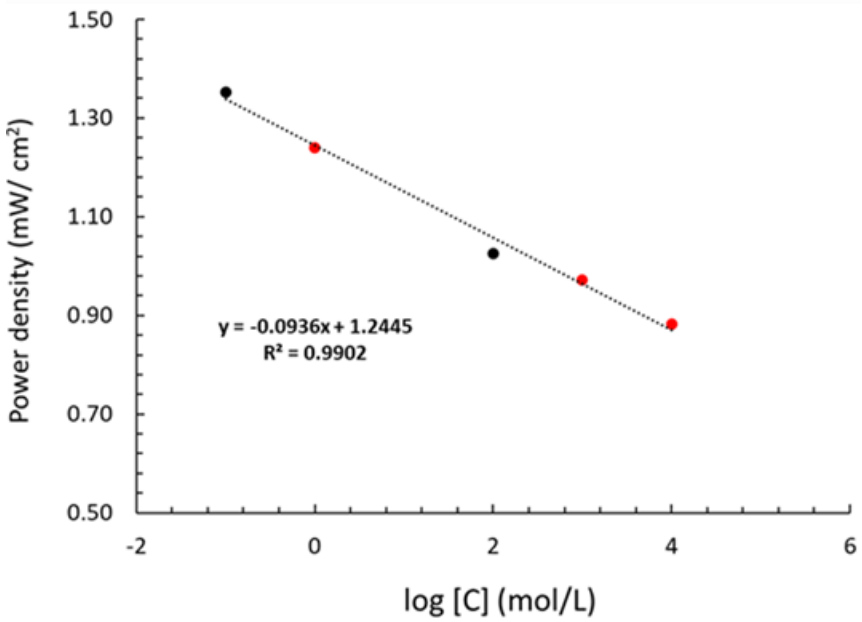

Figure 3.13 - Maximum power density in function of log CEA concentrations for a calibration with standard solutions prepared in Cormay® serum, and an independent signal of similar standards (red dots) obtained simultaneously from another independent calibration (using a different DMFC and sensor unit).

The proximity between the red dots and the linear trend confirmed the good accuracy of the system. The calculated CEA concentration deviated in a range of 1–5% from the expected values present in that specific spiked serum solution, thereby confirming the accuracy of the method.

3.3.5 Comparison to previous CEA (bio)sensors

There are several works in the literature targeting CEA, from which the most common employ antibodies or MIPs as biorecognition elements (Table 3.1). In general, the specific analytical features in each work depend on many variables, but the lowest limits of detection achieved so far come from immunosensors. Yet, this was not directly linked to the use of antibodies, as there are MIP-based works with better limits of detection than some works employing antibodies.

When comparing to other MIP-based approaches, this work displays the better limit of detection (0.08 ng/mL), which is of the same order of magnitude as another work using SERS detection [178]. When comparing to the work of [170], it may be said that this specific low limit of detection was a particular outcome of the overall configuration, in which the sensor was integrated in the circuit of a methanol fuel cell as energy source. Considering the MIP systems with electrochemical detection, this work shows a wide linear response range, which is an important feature in terms of analytical application, as it increased the probability of having clinical samples with levels of interest lying within the response range of the sensor. Overall, the combination of a suitable MIP film with a methanol fuel cell operating in passive mode compared favorably to other works reported. The concentration range for CEA detection within clinical interest and the autonomy of the presented work are considered important advantages for point-of-care use.

Table 3.1- Previous works reporting molecularly-imprinted polymers for CEA detection in the literature.

Type	Detection	Support	Bioreceptor element	Autonomy	Linear response	LOD	Reference
Immunosensor	SPR	Gold nanoparticles on Biacore Sensor Chip CM5	Anti-CEA (linked with carboxymethylated dextran)	No	1–60 ng/mL	1.0 ng/mL	[179]
Immunosensor	Electrochemical	Conductive Paper (PEDOT:PSS)	Anti-CEA (linked by physiological adsorption)	No	4 to 25 ng/mL	-	[180]
Immunosensor	Electrochemical	β-cyclodextrin/multiwalled carbon nanotubes	Anti-CEA (linked by physiological adsorption)	No	0.0001–0.5 ng/mL 0.5–10 ng/mL	0.03 pg/mL	[181]
Immunosensor	Electrochemical	Exfoliated graphite electrode with polypropylene imine dendrimer and carbon nanodots	Anti-CEA (linked with glutaraldehyde)	No	0.005 to 300 ng/mL	1.45 pg/mL	[175]
Aptasensor	Electrochemical	Glassy carbon electrode	DNA Aptamer	No	0.5 fg/mL to 0.5 ng/mL	0.34 fg/mL	[182]
MIP	SERS	Gold screen-printed electrode	MIP, electropolymerization of gallic and benzoic acids	No	1 to 1000 ng/mL	1.0 ng/mL	[183]
MIP	SERS	Glass slide	MIP, electropolymerization of 4-Vinylphenylboronic acid and Ethylene glycol dimethylacrylate	No	0.1 ng/mL to 1 mg/mL	0.1 ng/mL	[178]
MIP	Electrochemical	Silicon wafers coated with gold	MIP, electropolymerization of 11-Mercapto-1-undecanol, in DMSO	No	0 to 15 ng/mL	0.5 ng/mL	[184]
MIP	Electrochemical	Hydrophobic Paper (carbon and silver/silver chloride inks)	MIP, electropolymerization of Dopamine	No	1.0–500.0 ng/mL	0.32 ng/mL	[185]
MIP	Electrochemical	FTO glass	MIP, electropolymerization of EDOT and Py	Yes	0.1 ng/mL to 100 µg/mL	0.14 ng/mL	[170]
MIP	Electrochemical	FTO glass	MIP, electropolymerization of EDOT and Py	Yes	0.1 ng/mL to 100 µg/mL	**0.08 ng/mL**	This work

3.4 Conclusions

In summary, the integrated DMFC/Sensor setup dimensioned for CEA displayed power values that were CEA concentration dependent, thereby enabling its use as a transduction unit of the MIP sensing film. This was proven feasible in standard solutions prepared in different background medium, including buffer and more complex medium compositions, yielding accurate and precise data. It is most important to highlight the good performance of the integrated setup in Cormay® serum, which in turn confirmed the high selectivity of the response of the MIP film for CEA and suggested its ability to perform accurate analysis in real samples. In addition to this, the setup proposed hereincould detect concentrations of CEA that were 100 × lower than those previously reported for the same MIP film, thereby advancing the possibility of introducing additional improvements in terms of analytical features just by adjusting the setup configuration and proving that the power source carries an important role as the transducer element. Overall, the integrated DMFC/Sensor setup is promising and suitable tool for point-of-care use, capable to screen CEA in very low concentrations with high selectivity and reproducibility. The final DMFC/Sensor set-up could be further improved in a future work, about which the development of self-powered electrochemical sensor may place these devices as powerful tools in cancer diagnostic/monitoring in a nearby future.

Chapter 4

4. An all-in-one approach for self-powered sensing: A methanol fuel cell modified with a molecularly imprinted polymer for cancer biomarker detection

The results presented in this chapter were published in Liliana P.T. Carneiro, Alexandra M.F.R. Pinto, Adélio Mendes, M. Goreti F. Sales, *" An all-in-one approach for self-powered sensing: A methanol fuel cell modified with a molecularly imprinted polymer for cancer biomarker detection "*, *Journal of Electroanalytical Chemistry* (2022), 906, 116009. **https://doi.org/10.1016/j.jelechem.2022.116009.**

4.1 Introduction

Although miniaturization is creating new dimensions of portability and helping to move biosensors from the laboratory to the healthcare setting, commercial electrochemical systems remain limited to glucose test strips [186,187]. Apart from needing to be connected to an electrical reader, electrochemical biosensors require a power source or battery, which limits their autonomy and lifetime.

Combining electrochemical biosensors with a renewable energy supply can overcome the lack of autonomy of these devices and help to extend the limited transition from laboratory to PoC. This has been mainly implemented in the literature with microbial [188–190] and enzymatic fuel cells [191,192]. While these are excellent approaches for developing sustainable devices, the inclusion of compounds/elements of biological nature hinders device performance in terms of stability, reproducibility, and/or durability. Other approaches to autonomous biosensing use synthetic bio-recognition elements such as molecularly imprinted materials (MIPs), limiting the use of biological materials. This has been done with dye-sensitized solar cells [169,170] or with direct methanol fuel cells (DMFCs) [173]. These are very different autonomous systems that generate energy from light and chemical fuel, respectively.

The interface between MIP sensor films and DMFCs was first explored by Sales and co-worker [173]. The system reported by these authors requires a peristaltic pump to supply MeOH to the cell, which severely hinders its practical use as an autonomous and portable biosensor. This challenge has been overcome with DMFCs operating in a passive mode [193]. The passive DMFC was used to power supply the MIP sensor as an external device, not as an integrated part of the sensor itself.

This work reports for the first time a passive DMFC integrating a MIP sensing film with a target biomarker printed on it, making the whole cell operation concentration dependent. Compared to previous work, the MIP structure was improved here by building the MIP film in-situ, on the anode electrode, by electropolymerization. The DMFC device used in this work was adapted from [172] and operates with only a few milliliters of a dilute MeOH/water solution and atmospheric air, at room temperature, without the need for external flow. Since the biosensor film is housed within the passive DMFC, the final configuration is compact and easy to use, with the potential to be applied outside the laboratory to target CEA, an important cancer biomarker. In the literature, CEA has been

determined using a variety of technical approaches, but none of them include the innovative approach proposed here.

Overall, this work enabled the fabrication of a single, portable, and autonomous device that is sensitive to the cancer biomarker CEA and has the potential to be used anywhere. The MIP sensor film was fabricated on a commercial carbon fabric (CC) loaded with Pt/Ru nanoparticles (CC-Pt/Ru) by electropolymerization of 3,4-ethylenedioxythiophene (EDOT) and Py monomers under buffered conditions. The biosensor DMFC system was optimized with respect to several variables. The optimal setup was characterized in buffer/Cormay® human serum media and showed CEA interaction dependence. Selectivity assays were also addressed, confirming the high selectivity of the sensing anode electrode for CEA determination. Furthermore, as a proof-of-concept test, an ethanol solution was tested as fuel in the developed biosensor DMFC system without further modification and provided promising analytical data.

4.2 Experimental section

4.2.1 Reagents and solutions

All chemicals were of analytical grade and the water was ultra pure Milli-Q laboratory water. 10 mM MES buffer at pH 6.0 was obtained by dissolving 2-morpholinoethanesulfonic acid buffer grade (AppliChem). A CEA stock solution was prepared by diluting the commercial reagent (MyBiosource) in MES buffer, and less concentrated standards ranging from 30 ng/mL to 30000 ng/mL were obtained by accurately diluting the stock solution. Phosphate buffered saline (PBS) (Amresco) was used in the polymerization of the sensor layers. The polymerization mixture consisted of 0.010 M EDOT (97%, Alfa Aesar) and 0.0050 M Py (TCI) in PBS buffer. CEA was used as template during polymerization. Template removal was performed electrochemically in a 0.5 M H_2SO_4 solution. Electrochemical measurements were performed with 2.0 M and 0.050 M MeOH aqueous solutions (activation and calibration processes, respectively).

For selectivity studies, human serum (Cormay® HN, PZ Cormay S.A) was used with 1000x dilution in buffer and spiked with selected biomarker concentrations. This media was spiked with the same biomarker concentrations made in buffer. Selectivity assays preparing CEA standards in the presence of interferents were addressed using

Cancer Antigen 15–3 (13 U; MyBiosource), D-Glucose Monohydrate (0.9 mg/mL; Alfa Aesar) and Urea (0.3 mg/mL; Fagron) prepared in the previously described buffer.

4.2.2 Fuel cell assembly

The structure of the passive DMFC unit was adapted from [172] and characterized as described by [194]. Images of the system are shown in Figure 4.1-A, along with the corresponding membrane electrode unit (MEA).

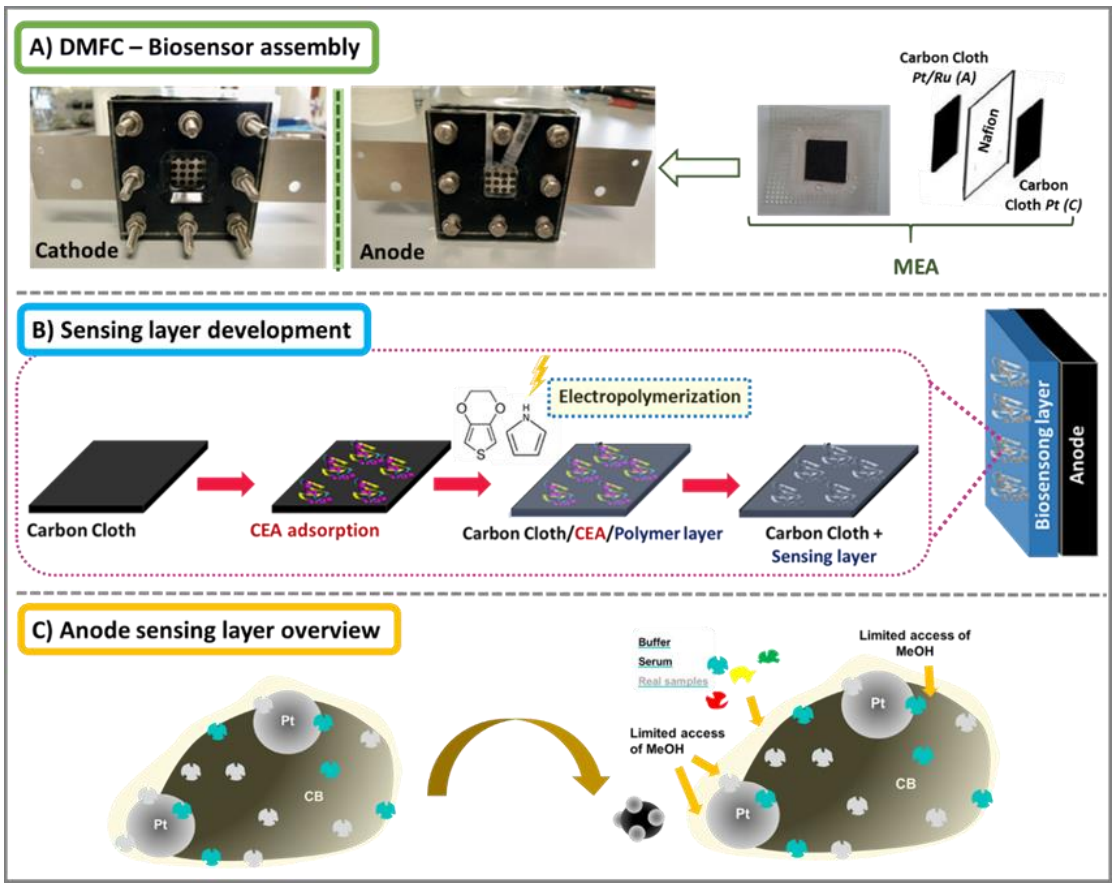

Figure 4.1 - Schematic representation of the components of the DMFC sensing device, including (A) the MeOH fuel cell device and the membrane electrode assembly (MEA) and (B) the various steps in the development of the sensing layer on the anode, which is sensitive to CEA and is obtained by a surface electropolymerization process using EDOT/PPy monomers; (C) Schematic representation of the soot surface with an anchored MIP polymer film showing the cavities (binding sites) and the different pathways limiting the access of MeOH molecules.

The device structure includes two acrylic plates (end plates) and two metal plates (current collectors), each sealed with a rubber gasket that also serves as an electrical insulator to prevent short circuits. The cathode was in contact with atmospheric air through several small holes. On the anode side, there was a special deposition unit into which the MeOH solution and CEA standards were sequentially introduced. Figure 4.2 shows the opened DMFC device.

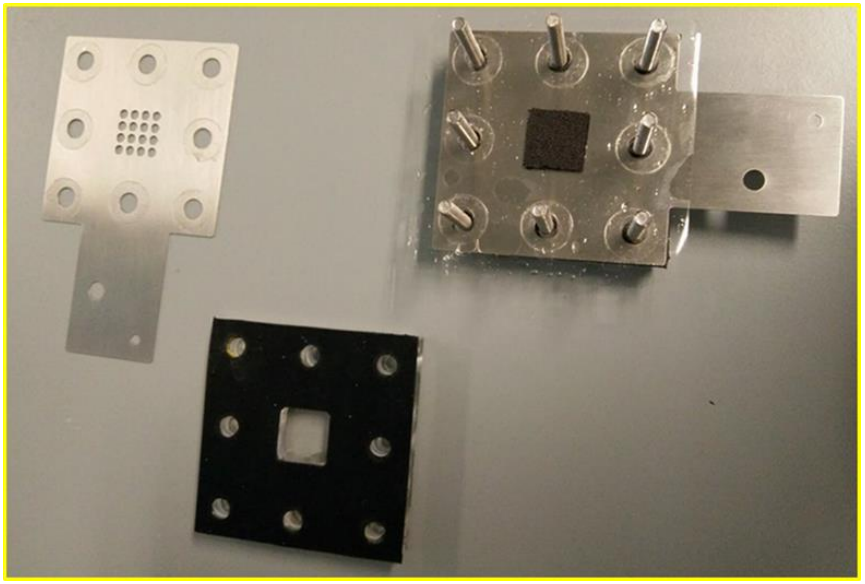

Figure 4.2 - Opened fuel cell set-up showing all the constituent components, including the MEA (Nafion® membrane and carbon cloth electrode).

The MEA consists of an anode electrode and a cathode electrode separated by a solid ion exchange polymer membrane made of Nafion®, Nafion-115 from Quintech. The anode electrode consisted of a 2.25 cm^2 square of carbon fabric (Quintech) containing carbon black (Vulcan XC72) loaded with 2 mg/cm^2 Pt-Ru (40:20 wt%) catalyst (C/Pt-Ru). The cathode electrode consisted of a 2.25 cm^2 square of carbon fabric containing carbon black (Vulcan XC72) loaded with 1 mg/cm^2 Pt (10 wt%). The electrochemical reactions take place at the catalyst layers and the (bio)sensing layer was later built directly on the surface of the commercial anode electrode by electropolymerization. This modified anode was then incorporated into the MEA of the DMFC.

The passive DMFC device was operated at room temperature and atmospheric pressure. The anode was loaded with an aqueous MeOH solution (2.0 M for activation and 0.050 M for calibration) and the cathode was exposed to atmospheric air. DMFC and

biosensor DMFC measurements were performed using the corresponding polarization curves (obtained by Sampled DC Voltammetry). Polarization curves were recorded sequentially at two different times: (1) during activation and (2) during calibration time points. Activation was performed by loading the DMFC with a 2.0 M MeOH solution until OCV and power output of the device reached stable values (one-time change 1–2%). Calibration was performed with a 0.050 M MeOH solution loaded onto the biosensor DMFC using a MIP-modified DMFC or a DMFC with a non-imprinted polymer material, NIP, as a control.

4.2.3 Preparation of the biosensing element

The biosensor layer (Figure 4.1-B) was prepared by electropolymerization in a 3-electrode configuration with the CC-Pt/Ru electrode of the DMFC as the working electrode, a leakage-free Ag/AgCl plastic electrode as the reference electrode, and a platinum rod electrode as the counter electrode. The electrodes were immersed in a solution of EDOT (0.01 M) and Py (0.005 M) in PBS buffer (previously rinsed with N_2). Before electropolymerization, the working electrode was subjected to a cleaning process, by cyclic voltammetry (CV), 5 cycles, from −0.3 V to 1.0 V, in a 0.5 M H_2SO_4 solution. This procedure ensured mild oxidation of the electrode surface and removal of impurities, which was an important step to ensure the reproducibility of the electrode properties.

The preparation of the MIP film began with the incubation of a CEA solution (60000 ng/mL) prepared in PBS on the surface of the cleaned CC-Pt/Ru electrode for 2 h to adsorb it and serve as a molecular template. After this time, the electrode was washed with PBS and the 3-electrode system was immersed in a solution containing the monomers (previously rinsed) to perform electropolymerization by CV (10 cycles, −0.3 V to 1.2 V, 50 mV/s). After polymer formation, the electrodes were washed with PBS buffer and the protein template was removed by incubating the electrode in a 0.5 M H_2SO_4 solution. Then, the same CV procedure was used to remove unreacted monomers (10 cycles, −0.3 V to 1.2 V, 50 mV/s) and terminate polymer formation, and the electrodes were finally washed with ultrapure water. In parallel, NIP films were prepared using a similar procedure, keeping the same steps and protocols, except for the CEA template, which was not present. Until use, the modified electrodes were stored in the dark, at room temperature and in a dry environment.

The polymeric layers on the MIP and NIP electropolymerized electrodes were visible to the naked eye, translated by a visible homogeneous layer on top of the electrodes. This layer had an effect of barrier influencing the access and electrochemical activity of MeOH. Special care was paid in preparing a permeable layer for allowing MeOH molecules reaching the catalytic Pt nanoparticles. The MIP sensing electrode and the respective control (NIP) were assembled as the anode electrode in the DMFC, the cell was afterward calibrated and the anode electrode discarded and replaced by a new one (not reusable).

4.2.4 Electrochemical assays and equipment

Electrochemical measurements were performed in a potentiostat/galvanostat from Methrom Autolab and a PGSTAT302N, controlled by Nova software (NOVA 2.1). Electrochemical data were collected at room temperature and atmospheric pressure. The electrochemical performance of the DMFC and DMFC biosensor was evaluated using Sampled DC Voltammetry, which allowed the polarization curves to be obtained up to signal stabilization (OCV and current density). The DMFC device was previously activated by recording several polarization curves with a 2 M MeOH solution until a stable response was obtained. Then, the fuel cell was washed several times with Milli-Q water and left with water for 24 h to extract the residual MeOH on the electrode surface.

Calibration curves were established in buffered media, measuring the polarization curves (Sampled DC Voltammetry) after incubation of CEA standard solutions (30, 300, 3000, 30000 ng/mL) prepared in MES buffer. Each sample (250 µL) was incubated on the sensor surface of the anode electrode for 30 min, starting with the lowest standard concentration. After this time, the anode electrode was washed with MES buffer, and a polarization curve was plotted for a 0.05 M methanol loading solution. To analyse the DMFC and biosensor DMFC behaviour, all polarization curves obtained during the experiments were normalized with respect to the electrode area (2.25 cm^2) and the maximum power of the system was calculated and used to compare the responses to the loaded samples, including the response of the pristine DMFC. Concerning the comparison between the different biosensor DMFC assemblies the power values were normalized by the corresponding blank signal ($powe_{rsample}/power_{blank}$).

The anode electrodes (unmodified and modified with MIP or NIP films) were characterized by Raman spectrometry with a DXR Raman spectroscope from Thermo

Scientific equipped with a confocal microscope. Spectra were recorded with an excitation laser at 532 nm, from 47 to 3500 cm^{-1}, with a power of 2 mW and a 10x objective. The confocal aperture was set to 50 μm slit.

4.3 Results and discussion

4.3.1 Production of the sensing anode electrode

4.3.1.1 Assembly of the sensing film on Carbon Cloth-Pt/Ru supports

The sensing layer was built on commercial CC-Pt/Ru electrodes commonly used as anodes in MeOH fuel cells. CC was chosen as the support for the MIP film because it has a highly macroscale porous structure with a homogeneous distribution that confers high permeability properties and allows protein diffusion through its porous structure [195]. These properties appeared to be advantageous for combination with imprinted polymers and were essential to obtain semipermeable nanocomposite electrodes with the dual task of acting as anode electrodes in a fuel cell and as a sensing layer support material.

The sensing layers were prepared in-situ, on the anode electrode, by electropolymerization with CV. This was a novel approach in the context of sensing fuel cells and used a combination of EDOT and Py monomers to obtain polymeric films with good electrical properties. Conductive polymers, such as PEDOT and PPy, show promise as non-metallic electrocatalytic materials for energy applications [196]. The conductive properties and electrocatalytic characteristics of PEDOT/PPy polymers make these materials suitable for direct application on the fuel cell anode. This approach reduces the electrical blockage caused by non-conductive polymers and improves the sensing capability intended for the anode electrode.

To maximize the density of CEA-imprinted sites, CEA was incubated on the electrode surface before polymerization (t = 2 h). This approach is known as surface imprinting and results in a higher number of imprinted sites on the electrode surface. Removal of CEA from this polymeric network was achieved by pouring a sulfuric acid solution onto the electrode surface. This denatures the adsorbed protein molecules on the electrode surface, emptying the imprinted cavities and allowing future rebinding of other CEA molecules. Removal of CEA with proteinase k was also tested, but the results

obtained indicated intense adsorption of the enzyme on the anode surface, which hindered subsequent fuel cell activation.

The cyclic voltammograms in a 3-electrode configuration of the CC-Pt/Ru electrodes and the modified MIP forms are shown in Figure 4.3. Overall, the presence of the PEDOT/PPy layer with CEA resulted in a significant decrease in the electrical current resistance values over the entire voltage range tested. These increases in ohmic resistance were attributed to the presence of the protein, as its removal allowed the recovery of the original voltammogram.

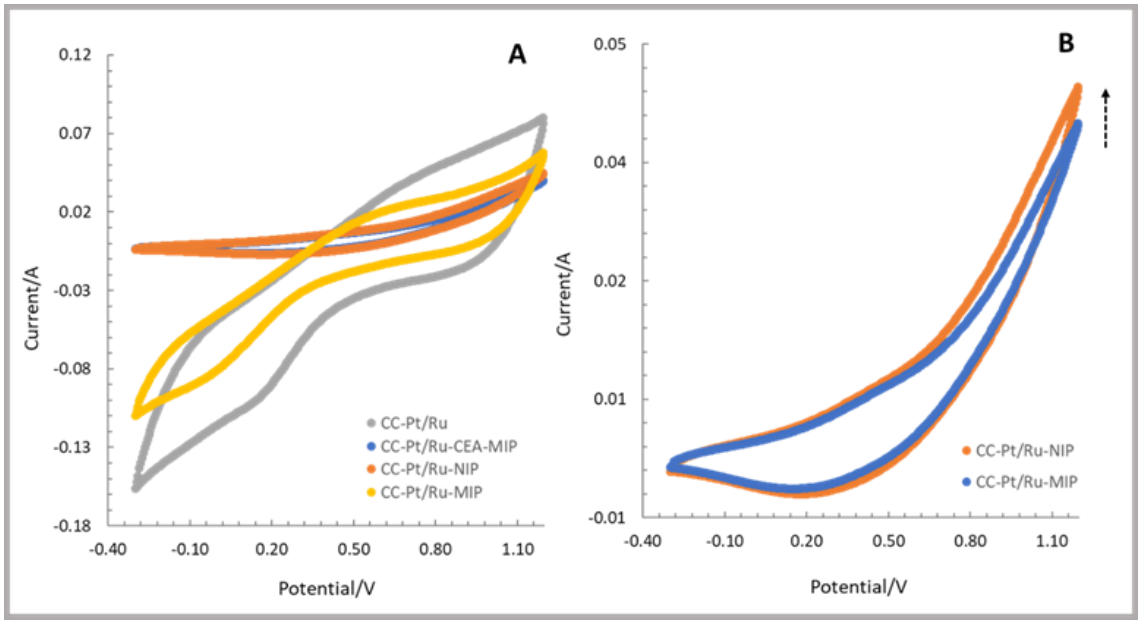

Figure 4.3 - Cyclic voltammograms obtained in a 3-electrode system in a PBS buffer solution, for the different steps involved in the assembly of the sensing polymers on CC-Pt/Ru electrodes. (A) Highlights the results of the MIP (CC-Pt/Ru-CEA-MIP) and NIP (CC-Pt/Ru-NIP) electrodes, as well as MIP electrodes after removal of the CEA template (CC-Pt/Ru-MIP). (B) Zooms in the voltammograms of-CC-Pt/Ru-MIP and CC-Pt/Ru-NIP electrodes.

4.3.1.2 Chemical characterization

Raman spectroscopy was used to confirm the presence of the polymer film on the top of the CC-Pt/Ru electrodes. Spectra were collected at 532 nm for CC-Pt/Ru and CC-PEDOT/PPy supports, as controls, and for CC-Pt/Ru-MIP and CC-Pt/Ru-NIP materials (Figure 4.4-A).

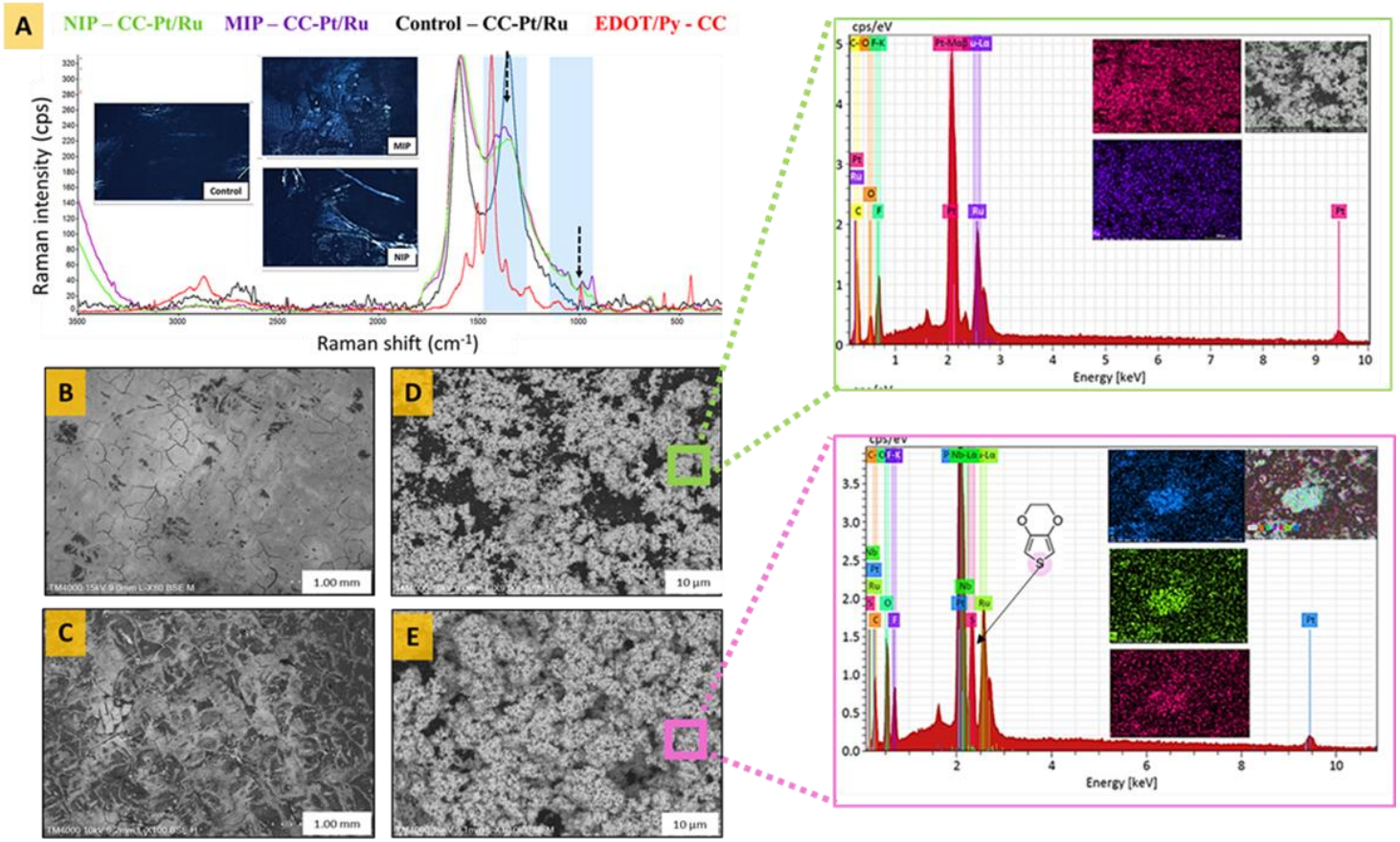

Figure 4.4 - Characterization results obtained by (A) Raman analysis of the different electrodes (Carbon Cloth supported EDOT/PPy, untreated Carbon Cloth-Pt/Ru and Carbon Cloth-Pt/Ru- MIP/NIP) and the corresponding confocal images; scanning electron microscopy analysis (SEM) of different electrodes including a (B) Carbon Cloth-Pt/Ru-MIP electrode, (C) Carbon Cloth-Pt/Ru-NIP electrode, (D) unmodified Carbon Cloth-Pt/Ru (control) with the corresponding elemental assignment of Pt, Ru and other chemical elements and (E) Carbon Cloth-Pt/Ru-MIP electrode with the corresponding elemental assignment of Pt, Ru and other chemical elements evidencing the S peak derivate for the presence of EDOT co-polymer.

The typical spectra obtained are shown in Figure 4.4-A and evidence clear differences between the common carrier (CC-Pt/Ru, dark line) and the polymerized materials (CC-Pt/Ru-MIP in purple and CC-Pt/Ru-NIP in green). Two regions marked in blue were highlighted, representing the areas in the spectra range where it is possible to observe significant differences between the different analysed electrodes. The peaks generated by the presence of PEDOT/PPy on the MIP/NIP materials were compared with those generated by the same polymer mounted on a CC support used as a gas diffusion layer (GDL, without carbon black and Pt/Ru). The clearest peak of PEDOT/PPy polymer was at 1435.31 cm^{-1}, but several other peaks with low Raman intensity could be assigned to this co-polymer (red spectra), as described in the literature [170,197].

In the MIP and NIP CC-Pt/Ru-based materials, not all the characteristic peaks of the PEDOT/PPy polymer could be observed. This was apparently due to the presence of Pt/Ru, which reduced the overall Raman intensity of the spectra with these metallic nanoparticles (Pt and/or Ru) [198]. Overall, it showed well-defined G (1594.23 cm^{-1}) and D (1349.27 cm^{-1}) bands, but with a distorted D band and with small bands at 963.57 cm^{-1} and 1375.11 cm^{-1} (marked as arrows) originating from the PEDOT-PPy polymer. The D band is related to structural defects in the material and generally indicates changes in the structure of the carbon material, while the G band has been associated with the stretching mode of graphite [199]. The I_D/I_G ratios allow an assessment of whether defects are present in a particular material and were calculated for all samples (Table 4.1).

Table 4.1- Calculated I_D/I_G ratio obtained from Raman Spectra for Carbon Cloth-Pt/Ru (control), MIP and NIP Carbon Cloth polymerized samples.

Sample	**Raman shift**	**Raman intensity**	**I_D/I_G**
Control	D: 1351.73	17.193	1.03 ± 0.01
	G: 1593.74	16.763	
MIP	D: 1375.11	178.937	0.72 ± 0.02
	G: 1590.03	250.153	
NIP	D: 1359.81	220.213	0.67 ± 0.01
	G: 1584.86	328.565	

The control has an I_D/I_G ratio of 1.03, while the polymerized samples have a ratio of 0.72 (MIP) and 0.67 (NIP). These values confirm the presence of a polymer anchored in the structure of CC-Pt/Ru. The NIP had the lowest ratio, which is consistent with the absence of protein within the polymeric network. The presence of PEDOT in the materials was further confirmed by confocal microscopy, producing images with blue fibers characteristic of PEDOT [200].

4.3.1.3 Morphological characterization

The SEM images and EDS analyses of untreated CC-Pt/Ru and CC-Pt/Ru-MIP/NIP electrodes are shown in Figure 4.4-B/C-E. The morphology of the surface analysis of untreated CC-Pt/Ru (control), CC-Pt/Ru-MIP and CC-Pt/Ru-NIP was different, indicating different roughness of the samples (Figure 4.4-B/C - E). These results indicated the presence of a uniform polymer layer anchored on the surface of the carbon support. Analysing the EDS results (Figure 4.4-D/E) is possible to verify that both materials showed similar assignments in terms of nanocatalysts (Pt and Ru) and fluorine (derived from Nafion® ionomer, which is normally used as a binder in this type of materials [201]. Among other common elements, the MIP-CC-Pt/Ru sample also contained sulphur, which was assigned to the contribution of the PEDOT polymer, confirming the presence of a PEDOT layer on the surface of the carbon-based substrate material.

4.3.2 Integration of the anode sensing electrode on the DMFC

The effect of inserting modified anodes (MIP- and NIP-anodes) into a DMFC device was evaluated by recording experimental polarization curves (Sampled DC Voltammetry technique) until the electrochemical system reached a stable maximum potential (OCV) and power. These polarization curves were compared to a DMFC with a commercial unmodified anode (control). Interestingly, the activation and stabilization behaviour depends on the type of anode used in the fuel cell system (control, MIP and NIP), revealing the great influence of the anchored polymer layer on the surface of the electrodes (Figure 4.5).

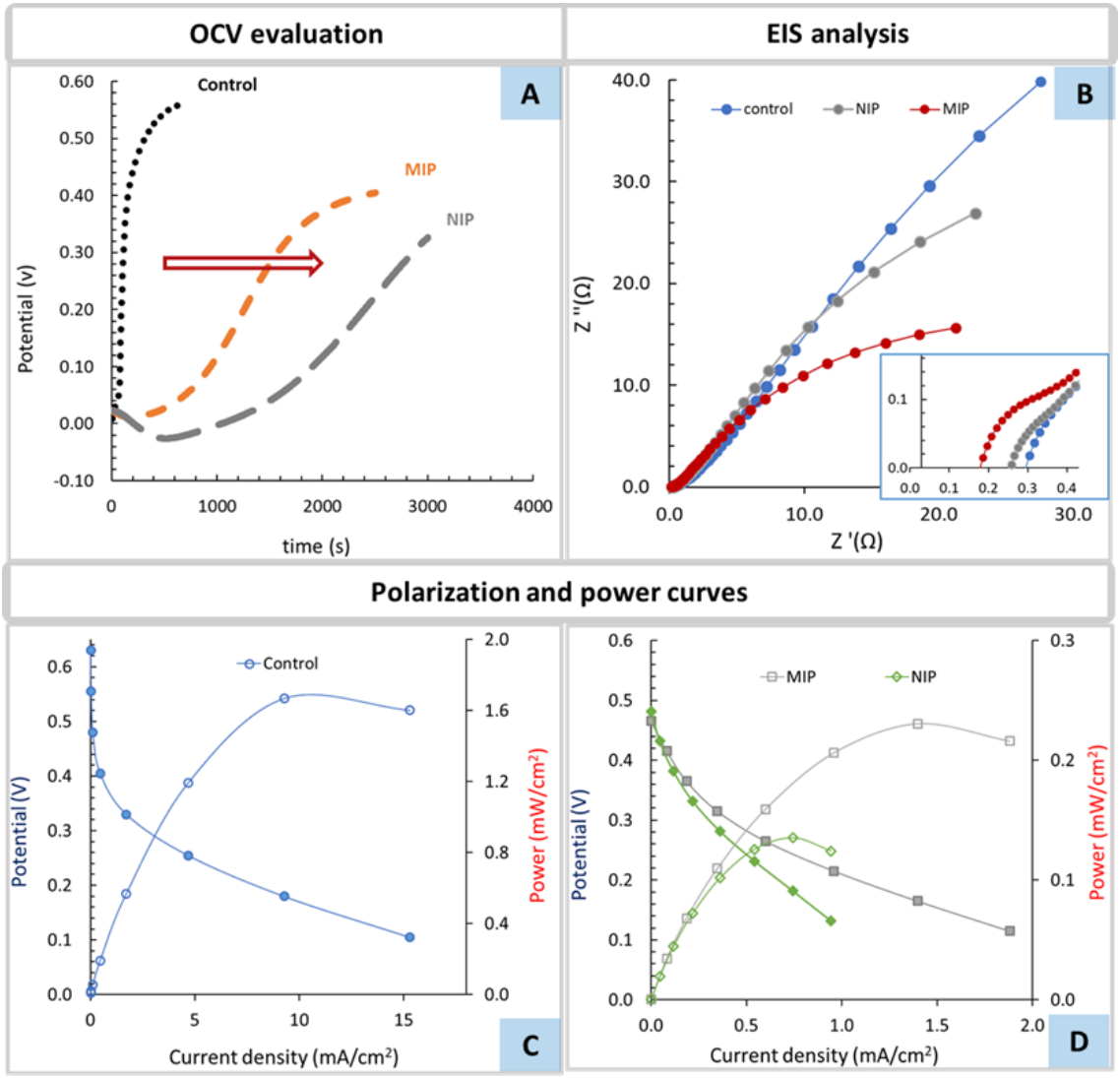

Figure 4.5 - Electrochemical data obtained with 2 M MeOH for the passive DMFCs assemblies integrating different anodes in terms of (A) OCV start-up for control, MIP and NIP anodes and (B) respective EIS analysis; (C) current and power curve of a DMFC assembly including a control anode (without polymer) and (D) current and power curves obtained with MIP and NIP anode electrodes.

Figure 4.5-A shows the measured OCV values at the start of the DMFCs, i.e. the first measurement after filling an aqueous 2 M MeOH solution into the anode container. Overall, there is a time delay in the activation of the DMFCs with the modified anodes (MIP and NIP) compared to a DMFC fabricated with a control anode. The potential values were also lower for the MIP/NIP-based anodes. In particular, the control anode reached an OCV of 0.56 V within 700 s, while the MIP-DMFC reached 0.40 V within 2500 s and the NIP-DMFC reached 0.33 V within 3000 s. These results were attributed to the presence of the polymeric network that hinders the diffusion and supply of MeOH to the

catalyst at the carbon fabric gas diffusion layer. The NIP-DMFC has an anode electrode without cavities impressed in the polymeric structure, which presents a higher "resistance" to this diffusion process than the MIP. Therefore, the time required to reach a steady state for the NIP-electrode was longer than for the MIP, which ultimately could not reach the same potential values as the MIP electrode. The MIP-DMFC showed intermediate behaviour between the control and the NIP-DMFC, as the cavities allowed faster permeation of MeOH and water. The differences observed here were also reflected in the time required to perform stable and complete activation of each electrode type.

The OCV value of a starting DMFC system appeared to be related to MeOH permeation at the electrode. This start-up was not instantaneous but required successive polarization curves (typically 5 or 6, depending on the cell) until maximum power was reached (maximum OCV value and power). After performing all the necessary polarization curves, the controls showed average OCV values of 0.66 V (n = 3, for independent cells), while the MIP-DMFCs showed 0.48 V and the NIP-DMFCs showed 0.42 V.

The EIS analysis of the different DMFC assemblies (unmodified, MIP and NIP anode electrodes) were performed using 0.05 M of MeOH solution in the respective OCV values, and the results presented in Figure 4.5-B. Some differences were observed analysing the EIS plots of the different assemblies studied in terms of change transfer and ohmic resistance, evidencing an improvement of the PEDOT/PPy anode electrodes in relation to the unmodified commercial anode electrode for both parameters. This improvement can be assigned to a synergetic effect among Pt, PEDOT polymer and CC electrode evidencing that anchoring a conductor polymer in the anode electrodes has potential to improve the electrical conductivity. These effects are already verified in another similar combinations of PEDOT-Pt [202] and also PEDOT-Au-CC [203], which contribute to enhancing the performance of fuel cells.

In addition to the differences in OCV and EIS, the power values were also dependent on the anode used in the DMFC assemblies. Comparing the polarization curve obtained for an unpolymerized control (Figure 4.5-C) with the polarization curves obtained for a MIP and NIP-DMFCs integrated anodes (Figure 4.5-D), large differences between the different devices can be observed. The control shows a maximum power of 1.67 mW/cm^2, while the MIP-DMFC reaches the maximum value of 0.23 mW/cm^2, while the NIP-DMFC shows a power value of 0.14 mW/cm^2. Overall, the presence of the

polymer layer at the anode hinders the MeOH permeation, which restricts the access to the Pt/Ru nanoparticles entrapped in the polymeric network, thus affecting the overall electrochemical reaction rate. This effect is also observed when a protein enters the imprinted cavity, restricting the access of the MeOH molecule to the Pt catalyst. These effects are shown schematically in Figure 4.1-C.

Overall, the control, MIP, and NIP electrodes exhibit very different behaviours when integrated as anodes in the DMFC, and these differences reflect the permeance of the polymeric network that impedes the access of MeOH to the catalyst. Although the polymerization on the electrodes (MIP/NIP) affects the power output of the fuel cell (low current, power and OCV), the final signals allow the generation of sufficient power to supply the sensor.

4.3.3 Selection of ideal MeOH concentration for biosensor DMFC operation

Normal DMFCs operated under steady-state conditions use concentrated aqueous MeOH solutions (between 1 and 5 M) [204,205], most commonly a 2 M solution. Therefore, DMFCs were first activated with a 2.0 M aqueous MeOH solution to obtain a stable signal in a relatively fast way. This concentration was also confirmed to be ideal in a previous work using the same steady-state DMFC with a regular anode [194]; however, using a 2.0 M MeOH solution is not ideal for a biosensor DMFC. After performing several experiments, including multiple calibrations, it was observed that the power output of the MIP-DMFC remained virtually unchanged after successive incubations of CEA standards (Figure 4.6). Occasionally, operation of the cell without refueling was tested, and surprisingly, the electrical output did not change (Figure 4.7). This was confirmed by repeated experiments, and it was concluded that such higher MeOH concentration resulted in intense adsorption of MeOH molecules on the electrode surface, which remained unreacted and thus masked the response of the sensor. Nevertheless, the hybrid biosensor DMFC device proposed here aims to respond to different CEA concentrations. Moreover, the response time of the sensor is expected to be only a few minutes, thus requiring smaller MeOH concentrations.

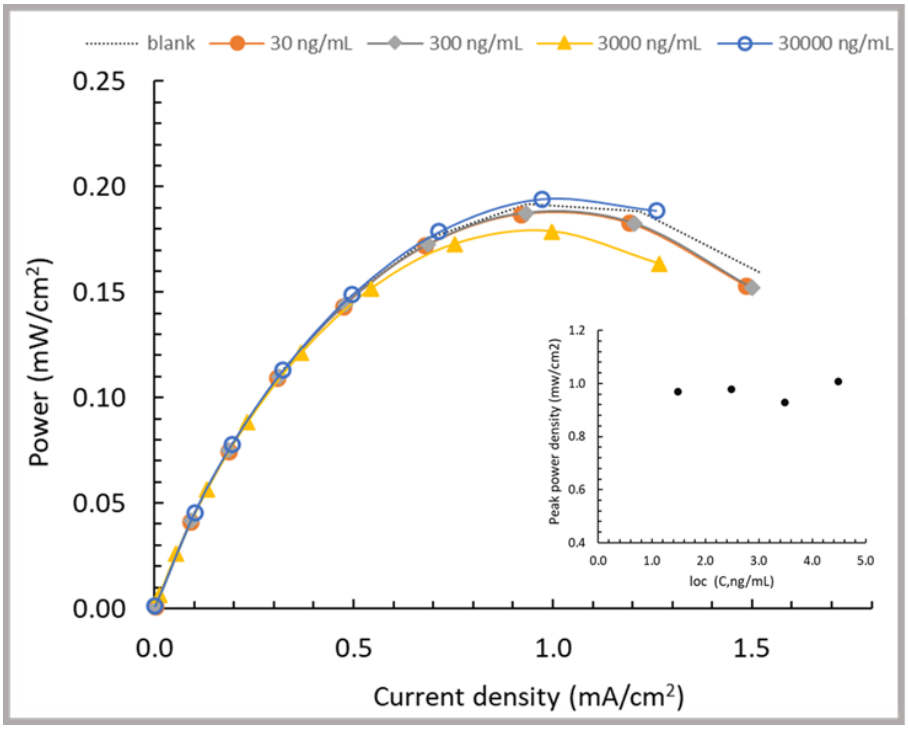

Figure 4.6 - Power curves of a biosensor DMFC obtained in a calibration experiment with consecutive incubations of CEA standards using 2 M of a MeOH solution for the readings.

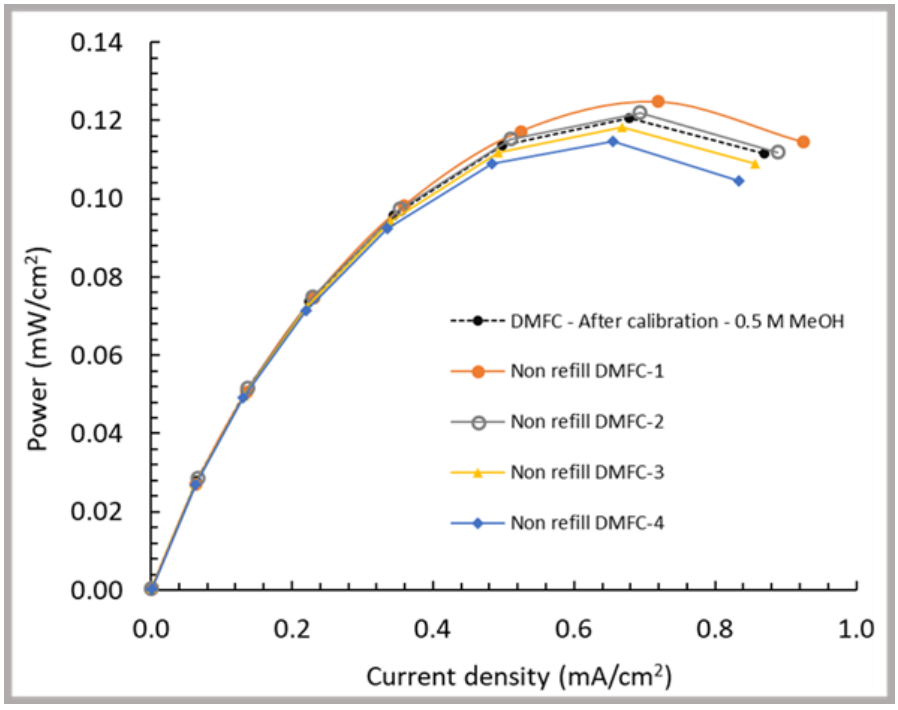

Figure 4.7 - Power curves of a biosensor DMFC after a complete calibration, first with a solution of 0.5 M of MeOH until stabilization (dashed line) and later in the absence of the MeOH solution (empty container) in consecutively readings.

Briefly, the sample is incubated in the anode container for 30 min. Then, the container is washed and an electrochemical measurement is performed by adding the MeOH solution; after this measurement, the anode is washed again and a new sample is incubated, repeating the cycle with measurements for 15–20 min. The methanol concentration was optimized between 0.05 and 2.0 M, finding a balance between a fast reaction with minimal storage and a reaction strong enough to deliver energy to the sensor. The polarization and power curves obtained are shown in Figure 4.8-A/B.

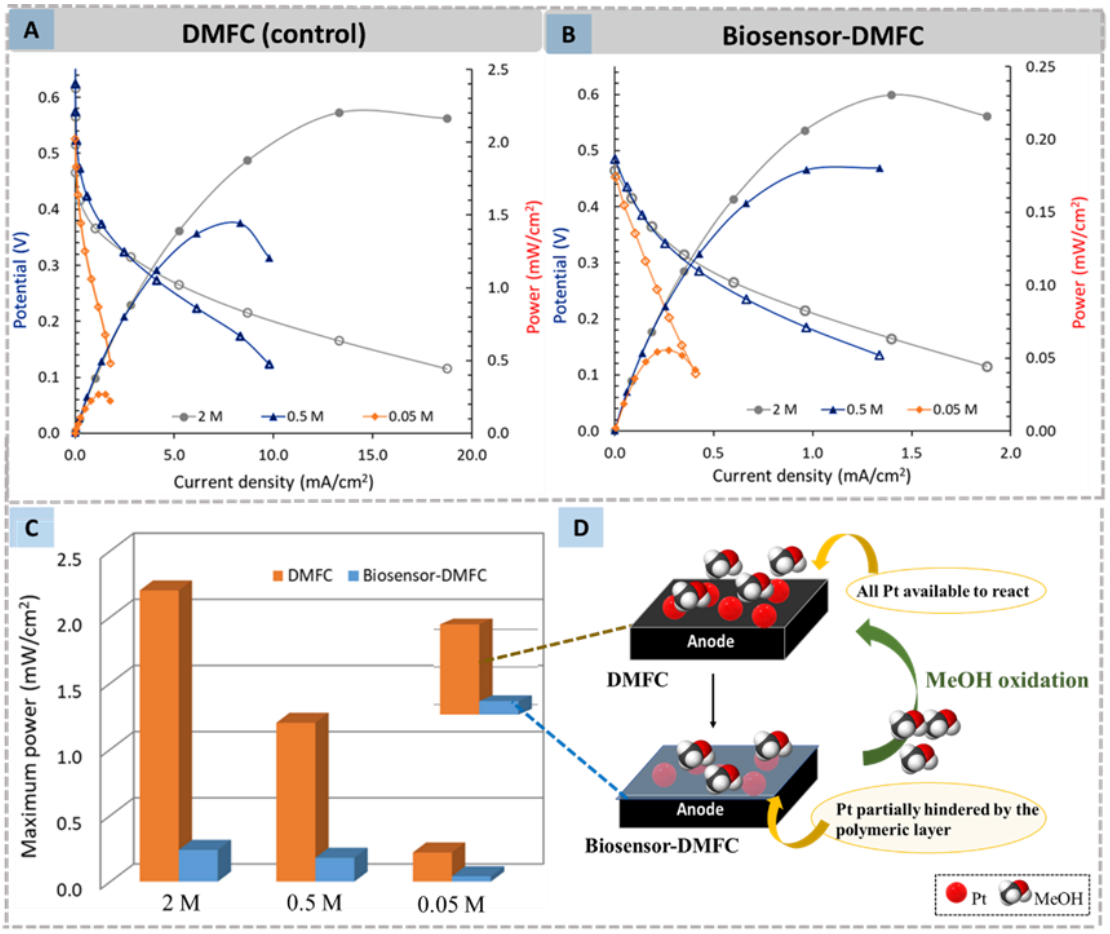

Figure 4.8 - Polarization and power curves of the passive DMFC assemblies using different MeOH concentrations for a DMFC with (A) an unmodified anode as a control and (B) a MIP-assisted anode and (C) the effect on the power in both the DMFC and the biosensor DMFC with different MeOH concentrations; (D) simplest scheme representing and visually explaining the Pt-block by the polymeric layer which conditionate the MeOH oxidation and thus the power output recorded for both systems.

As expected, as the MeOH concentration decreases, the current/performance of both the DMFC and the biosensor DMFC decreases. Figure 4.8-C shows the effect of decreasing MeOH concentration on the maximum power of the DMFC. As schematized in Figure 4.8-D, some Pt nanoparticles in the biosensor DMFC were trapped in the polymeric network, which difficult their catalysis of MeOH molecules in comparison to the commercial anode electrode. Therefore, is important that the PEDOT/PPy polymer layer grows near Pt nanoparticles, since the signal of the biosensor DMFC arises from the efficient blocking of the Pt catalysts, hindering the MeOH oxidation and consequently affecting the power produced by the fuel cell.

It is important to emphasize that the DMFC was washed and refueled after each measurement until a steady state was reached. Figure 4.9 shows some successive polarization curves obtained for a biosensor DMFC system loaded with 0.5 M and 0.05 M MeOH solution. Decreasing the MeOH concentration leads to lower performances, but all the conditions studied showed good electrical stability.

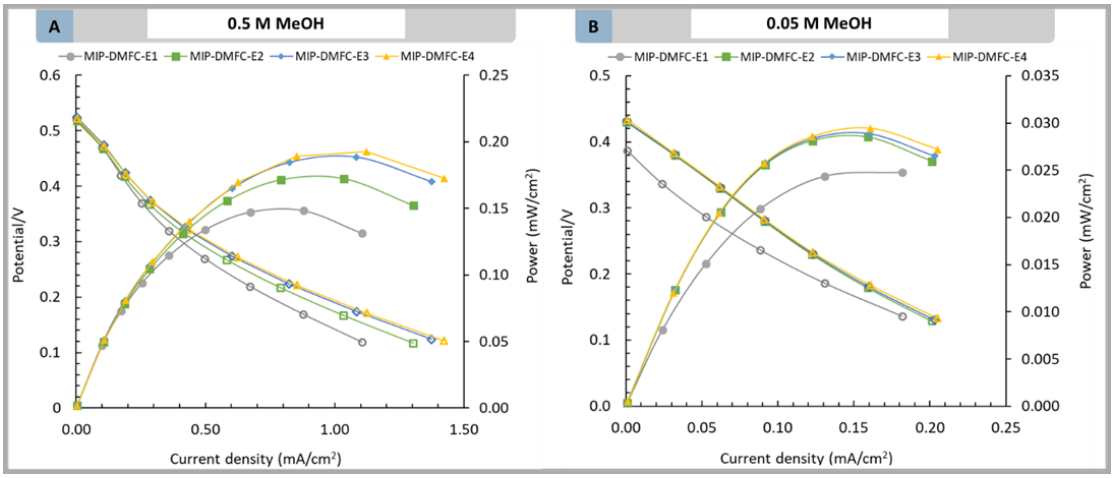

Figure 4.9 - Polarization and power curves of a passive DMFC assembly with a MIP supported anode using (A) 0.5 M and (B) 0.05 M of MeOH feed solution until electric signal stabilization.

To determine the best MeOH concentration, calibrations were performed incubating progressively higher CEA concentrations and refueling the cell with diluted MeOH concentrations (0.5 M and 0.05 M). The results obtained showed that the DMFC was more sensitive to CEA concentration changes at more dilute MeOH concentrations. At a MeOH solution of 0.5 M, the signal from the biosensor DMFC was less sensitive and showed a large background signal, even after washing with water and drying with

nitrogen (Figure 4.10). Therefore, to convert the DMFC into an autonomous sensing device for CEA targeting, the use of a small amount of MeOH (0.05 M) is an important requirement.

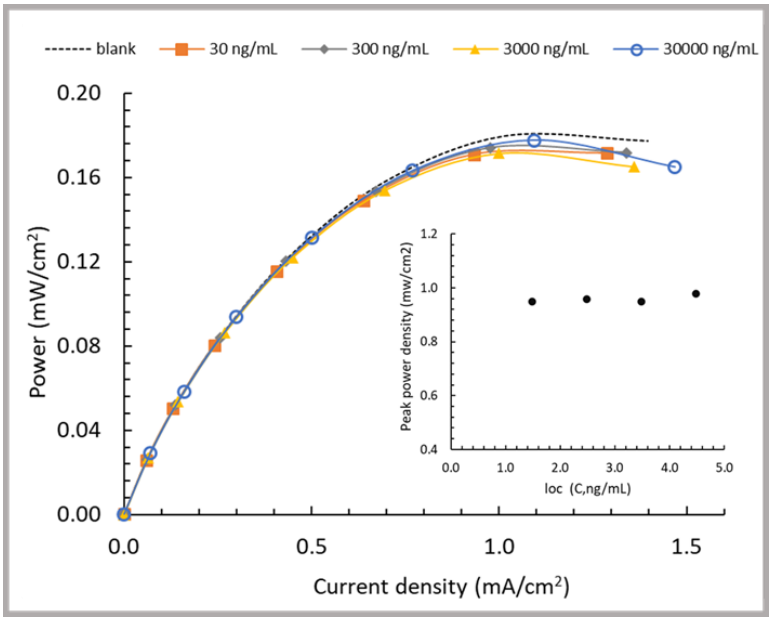

Figure 4.10 - Power curves of a biosensor DMFC obtained in a calibration experiment with consecutive incubations of CEA standards using 0.5 M of MeOH for the readings.

4.3.4 Calibrations of the biosensor DMFC

All biosensor DMFC devices evaluated were first activated with 2.0 M MeOH solution until OCV and power were stabilized. Then, the MeOH was completely removed (the DMFC was washed and left in water until the next day). Prior to calibration, the device was also incubated sequentially in the same background medium used to prepare the CEA standard solutions until stable electrical output was achieved (a stabilization example was shown in Figure 4.11). The background medium used to prepare the solutions was MES buffer and diluted Cormay® serum. This procedure was fundamental to ensure that any electrical signal displayed was indeed due to CEA and not the medium in which the standard solution was prepared. In the case of Cormay® serum media, the dilution factor was previously studied and evaluated regarding its impact upon the power and signal stability of the fuel cells. Two dilution factors were studied herein (100× and 1000×) and signal stability was only achieved when using a 1000× dilution factor. This was due to the presence of a high chloride concentration in Cormay® serum (0.1 M in the

sample without dilution). Chloride ions are recognized contaminants of fuel cells electrodes for blocking the Pt surface and decreasing the activity of the Pt catalyst, which in turn decreases the power of the fuel cell [206]. Therefore, in a real application, the sample needs to be pre-treated to remove chloride ions, to allow operating with lower dilution factors.

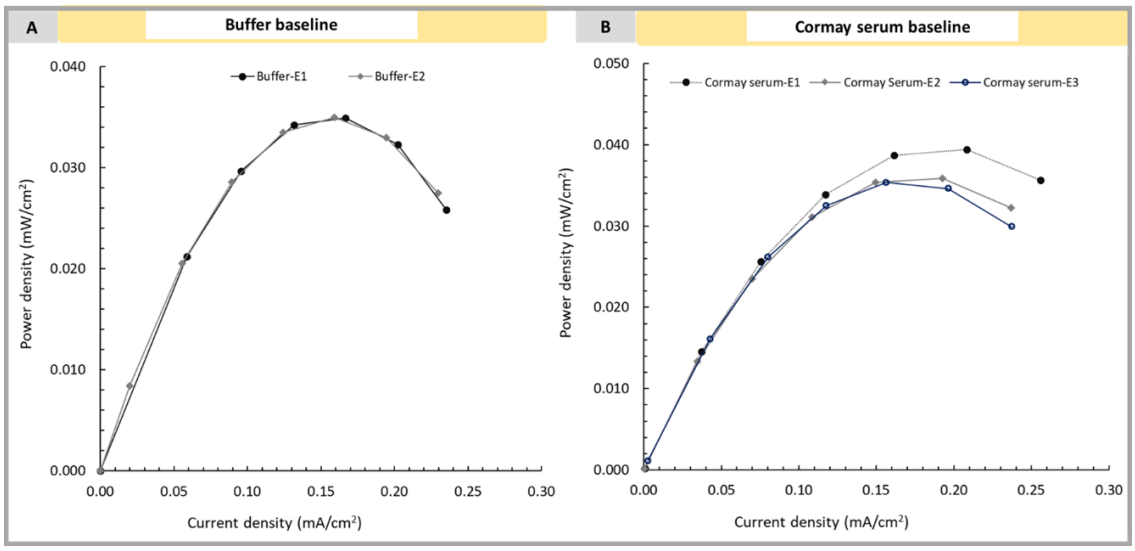

Figure 4.11 - Power curves obtained in electric signal stabilization after incubations of (A) buffer and (B) Cormay® serum. After 2 incubations of buffer the variation in the power signal is 0.05% which agrees with the normally variation observed with buffer before calibrations (0.05-1%). After 3 incubations of Cormay® serum the variation in the power signal is 1.4% which is in agreement to the variation observed in the system before calibrations (1-1.5%).

After stabilizing the fuel cell electrical signal, increasing concentrations of CEA standard solutions ranging from 30 to 30 000 ng/mL were incubated sequentially on the biosensor DMFC container and the biosensor performance was evaluated after incubation of each concentration. Each standard solution was left on the anode container for 30 min. After this time, the biosensor DMFC container was washed with the background medium solution and dried with N_2 for a few seconds. After filling the anode container with 0.05 M MeOH, a stabilization step (OCV determination) is performed (the duration of stabilization depends on the biosensor DMFC and should be maintained throughout the calibration protocol), followed by the recording of the polarization and power curves (obtained by the Sampled DC Voltammetry technique). The same procedure was

performed (in parallel) with the NIP-DMFC device, to monitor the response of the biosensor that corresponds to non-specific binding.

Several calibrations were performed to evaluate the standard analytical characteristics of the operation of this hybrid setup. A typical plot corresponding to calibration in buffer is shown in Figure 4.12-A, while Figure 4.12-B shows the corresponding calibration in diluted Cormay® serum.

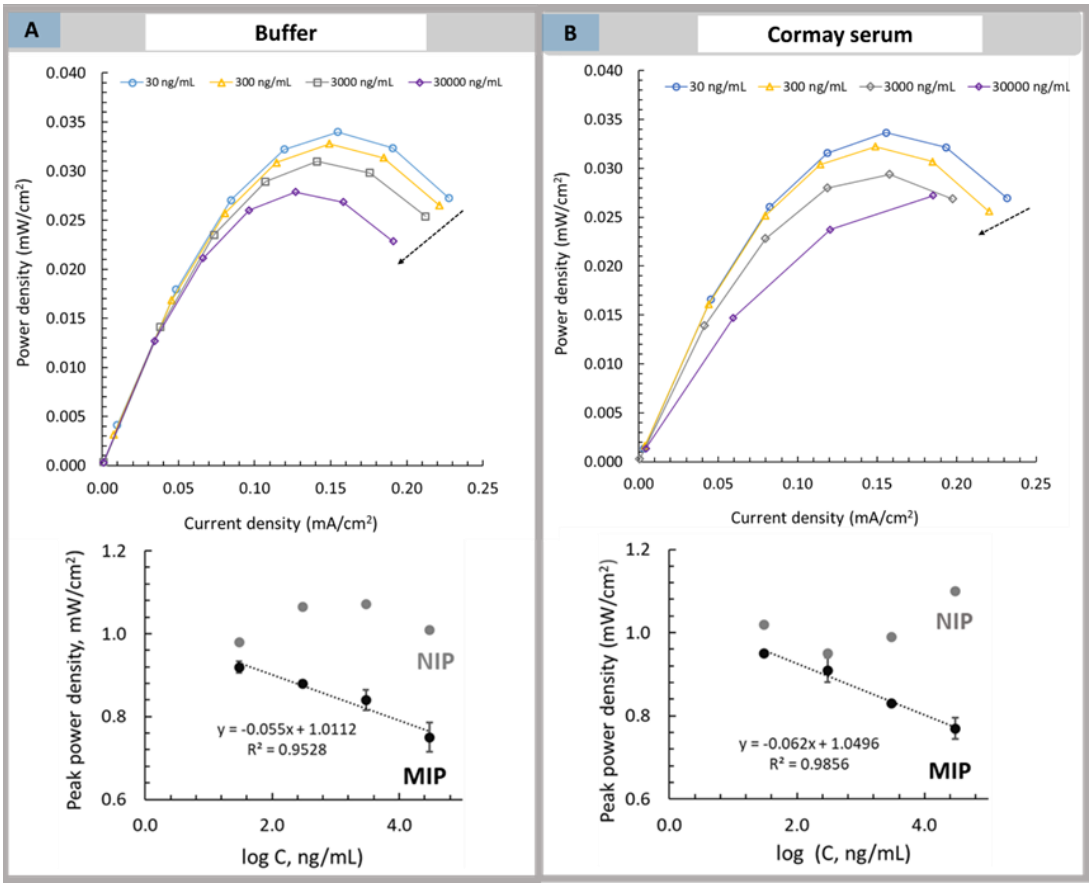

Figure 4.12 - Power-Current Density curves and the corresponding calibration curves obtained after incubation of CEA-increasing standards in the range of 30–30000 ng/mL prepared in (A) buffer and (B) Cormay® serum. Calibration curves for the MIP and NIP anode electrodes were traced using the average of the maximum power density obtained at each CEA concentration.

The corresponding calibration curves are also shown in the respective figures comparing the average power density values for the biosensor DMFC with those for the control DMFC NIP. The calibration curves correspond to the normalized power values ($power_{sample}/power_{blank}$). From the analysis of the calibration results, one can say that the

average power density decreases for higher concentrations of CEA, in a concentration-dependent mode for both media studied.

For buffer calibrations (Figure 4.12-A) the DMFC biosensor output power decreases from 0.035 mW/cm^2 (initial value after buffer stabilization) to 0.028 mW/cm^2 when measuring the maximum CEA concentration, with a squared correlation coefficient of ∼0.952. This deviation was generally consistent between different calibrations performed in buffer, indicating a signal loss of ∼20% compared to the original biosensor DMFC in blank experiments. The limit of detection (LOD) was 4.41 ng/mL, calculated using the equation ($average_{blank}$ + $3SD_{blank}$)/slope. Moreover, it was interesting to note that the control NIP-DMFC showed a random response in both media studied.

Compared to a previously published work where the sensing electrode was placed as an external element of the fuel cell [194], the loss in power density of the Sensor/DMFC was ∼60%, and the LOD of the system was better, being ∼20× lower. These results suggest that even when low MeOH concentrations are used, the consecutive MeOH adsorption during the stabilization/calibration experiments hinders the LOD of the final sensor and acts as a background memory signal. Nevertheless, this innovative hybrid device has other important advantages. Since the sensor layer (MIP) is directly attached to the anode of the fuel cell, this system is a 2-in-1 device that is much simpler and easier to use and requires fewer parts. In addition, the stability of the MIP-CC electrodes is higher, as they can be stored under the same conditions as the unmodified commercial anodes (room temperature, in any dry location) for several days without affecting the analytical response (the electrodes attached to the external circuit were more sensitive to storage conditions). For practical considerations, the sensor can be constructed like a normal DMFC by replacing the normal anode with another anode modified with a MIP polymer layer and printed in situ.

In calibrations with human serum (Figure 4.12-B), the output power of the biosensor DMFC decreased from 0.036 mW/cm^2 (initial value, after stabilization with Cormay® serum) to 0.027 mW/cm^2 towards the maximum CEA concentration, with a squared correlation coefficient of ∼0.986. These results confirm the behaviour of the biosensor DMFC to maintain sensitivity in more complex media, such as human serum. Compared to the buffer calibrations, the data obtained with Cormay® serum showed a better correlation coefficient and thus a better linear response. Since Cormay® serum has the same composition as real samples, this indicates a good behaviour of the biosensor

DMFC in the analysis of real samples. Therefore, real samples analysis requires a 1000× dilution, and consequently limit of detection is 1000 times higher than what is measured in the buffer. In terms of signal loss, this system is in the same range as the buffer calibrations and varies between 20 and 30% depending on the setup. In terms of application, the device can be used to monitor CEA levels in patients above 20 µg/mL, operating in an autonomous hybrid biosensor DMFC device. It can be used for screening and follow-up of cancers at any site without being limited to the analytical laboratory as in conventional methods.

To evaluate the selectivity of the developed biosensor DMFC, selectivity assays were made in buffer solutions against some common interfering compounds (CA15-3, glucose, urea). This was done by testing a CEA standard solution incubation (3000 ng/mL) in one biosensor DMFC and in parallel using different biosensor DMFC assemblies the same concentration of CEA is incubated spiked with the respective interferent. These assays were repeated 3 times using different sensing MIP anodes and different DMFCs assemblies. The data obtained are presented in Figure 4.13. The obtained data confirmed the high preference of this sensor for CEA with signals changing 0–5%, both in positive and negative directions.

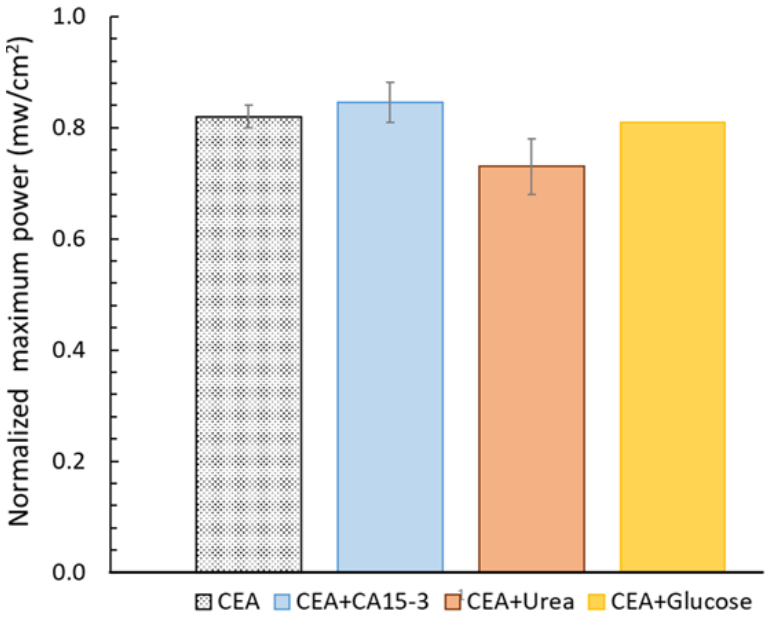

Figure 4.13 - Selectivity assays results (average of 3 different MIP-anodes with the respective standard deviation as error bars) performed with different possible interferents (CA15-3, glucose, urea) obtained in parallel, using different DMFC assemblies.

4.3.5 Device operation with an alternative fuel: Ethanol

In addition to MeOH, ethanol (EtOH) was also assessed as a fuel. This was an attempt to have an alternative fuel solution that is readily available to the population and less toxic than MeOH [207,208]. Both MeOH and EtOH fuel cells are designed to operate at ambient temperature and are therefore promising for powering portable electronic devices. The new self-powered sensor was then investigated using ethanol as fuel. The activation behaviour of the biosensor DMFC powered by EtOH is shown in Figure 4.14-A and typical polarization and power curves for the calibration experiments are shown in Figure 4.14-B with the corresponding calibration curve.

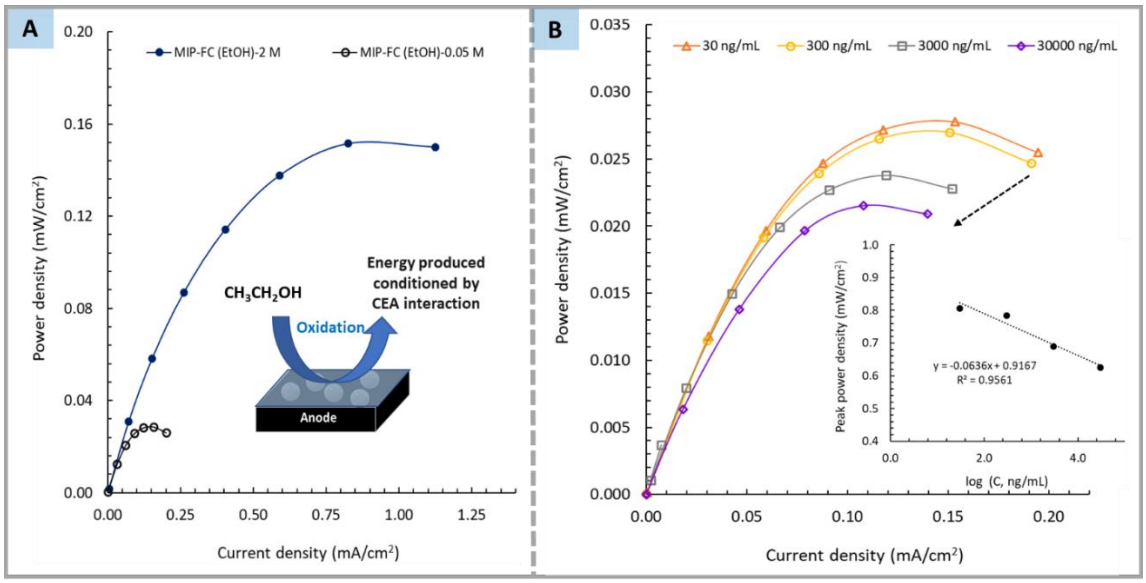

Figure 4.14 - Power-Current Density curves obtained with (A) the fuel cell stack (MIP anode) fed with ethanol solution (2 M and 0.05 M) and a (B) calibration test of a MIP-DMFC with the 0.05 M ethanol solution (including the corresponding calibration curve, inset) against increasing CEA concentrations in the range of 30–30000 ng/mL, prepared in buffer.

When replacing the fuel MeOH with EtOH, a 35% decrease in the performance of the MIP/fuel cell loaded with a 2 M concentration was observed during the activation phase. Using the lowest concentration of 0.05 M, the obtained power remained sufficient to calibrate the fuel cell with the MIP modified anode electrode (Figure 4.14-B). However, using the lowest concentration, the control (NIP -anode) did not provide enough power to proceed with the calibration. However, the results obtained are like those obtained using MeOH as fuel in terms of slope and correlation coefficient. The resulting

LOD was 3.52 ng/ mL, which was slightly lower than the value obtained with MeOH as fuel. The slower electrochemical oxidation of ethanol [209] that involves a higher number of electrons (12 electrons per molecule of ethanol) in addition to the difficulty in breaking C-C bond, seems to be an advantage that allowed increase the sensitivity of the sensor; it seems easier the CEA protein interfering with the ethanol oxidation (by blocking the platinum catalyst) in comparison with methanol, traducing in a slight improvement of the response and consequently the lower LOD obtained. This find can opens a new door for the development of autonomous fuel cell-based sensors powered by EtOH.

4.4 Conclusions

The developed biosensor DMFC hybrid device showed exceptional performance as a function of CEA concentration in a 2-in-1 approach combining in a single unit a DMFC cell as energy source and a MIP anode as sensing element. This was confirmed by the analysis of standard solutions prepared in different background media, including buffers and a complex human serum, resulting in sensitive data and low LOD values. The superior performance of this hybrid biosensor DMFC in Cormay® serum confirms the high selectivity of the response of this device, indicating that it can be successfully used for the analysis of real samples. Moreover, this setup can be operated with EtOH, which can be used in dilute concentrations, promoting the possibility of improving the analytical properties of the developed hybrid system. To improve the developed biosensor DMFC to achieve a full electrical independence, a self-signaled function can be incorporated in the biosensor DMFC system, transducing the electrochemical events in a more simple and friendly mode, for example by colour change mediated for electrochromic compounds, in a similar way to the approach described in [170].

Overall, the developed hybrid biosensor DMFC device is promising and suitable for application as a tool in point-of-care analysis, as it is capable of screening CEA in a wide range of concentrations, even in a complex human medium. The final hybrid biosensor DMFC could be further improved by using different fuels and conditions or even different setups, opening new opportunities for the development of self- powered electrochemical instruments as powerful tools in cancer diagnostics/monitoring.

Chapter 5

5. Development of an innovative flexible paper-based methanol fuel cell (PB-DMFC) sensing platform – Application to sarcosine detection

The results presented in this chapter were published in Liliana P.T. Carneiro, Alexandra M.F.R. Pinto, M. Goreti F. Sales, *" Development of an innovative flexible paper-based methanol fuel cell (PB-DMFC) sensing platform – Application to sarcosine detection*", *Chemical Engineering Journal* (2023), 452, 139563. **https://doi.org/10.1016/j.cej.2022.139563**

5.1 Introduction

Paper-based analytical devices appear to be a promising technology to produce simple, low-cost, lightweight, disposable, and portable devices that have greater potential for point-of-care (POC) applications [210,211]. Paper is considered a promising and ideal substrate for the development of analytical devices because it is inexpensive, available, environmentally friendly, biocompatible, flexible, and easily modified [212,213]. Compared to plastics and synthetic polymers, the biodegradability of paper substrates makes them promising environmentally friendly biomaterials for use in flexible electronic applications, combined with the ability to tailor treatments to desired properties [214,215]. Since Whitesides and colleagues [216] combined paper-based devices with microfluidic technology, a large number of new multifunctional devices with different architectures and detection modes can be found in the literature [217–220]. The combination with electrochemical detection is of particular interest as it allows faster response with higher sensitivity and selectivity [221].

An ideal paper-based electrochemical analyzer should have all functions built directly into the integrated instrument, including independence from the power source, so that it can be easily operated outside the laboratory [107]. To obtain self-powered paper-based analytical platforms, paper-based microfluidic fuel cells have shown promise for diagnostic and sensing applications [222,223]. These types of devices consist of cellulose paper as the support of the electrode/membrane system and are based on the laminar flow of anolyte and catholyte side by side, powered by different types of fuels. Several examples of these types of systems have been described in the literature, including microfluidic fuel cells driven by an ethanol-dichromate fuel oxidant mixture [224], hydrogen fuel cells [225,226] , methanol-KOH fuel cells [227] and formic acid fuel cells [228,229]. All of these systems appear to be capable of powering small devices for short periods of time. However, in most cases, their architecture is not simple and additional components such as valves, mixers, separators, and pumps are required. In addition, the analysis of samples and the incubation process are poorly understood in terms of the design of the platform relative to the energy generated.

In the work presented here, this drawback has been overcome by developing a paper-based methanol fuel cell platform that functions simultaneously as power source and biosensor, all combined in a simple square paper layer. A strip was developed to build a direct methanol fuel cell using a commercial Whatman paper as the substrate (PB-

DMFC) that supports all the fuel cell components, such as the electrolyte membrane (Nafion®), carbon anode and cathode electrodes, and current collector. No additional components are needed; the system works with only 100 µL of an aqueous methanol solution added directly to the anode side of the paper device. Since the device is primarily made of paper, it is completely flexible and represents an innovative, flexible paper-based fuel cell platform. Apart from some similarity to microfluidic fuel cells, the system presented here cannot be considered a microfluidic fuel cell as it operates on a completely different approach, which is more like conventional passive methanol fuel cells (DMFCs). Passive DMFCs appear to be a promising power generation technology that can be applied in the field of portable power [230,231], and the simple setup we have developed may open up new opportunities to bring biosensors from the laboratory to the field.

Integration of the biosensor function was achieved by developing a biosensor film of molecularly imprinted polymer (MIP) directly on the anode of the paper device. This sensor film was prepared by electropolymerization of charged poly(3,4-ethylenedioxythiophene) (PEDOT) and PPy monomers in situ, in the presence of sarcosine, which was selected as the target molecule here. The electropolymerization approach used here makes it possible to obtain a sensing polymeric layer with cavities tailored to sarcosine, capable of affecting the power generated by PB-DMFC in a concentration-dependent manner. When the rebinding of sarcosine occurs, the access of methanol to the platinum catalyst nanoparticles is hindered and consequently the performance of the device decreases, transforming the paper-based fuel cell into a biosensor sensitive to the detection of sarcosine. It is important to highlight that this fuel cell paper strip allows direct incubation of the sample in the sensing area, indicating that this fuel cell setup is suitable as a user-friendly sensing platform. In addition, simple and user-friendly self-powered sensor platforms can also be used in resource-limited areas to promote the worldwide diffusion of biosensors.

To the best of the authors knowledge, this is the first work to report on a flexible, single-layer, paper-based methanol fuel cell platform that serves simultaneously as an energy source and biosensor and can actually be used as a wearable device. The selection of sarcosine as a target is related to the increasing importance of this biomolecule in the diagnosis and progression of prostate cancer [232]. Sarcosine levels have been reported

to increase with progression of prostate cancer [233], from the normal concentration value of 0.60 μM to over 2.67 μM which is a strong indication of prostate cancer [234] .

Thus, a simple paper-based methanol fuel cell (bio)sensor platform was developed, to be fed with few microliters of an aqueous methanol solution and atmospheric oxygen, without auxiliary components. The sensing element layer is developed on the anode side of the fuel cell strip, which is fabricated by an electropolymerization process of EDOT/Py monomers. The final sensor platform was tested against sarcosine under buffered conditions and in real human urine sample. In addition, selectivity studies were performed with various interfering factors to verify the reliability of the developed sensor platform.

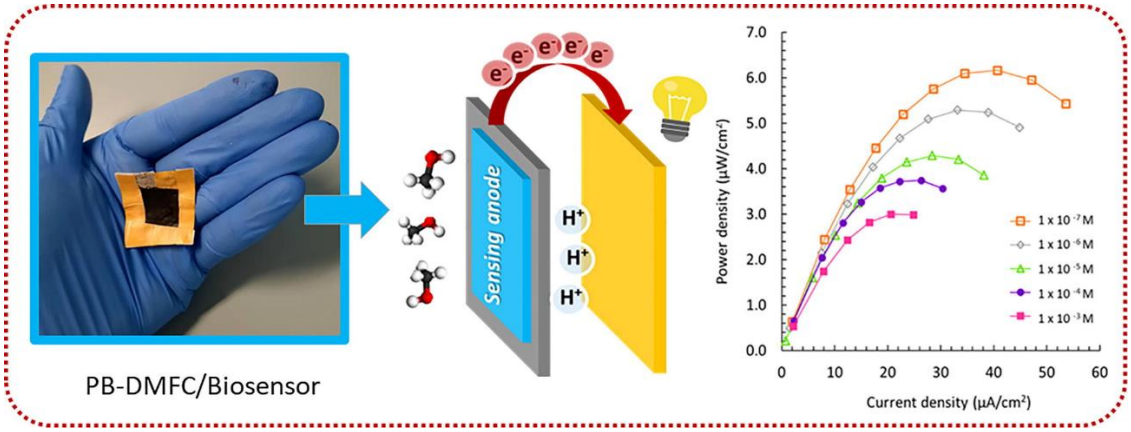

Figure 5.1 – Overview of the PB-DMFC/Biosensor developed in this work with an example of the power curves obtained during a calibration against sarcosine (buffer).

5.2 Experimental section

5.2.1 Reagents and solutions

All reagents used in this work were of analytical grade and the water was ultra-pure Milli-Q laboratory water. Liquid Nafion® (20 wt.% in alcohols, Quintech) was applied in a 2.25 cm^2 paper strip (Whatman filter papers grade 40) and covered both sides with appropriate carbon inks consisting of Carbon Black with PtRu (40:20 wt%) catalyst (C/PtRu) on Vulcan XC-72R (Quintech), for anode side, and Carbon Black with Pt (10 wt%) catalyst (C/Pt) on Vulcan XC-72R (Quintech), for cathode side. The inks were prepared in 2-propanol (99.8%, Panreac) with Nafion® (20 wt.%) as binder. A solution of paraffin (Sigma Aldrich) diluted in propanol (50/50) was applied to the PB-DMFC

assembly as an impermeable agent. For electrical connection, conductive silver ink (RS Pro) was applied to the edges. Phosphate buffered Saline (PBS) (Amresco) was used in the polymerization process to obtain the sensing layers on top of the anode side of the PB-DMFC. The polymerization mixture consisted of 0.01 M of 3,4-ethylenedioxythiophene (EDOT, 97%) (Alfa Aesar) and 0.005 M of Py (TCI) in PBS buffer. Sarcosine (Acros Organics) was used as template during polymerization (1.0×10^{-3} M). The removal of the sarcosine template was performed electrochemically using 0.5 M of a H_2SO_4 solution. MES buffer, 10 mM, pH 6.0, was obtained by dissolving 2-morpholinoethanesulfonic acid buffer grade (obtained from AppliChem). Stock solutions of sarcosine template (Acros Organics) were prepared in MES buffer, and less concentrated standards were obtained by accurate dilution of the previous concentrated solution. For selectivity studies, human urine of healthy individual was used with a dilution of 100×, spiked with the same sarcosine concentrations, tested in buffer. Selectivity assays were addressed by preparing sarcosine standards in the presence of interferents using histidine (2 mg/mL/Combi-Blocks), glutamic acid (1 mg/mL; Sigma Aldrich), creatinine (0.08 mg/mL; Fluka), uric acid (0.06 mg/mL; Sigma Aldrich), and Urea (0.3 mg/mL; Fagron), all prepared in the previously described MES buffer.

Electrochemical measurements were performed with 0.5-2.0 M Merck aqueous methanol solutions (HPLC grade) prepared in Mili-Q water. The methanol solution (100 µL) was added to the PB-DMFC anode side and adsorbed in a square of adsorption paper (VWR Spec-wipe of polyester/cellulose blend). A 2.25 cm^2 square of glass (FTO) was used to cover the anode side of the PB-DMFC assembly and prevent evaporation of the methanol.

5.2.2 Apparatus and equipment

Electrochemical measurements were performed at room temperature and atmospheric pressure in a Methrom Autolab potentiostat/galvanostat and a PGSTAT302N, controlled by Nova software (NOVA 2.1). The performance of the PB-DMFC and PB-DMFC/biosensor was evaluated using the Sampled DC technique in terms of polarization curves up to OCV, current and power stabilization. In analyzing the behavior of PB-DMFC and PB-DMFC /biosensor, all polarization curves recorded during the experiments were normalized with respect to the electrode area (2.25 cm^2). The maximum peak power for each curve was calculated and used to track system

performance and sensor response. For comparison between the calibration results of the different PB-DMFC/biosensor assemblies, the power values were normalized to the corresponding blank signal ($power_{sample}/power_{blank}$).

The anode electrode layers (modified and unmodified) were characterized by Raman spectrometry using a Thermo Scientific DXR Raman spectroscope with a confocal microscope. Spectra were recorded using an excitation laser at 532 nm in the range of 47 to 3500 cm^{-1} with a power of 2 mW and a 10× objective. The confocal aperture was set to 25 μm slit. Thermogravimetric analysis was also performed in an inert atmosphere (nitrogen, 20 ml min^{-1}, heating rate 30 °C/min). The morphology of the PB-DMFC assembly was evaluated using a scanning electron microscope (SEM) with cross-sectional and microstructural analysis.

5.2.3 Electrochemical assays

Electrochemical measurements were performed at room temperature and atmospheric pressure. The response of PB-DMFC and PB-DMFC/biosensor was evaluated using the sampled DC technique, running some polarization curves until OCV and maximum power stabilization (differences in signal < 2%). Prior to running the electropolymerization protocol to assemble the biosensor, all fuel cells were checked and activated to rule out an electrical problem or significant methanol crossover. Consecutive polarization curves were generated and evaluated, and the fuel cells with an OCV value between 0.35-0.45 V were accepted for sensor installation (using a 0.5 M methanol solution).

Calibrations of the PB-DMFC/biosensor were performed by incubating sarcosine standard solutions ranging from 1.0×10^{-7} M - 1.0×10^{-3} M in MES buffer. Prior to this, blank stabilization was performed by incubating the MES buffer until the electrical signal was stabilized. During calibration, each solution (200 μL) was incubated on the modified anode region of the sensor for 20 minutes, starting with the lowest concentration. After each incubation, the sensor area was carefully washed with ultrapure water and dried with nitrogen. This procedure was repeated for increasing concentrations of sarcosine prepared first in MES buffer and then in diluted human urine (100×) to evaluate the ability of the PB-DMFC/biosensor to discriminate sarcosine. For the selectivity assays, a selected concentration of sarcosine (1.0×10^{-5} M) was selected and measured.

5.2.4 Paper based fuel cell assembly

The PB-DMFC involves several steps, including electrolyte deposition, anode/cathode electrode deposition, impermeability stabilization, and current collector deposition. The different steps involved in this setup have been schematically shown in Figure 5.2-A.

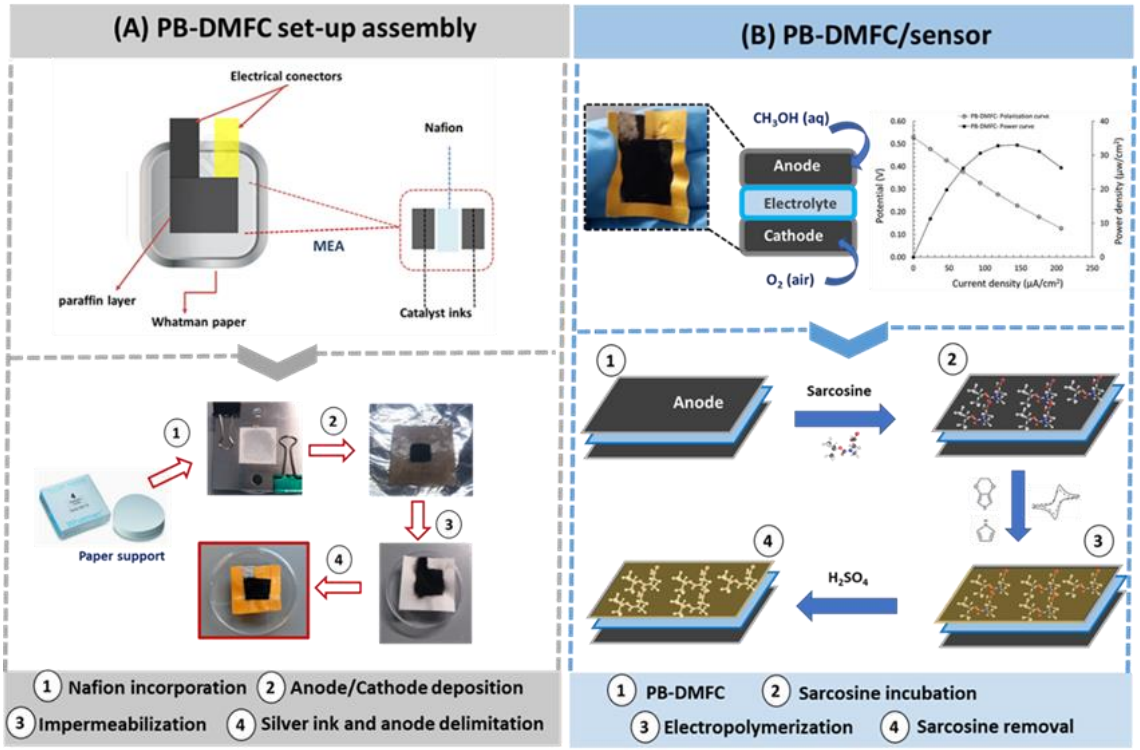

Figure 5.2 – Schematic representation of the various steps required to obtain an (A) PB-DMFC assembly on the paper substrates, which includes: the incorporation of the electrolyte, the deposition of the anode/cathode inks, the paraffin impermeabilization and the silver ink current collectors; after the fabrication of the PB-DMFC platform and the evaluation of the electrochemical reaction (B) a sarcosine-sensitive MIP layer was obtained by electropolymerization on the anode side using EDOT/PPy monomers, and later the sarcosine template is removed under acidic conditions.

All components form a single layer consisting of a commercial Whatman strip paper impregnated with 200 µL of a Nafion® solution (20 wt% in alcohols, 100 µL per side of the paper), which acts as a solid protonic electrolyte allowing the protons transport and preventing electrons conduction (electron insulator). A square metal mould with an area greater than 2.25 cm^2 was used to ensure complete distribution of the electrolyte. The mould was left at room temperature for 20 min and then at 60 ˚C for 10 min to dry

the polymer (not completely). The resulting composite material acts as a proton exchange membrane (PEM), replacing the solid Nafion® film used in typical methanol fuel cell devices. The impregnated paper was glued to another mould with the desired active area of 2.25 cm^2 and placed on a hot plate at 60 ˚C. Using an airbrush pen, the composite membrane was coated on both sides with two different carbon inks prepared in propanol, which also contained 20% Nafion® as a binder. For the anode side, an ink containing carbon black with Pt/Ru (40:20 wt%) was used, and for the cathode side, an ink containing carbon black with Pt (10 wt%) was used. The catalyst inks were stirred overnight to obtain a homogeneous solution and to avoid clogging of the airbrush. The Pt/Ru alloy in the anode and the Pt nanoparticles in the cathode are the best catalysts for the oxidation of methanol and the reduction of oxygen in the respective electrodes used in methanol fuel cells [235].

A solution of diluted paraffin in propanol (50/50) was added surrounding the active area of the PB-DMFC, at 90 ˚C, in order to waterproof the paper and avoid the paper breakdown. On top of the anode surface, a thin layer of a diluted solution of paraffin (~10%) was added to slightly hydrophobized the surface, in order to hinder the MeOH crossover from the anode to the cathode side.

Later, the system was electrically connected with a silver conductive ink on the upper edges of the device (one connecting the anode and the other the cathode) in different paths. The setup was left at 60 ˚C for 10 min to cure the silver ink. To complete the paper device, tape was placed on the back of each electrical connection to prevent short circuits, and it was also placed around the entire anode side to delineate the active area.

The PB-DMFC works with aqueous methanol solutions with concentrations between 0.5 and 2 M (adsorbed in adsorbent paper) and with atmospheric O_2. The adsorbent square paper covers the entire anode surface and distributes the methanol solution homogeneously over the entire surface of the electrode (which also prevents methanol leakage). During the electrochemical measurements, a square glass (FTO) was used to cover the anode side of the PB-DMFC unit to prevent the methanol from evaporating. The fuel cell device can also be operated without the cover glass and without the adsorbent paper, but with these two components the system reaches stability in a shorter time, so that several consecutive measurements can be performed without changing the methanol solution.

5.2.5 Biosensor element preparation

The Pt nanoparticles in the anode are the material directly related to the sensing capability, because the obstruction of the Pt nanoparticles by sarcosine molecules affects the methanol oxidation rate, which is key to the sensing capability of the fuel cell. To incorporate this sensing capability, a suitable PEDOT/Py semiconductor polymer was developed on the anode in the presence of sarcosine, which allows specific sites to be obtained in the polymer after the release of sarcosine by acid electrochemical treatment. The incorporation of the sensing element into the system PB-DMFC (Figure 5.2-B) was achieved by an electropolymerization process (in a 3-electrode system) of a solution of EDOT (0.01 M) and Py (0.005 M) in PBS buffer (previously flushed with N_2) directly on the anode side of the fuel cell unit. First, a solution of sarcosine (1.0×10^{-3} M) was incubated in the anode for t = 2 h. Then, the PB-DMFC was carefully washed with ultrapure water and dried with nitrogen and incorporated into the 3-electrode system; in this configuration the anode layer of the PB-DMFC is the working electrode, a leakage-free Ag/AgCl plastic electrode is the reference electrode, and a platinum rod electrode is the counter electrode. Electropolymerization was performed by cyclic voltammetry (CV) (10 cycles, − 0.3 V to 1.2 V) at a scan rate of 25 mV/s. The same CV protocol was used to remove the sarcosine template, but a 0.5 M H_2SO_4 solution was used instead of the monomer solution.

In parallel, the non-imprinted fuel cells (PB-DMFC/NIP) were prepared using exactly the same steps and protocols, except for the incubation of the sarcosine template. The polymer layer was a barrier to the spread of methanol on the anode surface. Therefore, special care was taken to ensure that the polymer was semipermeable enough to allow the methanol molecules to reach the catalytic Pt nanoparticles and maintain the electrochemical activity (hence, in the unprinted PBDMFCs, the electrochemical signal is attenuated by the presence of the polymer film). The polymer-modified PB-DMFCs (printed and unprinted) were not reusable and were discarded after calibration.

5.3 Results and discussion

5.3.1 Assembly of the paper-based fuel cell device

5.3.1.1 Configuration

The design of the paper-based fuel cell includes all components necessary for operation, which are built into the paper strip. Several prototypes were tested to find a suitable design that would provide a simple and durable configuration with a stable electrical signal. Figure 5.3 shows and describes all the prototypes that were studied during the work, as well as the changes that were made to each setup until the final prototype presented here, PB-DMFC, was found.

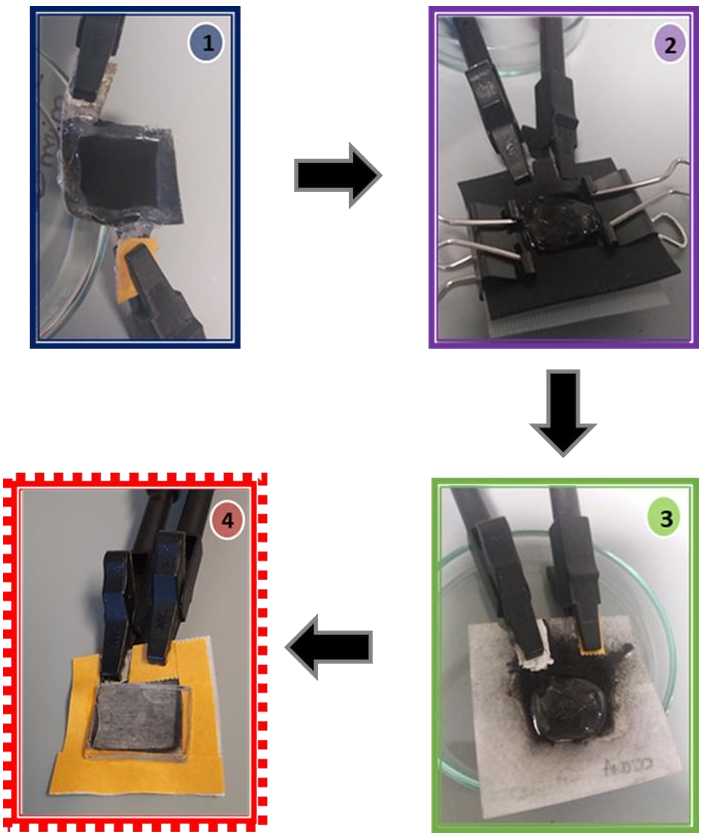

Figure 5.3 Paper based methanol fuel cell prototypes tested during this work until meet the appropriate prototype n° 4.

Prototype paper-based methanol fuel cells (PB-DMFC) were assembled in a square of Whatman paper (2.25 cm^2 area), and various setups were evaluated for

durability, electrical stability, and OCV/power. In an initial experiment, after the electrolyte was added and the anode and cathode were deposited, the active region was insulated with a layer of hot glue, and the current collectors were pulled out of the assembly, formed with silver ink, and reinforced on the opposite side with tape to prevent short circuits (1). This setup was abandoned because the electrical connections became brittle during long-term experiments. To solve this problem, the current collectors were placed inside the square fuel cell unit and reinforced to prevent breaking or damaging the electrical connections (2). To isolate the active area, the adhesive layer was replaced with a rubber layer on the anode side and a plastic layer on the cathode side, which was attached with two clips. This setup was abandoned because it was not possible to prevent the methanol from penetrating the paper, resulting in methanol leakage and, in some applications, paper degradation. To address this deficiency, a solution of paraffin (diluted in propanol) was applied as an impermeable agent to both sides of the fuel cell paper strip surrounding the active anode/cathode region. This step was critical to prevent the methanol from spreading in the paper and also strengthens the structure of the paper so that it can be used multiple times without damaging it. In addition, the paraffin/paper arrangement forms a kind of flexible "composite" that gives this sensitive platform a suitable property for use in POC systems.

Final improvements were made to the system to narrow the sensor area and optimize electrical stability (4). The anode was wrapped with tape and insulated, as it is the part of the fuel cell platform where the sensor is integrated, in a fully flexible and self-powered platform. To improve electrical stability, the methanol solution was impregnated into a square of cellulose fibers that allowed efficient distribution of the methanol solution over the entire active anode area. A glass square was used to cover the anode and prevent evaporation of the methanol during electrochemical measurements. It is important to emphasize that setup number 4 works perfectly without these additional components in a single layer setup. However, to ensure that any external interference would affect the system performance (temperature/vibration), this setup was used as a simple, stable and flexible self-powered paper-based methanol fuel cell strip.

Additional studies were performed on the selected prototype to improve the measured OCV and output power. The ideal amount of Nafion® electrolyte impregnated into the paper and the amount of paraffin solution to efficiently hydrophobize the fuel cell system were evaluated in terms of the overall performance of the PB-DMFCs by tracking

the polarization and power curves for all assembled systems. Figure 5.4-A/B shows the obtained results normalized to the active area (2.25 cm^2) of the assemblies recorded with 2 M MeOH.

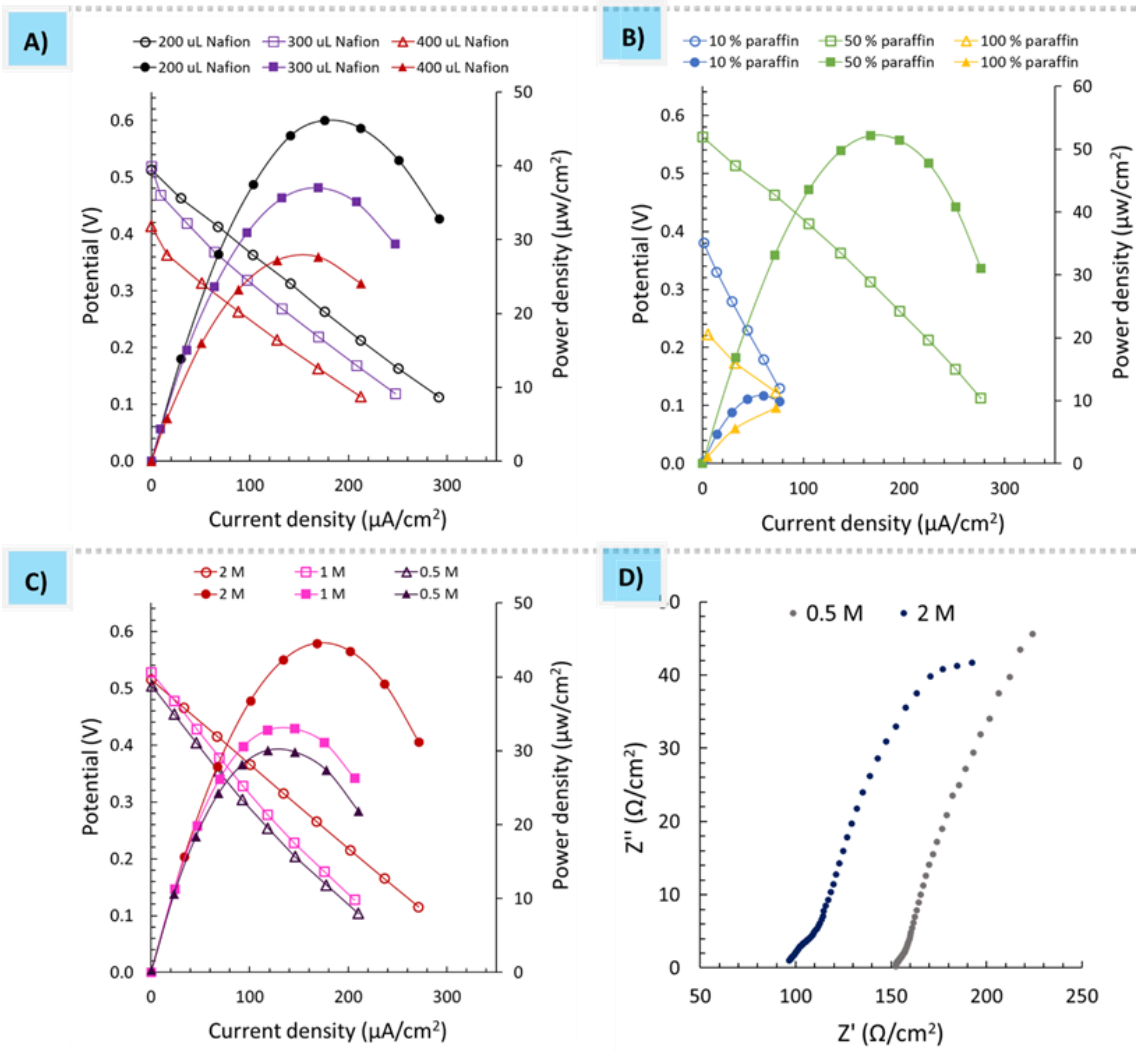

Figure 5.4 Electrochemical data of PB-DMFCs in terms of polarization (empty symbols) and power curves (full symbols) obtained under different test conditions: (A) the Nafion® electrolyte incorporated into the paper matrix; (B) the paraffin amount used as an impermeabilizing agent; (C) operation of the device using various methanol concentrations in the range of 0.5–2.0 M; and (D) electrochemical impedance spectroscopy measurements under open-circuit conditions (OCV) using 0.5 and 2.0 M methanol concentrations.

The ideal amount of Nafion® electrolyte incorporated into the paper was studied and the results are shown in Figure 5.4-A. As one can see, using a small amount of Nafion® solution (200 µL) gives better results in terms of power/current density and OCV

of the different PB-DMFCs assemblies tested. The use of larger amounts of Nafion® electrolyte makes it difficult to produce a homogeneous layer, resulting in some roughness on the surface of the electrolyte dry film. This roughness, achieved with larger amounts of Nafion®, can affect the proton conductivity of the system, resulting in lower performance, which is more evident in the 400 µL impregnated PB-DMFC. Considering these results, the selected volume of Nafion® electrolyte was set at 200 µL, which is the minimum volume required to cover the entire active area of the paper substrate.

The paraffin-impermeabilizing agent was first tested without dilution (100%) and later diluted in isopropanol (10% and 50%), as shown in Figure 5.4-B. The results obtained show a significant difference when the paraffin amount was varied from 10% to 100 %, with the ideal value being in the middle (50%). These results are easily understood considering the important and crucial role of the paraffin component. With only 10% of this compound, the transfer of methanol from the anode to the cathode cannot be avoided, resulting in a lower OCV value and lower power. The poisoning of the cathode electrode by methanol molecules is a problem of DMFCs that lowers their performance and makes their conversion difficult so far. In a system of this type, composed mainly of paper, it is even more difficult to limit the methanol crossover, but a compromise was found with a solution of 50% paraffin and a stable system with a fairly acceptable OCV (≈0.55 V) and a reasonable performance was obtained. Paraffin works very well in preventing methanol crossover, but it has an insulating behaviour (no conductive link) that was observed when a pure paraffin solution was spread in the PB-DMFC array. When undiluted paraffin is used, the conductivity of the system is severely compromised, resulting in the lower measured OCV (0.22 V) and power output. Based on these results, the selected amount of impermeabilizing agent was set at 50% (paraffin/IPA) and adopted in the work. It is important to emphasize that this paraffin/IPA ratio refers to the vicinity of the active anode/cathode region. A light layer of 10% (paraffin/IPA) was applied to the anode side of the PB-DMFC to limit the transfer of methanol.

5.3.1.2 Selection of ideal MeOH concentration

Passive direct methanol fuel cells are usually operated with concentrated MeOH solutions (between 1 and 5 M) [205]. A compromise between the ideal MeOH

concentration in the anode layer and the rate of MeOH transfer from the anode to the cathode layer is essential to maximize cell voltage and reduce power losses. This compromise strongly depends on the fuel cell structure and design [164]. Thus, in this PB-DMFC setup, the generated power is mainly limited by the simplest arrangement, and the use of higher methanol concentrations can lead to higher methanol crossover, which affects the performance of PB-DMFCs, especially the useful life, since the methanol crossover poisons the Pt nanoparticle catalysts on the cathode side. In addition, the interface between the fuel and the Nafion® paper-based electrolyte is very narrow in this developed setup, so the ideal methanol concentration to achieve a stable electrical signal in successive measurements was investigated. Various methanol concentrations were tested, ranging from 2.0 to 0.5 M. The corresponding polarization and power curves are shown in Figure 5.4-C. These results were obtained using the same PB-DMFC starting with the higher MeOH concentration to the lowest MeOH concentration, washing with ultrapure water, and drying with N_2 after stabilization at each concentration. The results show that both the power density and current density increase with increasing MeOH concentration, and the MeOH concentration varies more in the range of [2.0–1.0 M]; in the range of [1.0–0.5 M], the difference in power density and current density is very small. Therefore, after successive measurements (washing and changing the MeOH fuel), the electrical signal is more stable when using 0.5 M MeOH than when using the 2 M concentration (results obtained with different PB-DMFCs), with relative standard deviations ranging from 2% to 4% for the lowest concentration, while the relative standard deviations range from 10% to 14% for the 2.0 M MeOH concentration (data in Figure 5.5).

Therefore, when using the less concentrated MeOH solution (0.5 M), the loss in performance is compensated by the gain in long-term stability of the PB-DMFC platforms, as the MeOH crossover is significantly reduced (fewer MeOH molecules involved in the reaction also means fewer MeOH molecules passing through the Nafion®/paper membrane to the cathode side).

Electrochemical impedance spectroscopy (EIS) measurements were also performed to record the resistance of the PB-DMFCs under open circuit voltage (OCV) in two different methanol concentrations. The obtained results are shown in Figure 5.4-D, normalized to the active area of the PB-DMFC assembly (2.25 cm^2).

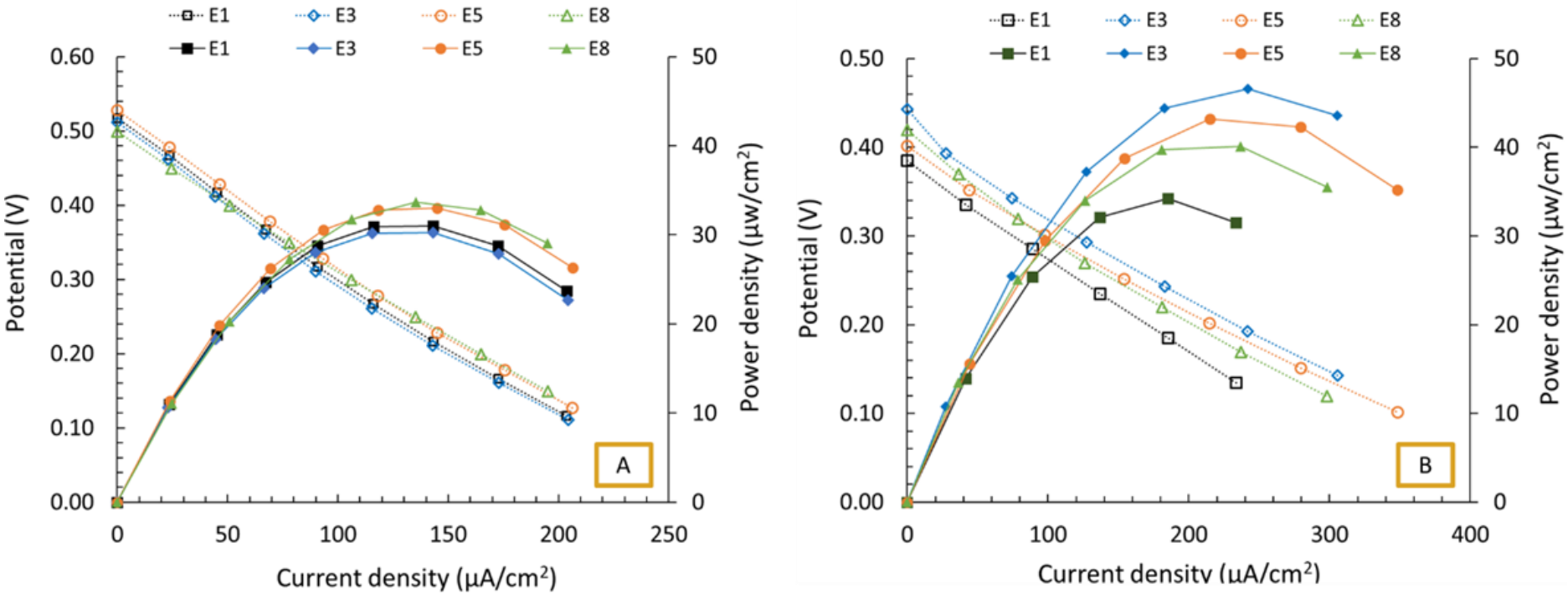

Figure 5.5 Polarization and power curves obtained in consecutive electrochemical readings of two PB-DMFCs assemblies using (A) 0.5 M of MeOH and (B) 2 M of MeOH.

The EIS data was also fit to obtain the equivalent circuits of each individual fuel cell set-up (Figure 5.6), to estimate the ohmic resistance (Rohm), activation resistance (Ract) and mass transfer (Rmt) of the whole fuel cell.

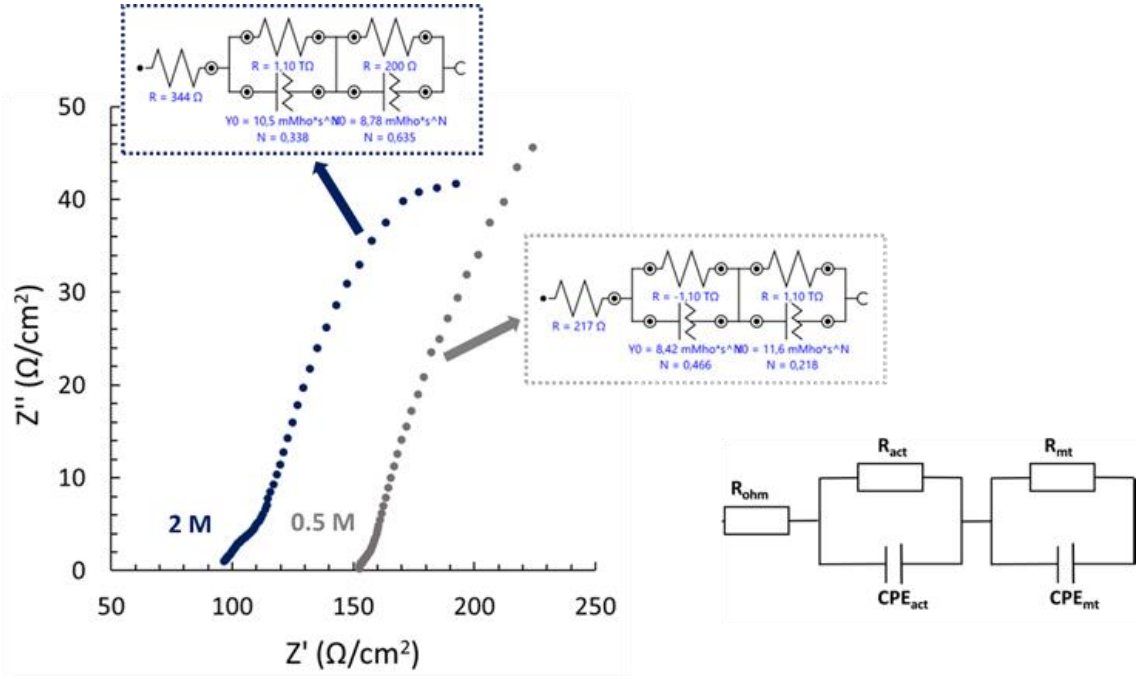

Figure 5.6 EIS data with the equivalent electric circuits (EEC), under open-circuit conditions (OCV) using 0.5 and 2.0 M methanol concentrations.

The measured resistance values are quite high compared to a complex typical DMFC array consisting of all components [236]. However, higher values have been observed in simpler arrays with micro-DMFC systems because the simplicity of the system conditions the various mass transport phenomena [237,238]. This measured electrical resistance is related to the electrical resistances of the two anode/cathode electrodes, the proton transfer of the membrane, the current collector pathways and also the resistances between the individual components. Since the PB-DMFC contains all the components in a simple paper square without hot pressing and additional components, these resistance values in the order of 100–150 Ω/cm^2 are quite acceptable for a first simple prototype. When the highly concentrated 2.0 M MeOH solution is used, a lower resistance is measured compared to the dilute 0.5 M MeOH concentration. Therefore, the difference in measured resistance using the two different MeOH concentrations is not significant and considering that this platform needs to be activated and calibrated in a

process with several consecutive measurements, higher signal stability is very important, so the lowest methanol concentration of 0.5 M is selected for further studies.

5.3.2 PB-DMFC device characterization

The PB-DMFC assemblies (unmodified and modified with polymer sensing material) were analysed with a scanning electron microscope (SEM) to evaluate the distribution of the different assembled layers (anode, electrolyte, and cathode) and to obtain evidence of the anchored polymer layer in the anode-side surface. The SEM diagrams of a PBDMFC and a PB-DMFC/MIP in cross-section and surface topography are shown in Figure 5.7A–F.

Analysing the cross-sectional images of PB-DMFC (Figure 5.7-A) and PB-DMFC /MIP (Figure 5.7-B), a clear difference in the 3-layer anode/electrolyte/cathode distribution can be seen. In PB-DMFC without modification, the layers were not so well defined because they were easily damaged by breaking with liquid nitrogen. In the polymer modified PBDMFC/MIP, the 3 layers were very well defined, indicating that some kind of reinforcement protected the layers during fracture with liquid nitrogen. In the polymer modified PBDMFC/MIP, the 3 layers were very well defined, indicating that some kind of reinforcement protected the layers during fracture with liquid nitrogen. The same results were obtained in the PB-DMFC/NIP samples (Figure 5.8-A/C), indicating the presence of a modification consisting of a homogeneous polymer layer in both the MIP and NIP assemblies. In addition, a higher, well-defined thickness of the anode layer can be seen, indicating the presence of the EDOT-PPy polymer (Figure 5.8-C/D). When analysing the surface topography of the PB-DMFC samples (Figure 5.8-E/F), a differentiated roughness is observed in the PB-DMFC/MIP sample compared to the unmodified PB-DMFC. These results could indicate the presence of a uniform polymer layer anchored on the surface of the PBDMFC/MIP sample.

Both fuel cell configurations showed similar assignments in terms of nanocatalysts (Pt and Ru) and fluorine (from Nafion®, which was used as a binder). However, an increase in the sulphur element was observed, which could be another indication of the anchoring of PEDOT in the carbon surface (Figure 5.8-D/E).

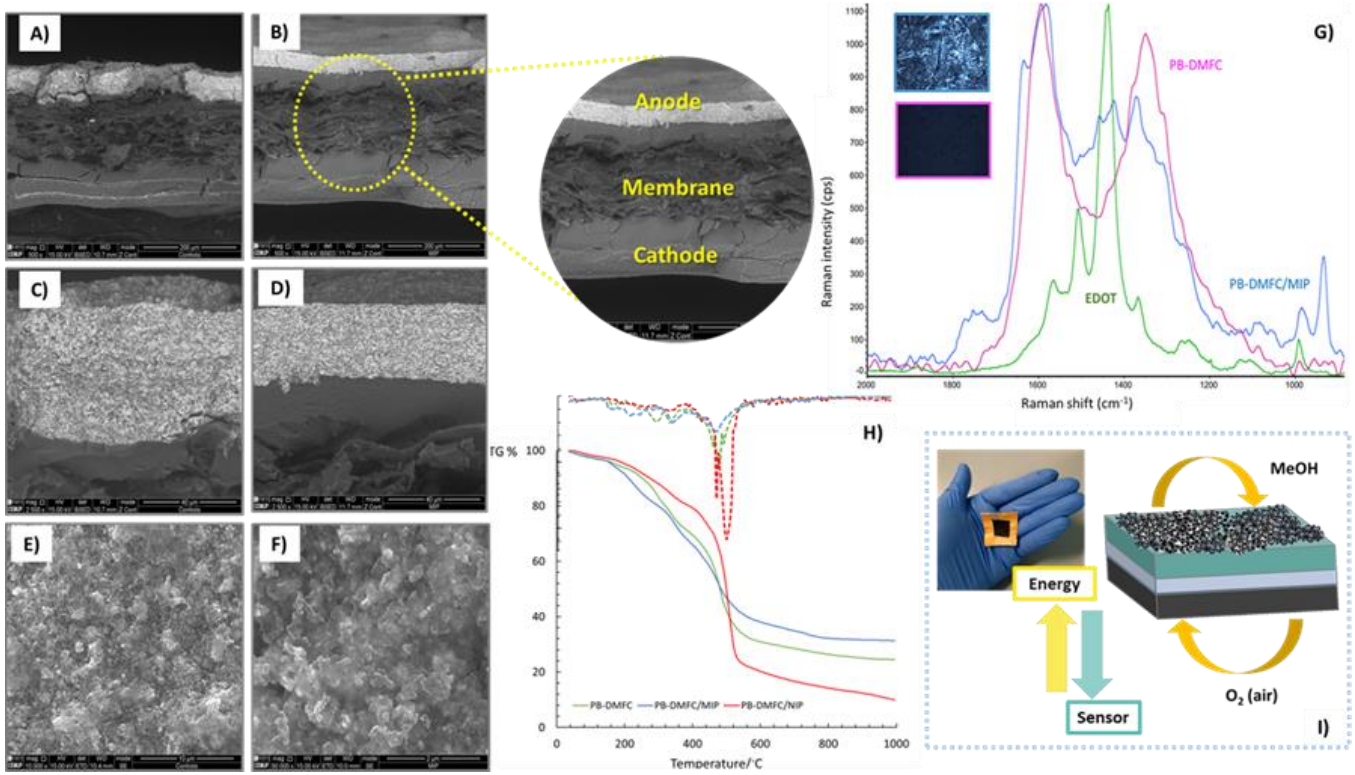

Figure 5.7 Characterization results of the paper fuel cells developed in this work: SEM Cross-sectional images of a (A) control cell PB-DMFC and a (B) polymer modified PB-DMFC /MIP; (C) overview of the anode layer of PB-DMFC and (D) PB-DMFC /MIP showing differences in the structure of the catalytic layer; topography analysis of (E) PB-DMFC and (F) PB-DMFC /MIP showing different roughness. Raman analysis at 532 nm for a control sample PB-DMFC, PB-DMFC /MIP and a sample with EDOT carbon support for comparison; confocal images of a PB-DMFC and PB-DMFC /MIP assemblies highlighting the color difference (blue) (G). TGA and DTG curves of different paper fuel cell units (PB-DMFC, PB-DMFC /MIP, PB-DMFC / NIP) in an inert atmosphere (nitrogen, 20 mL min^{-1}, heating rate 30 °C/min) (H). Overview of a PB-DMFC strip showing the chemical reactions responsible for the dual function (power and sensor) of the developed platform (I).

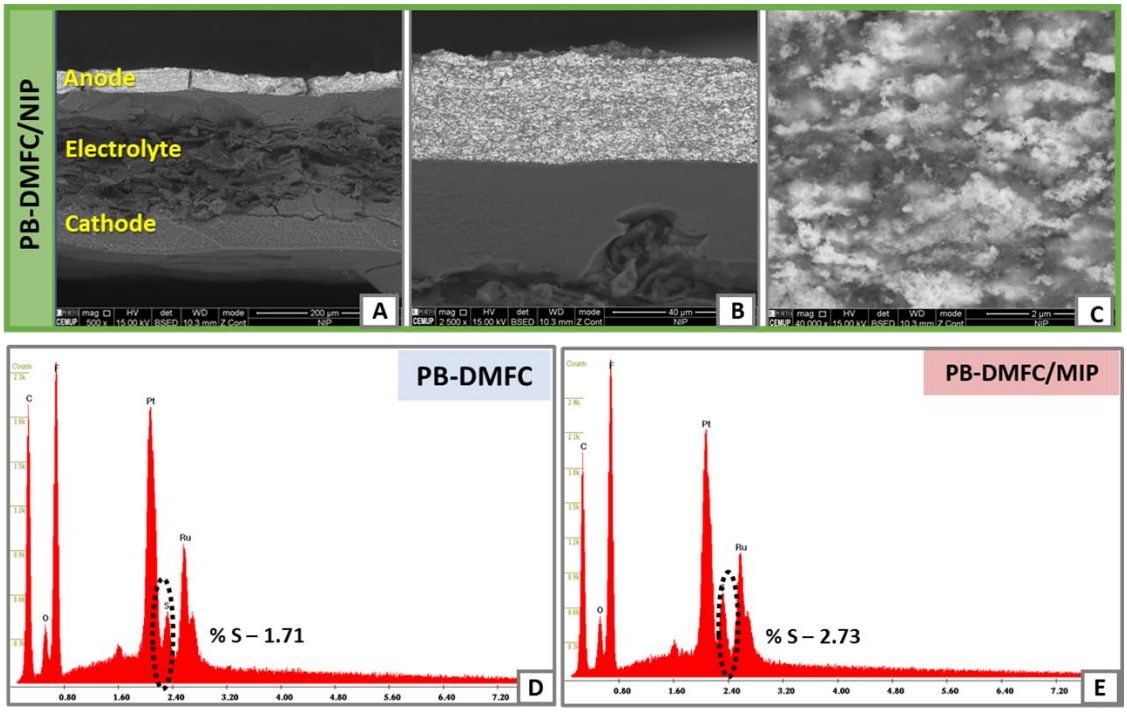

Figure 5.8- SEM images of the polymer modified PB-DMFC/NIP in: (A-B) cross-section and (C) topography surface analysis. EDS analysis of a (D) non-modified PB-DMFC assembly and a (E)) PB-DMFC/MIP configuration, evidencing the sulphur percentage detected in the sample.

It is important to highlight that the amount of Pt and Ru catalysts was similar in both samples, indicating that the anode electrode was structurally damaged by the electrochemical polymerization/removal cycles applied to fabricate the PB-DMFC/biosensor.

The PB-DMFC and the PB-DMFC/MIP assemblies are also tracked using the Raman technique (Figure 5.7-G). The spectra obtained for the anode side of the unmodified PB-DMFC show the two broad G-bands (1592 cm^{-1}) and D-bands (1344 cm^{-1}) typical of carbon black nanostructures, usually around 1585 cm^{-1} and 1350 cm^{-1} [239]. Significant differences are observed when comparing with the spectra obtained for PB-DMFC/MIP, which can be attributed to the polymer anchor in the electropolymerization protocol. The results show a significant distortion of the D-band (1346 cm^{-1}) and the overlapping of some characteristic peaks of the PEDOT polymer (green line, polymer obtained by electropolymerization under the same conditions as the sensors anchored on a square of commercial carbon for comparison). The overlapping peaks of PEDOT appear in the PB-DMFC/MIP spectra at 992 cm^{-1}, 1117 cm^{-1} and 1433

cm^{-1}. Moreover, when analysing the confocal images, one can also observe the difference in the surface colour of PB-DMFC and PBDMFC /MIP (see Figure 5.7-G). This shows that the polymer-modified sample has a stronger blue hue, which is characteristic of PEDOT-based polymers [200]. The relative intensity of the D and G bands can be an indicator of the disorder present in a sample, and the ratio I_D/I_G can be calculated to evaluate the defects present in a particular carbon material [240]. The I_D/I_G ratios for the PB-DMFC and the PB-DMFC/MIP sensor were calculated and the final values are the average of 3 independent measurements at different points on the anode surface (Table 5.1).

Table 5.1- Calculated I_D/I_G ratio obtained from Raman Spectra for the PB-DMFC and polymerized PB-DMFC/MIP samples

Sample	Raman shift	Raman intensity	I_D/I_G
PB-DMFC	D: 1343.65	14.161	0.91
	G: 1592.97	15.502	
PB-DMFC/MIP	D: 1369.02	18.278	0.68
	G: 1585.38	27.006	

The PB-DMFC (control) has an I_D/I_G ratio of 0.91, while the sensor PBDMFC/MIP sensor has a ratio of 0.68. This ratio difference is significant and supports the presence of a uniform polymer layer anchored to the anode surface PB-DMFC.

The TGA thermograms and DTG curves of PB-DMFC and polymer modified PB-DMFC/MIP-NIP fuel cells are shown in Figure 5.7-H. When analysing the corresponding weight loss curves, a differential thermal decomposition behaviour of the different analysed samples can be observed, with PB-DMFC/NIP showing the sharpest mass loss profile. This result is to be expected since PB-DMFC/NIP is the sample with a more homogeneous upper polymer layer, which also has a "protective effect" that causes a shift in the temperature range of decomposition and delays the thermal decomposition of this sample. Thus, the cavities presented in PB-DMFC/MIP do not cause significant differences in the decomposition profile compared to the control (PB-DMFC) because

the polymer layer is not as homogeneous due to the presence of the sarcosine template during electropolymerization. All samples can be considered thermally stable, with minimal percent weight loss occurring up to 200 ˚C, including the Nafion® layer (membrane adsorbed in the paper separating the anode and cathode sides) and the paraffin hydrophobic agent. The results of comparing a PB-DMFC, a Nafion® impregnated paper and a paraffin impregnated paper are shown in Figure 5.9 and demonstrate the stability and thermal decomposition of these materials in isolated form.

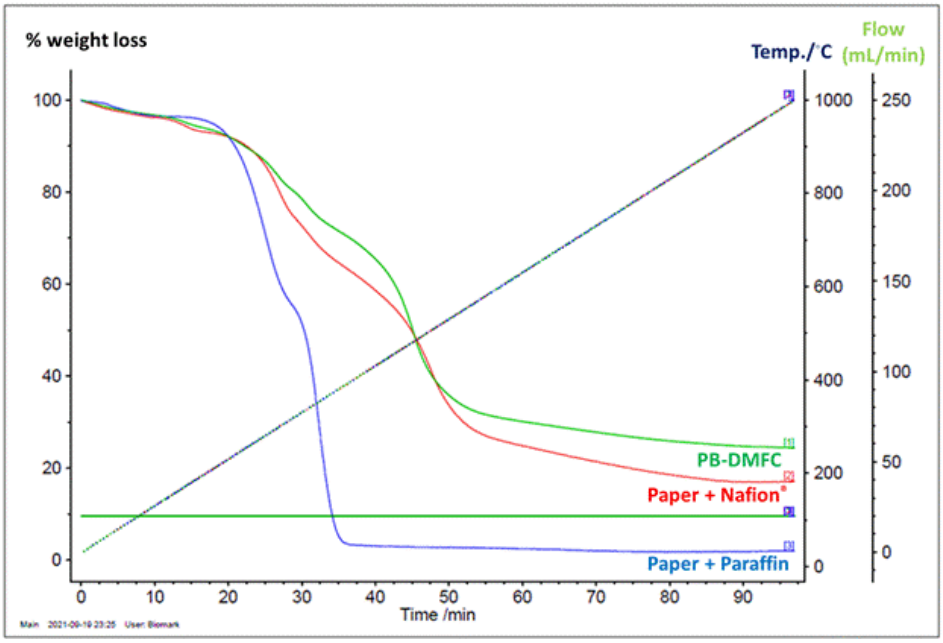

Figure 5.9- TGA thermograms of a control PB-DMFC in comparison with a paper impregnated with Nafion® electrolyte (Paper + Nafion®) and a paper impregnated with the paraffin hydrophobic agent (Paper + Paraffin) performed in an inert atmosphere (nitrogen, 20 mL min^{-1}, heating rate 30 ˚C/min).

Moreover, the described PB-DMFC platforms are stable for several weeks and can be stored at room temperature in a dark and dry environment until use. They can be reused several times without degrading performance if stored under proper conditions. These properties are completely novel for a system of this type and combined with the very simple structure of this assembly (a square of paper) makes this system very promising for use as a portable biosensor that can be used in any location.

In summary, the characterization results of this innovative methanol fuel cell yield a stable, durable, and robust system that can be modified with a sensory polymer,

transforming this simple, low-cost paper platform into a self-powered system that serves as both an energy source and a sensor (Figure 5.7-I). Thus, this platform is user-friendly and easy to transport, which is an important requirement for a point-of-care application.

5.3.3 Integration of the sensing area on the PB-DMFC

5.3.3.1 Imprinted film layer development

The sensor layer was built on the surface of the anode layer of the PB-DMFC, creating the PB-DMFC/biosensor. The combination of the imprinted polymers with the anode carbon catalysts makes it possible to obtain a hybrid nanocomposite electrode with a dual function: methanol catalytic activity and sensing property. In fact, this dual function is closely related, since both steps involve the oxidation of methanol in the Pt catalyst sites: in the PB-DMFC the Pt active sites are fully available to react with the methanol molecules, while in the PB-DMFC/biosensor the Pt catalyst sites are less accessible (polymer film) and can be hindered by the incubation of the template or even in a control experiment (nonimprinted polymers, NIP) the Pt active sites are partially blocked by the polymer layer (Figure 5.10-A). The SEM images also show the modifications in the surface of the different anode electrodes.

The sensory area in PB-DMFCs was obtained in situ by electropolymerization using cyclic voltammetry (10 cycles in PBS buffer) of EDOT and Py monomers. This electropolymerization approach was investigated and validated in a previously published work [241] in the context of (bio)sensory methanol fuel cells. In this work, a carbon fabric containing PtRu nanoparticles (C/PtRu) was directly modified by the electropolymerization of EDOT/Py and later assembled in a typical passive methanol fuel cell configuration, which showed good electrical properties and sensitive responses to CEA detection.

The PB-DMFCs developed in this work are very simple systems compared to the conventional passive fuel cell units used in previous works [193,241]. The advantages of this innovative PB-DMFC strip compared to previous fuel cells developed with a passive configuration [193,241] are based on the simplicity of this new single-layer configuration. The single-layer PB-DMFC allows easy insertion and removal of the methanol fuel and sample for analysis, the volume required for the fuel was very small (100 µL) compared to the volume required to operate the first setup (1500 µL), and no special tools or screws

were required to open and close the device. The disadvantage of this simpler fuel cell setup is its low power density compared to the fully passive system developed previously.

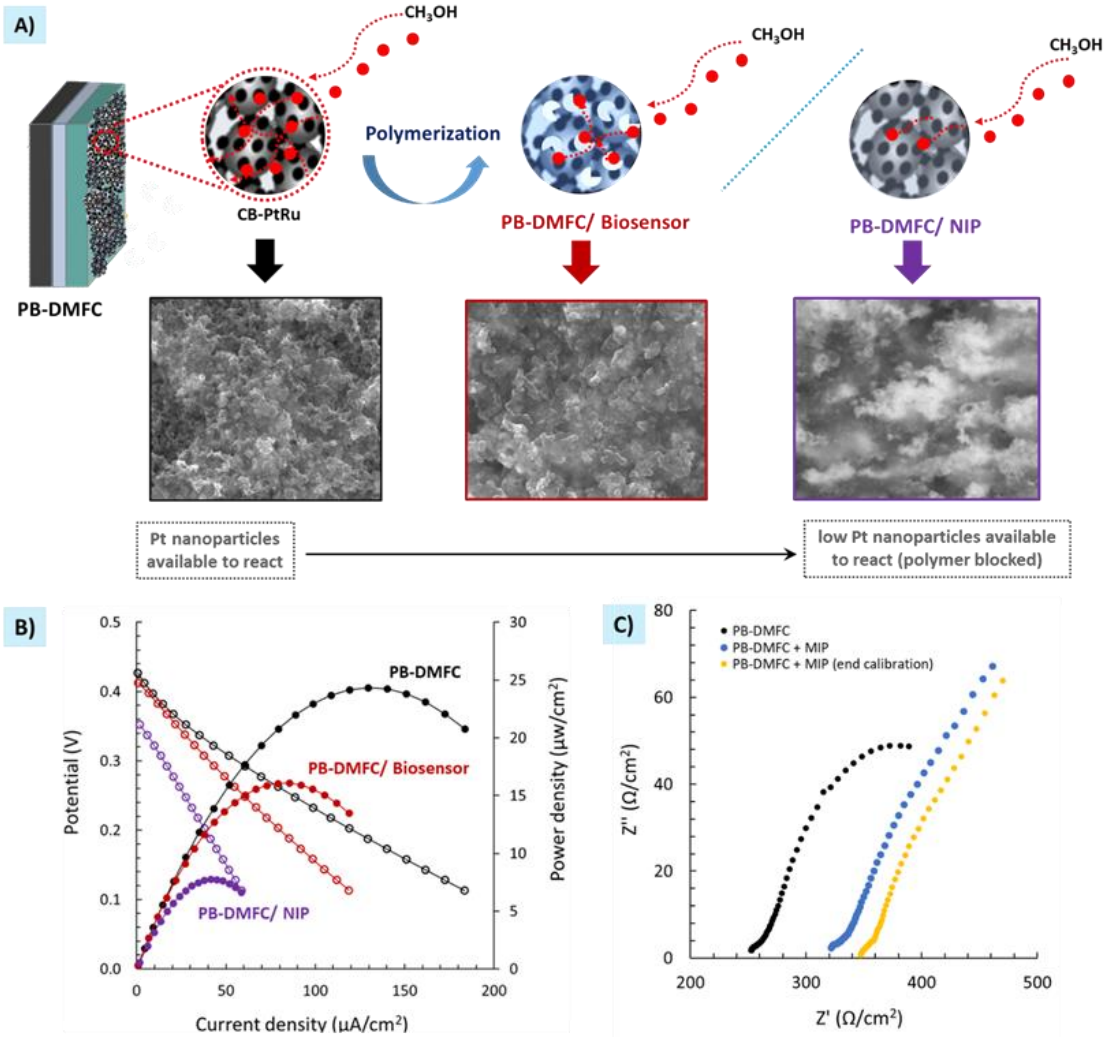

Figure 5.10- Analysis of the behavior of the different fuel cell platforms with respect to (A) general scheme complemented with surface SEM images evidencing the possible different methanol pathways in the fuel cell anode electrode and showing the blocking effect of the catalytic Pt active sites in the polymer modified fuel cells (PB-DMFC/Biosensor and PB-DMFC/NIP). The CB-PtRu is covered by a sarcosine imprinted film in the PB-DMFC/Biosensor, shown in blue color, or a control film without printed sites in the PB-DMFC/NIP, shown in gray color. The voids in the anode of the PB-DMFC/Biosensor allow a faster and more efficient reaction of the methanol fuel on the surface of the Pt catalysts compared to the polymer layer of the control (without voids), which acts as a barrier for the reaction of the methanol molecules. Comparison of the measured polarization and power curves recorded for the different paper fuel cell systems (PB-DMFC, PB-DMFC/Biosensor, PB-DMFC/NIP) (B) and evaluation of the EIS analysis of a PB-DMFC before, after polymerization and at the end of a calibration (C).

The lower power density of the PB-DMFC system is compensated by its higher sensitivity and user-friendly approach (since the sensor can only be used once, a higher power output was not a requirement for it to work well). This new design is also less expensive and more environmentally friendly, considering all the materials needed to build the system.

The good conducting and electrocatalytic properties of the PEDOT/ PPy polymer are important to improve the stability of the PB-DMFC/ biosensor compared to the unmodified PB-DMFC. The hydrophobic nature of the PEDOT/PPy polymers also contributes to the signal stabilization of the paper-based systems by acting as a barrier to methanol penetration through the anode surface (methanol crossover) and also reduces the electrical blockage caused by the small amount of paraffin added to hydrophobized the anode surface. Therefore, these types of conductive materials have been widely explored to improve the performance and durability of fuel cell systems, which makes them suitable for fuel cell electrode applications [242]. Among the common conductive polymers, PEDOT polymer is particularly attractive and suitable for use in fuel cell electrodes because it is stable and exhibits high electronic conductivity (between 1 and 100 S/cm, depending on whether a dopant has been added) [243].

To obtain a higher density of sites impregnated with sarcosine on the anode surface, the surface was incubated (t = 2 h) before polymerization. Removal of sarcosine from the polymeric network was achieved electrochemically in a sulfuric acid solution. This procedure allows the adsorbed sarcosine molecules to be removed and the imprinted cavities to be emptied for subsequent rebinding. In addition to releasing the imprinted molecules from the polymeric network, this removal step in acid also allows the removal of unreacted monomers from the surface and of the paraffin added for the previous activation of the fuel cells (paraffin solution is not acid resistant). Interestingly, the sensor layer obtained in situ is sufficient to control the methanol crossover, resulting in a faster and more durable PB-DMFC system where the right polymer layer takes over the role of paraffin and the sensing property (in the case of PB-DMFC/MIP).

An example of a cyclic voltammogram (last n◦10 cycle) in a 3-electrode configuration of the PB-DMFC/biosensor and control PB-DMFC (NIP) are shown in Figure 5.11, as are the corresponding removal steps. These voltammograms were referenced to a pair of PB-DMFCs that were fabricated on the same day and had similar performances.

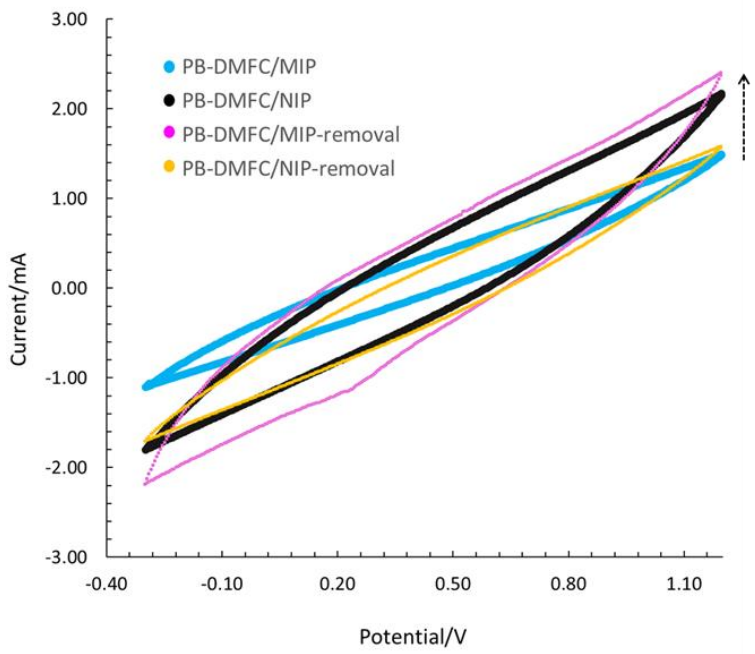

Figure 5.11- Cyclic voltammograms obtained in a 3-electrode system in a PBS buffer solution (10 cycles, −0.3 V to 1.2 V, 25 mV/s), for the assembly of the PEDOT/PPy sensing polymer on the anode layer of PB-DMFCs (MIP and NIP) and corresponding removal step in sulfuric acid solution.

Exceptional care was taken in the selection of the PB-DMFCs to ensure that they had similar electrical characteristics, despite the "handmade" process involving the various steps in the fabrication of the PB-DMFCs. The analysis of the obtained voltammograms shows that the presence of sarcosine in the PEDOT/PPy electropolymerization leads to a decrease in the electrical resistivity values over the whole applied voltage range. The presence of sarcosine seems to hinder the polymer formation in the anode surface PB-DMFC and its removal allows a significant increase in the electric current, while for the non-printed PB-DMFC /NIP the effect of removal is in the opposite direction; this decrease in PB-DMFC/NIP current could be due to over-oxidation of the PEDOT polymer layer in acidic media causing a decrease in the electrical conductivity [244,245]. Overall, the PB-DMFC/NIP samples allow us to evaluate the influence of the polymer layer on the PB-DMFC performance and also the nonspecific behaviour in sarcosine target binding.

5.3.3.2 Impact of the imprinted film in the PB-DMFC

The effect of modifying the anode side of the PB-DMFCs with the EDOT/PPy polymer was evaluated by recording and comparing the experimental polarization curves (sampled DC voltammetry technique) until the electrochemical system reached stable maximum potential (OCV) and power. Different paper fuel cell units with similar initial values (before modification) were used for the studies. The obtained results are shown in Figure 5.10-B. Analysis of the polarization curves (blank points) and power curves (filled points) of the two PB-DMFC units indicates that adding the EDOT/PPy polymer on the anode side causes the measured maximum OCV and generated current/power to decrease more significantly for the control (PB-DMFC/NIP). These results were expected since the polymer layer has a blocking effect on the Pt catalyst nanoparticles, which is more pronounced for the sample without voids (PB-DMFC/NIP) than for the PB-DMFC/Biosensor, which is in the middle range in terms of current and power. In terms of maximum power, the initial PB-DMFCs produce 22–25 $\mu A/cm^2$ until the PB-DMFC/ biosensor produces 16 $\mu A/cm^2$ and the control PB-DMFC/NIP produces only 8 $\mu A/cm^2$ after stabilization (successive polarization curves were followed for all systems until the signal deviation is less than 1%). Therefore, the effect of PEDOT/PPy is more pronounced for PB-DMFC/NIP because it does not have imprinted cavities in the polymer structure that only partially hinder the diffusion of methanol/water to the electrode surface. The different assemblies also show differences in OCV values, with PB-DMFC/NIP having the lower OCV value (0.35 V) compared to PB-DMFC/Biosensor (0.41 V) and the unmodified PBDMFC (0.43 V). Therefore, the time for stable and complete activation is longer for the PB-DMFC/NIP assembly than for PB-DMFC/Biosensor and the unmodified PB-DMFC. The PB-DMFC/NIP could not reach the same potential values due to the barrier effect of the PEDOT/PPy polymer.

In the EIS analysis (Figure 5.10-C), the same PB-DMFC was analysed before/after the polymerization protocol and after calibration. The equivalent electric circuits of these samples were shown in Figure 5.12. Analysis of the results shows an increase in ohmic resistance and charge transfer after the electropolymerization procedure. After calibration, the PB-DMFC with the sensing layer (PB-DMFC + MIP) shows an increase in ohmic resistance, which could be related to the presence of the sarcosine binding in the polymer cavities.

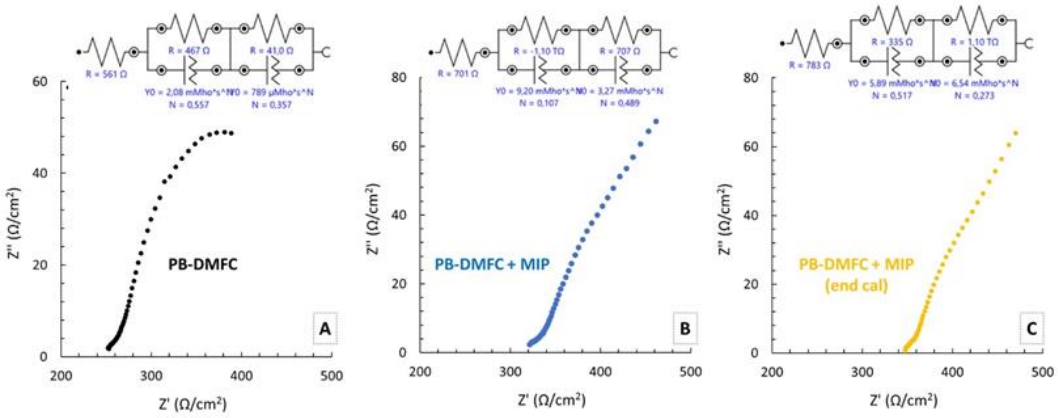

Figure 5.12- EIS data and equivalent electric circuits (inlet) of a PB-DMFC before polymerization protocol (A), after polymerization (B) and after calibration (C). Measurements conducted under open-circuit conditions (OCV) using 0.5 M methanol concentrations.

5.3.4 Calibrations of the PB-DMFC/biosensor

The various PB-DMFC/biosensor assemblies were activated by running multiple polarization curves until the systems reached maximum OCV and power levels (the number of polarization curves required for full activation depends on PB-DMFC and can range from 5 to 10 consecutive trials). After running a polarization curve, the PBDMFC/biosensor was washed with water, dried with N_2, and 100 µL of a 0.5 M methanol solution was added. This procedure was repeated continuously throughout the calibration experiment. Prior to calibration, stabilization was performed in the same background medium used to prepare the sarcosine standards by incubating the sensor surface sequentially with the same volume used to incubate the standards (200 µL). This procedure was repeated until stable electrical performance was achieved for both media. Two background media were used to prepare the sarcosine standards: MES Buffer and diluted healthy human urine. This stabilization procedure was essential to ensure that the measured electrical signal was due to the sarcosine interaction and not to the medium in which the standard solution was prepared. In the case of the medium containing healthy human urine, a dilution factor (10× and 100×) was previously investigated for its effects on signal stability and final performance of the PB-DMFCs assemblies. An example of the stabilization of the PB-DMFC /biosensor assemblies with MES buffer and human urine is shown in Figure 5.13 in the form of power curves, which show that the successive MES incubations cause little disturbance to the signal (Figure 5.13-A) compared to the urine incubations (Figure 5.13-B/C).

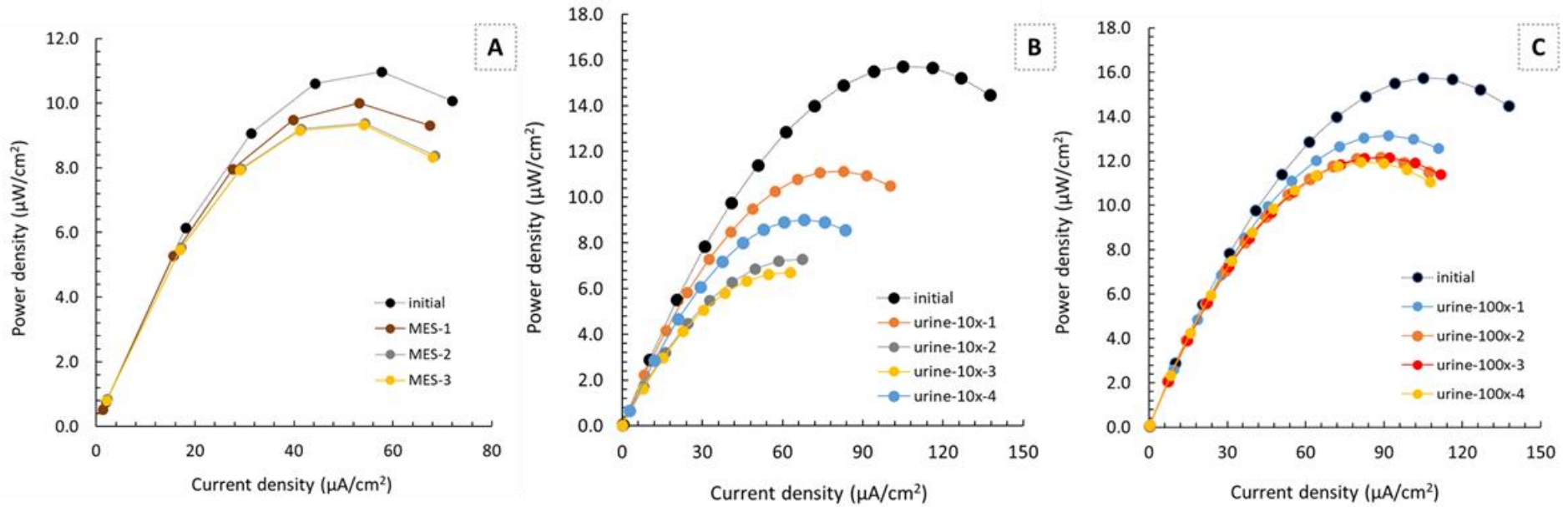

Figure 5.13- Power curves obtained in consecutive electrochemical readings using independent PB-DMFCs assemblies after stabilization and prior incubation with MES buffer (A), human urine 10x times diluted (B) and human urine 100x times diluted (C) using 0.5 M of MeOH solution for the readings.

Therefore, to obtain a smaller effect on the initial current of the PB-DMFC/biosensor, a 100-fold dilution was chosen for the urine calibrations.

After stabilizing the electrical signal of the PB-DMFC/biosensor in the appropriate media, successively increasing concentrations of sarcosine standard solutions in the range of [1.0×10^{-7} M – 1.0×10^{-3}] were incubated directly on the surface of the anode sensor, and the polarization curve was followed after incubation of each concentration (from the OCV potential to the predefined final potential of 0.1 V). It is important to highlight that the initial OCV potential of the polarization curve is not the same after each sarcosine standard incubation but decreases over the course of the calibration experiment as the sensor loses the ability to return to initial values when sarcosine is bound in the polymer cavities. The time required to reach a stable OCV potential must be determined at the beginning of the experiment and maintained until the end of the calibration (depending on PB-DMFC, t = 100 s is sufficient to reach a stable OCV value). The response of a methanol fuel cell biosensor is determined by the oxidation of methanol at the active sites of the Pt catalyst. The kinetics of this reaction is time-dependent and is favored by the fact that methanol is a small molecule that can easily penetrate through the polymer, depending on the contact time. The major advantage of this system over previously published systems [193,241] is that the methanol solution can be completely removed from the anode sensor region, ensuring that the system is in a similar "true steady state" for all measurements. Each sarcosine standard solution was left on the anode surface for 20 min and covered with a square glass to prevent evaporation and ensure efficient distribution of the sample over the entire sensor area. After this time, the PB-DMFC/biosensor was washed with ultrapure water, dried with nitrogen, and 100 µL of a 0.5 M MeOH solution was distributed on the anode side, followed by an electrochemical measurement (OCV stabilization + sampled DC voltammetry technique). This procedure was performed in parallel with a PB-DMFC/NIP to monitor the non-specific interactions of sarcosine in the non-imprinted polymer.

Several calibrations were performed to evaluate the standard analytical response of this hybrid paper biosensor. A typical plot of the performance curves obtained during a calibration is shown in Figure 5.14-A for buffer media, with the average calibration curves in Figure 5.14-B, for PB-DMFC/biosensor compared to the control (PB-DMFC/NIP). Figure 5.14-C shows a typical calibration obtained in diluted healthy human urine, with the corresponding average calibration curves in Figure 5.14-D. The calibration

curves correspond to the normalized maximum peak power calculated for each standard (power $_{standard}$/power$_{blank}$).

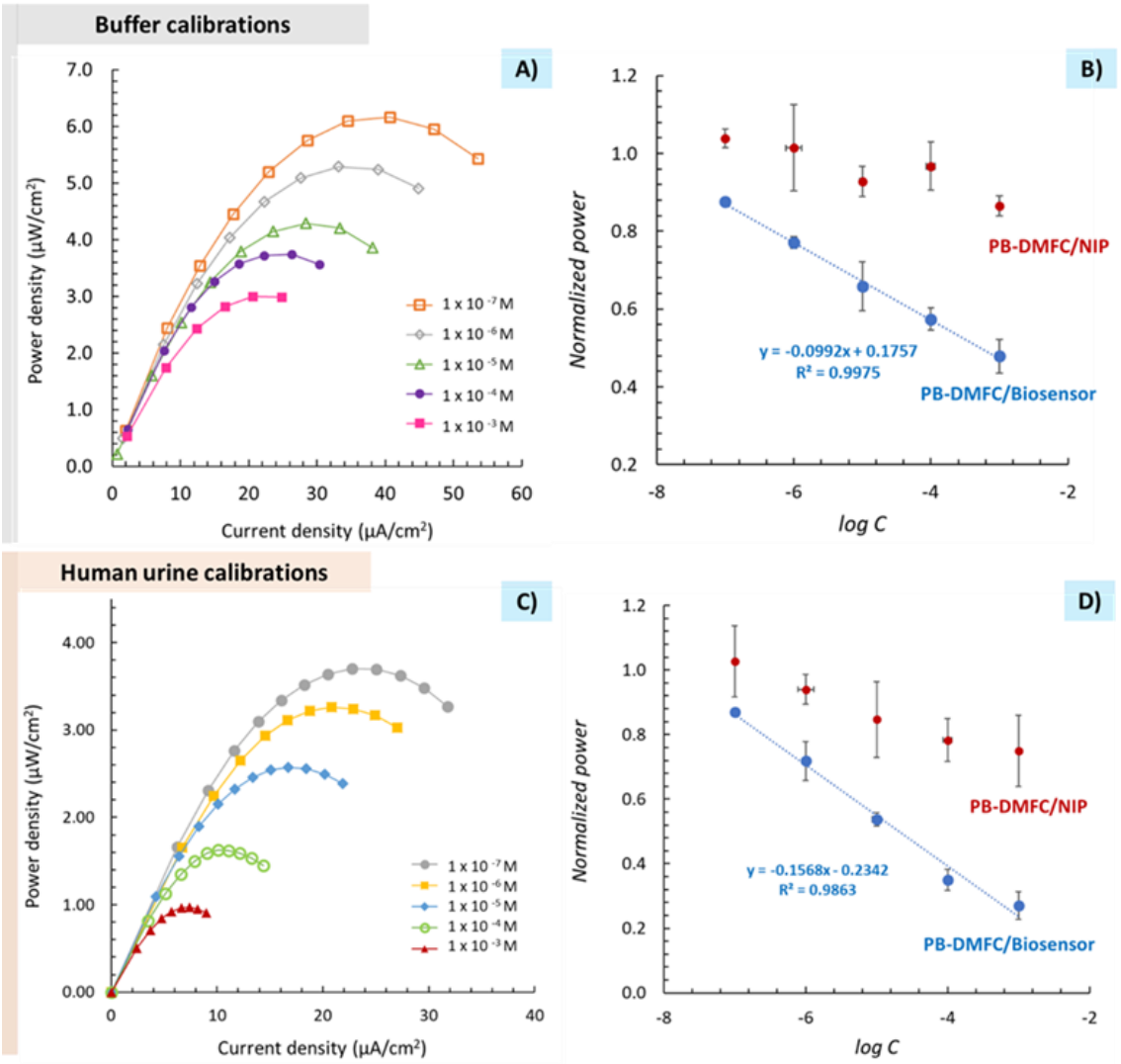

Figure 5.14-Power-current density curves obtained during calibration after incubation of sarcosine standards of increasing concentrations prepared in buffer (A), with the respective calibration curve compared with a control experiment (NIP) in the range $1.0 \times 10^{-7} - 1.0 \times 10^{-3}$ mol/L (B); Power-current density curves obtained during calibration with sarcosine standard solutions prepared in healthy human urine in the same concentration range used in buffer (C), with the respective calibration curve compared with the NIP sample (D). All calibration curves were traced using the average of the maximum power density obtained at each sarcosine concentration.

Analysis of the calibration results shows that the average power density decreases with successive concentrations of the sarcosine standards for both media studied, confirming that it is possible to transform the PB-DMFC activity into a PB-DMFC/biosensor with an operating mode dependent on the sarcosine concentration.

For calibrations performed in MES buffer media (Figure 5.14-A), the final PB-DMFC /biosensor output power decreases by ~ 50 % compared to the initial value after blank (background stabilization) experiments against the maximum sarcosine concentration, with a squared correlation coefficient of ~0.997. This variation was generally consistent between different calibrations performed in buffer when the PB-DMFCs assemblies have similar initial power values. The limit of detection (LOD) was 6.6×10^{-8} M calculated using the equation LOD = ($y_{blank}3SD_{blank}$)/Slope. Comparing the PB-DMFC/biosensor with the nonimprinted, PB-DMFC/NIP, a random response can be observed (Figure 5.14-B), indicating minor nonspecific interactions of sarcosine molecules.

In the calibrations with human urine (Figure 5.14-C), the final PB-DMFC/ biosensor output decreases by ~ 75% (compared with the initial value after stabilization of the blank) toward the maximum concentration of sarcosine with a squared correlation coefficient of ~0.986. These results demonstrate the good performance of this paper-based biosensor, which can maintain its sensitivity in more complex media such as human urine. Indeed, the results obtained in human urine are more meaningful in terms of impact on fuel cell performance, since the behavior of the PB-DMFC depends entirely on the sarcosine concentration, with a higher impact on the potential, current density, and performance. This behavior highlights that the developed PB-DMFC/biosensor is suitable to target the sarcosine molecule in real samples and can be used in a wide range of concentrations. Considering the non-specific interactions, some differences were observed in the performance curves obtained after the incubation of sarcosine in the non-imprinted anode (PB-DMFC/NIP) in this medium. However, the response can be considered negligible when compared to the response obtained for the PB-DMFC/ biosensor. Thus, this self-powered paper strip PB-DMFC /biosensor can be used for screening and monitoring sarcosine biomarkers without being limited to standard analytical laboratory methods. Common sarcosine oxidase assays can achieve a LOD of 1.18×10^{-6} mol/L with a linear range of $2.05–125.65 \times 10^{-6}$ mol/L. It is generally accepted that the diagnosis of prostate cancer is associated with elevated levels of

sarcosine in body fluids (even in early stages of the disease) [246]. Considering these findings, this autonomous paper platform may be a useful tool to detect abnormal sarcosine levels that may be associated with a prostate cancer diagnosis.

5.3.5 Selectivity studies

To evaluate and complete the selectivity of the designed PB-DMFC/ biosensor, selectivity assays were performed in buffer solutions against some common interfering compounds [urea (U), uric acid (UA), creatinine (C), glutamic acid (GA), and histidine (H)]. The assays were performed with different PB-DMFCs units, incubating a sarcosine standard solution (1.0×10^{-5} M) in a PB-DMFC/biosensor. In parallel, the same procedure was repeated with different PB-DMFC/biosensor units by incubating the same concentration of sarcosine with the respective interfering substance. Both PB-DMFC/biosensors were analysed by following their respective polarization curves. An example of one set of selectivity assays is shown in Figure 5.15-A with the corresponding interference analysis in Figure 5.15-B.

The data presented in Figure 5.15-A show that the different PB-DMFCs prepared in the same batch for performing the selectivity assays exhibit a consistent response to the detection of sarcosine, with little signal variation in the presence of interfering factors. These data confirm the high preference of this sensor for sarcosine with signal changes of 1–10%, in both positive and negative directions (Figure 5.15-B). Urea and uric acid are the interfering factors that cause the largest deviations from the sarcosine signal (10%), while the other interfering factors cause almost no signal change (~1%). The concentrations of all tested interfering factors are compatible with the average values found in real human urine samples, which can support the exceptional performance of this hybrid autonomous fuel cell paper strip.

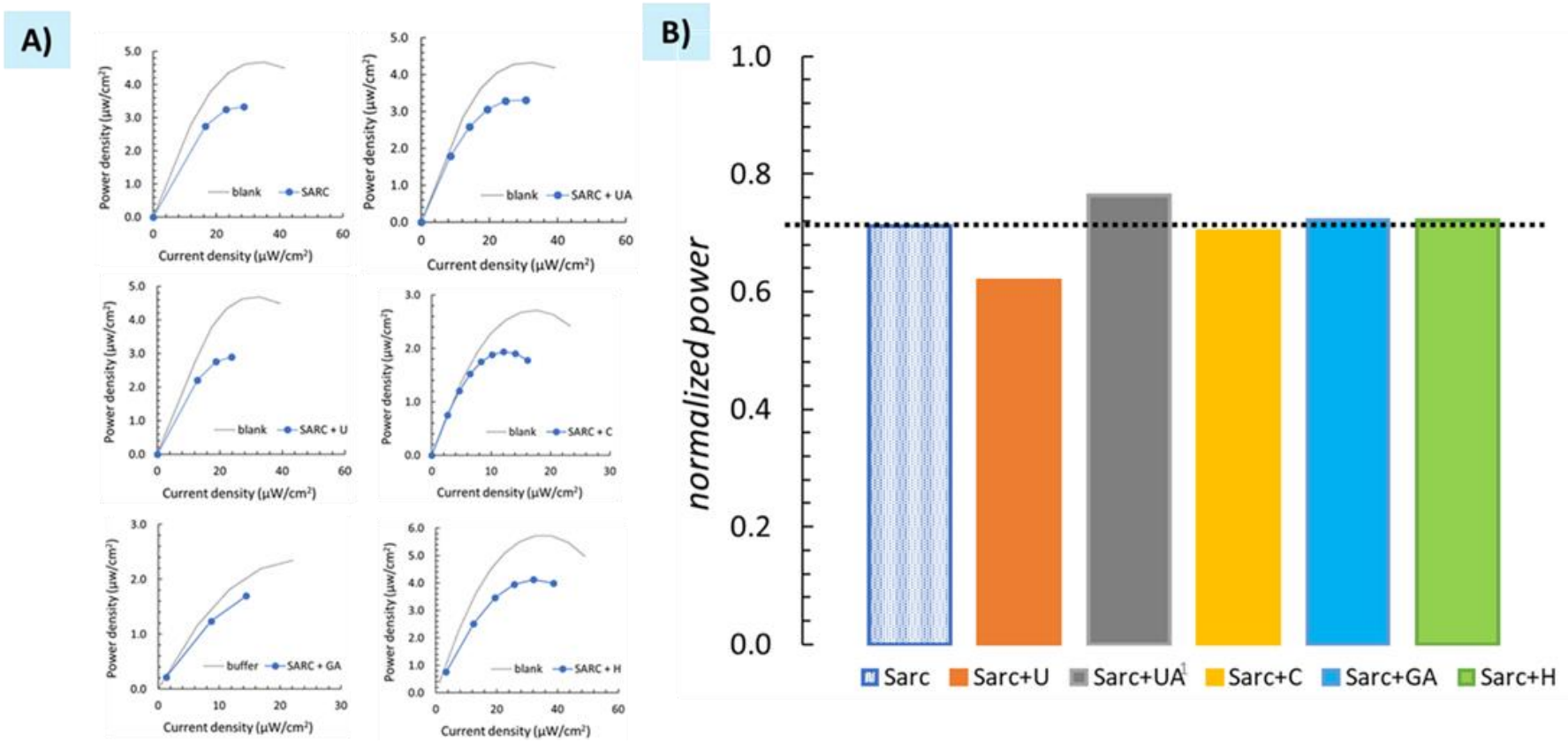

Figure 5.15- Selectivity assays in buffer using independent PB-DMFCs after incubation of a sarcosine standard solution (1.0×10^{-5} M) and sarcosine spiked with interfering compounds [urea (U), uric acid (UA), creatinine (C), glutamic acid and histidine (H)], recording of the respective power curves (A) and the respective interference analysis in normalized values (B).

5.4 Conclusions

The developed PB-DMFC/biosensor prototype showed promising results as a self-powered sensing platform for the detection of sarcosine in a hybrid approach combining the potential of a paper methanol fuel cell as an energy source with a MIP sensing element. The improvement in the response of the PB-DMFC/biosensor in real samples (human urine) confirms the high selectivity of the response of this array, which is also confirmed by the different selectivity assays performed. Overall, the presented PB-DMFC/biosensor can be considered as a promising and suitable instrument for point-of-care applications, capable of analysing sarcosine in a wide concentration range, even in complex real samples. The developed PB-DMFC/biosensor opens the doors to a novel strategy in the development of autonomous electrical biosensors by combining two powerful technologies (fuel cells and MIPs). Further improvements of the current prototype in terms of materials used (catalysts, carbon support, electrolyte, impermeabilization), fabrication process, and even different fuels can be explored, opening new opportunities for the expansion of self-powered electrochemical instruments as powerful tools in health diagnostics/monitoring.

Chapter 6

6. Portable and autonomous PEDOT modified flexible paper-based methanol fuel cell sensing platform applied to L1CAM recombinant protein detection

The results presented in this chapter are currently submitted as Liliana P.T. Carneiro, Alexandra M.F.R. Pinto, Dzmitry Ivanou, Adélio M. Mendes, M. Goreti F. Sales, *"Portable and autonomous PEDOT modified flexible paper-based methanol fuel cell sensing platform applied to L1CAM recombinant protein detection*", *accepted* to *Applied Polymer Materials.*

6.1 Introduction

Rapid and accurate quantification/monitoring of circulating biomarkers is an urgent need for point-of-care and/or point-of-use systems, where the combination of portable and flexible disposable electrochemical systems and biosensors is emerging as a promising alternative [247–249]. The growing interest in portable point-of-care sensing devices is supported by their advantageous features such as cost-effectiveness, compact structure, sensitive readings, and the possibility of online detection that allows real-time measurements of various biological entities [250]. Among the different types of biosensors, electrochemical-based systems emerge as the most promising technology that can meet all the requirements of flexible biosensors. This bioelectronic technology requires a recognition element, a transducer, and an energy source. It involves the interaction between the recognition element and the transducer being the generated signal directly related to the analyte concentration and later displayed via an output system [59,251].

Various materials and manufacturing techniques are used to produce portable and wearable electrochemical devices [252–254]. To improve the detectability and suitability of these devices, flexibility is a key factor in the fabrication of each component, including a flexible output display and flexible power sources [255,256]. Among the other substrates that can be used for the production of flexible and disposable biosensors, the paper seems to be the most promising as it is cheap , abundant, biodegradable, biocompatible, flexible, and can be easily modified [257,258]. The combination of paper-based substrates, conductive nanoinks, and electrochemical detection has recently emerged as a trend in the development of a larger number of bioelectronic devices with different setups, configurations, and detection modes [259,260]. The nanoinks for incorporation into bioelectronic sensors consists of three components: a conductive material, a binder, and a solvent [261,262] all can be produced biocompatible. Conductive materials typically include metallic nanoparticles (e.g., platinum, silver, copper) [263] and/or carbon structures (e.g. carbon black, carbon nanotubes, graphene) [264,265]; chemical modifiers, such as conductive polymers, can be also added to improve conductivity and performance of electrochemical sensors [266]. Apart from the large number of configurations developed so far, a lack of self-sufficient devices is still observed in the available electrochemical biosensors with simpler setups, so it is still

necessary to use a potentiostat to perform the measurements and track the response of the sensor.

In the work presented here, the requirement for an energy source was met by developing paper-based methanol fuel cells (PB-DMFCs) that can act simultaneously as a biosensor and energy source and integrate a signaling function, all in simple, flexible, lightweight, and user-friendly modified paper strips. Several methanol fuel cells have been built using a commercial Whatman paper as a substrate, which combines all fuel cell components in a single strip layer. A similar system PB-DMFC was recently published by the authors in a single cell mode prototype that integrates a biosensor for the detection of sarcosine with excellent sensitivity and selectivity results [267]. Thus, the power and voltage output of these PB-DMFCs/biosensors is quite low, which limits their implementation as a fully portable biosensor system. In this work, the power and output voltage of the PB-DMFCs were improved by developing a hybrid sensor anode electrode. The combination with the conductive PEDOT polymer and MWCNTS-COOH enables to obtain a system with higher stability, current, voltage and sensitivity to the target. This higher voltage and stability also enable the fabrication of a PEDOT/PB-DMFC/biosensor stack with sufficient potential to connect and trigger a PEDOT electrochemical cell. This cell was designed here to monitor the interaction of the recombinant protein (L1CAM) with the PEDOT/PB-DMFC/biosensor stack by color change. The L1CAM protein is a cell adhesion molecule originally identified in the neuronal system and currently associated with advanced stages of various cancers [47,48,50]. Overexpression of L1CAM in advanced tumor stages and metastases has been reported [53–55], and this association with cancer progression makes L1CAM an important target.

The combination of self-power/self-signal features in a methanol fuel cell paper strip system has never been described before. This concept was recently investigated using a stack of conventional passive methanol fuel cells, which have a complex mechanical structure, in combination with an inorganic electrochromic system of tungstate and tungsten oxide nanoparticles. In this work, a promising system for the detection of a small metabolite (sarcosine) was demonstrated using conventional assemblies and materials [268]. In the work presented here, the PEDOT/PB-DMFC/biosensor stack was connected to an organic electrochemical cell made of PEDOT:PSS, which was also developed on a single-layer paper strip, required no additional components, and was operated with a few microliters of an aqueous electrolyte

(lithium perchlorate 0.1 M). This PEDOT/PB-DMFC/biosensor- EC allows to obtain a completely flexible, innovative and portable paper-based fuel cell sensor platform with a very simple structure. This approach works like a conventional passive direct methanol fuel cell (DMFC), but with a simpler, more compact and miniaturized configuration that is more suitable for POC applications. Passive DMFCs are considered a promising and suitable technology for portable power generation, especially for small devices with low power requirements [269–271], such as the system presented here.

To the best knowledge of the authors, this is the first work to report on a hybrid paper-based methanol fuel cell system in a 5-stack configuration and in conjunction with a EC for visual display (PEDOT/PB-DMFC/biosensor- EC). The various properties of PEDOT as a conductive [272] and electrochromic material [273] have been explored in novel experimental setups suitable for fabricating medical fully wearable devices for POC use. This approach was optimized with particular attention to the composition of the anode sensor electrode, which consists of a novel PEDOT/carbon nanocomposite material that has not been previously described. The assembly was characterized for analytical performance against L1CAM using two different media (buffer and Cormay® serum). Operation of the system was tested in a single cell array connected to a potentiostat and in a 5-stack array using the EC display.

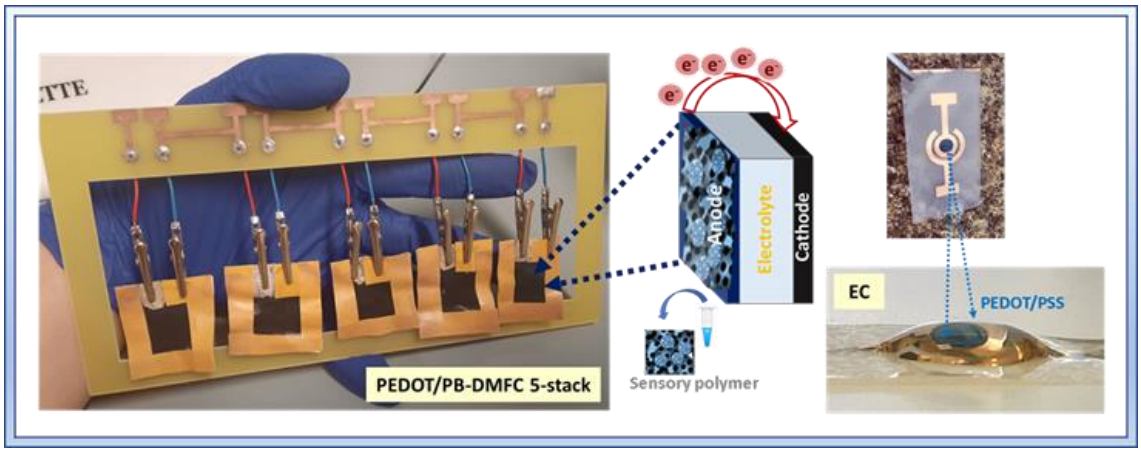

Figure 6.1 – PEDOT/PB-DMFC/biosensor strips assembled in a 5-stack configuration to produce a voltage of ~1.5 V, to allow the color change of the paper based PEDOT:PSS electrochromic cell.

6.2 Experimental and methods

6.2.1 Reagents and solutions

The reagents used in this work were of analytical grade and the water was an ultrapure Milli-Q. A solution of Nafion® [20 wt%, alcohol based (propanol/ethanol) Quintech] was applied to a ≈ 2.2 cm^2 square paper strip (Whatman grade 40 filter papers) and covered on both sides with carbon-based inks consisting of: Carbon Black with PtRu (40:20 wt%) catalyst (C/PtRu) on Vulcan XC-72R (Quintech) mixed with oxidized Multi Walled Carbon Nanotubes (MWCNT-COOH) (Sigma Aldrich) for the anode side, and Carbon Black with Pt (10 wt%) catalyst (C/Pt) on Vulcan XC-72R (Quintech) for the cathode side. The inks were prepared using 2-propanol (IPA) (99.8%, Panreac) as solvent and Nafion® (20 wt%.) as binder using a microtip ultrasonic system. A solution of 0.01 M EDOT (97%, Alfa Aesar) in IPA/H2O (4/1) was added to the anode ink and sonicated in ultrasonic bath for 60 s. Titanium (IV) oxide (anatase, Sigma Aldrich) was also added to the formulation for evaluating TiO_2 applicability as conductive component in ink. Different amounts of MWCNT-COOH were also tested in the ink formulation.

A paraffin solution (Sigma Aldrich) was diluted in 2-propanol (50/50) and applied around the active area of the PB-DMFC assembly (on both sides of the paper). It hydrophobizes and strengthens the paper substrate. Conductive silver ink (RS Pro) was applied to the top edges for electrical connection (each side with an independent terminal, insulated with tape on the non-electrical side to avoid short circuits). Two buffer media were used in this work: 10 mM MES buffer (pH 6.0) obtained by dissolving 2-morpholinoethanesulfonic acid buffer (AppliChem) and PBS buffer with (pH 7.2) obtained by dissolving phosphate-buffered saline (Amresco). A recombinant human L1CAM protein (His-tag) (MyBiosource) stock solution was prepared by diluting the commercial reagent in buffer; less concentrated standards were prepared by accurately diluting the stock solution in the range of $1.0 \times 10^{-12} – 1.0 \times 10^{-8}$ M.

The polymerization solution consisted of 0.01 M EDOT (97%, Alfa Aesar) prepared in PBS (25 mL solution for each electrode), and L1CAM protein was used as a template during polymerization. Template removal was performed electrochemically in 0.5 M H_2SO_4 (Sigma Aldrich). Electrochemical measurements were performed using an aqueous methanol solution (Honeywell) of 0.5 M for calibrations and 1.0 M for initial stabilization of the fuel cell. A pretreated human serum (Cormay® HN, PZ Cormay S.A) was used for

the selectivity studies. The pretreatment consisted of adding silver nitrate ($AgNO_3$, 0.1 M) to the pure serum, to reduce the effect of chloride ions (0.1 M Cl^-). In this procedure, 10 mg of $AgNO_3$ was added to 1 mL of pure serum and left in a stir plate for 30 min. The mixture was then centrifugated at 10 000 rpm for 10 min, and a solid white precipitate (AgCl) was deposited at the bottom of the flask (Figure 6.2). This treated serum was 100x diluted in MES buffer and spiked with selected target concentrations. This medium was spiked with the same biomarker concentrations that were prepared in the buffer.

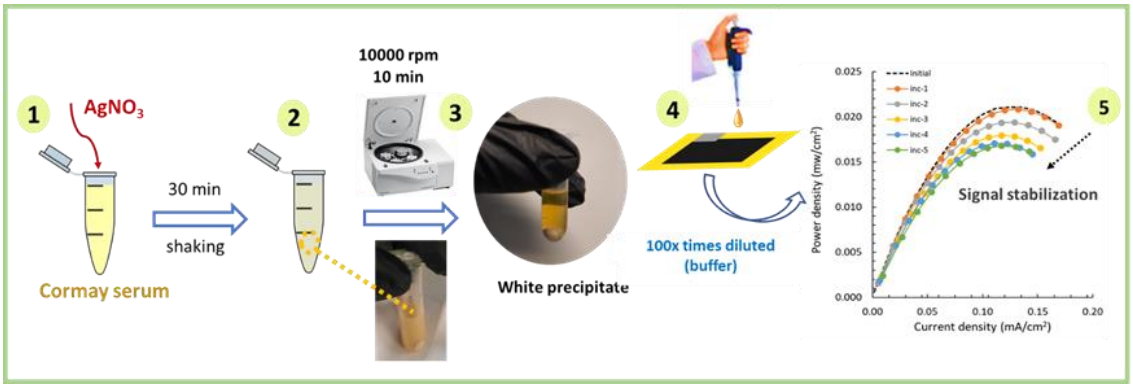

Figure 6.2 – Pre-treatment steps of the human serum (Cormay®) for L1CAM standards preparation: (1) – add $AgNO_3$ to the pure Cormay serum; (2)- stir in a stirring plate for 30 minutes until a yellow/white turve solution is formed; (3) – centrifugation at 10000 rpm during 10 minutes until the solution appears light yellow with a white precipitate in the bottom of the flask, indicating the removing of the chloride ions present in the initial serum; (0.1 M of Cl^- present in the initial serum) (4) – Cormay serum pre-treated is compatible for incubation in the anode side of the PEDOT/PB-DMFC with a 100x MES buffer dilution; (5)- example of a stabilization protocol using the diluted pre-treated serum in a PEDOT/PB-DMFC assembly containing the MIP sensor, evidencing a stable system after 4/5 incubations.

For the selectivity tests, L1CAM standard solutions were prepared in the presence of interfering species. These were carcinoembryonic antigen CEA (30 ng/mL), D-glucose (1.2 mg/mL; Alfa Aesar), and urea (1 mg/mL; Fagron) prepared in the buffer.

The paper-supported EC was developed on top of baking paper, modified with polydimethylsiloxane (PDMS commercial kit SYLGARDTM). After curing the PDMS, a promotor for gold adhesion, 3-Mercaptopropylmethyldimethoxysilane, MPTMS (Sigma Aldrich), was spin-coated on the surface of the paper/PDMS. A commercial dispersion of poly(2,3-dihydrothieno-1,4-dioxin)-poly(styrenesulfonate) (PEDOT:PSS)

(Sigma Aldrich) was diluted in dimethyl sulfoxide (DMSO, 95/5(%)) and spread in the middle ring of the EC. 0.1 M solution of lithium perchlorate (Sigma Aldrich®) was used as the electrolyte in the EC paper device.

6.2.2 Equipment and apparatus

Electrochemical measurements were performed at lab-ambient conditions (21±2 ºC) using a Methrom Autolab potentiostat/galvanostat with a PGSTAT302N, controlled by Nova software (NOVA 2.1). The electrochemical characterization and performance evaluation of the different PEDOT/PB-DMFCs were assessed using Sampled DC technique in the form of polarization curves, until OCV, current and power stabilization (single cell assembly). First, the PEDOT/PB-DMFC devices were activated by running several polarization curves using 1 M MeOH solution; polarization cycles were applied until a stable response of the cell (deviation of the obtained power $\leq$ 1%). A solution of 0.5 M MeOH was used for the calibration procedures. After each measurement, the PEDOT/PB-DMFC was washed with ultrapure water and dried with nitrogen to remove the unreacted methanol solution. Electrochemical impedance spectroscopy (EIS) was used to evaluate the electrical resistance of the PEDOT/carbon matrix/catalyst interface in OCV mode.

All electrochemical measurements recorded in the different experiments were normalized with respect to the area of the electrodes (2.2 cm^2). To follow and compare the electrochemical behaviour of the PEDOT/PB-DMFC assemblies, the maximum peak power was calculated. The calculated power values were normalized by the corresponding blank signal ($power_{sample}/power_{blank}$) to allow a better comparison between the different calibration experiments.

The anode and cathode nanoinks were performed using a Sonic Dismembrator (Fisherbrand™), with an operation frequency of 20 KHz, coupled to a 3 mm microtip.

The PEDOT/PB-DMFC, PEDOT/PB-DMFC/MIP, and PEDOT/PB-DMFC/NIP anode layers were characterized by Raman spectroscopy, with a Thermo Scientific DXR Raman spectroscope equipped with a confocal microscope. Spectra were recorded with a 532 nm excitation laser in the range of 50 to 3500 cm^{-1} at a power of 7 mW with a 50× objective. The confocal aperture was set to 50 μm pinhole. The ultrasonically polymerized PEDOT/CB-PtRu powder was analysed with FTIR/ATR spectra in a Thermo Scientific iS10 in the range of 550 to 4000 cm^{-1} with a germanium (Ge) crystal at 250 scans. For

comparison, spectra of the unmodified commercial CB-PtRu and EDOT monomer were also analysed (all solid samples were first dried in an oven at 37 ˚C before reading). Thermogravimetric analysis (TG) was used to follow the different steps of the anode ink nanocomposite formulation, in an inert atmosphere (nitrogen, 20 mL min^{-1}, heating rate 10 °C/min, from 30 to 800 ˚C), using a Hitachi (TG/DTA7200) instrument. The morphology of the PEDOT/PB-DMFCs was studied using a scanning electron microscope (SEM) with cross-section and microstructure analysis.

6.2.3 PEDOT Paper Based Fuel Cell (PEDOT/PB-DMFC) assembly

The paper-based PEDOT fuel cell platform (PEDOT/PB-DMFC) developed here was based on a first simple assembly published prototype [267]. The innovative idea of this study implies busting significantly the output power of the fuel cell by combining it with conductive materials such as conductive polymers or other conductive materials such as carbon nanotubes (MWCNTs) or titanium (IV) oxide (TiO2) nanoparticles. In the first developed assembly [267] a layer of a paraffin solution diluted in IPA (10%) was applied to the anode electrode to hydrophobized the surface and reduce methanol crossover, which is not the ideal solution because it is an insulating compound that affects the final performance of the paper fuel cell platform. The development of this improved PEDOT/PB-DMFC involves several steps, including the incorporation of the electrolyte, the preparation and deposition of the anode/cathode electrodes, the impermeability of the surrounding paper region, and the integration of the electrical connections (Figure 6.3). A general scheme for the fabrication of anode and cathode inks under ultrasonically-initiated polymerization is presented in Figure 6.4-A. It is known that carbon materials (carbon black, carbon nanotubes) have free radicals in their structure [274] which under the high frequency ultrasound initiate the polymerization of EDOT monomer [275–277]; nanocomposite is formed in a simple and fast way (60 s).

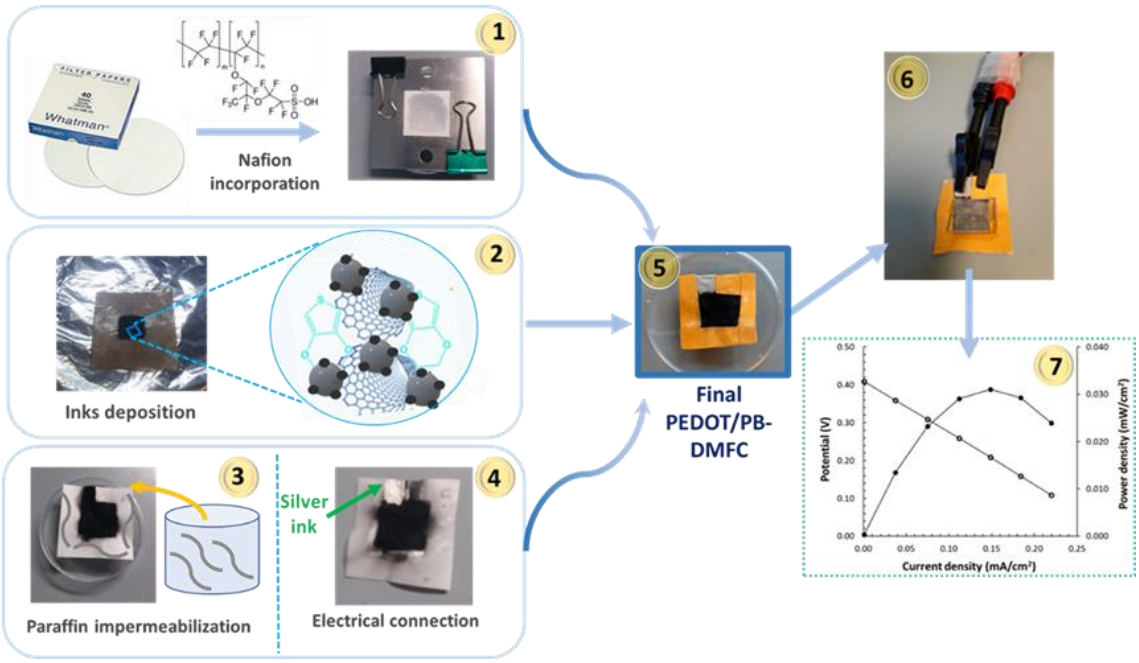

Figure 6.3 – Steps in the PEDOT/PB-DMFC development. (1) – the Nafion® electrolyte incorporation in the Whatman paper, (2) inks deposition (anode/cathode) in both sides of the electrolyte, (3) paraffin impermeabilization in the surrounding area of the electrodes (50/50 paraffin/IPA), and (4) electrical connector's integration on the top edges with silver ink.; (5) this final assembly is isolated with glue tape to avoid leaking of the methanol solution and avoid short circuit; (6) the final PEDOT/PB-DMFC operates with a solution of methanol (0.5 M – 1 M) which is adsorbed in a square of adsorbent paper and with the cathode exposed to Air; (7) a typical polarization and power curves after signal activation and stabilization; PEDOT/PB-DMFC contains a MIP sensor for L1CAM detection.

Interestingly, the presence of Nafion® in the ink formulation can also trigger the polymerization of EDOT when exposed to the ultrasound treatment (Figure 6.4-B). Using two different substrates (Whatman paper and FTO glass), a few microliters of two EDOT solutions (0.01 M) were poured into drops: EDOT/IPA/Nafion® and EDOT/IPA (in the absence of carbon materials and sonicated at the same time and frequency as the ink containing the carbon materials). When analyzing the results, the formation of blue color in the sonicated solution with the Nafion® compound is observed for both substrates, both at room temperature and on a hot plate at 60 ˚C (the coloration becomes more intense with temperature).

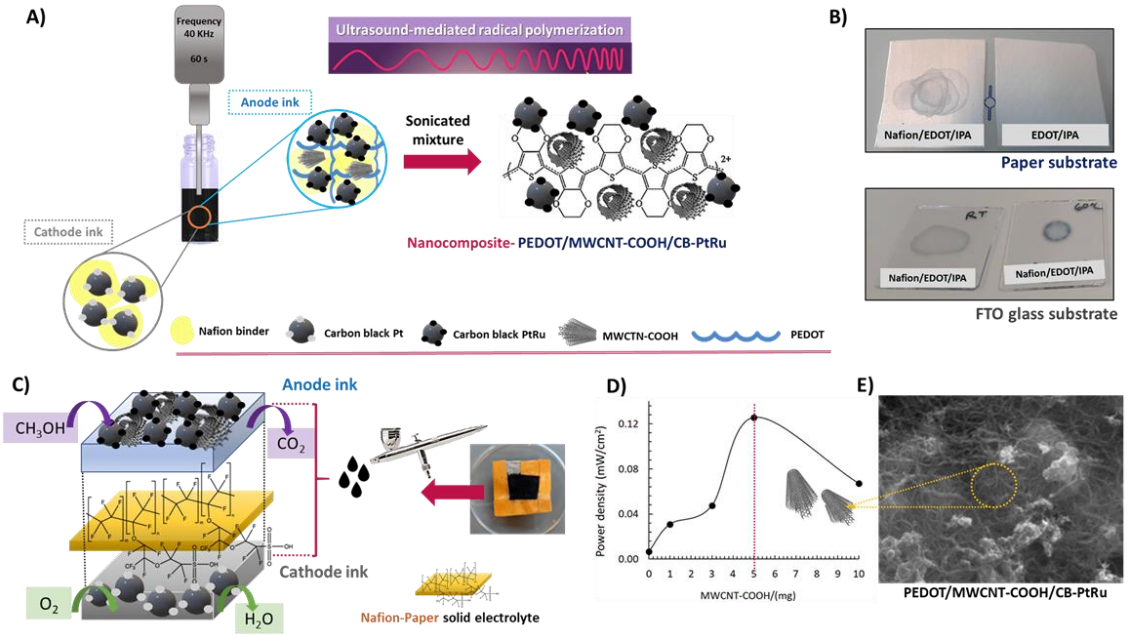

Figure 6.4 - Schematic representation of the preparation of the anode/cathode inks for the PB-DMFC assembly using a ultrasound with microtip: the anode ink is composed by a mediated ultrasound synthetized nanocomposite of PEDOT/MWCNT-COOH/CB-PtRu dispersed in IPA in the presence of Nafion®, and the cathode ink is obtained by ultrasonication of a solution of CB-Pt, Nafion® and IPA(A). Polymerization tests using two different substrates (Whatman paper and FTO glass) to drop-cast two ultrasonicated solutions: Nafion®/EDOT/IPA and EDOT/IPA, evidencing the formation of a blue color in the sonicated solution containing Nafion® compound, both at room temperature and at 60 ˚C (with temperature the coloration was more intense) In the absence of Nafion® no coloration was observed in any substrate (at least in the 30 min of the experience duration) (B). General scheme of a typical PB-DMFC evidencing the Whatman paper impregnated with the Nafion® electrolyte, which separates the anode and cathode, applied in both sides of Whatman/Nafion® electrolyte using the airbrush method (C). Maximum power density recorded using different PB-DMFCs assemblies in relation to the amount of MWCNTs (0-10 mg) in the ink formulation (D); Top-view SEM image of PB-DMFC with PEDOT/MWCNT-COOH/CB-PtRu composite (E).

In the absence of Nafion® in solution, no coloration was observed for any of the substrates (at least during the 30 minutes of the experimental period), so in addition to the initiation of EDOT polymerization by the free radicals in the carbon materials, a contribution from Nafion® was also observed. Indeed, this observation makes sense since PEDOT:PSS was stabilized by the sulfonic groups present in the PSS polymer through charge balance [278]. The Nafion® also contains sulfonic groups in its structure, which may increase the affinity of these two compounds in the solution [279]. Therefore, this

interaction alone is not beneficial for the best performance of the developed PEDOT/PB-DMFCs because the EDOT/Nafion® interaction and/or Nafion® degradation hinders the good functioning of the fuel cell system. The Nafion® solution added to the inks has a dual function in fuel cell devices (conventional fuel cells or this particular paper fuel cell): it serves as a binder and also as a proton conductor [280]. Modification of the Nafion® by ultrasound or by interaction with EDOT affects the proton conductivity of the anode, resulting in low power fuel cells that are very difficult to activate (Table 6.1). To avoid this problem, the Nafion® solution was added to the anode ink after sonication of all components and sonicated for only 10 seconds to prevent interaction with the unpolymerized EDOT. For the cathode ink, a mixture of CB -Pt, Nafion® and IPA was sonicated, mixing all components simultaneously without affecting the fuel cell performance.

Both the anode and cathode inks were airbrushed onto Whatman paper modified with Nafion® electrolyte to separate the anode and cathode electrodes. A general schematic to better understand the experimental setup and the chemical reactions taking place is shown in Figure 6.4-C. During preparation of the anode ink, gelation occurs due to the presence of EDOT in the ink; EDOT polymerizes under ultrasonic impact. Therefore, a volume of 300 µL of IPA was added before printing the anode ink to reduce the viscosity of the ink and prevent clogging of the airbrush. The cathode ink was painted on the other side of the Whatman/Nafion® directly from the ultrasonic device (without IPA dilution). Apart from the precautions taken in the preparation of the anode ink, an increase in hydrophobicity was observed in the anode electrode, limiting the spread of methanol on the surface of the electrode and thus the adsorption of methanol molecules on the Pt catalyst. To address this issue, the integration of "spacers" into the ink formulation was investigated, testing TiO_2 nanoparticles and MWCNTs-COOH.

Table 6.1- Summary of the electrochemical characterization of the different PB-DMFCs assemblies produced in this work and comparison with prototype 1.

PB-DMFC	OCV (V)	$Power_{Max}$(µW/cm^2)	Ohmic resistance (Ω)	Hydrophobic element	Activation	Stability
PB-DMFC-[267]	0.49	22.9	355	Paraffin layer	faster	good
PB-DMFC/PTFE-1	0.46	23.8	900	PTFE layer (50 µL)	fast	good
PB-DMFC/PTFE-2	0.38	18.5	360	PTFE layer (25 µL)	fast	good
PB-DMFC/PEDOT-1	0.44	18.7	1300	PEDOT layer (chrono)	moderate	good
PB-DMFC/PEDOT-2	0.47	28.3	450	PEDOT layer (CV)	moderate	good
PB-DMFC/PEDOT-3	0.40	11.8	480	Nano-ink (CB-PtRu+ PEDOT + Nafion®) + CV (PBS)	moderate	good
PB-DMFC/PEDOT-4	0.35	4.60	1550	*Nano-ink (CB-PtRu + EDOT 0.02 M + IPA + H_2O)	slow	moderate
PB-DMFC/PEDOT-5	0.38	8.50	500	Nano-ink 4* - 2x diluted in IPA	slow	moderate
PB-DMFC/PEDOT-6	0.48	23.4	190	Nano-ink 4* - 3x diluted in IPA and Nafion® added after sonication (10 s)	slow	moderate
PB-DMFC/PEDOT-7	0.42	16.5	570	PEDOT layer on anode surface (100 µL in H_2O)	slow	moderate
PB-DMFC/PEDOT-8	0.28	12.4	710	PEDOT layer on anode and cathode surface (100 µL in H2O)	moderate	moderate
PB-DMFC/PEDOT-9	0.41	29.9	165	Nano-ink 4* - 2x diluted in IPA + 5 mg Tio_2	moderate	moderate
PB-DMFC/PEDOT-10	0.38	12.0	420	Nano-ink 4* - 2x diluted in IPA + 10 mg Tio_2	moderate	moderate
PB-DMFC/PEDOT-11	0.40	67.1	95	Nano-ink 4* - 2x diluted in IPA + 10 mg MWCNTs-COOH	fast	good
PB-DMFC/PEDOT-12	0.41	125.7	75	Nano-ink 4* - 2x diluted in IPA + 5 mg MWCNTs-COOH	fast	good
PB-DMFC/PEDOT-13	0.40	31.0	280	Nano-ink 4* - 2x diluted in IPA + 1 mg MWCNTs-COOH	fast	good

The best results in terms of generated power of PEDOT/PB-DMFCs were obtained with the integration of 5 mg of MWCNTs-COOH into the ink formulation, comparing the power density output in a range of (0-10 mg) integration of this nanomaterial into the anode inks (Figure 6.4-D). In a SEM image topography, it is clear that the nanotubes are uniformly distributed on the surface of the anode electrode and act as "spacers" to help limit the interaction between EDOT-Pt and Nafion® and improve the conductivity of the system (Figure 6.4-E). The results of these tests are summarized in Table 6.1 and discussed in section 6.3.1.

6.2.4 PEDOT biosensor element preparation

The biosensor for L1CAM detection was anchored to the top of the anode electrode of the PEDOT/PB-DMFC assembly using a 3-electrode system to perform electropolymerization of a solution of EDOT (0.01 M) in PBS buffer (previously rinsed with N_2). The electropolymerization protocol should be performed immediately after the preparation of PEDOT/PB-DMFC to allow any free EDOT present on the anode surface to react with the polymerizing EDOT. This process results in a stable system where methanol crossover is controlled, eliminating the need of a paraffin layer [267]. This developed biosensor was made of PEDOT polymer, which comprises functions of a semiconductor, hydrophobic agent, and biorecognition element.

The first step of biosensor element preparation is incubation of L1CAM (1.0×10^{-7} M) in the freshly prepared anode for t = 2h. Then, the PEDOT/PB-DMFC was carefully washed with ultrapure water, dried with N_2, and incorporated into the 3-electrode system. Electropolymerization was performed by applying 5-10 cycles of electrode potential sweep (50 mV/s) from -0.3 V to 1.2 V and back to -0.3 V as sweep rate of 50 mV/s. The same CV protocol was used to remove the L1CAM template, but instead of EDOT solution, a 0.5 M H_2SO_4 solution was used, resulting in PEDOT/PB-DMFC/MIP with binding sites for L1CAM rebinding. In parallel, a non-imprinted PEDOT/PB-DMFC/NIP was developed using the same conditions and steps, except for the incubation of the L1CAM template. The polymer layer obtained by electropolymerization is porous and requries more time for the methanol to reach the Pt catalyst. Therefore, the polymer-modified MIP and NIP samples need more time for activation and stabilization. In addition, the PEDOT/PB-DMFCs modified with the MIP and NIP were not reusable after

calibration. The original current density was not retained; the electrodes were discarded at the end of each calibration.

6.2.5 Electrochromic cell (EC) preparation

The paper substrate EC was developed on a translucid baking paper selected for its suitable properties, such as homogeneity, light transparency and flexibility. The steps for the proper modification of the paper substrate are schematically shown in Figure 6.5.

Paper strips (5 cm × 5 cm) were PDMS covered by spin coating (1500 rpm, 60 s) of PDMS precursor solution and leaving in an oven at 60 ◦C for 1 h to cure the polymer (Figure 6.5-A). The PDMS provides a hydrophobic layer (Figure 6.5-B) which later supports the electrical connections and electrochromic material. After PDMS curing, the gold adhesion promoter (MPTMS) was spin-coated in the surface of the paper/PDMS (50 µL, spin coating: 800 rpm, 30 s) and the final paper/PDMS/MPTMS was dried at room temperature for 24 h (Figure 6.5-C). Metallic contacts were deposited by sputtering ca. 120 nm gold layer throughout a glass mask attached to the paper (Figure 6.5-D). After gold deposition, plasma treatment (2 min) was performed (Figure 6.5-E), to reduce the hydrophobicity of the surface, and a few microliters of a PEDOT:PSS dispersion diluted in dimethyl sulfoxide (DMSO,95/5(%)) was dispersed into the middle ring of the EC. Finally, the ECs were dried on a hot plate at 120 ◦C for 15 min and stored in a dark environment at room temperature before use.

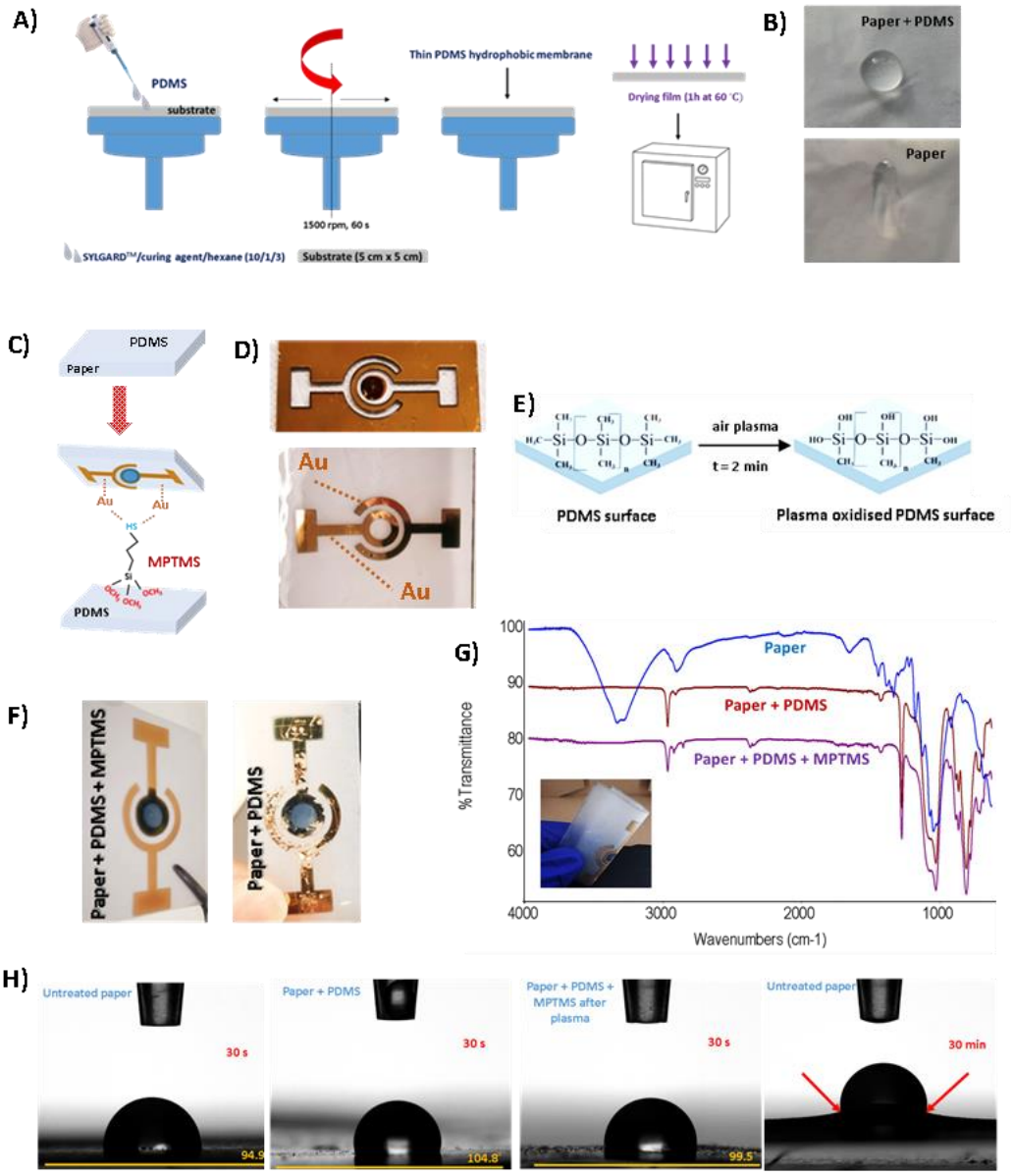

Figure 6.5 - Schematic representation of the steps for EC device preparation and its characterization. The steps involved consist: of PDMS spreading in the paper surface by spin coating (1500 rpm, 60 s) and curing at 60 ˚C (A) to obtain a hydrophobic paper/PDMS compared to the untreated paper (B). Adhesion promotor (MPTMS) anchoring in the paper/PDMS to improve binding of gold and PEDOT/PSS (C); gold electrical connections obtained after sputtering using a glass mask (D); a plasma treatment (inclusion of hydroxide groups) was applied in the EC surface to decrease hydrophobicity of the support, essential to bind PEDOT/PSS electrochromic compound (E). Differences observed in the presence and absence of MPTMS, after an electrochemical reading in terms of gold adhesion (F). FTIR-ATR analysis was used to follow the chemical modifications observed in the untreated paper, paper + PDMS, and paper + PDMS + MPTMS (G). Contact angle determination was also used to follow the water wettability and stability of the untreated paper and modified treated papers (H).

6.2.6 Electrochemical and electrochromic assays

The electrochemical performance of the PEDOT/PB-DMFCs was evaluated using the typical polarization curves used to characterize fuel cell systems (obtained by Sampled DC technique).

Calibrations of the PEDOT/PB-DMFCs/biosensor and the PEDOT/PB-DMFCs/NIP were performed by incubating L1CAM standard solutions in the range of 1.0×10^{-12} – 1.0×10^{-8} M in MES buffer. Prior to this, blank stabilization was performed by incubating the MES buffer on the modified anode until electrical signal stabilization was reached. During calibration, each solution (100 µL) was incubated on the anode surface for 20 minutes, starting with the lowest concentration. The system was covered with a glass square to efficiently distribute the solution over the entire active area and avoid evaporation. After each incubation and electrochemical measurement, the anode sensor area was carefully washed with ultrapure water and dried with nitrogen. This procedure was repeated for increasing L1CAM concentration standards prepared in MES buffer and diluted Cormay® serum (100 ×) to evaluate the ability of the PEDOT/PB-DMFC/biosensor to discriminate L1CAM. For the selectivity assays, 1.0×10^{-10} M L1CAM concentration was selected and incubated directly in the PEDOT/PB-DMFCs/MIP and the signal was measured. The same L1CAM concentration was doped with the different selected interferents and later incubated in the sensor area using different PEDOT/PB-DMFC assemblies (L1CAM standard + interferent for PEDOT/PB-DMFC/biosensor unit).

Calibrations with the hybrid PEDOT/PB-DMFC/biosensor-stack connected to the EC were performed in buffer after the hybrid stack stabilized to the maximum voltage (≈1.5 V). The anode region of the different PEDOT/PB-DMFCs electrically connected to each other was incubated with the same concentration standards of L1CAM used in the single-cell calibrations. After washing the sensing anode with ultrapure water, methanol was added to the fuel cells anodes. After 5 minutes of stabilization, a 48 Mp smartphone camera (Samsung) was used to take a photo of the EC center ring and the color coordinates of these images were analyzed using ImageJ software (blue coordinate selection).

6.3 Results and discussion

6.3.1 PEDOT/PB-DMFC device

6.3.1.1 Set-up assembly configuration and characterization

The PEDOT/PB-DMFC developed herein involves an innovative anode nanoink formulation which was modified by a nanocomposite containing MWCNTs-COOH and EDOT obtained in situ by a ultrasonic process. Figure 6.3, schematically shows the different steps for preparing the PB-DMFCs in this work. The focus in this part of the work is on the development of a suitable nanoink to modify the anode to obtain an assembly able to deliver a higher power density. The improvement in power density is related to the requirement of connecting the fuel cell stack to a signalling platform to get a fully portable, self-powered, and self-signalling paper-based device. The composition of the anode ink was selected as a target for improvement because it has the important function of hosting the biosensor element on its surface. Prototypes made from different formulations of the anode ink were tested to find the best combination that would provide PB-DMFC with higher electrical performance, stability, and ease of application by brush painting. The results are displayed in Table 6.1 and the polarization/power curves are shown in Figure 6.6 A-D.

Various attempts have been made to improve the electrochemical parameters (OCV, maximum power/current density, ohmic resistance) by combining hydrophobic compounds (polytetrafluoroethylene, PTFE) and conductive polymers (PEDOT). When applying a layer of the hydrophobic agent PTFE, the electrochemical parameters are similar to those obtained when using paraffin (Figure 6.6-A).

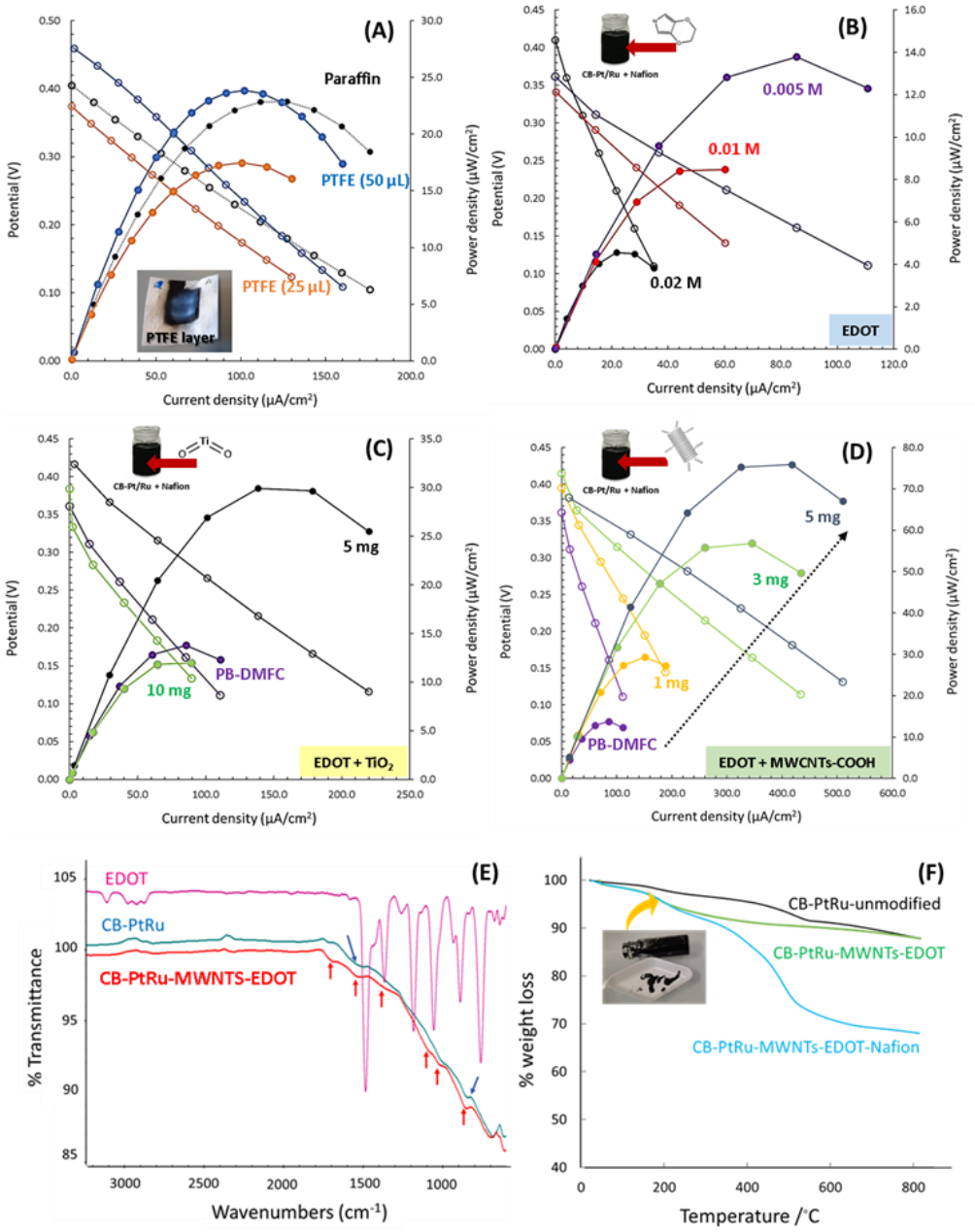

Figure 6.6 - Electrochemical data of PB-DMFCs in terms of polarization (empty symbols) and power curves (full symbols) obtained with different (nano)-ink formulations combining: hydrophobic components- layer of paraffin and PTFE (A) and the EDOT monomer in the ink formulations before applying ultrasonication in different concentrations of EDOT (B), doped with different amounts of TiO_2 (C) and doped with different amounts of MWCNTs-COOH (D); Characterization results by FTIR-ATR of the PEDOT-CB-PtRu powder nanocomposite obtained by ultrasonication in comparison with EDOT monomer and commercial CB-PtRu powder (E). Thermogravimetric analysis of the different steps involved in the anode nanoink preparation: commercial CB-PtRu powder (unmodified), CB-PtRu-MWNTs-EDOT ultrasonicated in IPA until gelification of the sample (30 s), and CB-PtRu-MWNTs-EDOT-Nafion® upon ultrasonication during 15s (F).

These results were expected since PTFE contributes to surface hydrophobicity, but its insulating properties are negatively reflected in the final performance of the system. Although the use of PTFE in the regular PEM fuel cell inks seems to be promising [281], in this PB-DMFC system the combination with hydrophobic insulating compounds was not the best choice.

Several configurations with conductive PEDOT polymer were tested. Conductive layers obtained by *in-situ* electropolymerization or by preparing different PEDOT-based nanoinks. The developed PB-DMFC/PEDOT-1,2 modified by conductive layers obtained by in situ electropolymerization did not show higher improvements in terms of OCV, power output and stability. As observed during the development of the biosensor layer, the PEDOT film on the anode electrode seems to block some platinum nanoparticles; methanol oxidation is delayed. When the EDOT monomer was added directly to the nanoink formulation, opposite behavior was observed. The presence of EDOT in the ink formulation leads to PB-DMFCs with poor electrochemical performance and very difficult to activate (Figure 6.6-B). This result seems to be confusing when compared with the previously obtained ones. The analysis of all parameters and fuel cell behaviour shows that the hydrophobicity of the EDOT monomer and the interaction with the sulfone groups of the Nafion® binder affect the MeOH oxidation and proton conductivity, respectively. These interactions have also been confirmed in other studies [282]. To compensate these undesirable interactions, two dopants (TiO_2, MWCNTs-COOH) were selected and added to the nanoink formulations. The idea of these dopants is to act as spacers and prevent the undesirable interactions that affect the electrochemical performance of the anode. With the combination of 5 mg TiO_2, a considerable improvement in the electrochemical parameters is observed compared to the first PB-DMFC prototype, but a larger difference is observed compared to the ink without TiO_2 dopant (Figure 6.6-C). When 5 mg of MWCNTs-COOH was added to the ink, a huge improvement in performance (Figure 6.6-D), and faster start-up of the paper fuel cell was observed. This final nanoink formulation was characterized by FTIR-ATR (Figure 6.6-E) and TG (Figure 6.6-F). Comparing the spectra of the CB -PtRu-MWNTs-EDOT (red line) with those of the CB -PtRu sample (blue line), one can observe the appearance of low intensity bands in the nanocomposite spectra (Figure 6.6-E), mainly due to the contribution of the EDOT molecule (pink line), since the carbon species have almost no characteristic vibrational bands (only carbon-carbon bonds). Analysing the spectra of the CB-PtRu-MWNTs-EDOT sample, one can

observe the appearance of weak, intense bands at 848 cm^{-1}, 1050 cm^{-1}, 1150 cm^{-1}, 1480 cm^{-1}, and 1509 cm^{-1}, which are characteristic of the vibrational spectra of the EDOT [283]; a small band at 1700 cm^{-1} also is perceptible and can be derived from the -COOH of the oxidized MWCNTs [284].

The TGA thermograms of CB-PtRu, CB-PtRu-MWCNTs-EDOT, and CB-PtRu-MWCNTs-EDOT-Nafion® were also performed to follow the different steps of the nanoink formulation. The results are shown in Figure 6.6-F, evidencing the different thermal decomposition behaviour of the different analysed samples. Analysing the corresponding weight loss curves, it can be observed that the CB-PtRu-MWCNTs-EDOT-Nafion® sample shows higher weight loss, when compared to the unmodified CB-PtRu and CB-PtRu-MWCNTs-EDOT. This result is to be expected since in the other two samples investigated the major component is carbon, which has a low degradation profile in the range of temperatures evaluated. Thus, all samples can be considered thermally stable, with a minimum percentage weight loss occurring up to 200 ˚C.

These results support the preparation of a solid nanocomposite (PEDOT/MWCNT-COOH/CB-PtRu) formed by ultrasound technique, which allows a perfect combination of the desired properties of each component. In this case, the inherent hydrophobicity of the PEDOT polymer [279] replaces the insulating paraffin element and helps to control the methanol transfer from the anode to the cathode electrode and also increases the electrical conductivity of the anode surface. This discovery is important for the improvement of this simple paper fuel cell system, but it could also be significant for the application in regular DMFC systems, since methanol crossover is still a current problem of this type of alcohol cell, which hinders its application and diffusion as an energy source [285]. MWCNT-COOH, added to the ink, contributes as a spacer and radical donor and also increases the electrical conductivity. To achieve these better performance results, the PEDOT/MWCNT-COOH/CB-PtRu nanocomposite should be synthesized in a 3-step ink fabrication method: 1 - stabilization of CB -PtRu + MWCNT-COOH in IPA (24 h); 2 - addition of EDOT solution and sonication for 30 s to form a solid material; 3 - addition of Nafion® and IPA (100 µL) and sonication for 10s to form a new solid matrix. This last step avoids unwanted interactions of Nafion® with EDOT, as Nafion® is essential for assure the proton conduction of the fuel cell system. The final PEDOT/MWCNT-COOH/CB-PtRu nanocomposite is then diluted in an appropriate amount of IPA before brush application. The volume required to obtain the better

properties of this material was also investigated and it was found that a higher dilution factor (5x) results in a low viscosity ink with medium performance and a lower dilution factor (1x) results in a high viscosity ink that is difficult to spread using the brush technique. To obtain a processable and well-tolerated nanoink for anode electrode fabrication, the nanocomposite must be diluted 3x in IPA.

6.3.1.2 Sensory layer development and characterization

The sensing layer was built up on the surface of the PEDOT/MWCNT-COOH/CB-PtRu anode immediately after the electrode was painted (Figure 6.7- A). The idea is that the free EDOT monomer present on the anode surface can react with the EDOT solution monomer in the electropolymerization protocol, resulting in the PEDOT/PB-DMFC/biosensor. This process makes it possible to obtain a hybrid nanocomposite carbon electrode with a dual function: methanol oxidation for energy production and sensing properties. The working principle of this hybrid system is related to the ability of methanol molecules to reach the catalytic sites of platinum. In a PEDOT/PB-DMFC, the active sites of the Pt are fully available to react with the methanol molecules, while in the PEDOT/PB-DMFC/biosensor the sites of the Pt catalyst are less accessible due to the presence of the polymer film. The voids present in the polymer film allow the methanol to spread on the Pt catalyst surface, but when the protein rebounds in the voids, the methanol molecules are prevented from reaching the catalyst and being oxidized. This phenomenon leads to a decrease in the potential and performance of the system, which can be correlated with the biosensor response [241].

The different developed PEDOT/PB-DMFCs were analyzed by Raman spectroscopy to follow the surface changes of the different anode electrodes (Figure 6.7-B). The spectra obtained show differences in the intensity of bands G (1570 cm^{-1}) and D (1340 cm^{-1}), which are more pronounced for the PEDOT/PB-DMFC/NIP control, the anode electrode with higher PEDOT loading. For the PEDOT/PB-DMFC/MIP, the anchoring of the electropolymerized PEDOT is hindered by the presence of the L1CAM previously incubated on the anode surface.

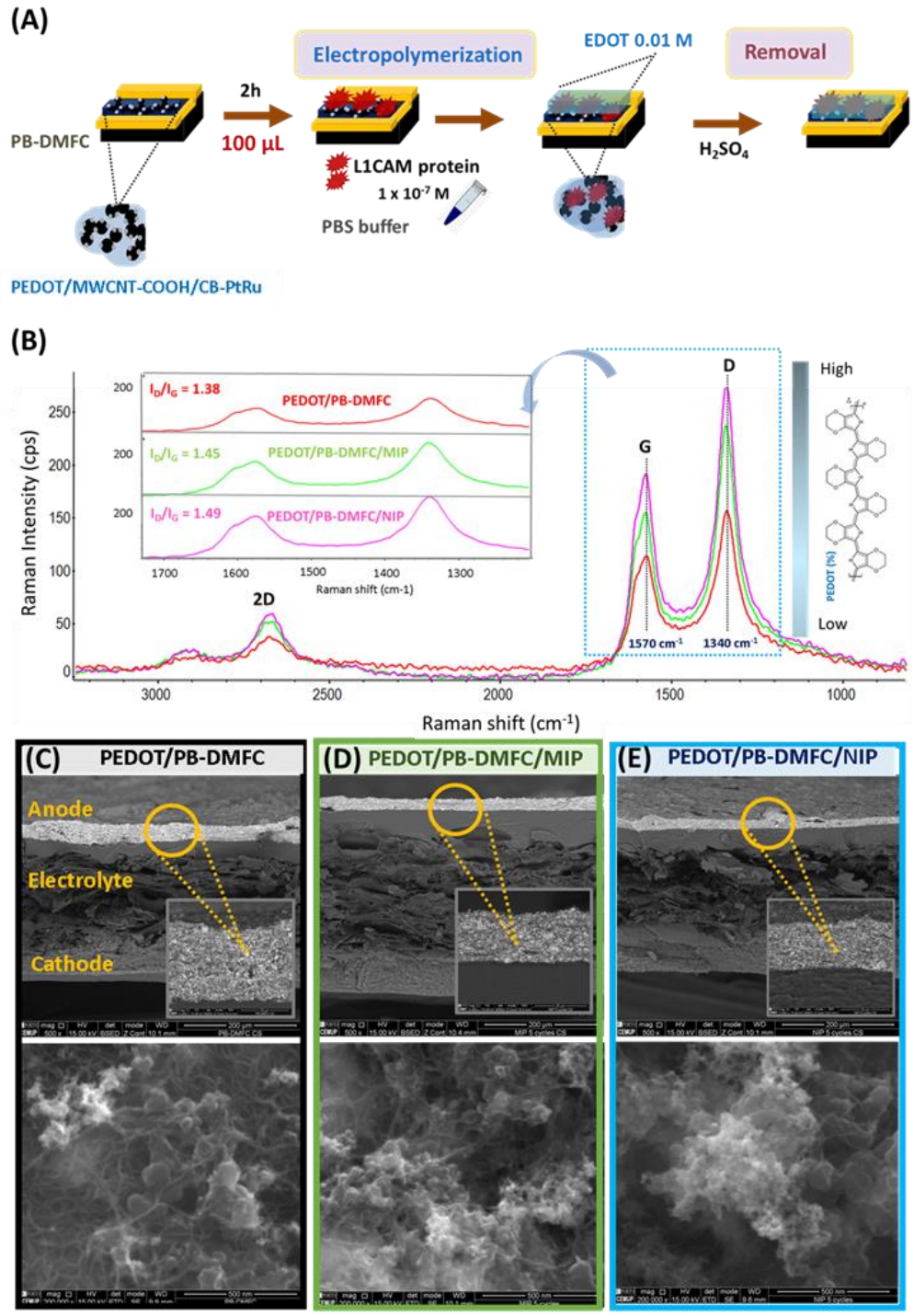

Figure 6.7 - Steps involved in the development of a PEDOT/PB-DMFC/biosensor by electropolymerization, evidencing the interactions of the PEDOT based anode with the EDOT solution in the MIP formulation (A) and characterization results obtained by Raman analysis at 532 nm of the different PEDOT/PB-DMFC assemblies (PEDOT/PB-DMFC/MIP and PEDOT/PB-DMFC/NIP) with the corresponding I_D/I_G calculated ratios (inset) (B); SEM images in cross-section and topography of a PEDOT/PB-DMFC (C), and electropolymerized samples to obtain the biosensor function (PEDOT/PB-DMFC/MIP) (D) and the control (PEDOT/PB-DMFC/NIP) (E).

These results were also confirmed by analysing the cyclic voltammograms of PEDOT/PB-DMFC/NIP and PEDOT/PB-DMFC/MIP obtained during the electropolymerization protocol (Figure 6.8).

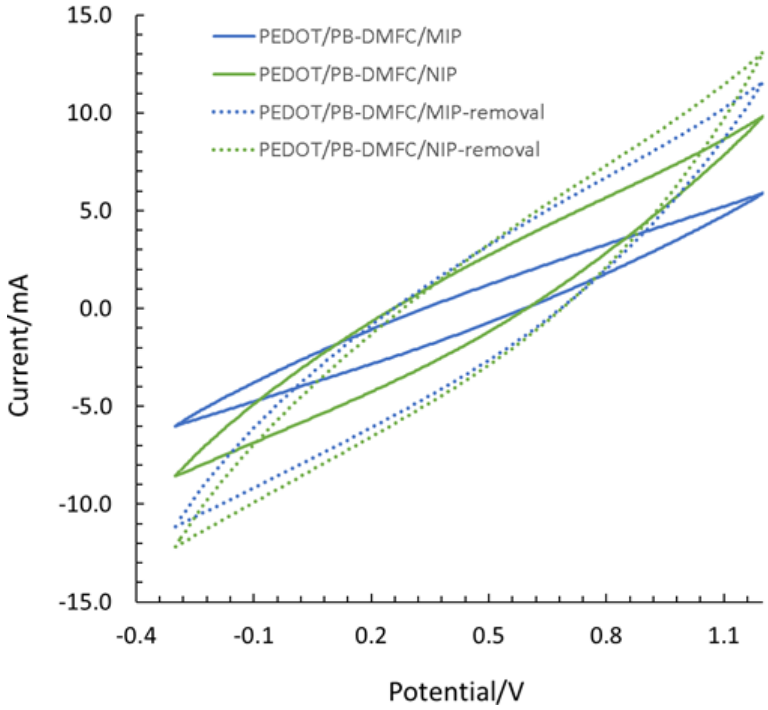

Figure 6.8 - Steady-state cyclic voltammograms obtained in a 3-electrode system in a PBS buffer solution (the 5th cycle is presented, −0.3 V to 1.2 V, 50 mV/s), for the assembly of the PEDOT sensing polymer on the anode layer of PEDOT/PB-DMFC-MIP in comparison with the control PEDOT/PB-DMFC-NIP and corresponding removal step in sulfuric acid solution.

The relative intensity of the D and G bands can be an indicator of surface modifications in a given carbon material and reveal the degree of disorder in a sample. The I_D/I_G was calculated for both fuel cells and an I_D/I_G ratio of 1.38 was obtained for the PEDOT/PB-DMFC. This value is significantly higher when compared to a PB-DMFC without EDOT in the ink formulation (0.91), which is further evidence that this newly developed nanoink is significantly different than the ink applied in the first prototype [267]. he I_D/I_G calculated for the PEDOT/PB-DMFC/MIP is 1.45, while it is 1.49 for the PEDOT/PB-DMFC/NIP. These results show that a higher percentage of PEDOT polymer on the surface leads to a more uniform and homogeneous surface, so the presence of the polymer anchored in the surface also prevents the interference of the PtRu metals present in the anode in the Raman spectra. Since the PtRu metals interfere with the intensity of the recorded bands, the sample with a higher PEDOT loading shows a higher intensity in

both the G, D, and 2D bands. This difference in the intensity of the ratios is significant and originated form a uniform polymer layer anchored to the anode surface of both PEDOT/PB-DMFC arrays.

To evaluate these surface modifications, a SEM analysis is performed to assess the topography of the surface of the different anode electrodes as well as a cross-sectional analysis evaluation of the different PEDOT/PB-DMFCs. The analysis of the cross-section obtained by SEM for all the fabricated experimental setups shows a uniform and well-defined 3-layer (anode-electrolyte-cathode) distribution for all the fabricated fuel cells. Interestingly, a decrease in layer thickness is observed for the PEDOT/PB-DMFC/MIP and PEDOT/PB-DMFC/NIP samples, indicating a more homogeneous surface. In the case of PEDOT/PB-DMFC, the presence of a network of MWCNTs-COOH is readily apparent. In the analysis of the electropolymerized samples for the sensor (PEDOT/PB-DMFC/MIP) and the control (PEDOT/PB-DMFC/NIP), a visible surface change is observed, with less distinction between the different network components, especially in the case of PEDOT/PB-DMFC/NIP.

6.3.2 Calibrations of the PEDOT/PB-DMFC biosensor (single cell configuration)

The PEDOT/PB-DMFC/biosensor and PEDOT/PB-DMFC/NIP assemblies were first activated by running multiple polarization curves until the systems reached maximum OCV and power density (the number of polarization curves required for full activation depends on the PEDOT/PB-DMFC set-up and can range from 3 to 5 consecutive trials). In the single cell configuration, the calibrations were performed with the potentiostat. Once a polarization curve was established, the PEDOT/PB-DMFC/biosensor was washed with water, dried with N_2 and 100 µL of a 0.5 M methanol solution was added to the anode layer. This procedure was repeated continuously throughout the calibration experiment. A prior stabilization in the background medium used was performed to ensure that the measured electrical signal was due to the L1CAM interaction and not to the medium in which the standard solutions were prepared. Two background media were used to prepare the L1CAM standards: MES Buffer and pre-treated human serum (Cormay®). In the case of human serum (Cormay®), a 100-fold dilution in buffer was performed to achieve signal stability. This stability procedure was performed by incubating the sensory layer successively with the same volume of

background medium used for the incubation of the L1CAM standards (100 µL) until a stable electrical signal was achieved (deviations of less than 2%). Figure 6.9 S4 shows an example of a stabilisation protocol with MES buffer and diluted Cormay® serum. It shows that the successive MES incubations hardly affect the signal, unlike the Cormay® serum, which needs to be pre-treated before use in the sensor area. It is therefore important to emphasise that the pre-treatment of the Cormay® serum serves to remove excess of salts and to preserve the proteins. This pre-treatment of a real sample does not limit the use of this system as a portable POC instrument, as it is a simple procedure to remove the salts and dilute the sample. For example, the COVID test strips developed by homemade analyses also require dilution in a buffer medium before use in the sensor area. Therefore, selectivity tests were also performed to evaluate the performance of this PEDOT/PB-DMFC/biosensor in the presence of interfering proteins.

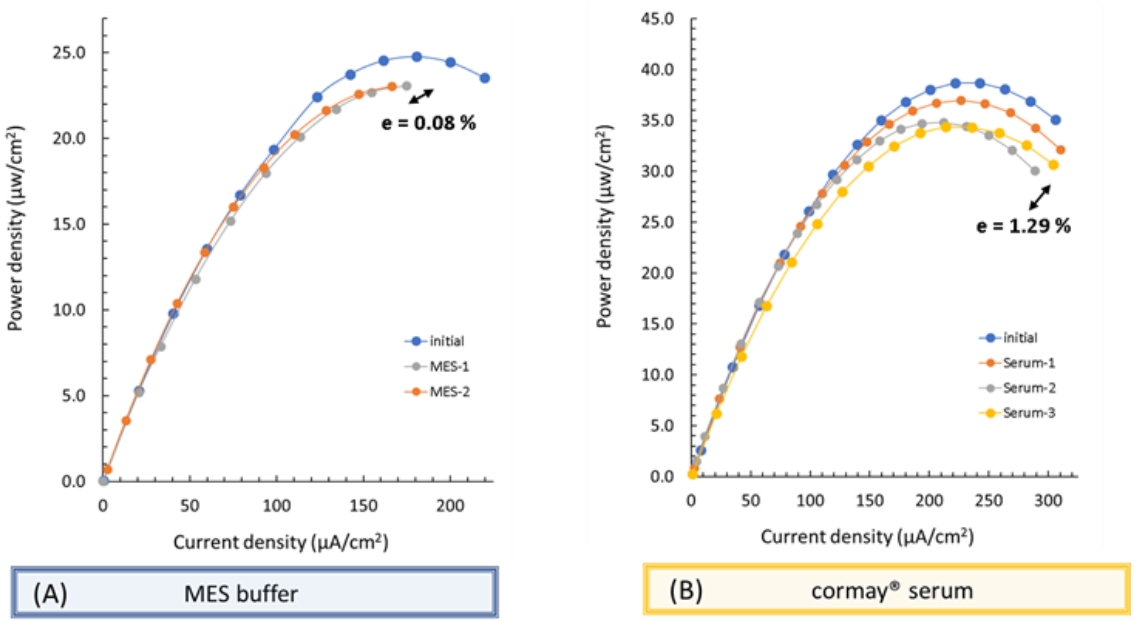

Figure 6.9 - Power curves obtained in consecutive electrochemical readings using independent PEDOT/PB-DMFCs assemblies after stabilization and prior incubation with MES buffer (A), pre-treated diluted (100x) Cormay® serum (B) using 0.5 M MeOH solution for the readings.

After stabilising the signal from the PEDOT/PB-DMFC/biosensor and, in parallel, the control PEDOT/PB-DMFC/NIP in appropriate media, successively increasing concentrations of L1CAM standard solutions in the range of [1.0×10^{-12} M – 1.0×10^{-8} M] were incubated directly on the surface of the anode sensor layer; the polarization curve

was followed after incubation of each concentration (from the OCV potential to a predefined stop potential of 0.1 V). It is important to note that the initial OCV of the polarization curve decreases as the calibration experiment progresses, while the sensor loses the ability to return to initial values when L1CAM is trapped in the polymer voids. However, the time required to reach a stable OCV varies during the calibration, but must be determined at the beginning of the experiment and maintained until the end of the calibration, as the kinetics of methanol oxidation are time-dependent and a long contact time favours that a small molecule such as methanol can easily enter the polymer and influence the results. This does not affect the sensor analysis and response, especially in this developed PEDOT/PB-DMFC/biosensor, as the pregnancy tests and COVID tests were also time dependent (the result is only valid for a short and specific period of time). Each L1CAM standard solution was left on the anode surface for 20 minutes and covered with a square glass to ensure efficient distribution of the sample over the entire sensory surface and also to prevent evaporation. After this time, a 0.5 M MeOH solution was spread on the anode side, followed by the electrochemical measurement (OCV stabilization + sampling DC voltammetry technique). This procedure was performed in parallel with a control fuel cell (PEDOT/PB-DMFC/NIP) to monitor the non-specific interactions of L1CAM with the non-imprinted polymer. Several calibrations were performed to evaluate the analytical response of this hybrid paper biosensor strip. Figure 6.10-A, shows a typical plot of the performance curves obtained during a calibration procedure in buffer media of a PEDOT/PB-DMFC/biosensor, and Figure 6.10-B shows the average calibration curves compared to the control (PEDOT/PB-DMFC/NIP). Figure 6.10-C, shows the differences in performance values recorded for a pair of PEDOT/PB-DMFC/biosensor and PEDOT/PB-DMFC/NIP from the same batch. This illustrates the differences between a paper fuel cell with a sensory anode integrating a polymer with cavities (PEDOT/PB-DMFC/biosensor) and without cavities in the polymer (PEDOT/PB-DMFC/NIP). The power generated is 5 times higher with the PEDOT/PB-DMFC/biosensor, as the cavities enable more efficient methanol enrichment and oxidation in the Pt catalysts.

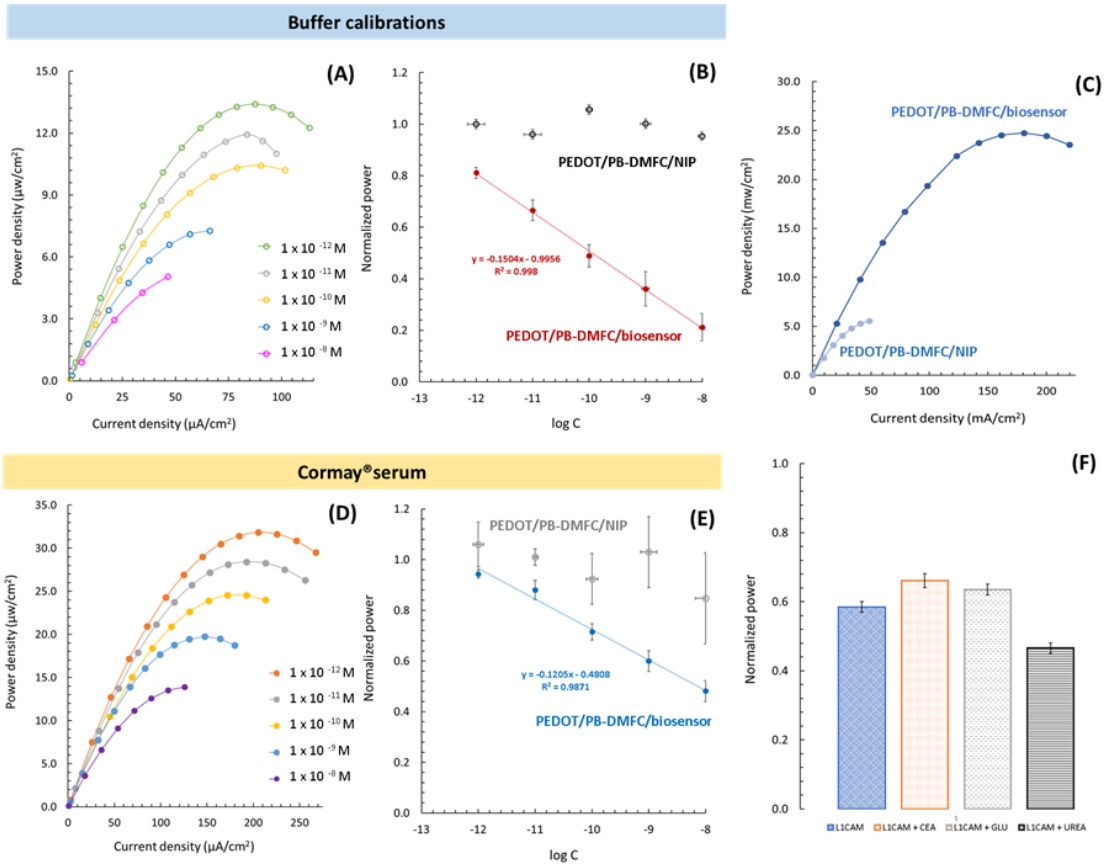

Figure 6.10 - Power-current density curves obtained during a calibration after incubation of L1CAM standards of increasing concentrations prepared in buffer (A), with the respective calibration curve compared with a control experiment (PEDOT/PB-DMFC/NIP) in the range $1.0\times10^{-12} - 1.0\times10^{-8}$ M (B); Comparison of the recorded power-current density curves of a pair of PEDOT/PB-DMFC/biosensor and PEDOT/PB-DMFC/NIP obtained in the same batch, showing the effect of the polymer cavities in the power produced by the two different set-ups (C). Power-current density curves obtained during a calibration with L1CAM standard solutions prepared in Cormay serum® in the same concentration range used in buffer (D), with the respective calibration curve compared with the control PEDOT/PB-DMFC/NIP sample (E). All calibration curves were drawn using the average of the maximum power density obtained at each L1CAM concentration. Selectivity assays results (buffer) obtained using independent PEDOT/PB-DMFC/biosensor strips after incubation of a L1CAM standard solution (1.0×10^{-10} M) and L1CAM spiked with interfering compounds [carcinoembryonic antigen (CEA), glucose (GLU) and urea] with the respective interference analysis presented in normalized values (F).

Figure 6.10-D shows a typical calibration graph obtained in pre-treated Cormay® serum with the corresponding average calibration curves in Figure 6.10-E. Calibration data show that the average power density decreases linearly with successive concentrations of the L1CAM standards for both media studied. Therefore, PEDOT/PB-DMFC can be tuned into a PEDOT/PB-DMFC/biosensor with activity dependent on L1CAM concentration. Analysis of the calibrations performed in MES buffer (Figure 6.10-B) shows that the PEDOT/PB-DMFC/biosensor performance decreases by ~70% compared to the maximum L1CAM concentration, compared to the initial value after the blank experiments (background stabilisation), with a squared correlation coefficient of ~0.998. This variation was generally consistent between the different calibrations performed in buffers using PEDOT/PB-DMFCs with similar initial power values. This result, compared to the first PB-DMFC prototype developed for sarcosine targeting [267], proves that this new system integrating EDOT into the ink allows a higher impact in terms of power density dependence on target concentration, which traduces in a higher sensitivity of the system.

The limit of detection of this PEDOT/PB-DMFC/biosensor was 1.17×10^{-13} M and was calculated by applying the equation $LoD = (y_{blank} - 3SD_{blank})/Slope$. Comparing the results of the PEDOT/PB-DMFC/biosensor with the non-imprinted PEDOT/PB-DMFC/NIP, a random response is observed, indicating minor nonspecific interactions of L1CAM molecules.

Analysis of calibrations performed in pre-treated Cormay® serum shows that the final PEDOT/PB-DMFC/biosensor signal output decreases by ~ 50% (compared to the initial value after stabilisation of the background medium) towards the maximum concentration of L1CAM. These results demonstrate the good performance of this paper-based biosensor, which also shows good sensitivity in more complex media such as Cormay® serum. Therefore, the sensitivity in this complex matrix medium is not as high as in buffer media, which is also a price to pay in more sensitive systems. The L1CAM target is thus a more complex molecule than sarcosine, so this result can be considered very promising, as the performance of the PEDOT/PB-DMFC/biosensor strip retains a higher impact on the potential, current density and performance of the fuel cell strip. The analysis of the non-specific interactions in the control fuel cell (PEDOT/PB-DMFC/NIP) shows that the behaviour of this system is random and the interactions are negligible in this medium.

Thus, this self-supplied paper strip PEDOT/PB-DMFC/biosensor can be used for screening and monitoring the L1CAM biomarker, with the possibility of connecting it to a EC cell for outdoor use, without being limited to standard analytical laboratory procedures. A cut-off value of 5.4 ng/ml for soluble L1CAM has been reported in the literature to define clinical risk groups associated with tumor progression [51]. This concentration (2.6×10^{-11} M) can be detected on paper strips using PEDOT/PB-DMFC/biosensor, suggesting that this autonomous paper platform may be a useful tool for detecting abnormal L1CAM levels associated with tumour diagnosis.

Selectivity tests of the PEDOT/PB-DMFC/biosensor were performed in buffer solutions against 3 major interfering species (carcinoembryonic antigen-CEA, glucose and urea). The assays were performed with different PEDOT/PB-DMFC units, incubating a standard L1CAM solution (1.0×10^{-10} M) in a PEDOT/PB-DMFC/biosensor area. In parallel, the same procedure was repeated with different PEDOT/PB-DMFC/biosensor units by incubating the same concentration of L1CAM in the presence of the respective interfering substance. Both PEDOT/PB-DMFC/biosensors were analysed using their respective polarization curves. The corresponding interference analysis is obtained from the normalized peak power between the average L1CAM response/average L1CAM + interference response. These data are shown in Figure 6.10-F. They show that the signal deviation is low in the presence of the interfering species CEA and glucose, with the urea species causing the largest deviation from the L1CAM signal (20%). Therefore, these data confirm the high preference of this sensor for the L1CAM target molecule with signal changes of 8-20%, both in the positive and negative directions.

6.3.3 EC assembly and characterization

The electrochromic device was mounted in a single-layer semi-transparent paper strip previously modified with PDMS (hydrophobic treatment and reinforcement) and MPTMS (adhesion promoter for Au and PEDOT:PSS). In the absence of the adhesion promoter MPTMS, the gold layer is not stable in the presence of the electrolyte and leaves the paper during the measurements. Figure 6.5-F, shows a real image after prolonged use of the ECs in the absence/presence of MPTMS and illustrates the differences in the adhesion of sputtered gold film. The chemical characterization of the EC paper support and the final assembly was conducted using the FTIR-ATR (Figure 6.5-G). In the unmodified paper strip sample, the characteristic absorption bands of cellulose are visible

at 3330 cm^{-1} (stretching of hydroxyl groups), at 2906 and 1373 cm^{-1} (stretching and deformation vibrations of C-H) and the strong, intense band at 1027 cm^{-1} (stretching of -C-O group) [286]. When analysing the paper modified with the PDMS layer, all the characteristic absorption bands of the PDMS molecule can be observed: 1257, 1008 and 786 cm^{-1}, representing the functional groups of $Si\text{-}CH_3$, O-Si-O and $Si\text{-}(CH_3)_2$, respectively [287]. The paper modified with PDMS and MPTMS shows two small bands around 2917 and 2849 cm^{-1}, which can be assigned to the C-H stretching vibration of -CH_3 of the MPTMS molecule [288]. These results confirm that the paper was successfully modified for EC. To evaluate the waterproof properties of the EC paper strip, the dynamic contact angles were determined and the results are shown in Figure 6.5-H. When analysing the results for untreated paper, paper + PDMS and paper + PDMS + MPTMS (after plasma treatment), differences in the water contact angle for the different paper strips can be observed. For untreated paper, the contact angle of the droplet in the first 30 s is 94.9°. After 30 minutes, the drop thus spreads to the inside of the paper and damages the paper surface. The sample of paper + PDMS shows higher hydrophobicity with an increase of the contact angle to 104.8° , which decreases to 99.5° after the plasma treatment protocol. These results show that the PDMS treatment increases the hydrophobicity of the paper strip, which helps to obtain a durable, resistant and reusable EC paper strip.

After the layer of electrochromic PEDOT:PSS polymer was built up, electrochemical characterization was carried out in a 3-electrode system with $LiClO_4$ as electrolyte. A colour change from dark blue (-2 V) to light blue was observed, with a colour gradient between the tested potentials (-2 V to 2 V) (Figure 6.11-E) with a reversible behaviour. An example of an obtained voltammogram corresponding to one cycle is shown in Figure 6.11-F. This single layer EC was suitable for integration with PEDOT/PB-DMFC/biosensor, resulting in a fully flexible, self-powered and self-signalling paper-based sensor with potential application as a wearable biosensor (Figure 6.11-H).

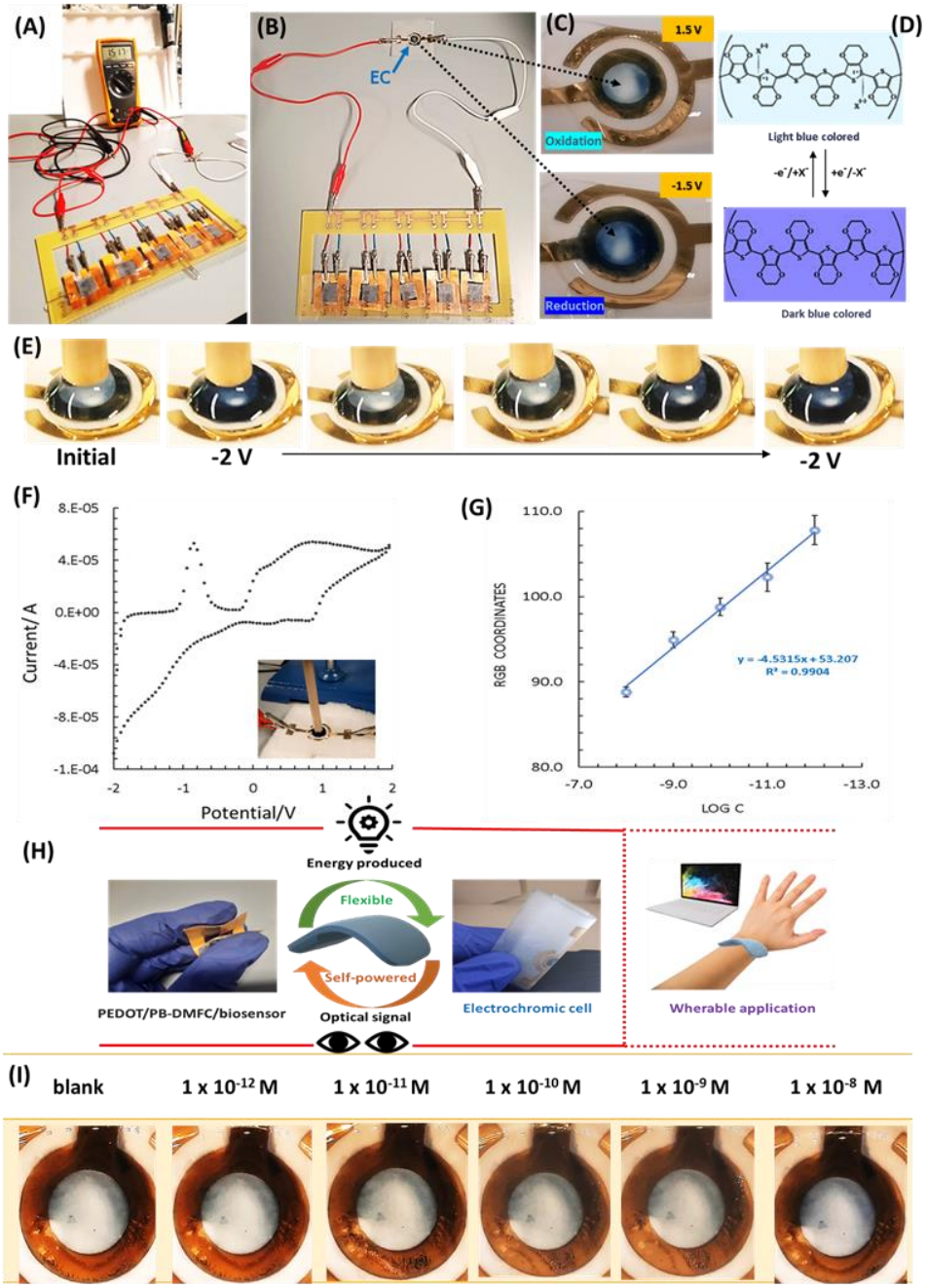

Figure 6.11 - PEDOT/PB-DMFC/biosensor assembled in a 5-stack configuration to produce a voltage of ~1.5 V (recorded with a multimeter) (A), connected to the EC cell (B) to promote the colour change of PEDOT:PSS polymer (C) from light to dark blue (inversion of polarization) (D). Colour variation of PEDOT:PSS polymer obtained in three electrodes system (E) and the respective voltammogram in the range of -2V to +2V (F). Calibration of PEDOT/PB-DMFC/biosensor-EC showing the RGB colour coordinates extracted from image J software (using blue coordinates) in three different spots (G). Schematic representation of the PEDOT/PB-DMFC/biosensor and EC evidencing the flexibility of each component and the overall properties suitable for wearable devices (H). Example of the pictures recorded during a calibration protocol after L1CAM incubation in the range of 1.0×10^{-12} – 1.0×10^{-8} M (I).

6.3.4 Assembly of the portable system – PEDOT/PB-DMFC/biosensor-stack interfaced with the EC

The PEDOT/PB-DMFC/biosensor-EC combines a stack with the ability to hold up to 5 fuel cell paper strips modified with the sensor function (Figure 6.12) and a PEDOT-based electrochromic cell. This portable prototype functions as a unique and fully autonomous sensing device and is lightweight, disposable and potentially inexpensive to commercialize.

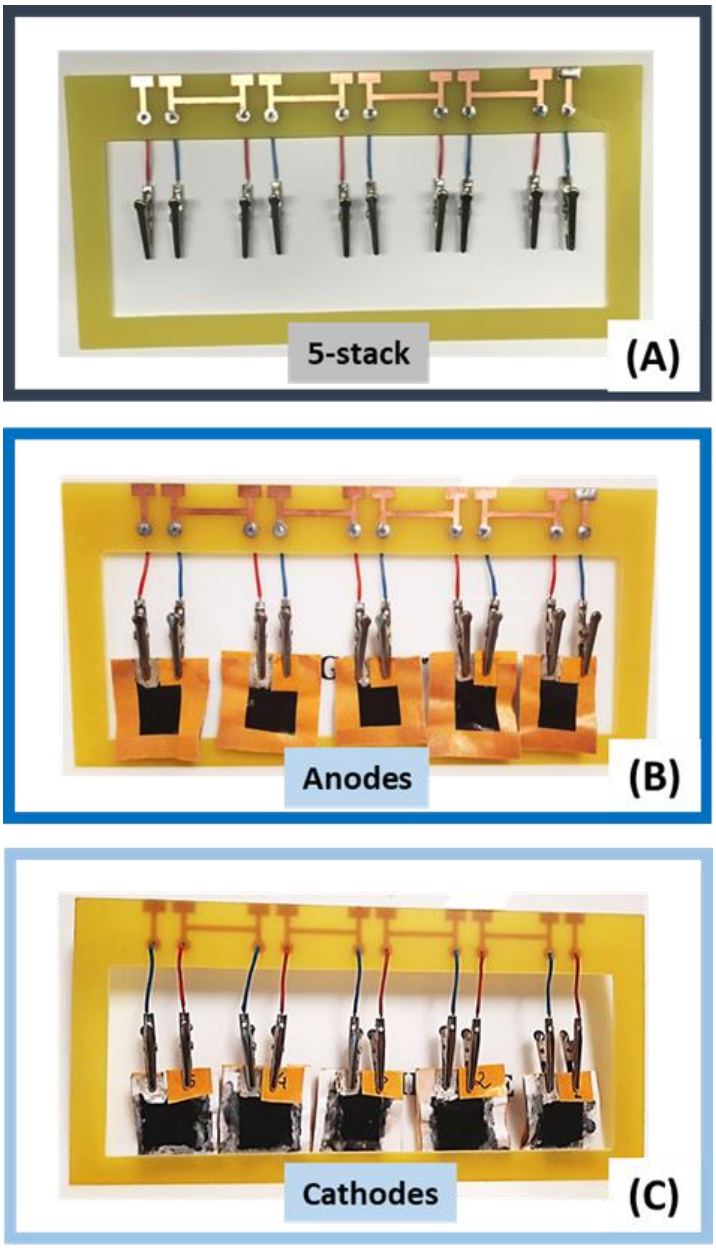

Figure 6.12 - Photographs of the PEDOT/PB-DMFC-stack; the electrical set-up (A), the anode sensing side(B), and connected to the cathodes (C).

The conductivity and electrochromic properties of PEDOT were explored to develop a simple, flexible and device-free paper-based fuel cell biosensor (Figure 6.11-A/B). Since the films prepared from the commercial PEDOT:PSS dispersion show a colour change from light to dark blue (Figure 6.11-C), with different shades of blue observed over a wide range of potentials (-1.5 V, +1.5 V), the PEDOT/PB-DMFC should generate enough potential to trigger the electrochromic device. The colour change of PEDOT:PSS is related to two different states: an oxidized state, which is light blue, and a reduced state, which is dark blue (Figure 6.11-D) [289]. With the developed PEDOT/PB-DMFC stack, it is possible to promote this colour change by simply connecting the EC to the PEDOT/PB-DMFC stack.

In order to achieve a voltage of at least 1.5 V, a stack of fuel cell strips had to be used, as each one produces ca. 0.3 V. The stack was assembled and connected to the EC. Then methanol solution was added to the anode layers and left for 30 minutes until a stable potential (~1.5 V) was reached, which was measured with a multimeter (Figure 6.11-A). After this stabilization, the multimeter was replaced with the EC and a few microliters of lithium perchlorate were added to the EC. After 2 minutes, a photo was taken to record the initial state of the system; then, each PEDOT/PB-DMFC/biosensor was washed, dried with nitrogen and incubated with the buffer (the incubation of the buffer and standards was set to 20 minutes). After washing and adding the methanol fuel again to the PEDOT/PB-DMFC/biosensor anodes, a new photo was taken after 2 minutes. This time is more than sufficient to observe the complete colour change (normally the EC, which is connected to the stack, changes colour in less than 1 minute). This procedure was repeated throughout the calibration and the standard concentrations tested were the same as those used in the single cell setup. The captured images were analysed using Image J software. The quantitative data obtained from the colour calibration are shown Figure 6.11-G. An example of the images taken during calibration is shown in Figure 6.11-I. The colour coordinates were determined at three different locations and the blue coordinate values were selected. When the blue RGB coordinates are plotted against the logarithm of the L1CAM concentration, a linear curve with squared correlation coefficient of $R^2 = 0.9904$ is obtained. Although the colour change is subtle and not ideally visible to the naked eye (the blue tone became slightly darker due to the calibration), the programme is sensitive to the changes and it is possible to observe the linear behaviour of the system with L1CAM detection by the developed sensor. In a future improvement,

a dopant can be used in the PEDOT:PSS formulation to shift the dark blue colour observed at negative potentials to the positive potentials where the colour change is less pronounced.

6.4 Conclusions

The developed PEDOT/PB-DMFC/biosensor-EC device is a new promising self-sufficient platform for clinically relevant L1CAM detection; it exploits methanol fuel cells as an energy source, a MIP sensing element, and an electrochromic indicator. The developed device is self-powered and self-signaling, with all components fully assembled on paper substrates for the first time.

The PEDOT/PB-DMFC/biosensor shows a linear sensing response within diagnostically significant L1CAM concentration of 2.6×10^{-11} M. High sensing selectivity of the developed system was proved in the assays in Cormay serum®. Overall, the presented PEDOT/PB-DMFC/biosensor-EC prototype can be considered as a promising and suitable tool for portable point-of-care applications and wearable biosensors with the ability to analyse L1CAM in a wide range of concentrations. This developed PEDOT/PB-DMFC/biosensor-EC can be classified as a novel strategy in the development of device-free and portable electrochemical biosensors, combining three emerging and powerful technologies (fuel cells, MIPs and electrochromic materials).

Further improvements to the current platform (catalysts, fabrication processes, fuels) could enable a low-cost and publicly available paper-based fuel cell biosensor for health monitoring and diagnostic applications.

Chapter 7

7. Conclusions and Future Perspectives

Overall, the development of electrical independent electrochemical biosensors achieved in this thesis showed that it is possible to merge the advantages of two current important research areas: biosensors and fuel cells. This technology merging allowed the design and development of two different biosensor/fuel cell sensing platforms for three cancer biomarkers screening. These biosensor/fuel cell assemblies were devices free of external batteries and their associated electronics, which was achieved by the successful coupling of bio-recognition functions with an autonomous transducer element. The final devices are compact, lightweight, disposable, low-cost, and user-friendly with good sensitivity, reproducibility, and selectivity.

The creation of a flexible paper-based fuel system allows the miniaturization of the first developed prototypes, evidencing that it is possible to create a fuel cell strip completely suitable for POC integration. This assembly was made in a single layer, completely settled on paper, which has the advantage of being environmentally friendly, requiring less amount of fuel for its operation and also less amount of sample to analyse. Thus, the simplicity of this paper fuel cell strip turns possible to improve the cost-effectiveness relation of this type of self-powered biosensor systems.

Nevertheless, despite the important and challenging scientific discoveries obtained with the works contained in this PhD thesis, some limitations remain, mainly associated with the function and “real” application of these self-powered sensing devices. In the future, several improvements in the last designed paper prototype can be achieved, to transpose this fuel cell paper strip sensor from the laboratory to commercialization. Thus, the prototype optimization can be made in several aspects, being the most important elements to optimize the precious rare electrocatalysts replacement and the alcohol

employed as fuel. In terms of setup configuration, some improvements can also be done with more sustainable nanomaterials and fabrication techniques.

In terms of electrocatalysts, currently the platinum is regarded as the most effective catalyst for the methanol oxidation in the DMFCs. Therefore, the high cost of this metal and the need to combine it with another metal, as ruthenium, to obtain PtRu alloy, which is required the prevent the platinum poisoning, still blocking the widespread of this power source technology. To overcome this shortfall, it is mandatory to developed non-Pt catalysts, which are suitable for application in devices with low power requirements and single readings (as biosensors). So far, the DMFCs technology has been developed to be power sources of diverse types of devices, but none of them are disposable devices, such the fuel cell biosensors developed in this thesis. Thus, the power requirements and time of operation of the fuel cells must be optimized for this specific application. Another non-precious metals or alloys can be studied to replace the PtRu alloy used as anode electrode and the Pt used in the cathode electrode, allowing decreasing costs and availability problems.

The alcohol fuel employed is another limitation that can be overpassed with more research in the nanomaterials selected for the fuel cell development. The modification methods include, the metal catalysts and the electrolyte selected, as the production methods. Ethanol, urea, glucose and even hydrogen can be employed as biosensor fuels, allowing to obtain a non-toxic and completely environment friendly sensing platform, Thus, depending on the selected path, more research is crucial to adapt the fuel cell/biosensor devices developed in this thesis to these novel conditions.

With the advent of nanotechnology, more noble and advanced carbonaceous materials have been explored, such as graphene and its derivatives as carbon nanofibers or carbon nanotubes. These novel nanomaterials seem to have high potential to replace the traditional materials and enhance the fuel cell performance, keeping a high electronic conductivity and decreasing the metal catalyst content required for fuel cells operation. The combination of these novel nanomaterials with non-precious catalysts is a higher scientific challenge pathway to disseminate the sensing fuel cell transduced platforms, as the developed herein.

The deposition methods available for the production of all the components of fuel cells (as anode, cathode, and electrolyte) are vast and represent a key role in the final features of the produced fuel cell assemblies. Also, the formulation of the different layers

is another key parameter involved in the performance of the fuel cells, and more research is needed to find the suitable formulation/deposition method relation for each type of fuel cell and application. Currently, the printing methods attracts great attention, since they allow the design of high reproducible electrodes with a cost-efficient and simple process with the advantage of easily scaling up to fabrication.

Overall, the research future in this area is massively vast, since the integration of fuel cell technology in the production of POC sensing devices is very recent. This possibility is explored in an exceptionally low number of works, so much work needs to be done to meet the best suitable fuel cell/biosensor assembly with marketable interest, tackling the worldwide dissemination of self-powered/signalled biosensors. Finally, the innovative work developed in this PhD opens new pathways in the design of novel self-powered biosensors and novel fuel cell configurations with application in the near future.

References

[1] World Health Organization, Health topics/Cancer, Cancer. (n.d.). https://www.who.int/health-topics/cancer#tab=tab_1 (accessed July 20, 2022).

[2] G. 2020, All-cancers-fact, (n.d.).

[3] H. Sung, J. Ferlay, R.L. Siegel, M. Laversanne, I. Soerjomataram, A. Jemal, F. Bray, Global Cancer Statistics 2020: GLOBOCAN Estimates of Incidence and Mortality Worldwide for 36 Cancers in 185 Countries, CA. Cancer J. Clin. 71 (2021) 209–249. https://doi.org/10.3322/caac.21660.

[4] L. Lu, C.S. Mullins, C. Schafmayer, S. Zeißig, M. Linnebacher, A global assessment of recent trends in gastrointestinal cancer and lifestyle-associated risk factors, Cancer Commun. 41 (2021) 1137–1151. https://doi.org/10.1002/cac2.12220.

[5] S.P. Lester, A.S. Kaur, S. Vegunta, Association Between Lifestyle Changes, Mammographic Breast Density, and Breast Cancer, Oncologist. 27 (2022) 548–554. https://doi.org/10.1093/oncolo/oyac084.

[6] J. Huang, Y. Deng, M.S. Tin, V. Lok, C.H. Ngai, L. Zhang, D.E. Lucero-Prisno, W. Xu, Z.J. Zheng, E. Elcarte, M. Withers, M.C.S. Wong, Worldwide Distribution, Risk Factors, and Temporal Trends of Testicular Cancer Incidence and Mortality: A Global Analysis Junjie, Eur. Urol. Oncol. 161 (2022) 1101–1111. https://doi.org/10.1016/j.chest.2021.12.655.

[7] Americam Cancer Society, Cancer Information and Resources, (n.d.). https://www.cancer.org/ (accessed July 25, 2022).

[8] C. Liu, X. Xiang, S. Han, H.Y. Lim, L. Li, X. Zhang, Z. Ma, L. Yang, S. Guo, R. Soo, B. Ren, L. Wang, B.C. Goh, Blood-based liquid biopsy: Insights into early detection and clinical management of lung cancer, Cancer Lett. 524 (2022) 91–102. https://doi.org/10.1016/j.canlet.2021.10.013.

[9] H. Sohrabi, N. Bolandi, A. Hemmati, S. Eyvazi, S. Ghasemzadeh, B. Baradaran, F. Oroojalian, M. Reza Majidi, M. de la Guardia, A. Mokhtarzadeh, State-of-the-art cancer biomarker detection by portable (Bio) sensing technology: A critical review, Microchem. J. 177 (2022) 107248. https://doi.org/10.1016/j.microc.2022.107248.

[10] M. Hasanzadeh, S. Tagi, E. Solhi, A. Mokhtarzadeh, N. Shadjou, A. Eftekhari, S. Mahboob, An innovative immunosensor for ultrasensitive detection of breast cancer

specific carbohydrate (CA 15-3) in unprocessed human plasma and MCF-7 breast cancer cell lysates using gold nanospear electrochemically assembled onto thiolated graphene quantum dots, Int. J. Biol. Macromol. 114 (2018) 1008–1017. https://doi.org/10.1016/j.ijbiomac.2018.03.183.

[11] N.L. Henry, D.F. Hayes, Cancer biomarkers, Mol. Oncol. 6 (2012) 140–146. https://doi.org/10.1016/j.molonc.2012.01.010.

[12] L. Wu, X. Qu, Cancer biomarker detection: Recent achievements and challenges, Chem. Soc. Rev. 44 (2015) 2963–2997. https://doi.org/10.1039/c4cs00370e.

[13] P. GOLD, S.O. FREEDMAN, Demonstration of Tumor-Specific Antigens in Human Colonic Carcinomata By Immunological Tolerance and Absorption Techniques., J. Exp. Med. 121 (1965) 439–462. https://doi.org/10.1084/jem.121.3.439.

[14] D.M. Thomson, J. Krupey, S.O. Freedman, P. Gold, The radioimmunoassay of circulating carcinoembryonic antigen of the human digestive system., Proc. Natl. Acad. Sci. U. S. A. 64 (1969) 161–167. https://doi.org/10.1073/pnas.64.1.161.

[15] C. Hall, L. Clarke, A. Pal, P. Buchwald, T. Eglinton, C. Wakeman, F. Frizelle, A review of the role of carcinoembryonic antigen in clinical practice, Ann. Coloproctol. 35 (2019) 294–305. https://doi.org/10.3393/ac.2019.11.13.

[16] S. Hammarström, The carcinoembryonic antigen (CEA) family: Structures, suggested functions and expression in normal and malignant tissues, Semin. Cancer Biol. 9 (1999) 67–81. https://doi.org/10.1006/scbi.1998.0119.

[17] W. Xiang, Q. Lv, H. Shi, B. Xie, L. Gao, Aptamer-based biosensor for detecting carcinoembryonic antigen, Talanta. 214 (2020) 120716. https://doi.org/10.1016/j.talanta.2020.120716.

[18] M. Goldstein, E.P. Mitchell, Carcinoembryonic Antigen in the Staging and Follow-up of Patients with Colorectal Cancer, Cancer Invest. 23 (2005) 338–351. https://doi.org/10.1081/cnv-200058878.

[19] P. Thomas, Carcinoembryonic Antigen, in: Springer (Ed.), Encycl. Cancer, Berlin, Heidelberg., 2008: pp. 493–495. https://doi.org/https://doi.org/10.1007/978-3-540-47648-1_836.

[20] PDB, Crystal structure of the N-terminal domain of carcinoembryonic antigen (CEA), (n.d.). https://www.rcsb.org/structure/2QSQ (accessed August 3, 2022).

[21] F. Zhou, M. Wang, L. Yuan, Z. Cheng, Z. Wu, H. Chen, Sensitive sandwich ELISA based

on a gold nanoparticle layer for cancer detection, Analyst. 137 (2012) 1779–1784. https://doi.org/10.1039/c2an16257a.

[22] Y. Zhang, X. Pang, D. Wu, H. Ma, Z. Yan, J. Zhang, B. Du, Q. Wei, A robust electrochemiluminescence immunoassay for carcinoembryonic antigen detection based on a microtiter plate as a bridge and Au@Pd nanorods as a peroxidase mimic, Analyst. 141 (2016) 337–345. https://doi.org/10.1039/c5an02053k.

[23] W. Dungchai, W. Siangproh, J.M. Lin, O. Chailapakul, S. Lin, X. Ying, Development of a sensitive micro-magnetic chemiluminescence enzyme immunoassay for the determination of carcinoembryonic antigen, Anal. Bioanal. Chem. 387 (2007) 1965–1971. https://doi.org/10.1007/s00216-006-0899-y.

[24] R.M.. P. Mach, T.P.; Jaeger, P.H.; Bertholet, M.M.; Ruegsegger, C.H.; Loosli, DETECTION OF RECURRENCE OF LARGE-BOWEL CARCINOMA BY RADIOIMMUNOASSAY OF CIRCULATING CARCINOEMBRYONIC ANTIGEN (C.E.A.), Lancet. 304 (1974) 535–540. https://doi.org/https://doi.org/10.1016/S0140-6736(74)91872-8.

[25] Y. Liu, H. Jiang, Electroanalytical determination of carcinoembryonic antigen at a silica nanoparticles/titania sol-gel composite membrane-modified gold electrode, Electroanalysis. 18 (2006) 1007–1013. https://doi.org/10.1002/elan.200603479.

[26] M. Hasanzadeh, N. Shadjou, Advanced nanomaterials for use in electrochemical and optical immunoassays of carcinoembryonic antigen. A review, Microchim. Acta. 184 (2017) 389–414. https://doi.org/10.1007/s00604-016-2066-2.

[27] M. Hasanzadeh, N. Shadjou, Y. Lin, M. de la Guardia, Nanomaterials for use in immunosensing of carcinoembryonic antigen (CEA): Recent advances, TrAC - Trends Anal. Chem. 86 (2017) 185–205. https://doi.org/10.1016/j.trac.2016.11.003.

[28] Z. El-Schich, Y. Zhang, M. Feith, S. Beyer, L. Sternbæk, L. Ohlsson, M. Stollenwerk, A.G. Wingren, Molecularly imprinted polymers in biological applications, Biotechniques. 69 (2020) 407–420. https://doi.org/10.2144/btn-2020-0091.

[29] A.A. Hasseb, N. din T. Abdel Ghani, O.R. Shehab, R.M. El Nashar, Application of molecularly imprinted polymers for electrochemical detection of some important biomedical markers and pathogens, Curr. Opin. Electrochem. 31 (2022) 100848. https://doi.org/10.1016/j.coelec.2021.100848.

[30] B.A.A. Manaf, S.P. Hong, M. Rizwan, F. Arshad, C. Gwenin, M.U. Ahmed, Recent advancement in sensitive detection of carcinoembryonic antigen using nanomaterials

based immunosensors, Surfaces and Interfaces. 36 (2023) 102596. https://doi.org/10.1016/j.surfin.2022.102596.

[31] A. Sreekumar, L.M. Poisson, T.M. Rajendiran, A.P. Khan, Q. Cao, J. Yu, B. Laxman, R. Mehra, R.J. Lonigro, Y. Li, M.K. Nyati, A. Ahsan, S. Kalyana-Sundaram, B. Han, X. Cao, J. Byun, G.S. Omenn, D. Ghosh, S. Pennathur, D.C. Alexander, A. Berger, J.R. Shuster, J.T. Wei, S. Varambally, C. Beecher, A.M. Chinnaiyan, Metabolomic profiles delineate potential role for sarcosine in prostate cancer progression, Nature. 457 (2009) 910–914. https://doi.org/10.1038/nature07762.

[32] O. Sheydaei, H. Khajehsharifi, H.R. Rajabi, Rapid and selective diagnose of Sarcosine in urine samples as prostate cancer biomarker by mesoporous imprinted polymeric nanobeads modified electrode, Sensors Actuators, B Chem. 309 (2020) 127559. https://doi.org/10.1016/j.snb.2019.127559.

[33] C.S. Pundir, R. Deswal, P. Kumar, Quantitative analysis of sarcosine with special emphasis on biosensors: a review, Biomarkers. 24 (2019) 415–422. https://doi.org/10.1080/1354750X.2019.1615124.

[34] T.E. Meyer, S.D. Fox, H.J. Issaq, X. Xu, L.W. Chu, T.D. Veenstra, A.W. Hsing, A reproducible and high-throughput HPLC/MS method to separate sarcosine from α- And β-Alanine and to quantify sarcosine in human serum and urine, Anal. Chem. 83 (2011) 5735–5740. https://doi.org/10.1021/ac201003r.

[35] C. Burton, S. Gamagedara, Y. Ma, Partial enzymatic elimination and quantification of sarcosine from alanine using liquid chromatography-tandem mass spectrometry, Anal. Bioanal. Chem. 405 (2013) 3153–3158. https://doi.org/10.1007/s00216-013-6740-5.

[36] H. Wu, T. Liu, C. Ma, R. Xue, C. Deng, H. Zeng, X. Shen, GC/MS-based metabolomic approach to validate the role of urinary sarcosine and target biomarkers for human prostate cancer by microwave-assisted derivatization, Anal. Bioanal. Chem. 401 (2011) 635–646. https://doi.org/10.1007/s00216-011-5098-9.

[37] P. Martínez-Lozano, J. Rus, Separation of isomers l-alanine and sarcosine in urine by electrospray ionization and tandem differential mobility analysis-mass spectrometry, J. Am. Soc. Mass Spectrom. 21 (2010) 1129–1132. https://doi.org/10.1016/j.jasms.2010.02.021.

[38] L.C. Soliman, Y. Hui, A.K. Hewavitharana, D.D.Y. Chen, Monitoring potential prostate cancer biomarkers in urine by capillary electrophoresis-tandem mass spectrometry, J. Chromatogr. A. 1267 (2012) 162–169. https://doi.org/10.1016/j.chroma.2012.07.021.

[39] N. Jornet-Martínez, C.J. Henderson, P. Campíns-Falcó, R. Daly, E.A.H. Hall, Towards sarcosine determination in urine for prostatic carcinoma detection, Sensors Actuators, B Chem. 287 (2019) 380–389. https://doi.org/10.1016/j.snb.2019.02.061.

[40] T.S.C.R. Rebelo, C.M. Pereira, M.G.F. Sales, J.P. Noronha, J. Costa-rodrigues, F. Silva, M.H. Fernandes, Analytica Chimica Acta Sarcosine oxidase composite screen-printed electrode for sarcosine determination in biological samples, Anal. Chim. Acta. 850 (2014) 26–32. https://doi.org/10.1016/j.aca.2014.08.005.

[41] A. Sassolas, L.J. Blum, B.D. Leca-Bouvier, Immobilization strategies to develop enzymatic biosensors, Biotechnol. Adv. 30 (2012) 489–511. https://doi.org/10.1016/j.biotechadv.2011.09.003.

[42] E.A. Struys, A.C. Heijboer, J. van Moorselaar, C. Jakobs, M.A. Blankenstein, Serum sarcosine is not a marker, Ann. Clin. Biochem. 47 (2010) 282. https://doi.org/10.1258/acb.2010.009270.

[43] D.P. Ankerst, M. Liss, D. Zapata, J. Hoefler, I.M. Thompson, R.J. Leach, A case control study of sarcosine as an early prostate cancer detection biomarker Urological oncology, BMC Urol. 15 (2015) 1–4. https://doi.org/10.1186/s12894-015-0095-5.

[44] S. Krishnan, S. Kanthaje, D.R. Punchappady, M. Mujeeburahiman, C.K. Ratnacaram, Circulating metabolite biomarkers: a game changer in the human prostate cancer diagnosis, J. Cancer Res. Clin. Oncol. 149 (2022) 951–967. https://doi.org/10.1007/s00432-022-04113-y.

[45] Y. Hu, S. Lv, J. Wan, C. Zheng, D. Shao, H. Wang, Y. Tao, M. Li, Y. Luo, Recent advances in nanomaterials for prostate cancer detection and diagnosis, J. Mater. Chem. B. 10 (2022) 4907–4934. https://doi.org/10.1039/d2tb00448h.

[46] N. Tarannum, D. Kumar, S.G. Surya, P. Dramou, Point-of-care detection assay based on biomarker-imprinted polymer for different cancers: a state-of-the-art review, Polym. Bull. 80 (2022) 1–46. https://doi.org/10.1007/s00289-022-04085-6.

[47] F.G. Rathjen, M. Schachner, Immunocytological and biochemical characterization of a new neuronal cell surface component (L1 antigen) which is involved in cell adhesion., EMBO J. 3 (1984) 1–10. https://doi.org/10.1002/j.1460-2075.1984.tb01753.x.

[48] S. Raveh, N. Gavert, A. Ben-Ze'ev, L1 cell adhesion molecule (L1CAM) in invasive tumors, Cancer Lett. 282 (2009) 137–145. https://doi.org/10.1016/j.canlet.2008.12.021.

[49] O. Coutelle, G. Nyakatura, S. Taudien, G. Elgar, S. Brenner, M. Platzer, B. Drescher, M. Jouet, S. Kenwrick, A. Rosenthal, The neural cell adhesion molecule L1: Genomic

organisation and differential splicing is conserved between man and the pufferfish Fugu, Gene. 208 (1998) 7–15. https://doi.org/10.1016/S0378-1119(97)00614-8.

[50] U.H. Weidle, D. Eggle, S. Klostermann, L1-CAM as a target for treatment of cancer with monoclonal antibodies, Anticancer Res. 29 (2009) 4919–4931. https://doi.org/0250-7005/2009.

[51] S. Bondong, H. Kiefel, T. Hielscher, A.G. Zeimet, R. Zeillinger, D. Pils, E. Schuster, D.C. Castillo-Tong, I. Cadron, I. Vergote, I. Braicu, J. Sehouli, S. Mahner, M. Fogel, P. Altevogt, Prognostic significance of L1CAM in ovarian cancer and its role in constitutive NF-κB activation, Ann. Oncol. 23 (2012) 1795–1802. https://doi.org/10.1093/annonc/mdr568.

[52] F.Y. Fu Tieng, N. Abu, S. Sukor, Z.A. Mohd Azman, N.M. Nadzir, L.H. Lee, N.S. Ab Mutalib, L1CAM, CA9, KLK6, HPN, and ALDH1A1 as potential serum markers in primary and metastatic colorectal cancer screening, Diagnostics. 10 (2020) 1–17. https://doi.org/10.3390/diagnostics10070444.

[53] T. Ito, S. Yamada, C. Tanaka, S. Ito, T. Murai, D. Kobayashi, T. Fujii, G. Nakayama, H. Sugimoto, M. Koike, S. Nomoto, M. Fujiwara, Y. Kodera, Overexpression of L1CAM is associated with tumor progression and prognosis via erk signaling in gastric cancer, Ann. Surg. Oncol. 21 (2014) 560–568. https://doi.org/10.1245/s10434-013-3246-5.

[54] P. Altevogt, K. Doberstein, M. Fogel, L1CAM in human cancer, Int. J. Cancer. 138 (2016) 1565–1576. https://doi.org/10.1002/ijc.29658.

[55] P. Altevogt, A. Ben-Ze'ev, N. Gavert, U. Schumacher, H. Schäfer, S. Sebens, Recent insights into the role of L1CAM in cancer initiation and progression, Int. J. Cancer. 147 (2020) 3292–3296. https://doi.org/10.1002/ijc.33177.

[56] P. Mehrotra, Biosensors and their applications - A review, J. Oral Biol. Craniofacial Res. 6 (2016) 153–159. https://doi.org/10.1016/j.jobcr.2015.12.002.

[57] H. Sharma, R. Mutharasan, Review of biosensors for foodborne pathogens and toxins, Sensors Actuators, B Chem. 183 (2013) 535–549. https://doi.org/10.1016/j.snb.2013.03.137.

[58] M.T. Giardi, D. Ph, M. Scalo, 18-Biotechnological Applications of Photosynthetic Proteins :, in: New York, Springer International Publishing, 2006: p. 220.

[59] M. Asal, Ö. Özen, M. Şahinler, H.T. Baysal, İ. Polatoğlu, An overview of biomolecules, immobilization methods and support materials of biosensors, Sens. Rev. 39 (2019) 377–386. https://doi.org/10.1108/SR-04-2018-0084.

[60] K. Wang, M. Wang, T. Ma, W. Li, H. Zhang, Review on the Selection of Aptamers and Application in Paper - Based Sensors, Biosensors. 13 (2023) 1–24. https://doi.org/https://doi.org/10.3390/bios13010039.

[61] J.P. Chambers, B.P. Arulanandam, L.L. Matta, A. Weis, J.J. Valdes, Biosensor Recognition Elements, Curr. Issues Mol. Biol. 10 (2002) 1–12.

[62] C.I.L. Justino, A.C. Freitas, R. Pereira, A.C. Duarte, T.A.P. Rocha Santos, Recent developments in recognition elements for chemical sensors and biosensors, TrAC - Trends Anal. Chem. 68 (2015) 2–17. https://doi.org/10.1016/j.trac.2015.03.006.

[63] O. Brandt, J.D. Hoheisel, Peptide nucleic acids on microarrays and other biosensors, Trends Biotechnol. 22 (2004) 617–622. https://doi.org/10.1016/j.tibtech.2004.10.003.

[64] M. Menger, A. Yarman, J. Erdossy, H.B. Yildiz, R.E. Gyurcsányi, F.W. Scheller, MIPs and aptamers for recognition of proteins in biomimetic sensing, Biosensors. 6 (2016) 1–19. https://doi.org/10.3390/bios6030035.

[65] T. Bhardwaj, T. Kumar Sharma, Aptasensors for full body health checkup, Biosens. Bioelectron. X. 11 (2022) 100199. https://doi.org/10.1016/j.biosx.2022.100199.

[66] O. Ramström, R.J. Ansell, Molecular imprinting technology: Challenges and prospects for the future, Chirality. 10 (1998) 195–209. https://doi.org/10.1002/(SICI)1520-636X(1998)10:3<195::AID-CHIR1>3.0.CO;2-9.

[67] M. Caldara, J. Kulpa, J.W. Lowdon, T.J. Cleij, H. Diliën, K. Eersels, B. Van Grinsven, Recent Advances in Molecularly Imprinted Polymers for Glucose Monitoring : From Fundamental Research to Commercial Application, Chemosensors. 11 (2023) 1–24. https://doi.org/https://doi.org/10.3390/ chemosensors11010032.

[68] K. Haupt, Molecularly imprinted polymers in analytical chemistry, Analyst. 126 (2001) 747–756. https://doi.org/10.1039/b102799a.

[69] J. Wackerlig, P.A. Lieberzeit, Molecularly imprinted polymer nanoparticles in chemical sensing - Synthesis, characterisation and application, Sensors Actuators, B Chem. 207 (2015) 144–157. https://doi.org/10.1016/j.snb.2014.09.094.

[70] L. Moreira Gonçalves, Electropolymerized molecularly imprinted polymers: perceptions based on recent literature for soon-to-be world-class scientists, Curr. Opin. Electrochem. 25 (2021) 100640. https://doi.org/10.1016/j.coelec.2020.09.007.

[71] A. Adumitrăchioaie, M. Tertiş, A. Cernat, R. Săndulescu, C. Cristea, Electrochemical methods based on molecularly imprinted polymers for drug detection. A review, Int. J.

Electrochem. Sci. 13 (2018) 2556–2576. https://doi.org/10.20964/2018.03.75.

[72] J. Erdossy, V. Horváth, A. Yarman, F.W. Scheller, R.E. Gyurcsányi, Electrosynthesized molecularly imprinted polymers for protein recognition, TrAC - Trends Anal. Chem. 79 (2016) 179–190. https://doi.org/10.1016/j.trac.2015.12.018.

[73] M. Peeters, P. Csipai, B. Geerets, A. Weustenraed, B. Van Grinsven, R. Thoelen, J. Gruber, W. De Ceuninck, T.J. Cleij, F.J. Troost, P. Wagner, Heat-transfer-based detection of l-nicotine, histamine, and serotonin using molecularly imprinted polymers as biomimetic receptors, Anal. Bioanal. Chem. 405 (2013) 6453–6460. https://doi.org/10.1007/s00216-013-7024-9.

[74] W. Naklua, R. Suedee, P.A. Lieberzeit, Dopaminergic receptor-ligand binding assays based on molecularly imprinted polymers on quartz crystal microbalance sensors, Biosens. Bioelectron. 81 (2016) 117–124. https://doi.org/10.1016/j.bios.2016.02.047.

[75] J.F. Masson, Surface Plasmon Resonance Clinical Biosensors for Medical Diagnostics, ACS Sensors. 2 (2017) 16–30. https://doi.org/10.1021/acssensors.6b00763.

[76] J. Ma, M. Yan, G. Feng, Y. Ying, G. Chen, Y. Shao, Y. She, M. Wang, J. Sun, L. Zheng, J. Wang, A.M. Abd El-Aty, An overview on molecular imprinted polymers combined with surface-enhanced Raman spectroscopy chemical sensors toward analytical applications, Talanta. 225 (2021) 122031. https://doi.org/10.1016/j.talanta.2020.122031.

[77] O.S. Ahmad, T.S. Bedwell, C. Esen, A. Garcia-Cruz, S.A. Piletsky, Molecularly Imprinted Polymers in Electrochemical and Optical Sensors, Trends Biotechnol. 37 (2019) 294–309. https://doi.org/10.1016/j.tibtech.2018.08.009.

[78] J.W. Lowdon, H. Diliën, P. Singla, M. Peeters, T.J. Cleij, B. van Grinsven, K. Eersels, MIPs for commercial application in low-cost sensors and assays – An overview of the current status quo, Sensors Actuators, B Chem. 325 (2020) 128973. https://doi.org/10.1016/j.snb.2020.128973.

[79] K. Shavanova, Y. Bakakina, I. Burkova, I. Shtepliuk, R. Viter, A. Ubelis, V. Beni, N. Starodub, R. Yakimova, V. Khranovskyy, Application of 2D non-graphene materials and 2D oxide nanostructures for biosensing technology, Sensors (Switzerland). 16 (2016) 1–23. https://doi.org/10.3390/s16020223.

[80] Y.T. Chen, Y.C. Lee, Y.H. Lai, J.C. Lim, N.T. Huang, C.T. Lin, J.J. Huang, Review of Integrated Optical Biosensors for Point-of-Care Applications, Biosensors. 10 (2020) 1–22. https://doi.org/10.3390/BIOS10120209.

[81] C. Chen, J. Wang, Optical biosensors: An exhaustive and comprehensive review, Analyst.

145 (2020) 1605–1628. https://doi.org/10.1039/c9an01998g.

[82] N. Khansili, G. Rattu, P.M. Krishna, Label-free optical biosensors for food and biological sensor applications, Sensors Actuators, B Chem. 265 (2018) 35–49. https://doi.org/10.1016/j.snb.2018.03.004.

[83] P. Skládal, Piezoelectric biosensors, TrAC - Trends Anal. Chem. 79 (2016) 127–133. https://doi.org/10.1016/j.trac.2015.12.009.

[84] M. Pohanka, The piezoelectric biosensors: Principles and applications, a review, Int. J. Electrochem. Sci. 12 (2017) 496–506. https://doi.org/10.20964/2017.01.44.

[85] M. Pohanka, Overview of piezoelectric biosensors, immunosensors and DNA sensors and their applications, Materials (Basel). 11 (2018) 1–13. https://doi.org/10.3390/ma11030448.

[86] S. Tombelli, M. Mascini, C. Sacco, A.P.F. Turner, A DNA piezoelectric biosensor assay coupled with a polymerase chain reaction for bacterial toxicity determination in environmental samples, Anal. Chim. Acta. 418 (2000) 1–9. https://doi.org/10.1016/S0003-2670(00)00943-0.

[87] F. Narita, Z. Wang, H. Kurita, Z. Li, Y. Shi, Y. Jia, C. Soutis, A Review of Piezoelectric and Magnetostrictive Biosensor Materials for Detection of COVID-19 and Other Viruses, Adv. Mater. 33 (2021) 1–24. https://doi.org/10.1002/adma.202005448.

[88] M.L. Verma, V. Rani, Biosensors for toxic metals, polychlorinated biphenyls, biological oxygen demand, endocrine disruptors, hormones, dioxin, phenolic and organophosphorus compounds: a review, Environ. Chem. Lett. 19 (2021) 1657–1666. https://doi.org/10.1007/s10311-020-01116-4.

[89] N. Hashemi Goradel, H. Mirzaei, A. Sahebkar, M. Poursadeghiyan, A. Masoudifar, Z.V. Malekshahi, B. Negahdari, Biosensors for the Detection of Environmental and Urban Pollutions, J. Cell. Biochem. 119 (2018) 207–212. https://doi.org/10.1002/jcb.26030.

[90] M. Yakovleva, S. Bhand, B. Danielsson, The enzyme thermistor-A realistic biosensor concept. A critical review, Anal. Chim. Acta. 766 (2013) 1–12. https://doi.org/10.1016/j.aca.2012.12.004.

[91] B. Lubbers, E. Kazura, E. Dawson, R. Mernaugh, F. Baudenbacher, Microfabricated calorimeters for thermometric enzyme linked immunosorbent assay in one-Nanoliter droplets, Biomed. Microdevices. 21 (2019) 1–7. https://doi.org/10.1007/s10544-019-0429-2.

[92] C. Dincer, R. Bruch, E. Costa-Rama, M.T. Fernández-Abedul, A. Merkoçi, A. Manz, G.A. Urban, F. Güder, Disposable Sensors in Diagnostics, Food, and Environmental Monitoring, Adv. Mater. 31 (2019) 1–28. https://doi.org/10.1002/adma.201806739.

[93] A. Kamiŝalić, I. Fister, M. Turkanović, S. Karakatiĉ, Sensors and functionalities of non-invasive wrist-wearable devices: A review, Sensors (Switzerland). 18 (2018) 1–33. https://doi.org/10.3390/s18061714.

[94] C. Sautter, Advances in Biochemical: Preface, in: Adv. Biochem. Eng. Biotechnol., Springer Berlin Heidelberg, 2007. https://doi.org/10.1007/978-3-540-71323-4.

[95] Bin Xie, B. Danielsson, Thermal Biosensor and Microbiosensor Techniques, in: Robert S. Marks, D.C. Cullen, I. Karube, C.R. Lowe, Howard H. Weetall. (Eds.), Handb. Biosens. Biochips, John Wiley & Sons, 2007.

[96] F. Arshad, F. Nabi, S. Iqbal, R.H. Khan, Applications of graphene-based electrochemical and optical biosensors in early detection of cancer biomarkers, Colloids Surfaces B Biointerfaces. 212 (2022) 112356. https://doi.org/10.1016/j.colsurfb.2022.112356.

[97] S. Mahari, S. Gandhi, Recent Advances in Electrochemical Biosensors for the Detection of Salmonellosis: Current Prospective and Challenges, Biosensors. 12 (2022) 1–20. https://doi.org/10.3390/bios12060365.

[98] A.K. Sari, S. Gaffar, Y.W. Hartati, A Review on the Development of Aptamer Immobilization Techniques in Aptamer-Based Electrochemical Biosensors for Viruses Detection, Anal. Bioanal. Electrochem. 14 (2022) 127–143. https://www.abechem.com/article_249328.html.

[99] U. Jain, K. Saxena, V. Hooda, S. Balayan, A.P. Singh, M. Tikadar, N. Chauhan, Emerging vistas on pesticides detection based on electrochemical biosensors – An update, Food Chem. 371 (2022) 131126. https://doi.org/10.1016/j.foodchem.2021.131126.

[100] L. Fu, S. Mao, F. Chen, S. Zhao, W. Su, G. Lai, A. Yu, C. Te Lin, Graphene-based electrochemical sensors for antibiotic detection in water, food and soil: A scientometric analysis in CiteSpace (2011–2021), Chemosphere. 297 (2022). https://doi.org/10.1016/j.chemosphere.2022.134127.

[101] X. Yang, H. Cheng, Recent developments of flexible and stretchable electrochemical biosensors, Micromachines. 11 (2020) 1–33. https://doi.org/10.3390/mi11030243.

[102] J.M. Moon, N. Thapliyal, K.K. Hussain, R.N. Goyal, Y.B. Shim, Conducting polymer-based electrochemical biosensors for neurotransmitters: A review, Biosens. Bioelectron. 102 (2018) 540–552. https://doi.org/10.1016/j.bios.2017.11.069.

[103] G. Liang, Z. He, J. Zhen, H. Tian, L. Ai, L. Pan, W. Gong, Development of the screen-printed electrodes: A mini review on the application for pesticide detection, Environ. Technol. Innov. 28 (2022) 102922. https://doi.org/10.1016/j.eti.2022.102922.

[104] V.N. Ataide, I.V.S. Arantes, L.F. Mendes, D.S. Rocha, T.A. Baldo, W.K.T. Coltro, T.R.L.C. Paixão, Review—A Pencil Drawing Overview: From Graphite to Electrochemical Sensors/Biosensors Applications, J. Electrochem. Soc. 169 (2022) 047524. https://doi.org/10.1149/1945-7111/ac68a0.

[105] R. Ahmad, O.S. Wolfbeis, Y.B. Hahn, H.N. Alshareef, L. Torsi, K.N. Salama, Deposition of nanomaterials: A crucial step in biosensor fabrication, Mater. Today Commun. 17 (2018) 289–321. https://doi.org/10.1016/j.mtcomm.2018.09.024.

[106] L. Wang, Q. Xiong, F. Xiao, H. Duan, 2D nanomaterials based electrochemical biosensors for cancer diagnosis, Biosens. Bioelectron. 89 (2017) 136–151. https://doi.org/10.1016/j.bios.2016.06.011.

[107] T. Akyazi, L. Basabe-Desmonts, F. Benito-Lopez, Review on microfluidic paper-based analytical devices towards commercialisation, Anal. Chim. Acta. 1001 (2018) 1–17. https://doi.org/10.1016/j.aca.2017.11.010.

[108] M.M. Bordbar, A. Sheini, P. Hashemi, A. Hajian, H. Bagheri, Disposable paper-based biosensors for the point-of-care detection of hazardous contaminations—a review, Biosensors. 11 (2021) 1–51. https://doi.org/10.3390/bios11090316.

[109] R. Ariati, F. Sales, A. Souza, R.A. Lima, J. Ribeiro, Polydimethylsiloxane composites characterization and its applications: A review, Polymers (Basel). 13 (2021) 1–21. https://doi.org/10.3390/polym13234258.

[110] D.R. Thévenot, K. Toth, R.A. Durst, G.S. Wilson, Electrochemical Biosensors: Recommended definitions and classification, Biosens. Bioelectron. 16 (2001) 121–131. https://doi.org/10.1081/AL-100103209.

[111] J.L. Hammond, N. Formisano, P. Estrela, S. Carrara, J. Tkac, Electrochemical biosensors and nanobiosensors, Essays Biochem. 60 (2016) 69–80. https://doi.org/10.1042/EBC20150008.

[112] T.A.N. (University of I. Douglas A. Skoog, (Stanford University), F. James Holler (University of Kentucky), An Introduction to Electroanalytical Chemistry, in: Princ. Instrum. Anal., 5th ed., Thomson Learning, 1998: pp. 566–567.

[113] P.M. Biesheuvel, S. Porada, J.E. Dykstra, The difference between Faradaic and non-Faradaic electrode processes, (2018) 1–16. http://arxiv.org/abs/1809.02930.

[114] O.J. Guy, K.A.D. Walker, Graphene Functionalization for Biosensor Applications, Second Edi, Elsevier Inc., 2016. https://doi.org/10.1016/B978-0-12-802993-0.00004-6.

[115] C. Batchelor-Mcauley, E. Kätelhön, E.O. Barnes, R.G. Compton, E. Laborda, A. Molina, Recent Advances in Voltammetry, ChemistryOpen. 4 (2015) 224–260. https://doi.org/10.1002/open.201500042.

[116] N. Elgrishi, K.J. Rountree, B.D. McCarthy, E.S. Rountree, T.T. Eisenhart, J.L. Dempsey, A Practical Beginner's Guide to Cyclic Voltammetry, J. Chem. Educ. 95 (2018) 197–206. https://doi.org/10.1021/acs.jchemed.7b00361.

[117] H.S. Magar, R.Y.A. Hassan, A. Mulchandani, Electrochemical impedance spectroscopy (Eis): Principles, construction, and biosensing applications, Sensors. 21 (2021) 1–21. https://doi.org/10.3390/s21196578.

[118] D. Grieshaber, R. MacKenzie, Janos Voros, E. Reimhult, Electrochemical Biosensors - Sensor Principles and Architectures, Sensors. 8 (2008) 1400–1458. https://doi.org/10.3390/s80314000.

[119] N.O. Laschuk, E.B. Easton, O. V. Zenkina, Reducing the resistance for the use of electrochemical impedance spectroscopy analysis in materials chemistry, RSC Adv. 11 (2021) 27925–27936. https://doi.org/10.1039/d1ra03785d.

[120] N. Brandon, Fuel cells, Encycl. Energy, Vol 2. (2004) 749–758.

[121] M. Muthukumar, N. Rengarajan, B. Velliyangiri, M.A. Omprakas, C.B. Rohit, U.K. Raja, The development of fuel cell electric vehicles - A review, Mater. Today Proc. 45 (2021) 1181–1187. https://doi.org/10.1016/j.matpr.2020.03.679.

[122] N.A. Baharuddin, W.N.A. Wan Yusoff, A.J. Abd Aziz, N.N. Mohd Tahir, Hydrogen fuel cells for sustainable energy: Development and progress in selected developed countries, IOP Conf. Ser. Mater. Sci. Eng. 1078 (2021) 012011. https://doi.org/10.1088/1757-899x/1078/1/012011.

[123] L. Wang, L. Yin, W. Yang, Y. Cheng, F. Wen, C. Liu, L. Dong, M. Wang, S. Ma, X. Feng, Evaluation of structural aspects and operation environments on the performance of passive micro direct methanol fuel cell, Int. J. Hydrogen Energy. 46 (2021) 2594–2605. https://doi.org/10.1016/j.ijhydene.2020.10.114.

[124] A. Kirubakaran, S. Jain, R.K. Nema, A review on fuel cell technologies and power electronic interface, Renew. Sustain. Energy Rev. 13 (2009) 2430–2440. https://doi.org/10.1016/j.rser.2009.04.004.

[125] J. Lindorfer, E. Al., Fuel cells: energy conversion technology, in: Futur. Energy Improv. Sustain. Clean Options Our Planet, 3rd ed., Elsevier Ltd, 2020: pp. 495–517.

[126] F. Cipitì, L. Pino, A. Vita, M. Laganà, V. Recupero, Experimental investigation on a methane fuel processor for polymer electrolyte fuel cells, Int. J. Hydrogen Energy. 38 (2013) 2387–2397. https://doi.org/10.1016/j.ijhydene.2012.11.143.

[127] N. Shaari, S.K. Kamarudin, R. Bahru, S.H. Osman, N.A.I. Md Ishak, Progress and challenges: Review for direct liquid fuel cell, Int. J. Energy Res. 45 (2021) 6644–6688. https://doi.org/10.1002/er.6353.

[128] Y. Wang, S. Luo, H.Y.H. Kwok, W. Pan, Y. Zhang, X. Zhao, D.Y.C. Leung, Microfluidic fuel cells with different types of fuels: A prospective review, Renew. Sustain. Energy Rev. 141 (2021) 110806. https://doi.org/10.1016/j.rser.2021.110806.

[129] N. Mahato, A. Banerjee, A. Gupta, S. Omar, K. Balani, Progress in material selection for solid oxide fuel cell technology: A review, Prog. Mater. Sci. 72 (2015) 141–337. https://doi.org/10.1016/j.pmatsci.2015.01.001.

[130] X. Li, A. Faghri, Review and advances of direct methanol fuel cells (DMFCs) part I : Design , fabrication , and testing with high concentration methanol solutions, J. Power Sources. 226 (2013) 223–240. https://doi.org/10.1016/j.jpowsour.2012.10.061.

[131] A.S. Aricò, S. Srinivasan, V. Antonucci, DMFCs: From Fundamental Aspects to Technology Development, Fuel Cells. 1 (2001) 133–161. https://doi.org/10.1002/1615-6854(200107)1:2<133::AID-FUCE133>3.3.CO;2-X.

[132] A.M.F.R. Pinto, V.B. Oliveira, D.S. Falcão, Direct Alcohol Fuel Cells for Portable Applications Fundamentals, Engineering and Advances, 1st Editio, Elsevier, 2018. https://doi.org/https://doi.org/10.1016/C2016-0-00632-0.

[133] L. Xing, W. Shi, H. Su, Q. Xu, P.K. Das, B. Mao, K. Scott, Membrane electrode assemblies for PEM fuel cells: A review of functional graded design and optimization, Energy. 177 (2019) 445–464. https://doi.org/10.1016/j.energy.2019.04.084.

[134] L. Chen, R. Zhang, Q. Kang, W.Q. Tao, Pore-scale study of pore-ionomer interfacial reactive transport processes in proton exchange membrane fuel cell catalyst layer, Chem. Eng. J. 391 (2020) 123590. https://doi.org/10.1016/j.cej.2019.123590.

[135] D. Niblett, A. Mularczyk, V. Niasar, J. Eller, S. Holmes, Two-phase flow dynamics in a gas diffusion layer - gas channel - microporous layer system, J. Power Sources. 471 (2020) 228427. https://doi.org/10.1016/j.jpowsour.2020.228427.

[136] K. Malek, M. Eikerling, Q. Wang, T. Navessin, Z. Liu, Self-organization in catalyst layers of polymer electrolyte fuel cells, J. Phys. Chem. C. 111 (2007) 13627–13634. https://doi.org/10.1021/jp072692k.

[137] F. Kadirgan, A.M. Kannan, T. Atilan, S. Beyhan, S.S. Ozenler, S. Suzer, A. Yörür, Carbon supported nano-sized Pt-Pd and Pt-Co electrocatalysts for proton exchange membrane fuel cells, Int. J. Hydrogen Energy. 34 (2009) 9450–9460. https://doi.org/10.1016/j.ijhydene.2009.09.028.

[138] A.G. Olabi, M.A. Abdelkareem, T. Wilberforce, E.T. Sayed, Application of graphene in energy storage device – A review, Renew. Sustain. Energy Rev. 135 (2021) 110026. https://doi.org/10.1016/j.rser.2020.110026.

[139] T. Page, R. Johnson, J. Hormes, S. Noding, B. Rambabu, Study of methanol electro-oxidation reactions in carbon membrane electrodes and structural properties of Pt alloy electro-catalysts by EXAFS, J. Electroanal. Chem. 485 (2000) 34–41. https://doi.org/10.1016/S0022-0728(00)00090-5.

[140] R.E. Schaak, A.K. Sra, B.M. Leonard, R.E. Cable, J.C. Bauer, Y.F. Han, J. Means, W. Teizer, Y. Vasquez, E.S. Funck, Metallurgy in a beaker: Nanoparticle toolkit for the rapid low-temperature solution synthesis of functional multimetallic solid-state materials, J. Am. Chem. Soc. 127 (2005) 3506–3515. https://doi.org/10.1021/ja043335f.

[141] E. Urbańczyk, A. Jaroń, W. Simka, Ni–Pt sinter as a promising electrode for methanol electrocatalytic oxidation, Int. J. Hydrogen Energy. 43 (2018) 17156–17163. https://doi.org/10.1016/j.ijhydene.2018.07.109.

[142] J.C.C. Gómez, R. Moliner, M.J. Lázaro, Palladium-based catalysts as electrodes for direct methanol fuel cells: A last ten years review, Catalysts. 6 (2016) 1–20. https://doi.org/10.3390/catal6090130.

[143] J. Lee, J.M. Yoo, Y. Ye, Y. Mun, S. Lee, O.H. Kim, H.W. Rhee, H.I. Lee, Y.E. Sung, J. Lee, Development of highly stable and mass transfer-enhanced cathode catalysts: Support-free electrospun intermetallic FePt nanotubes for polymer electrolyte membrane fuel cells, Adv. Energy Mater. 5 (2015) 1–9. https://doi.org/10.1002/aenm.201402093.

[144] O. Sahin, H. Kivrak, A comparative study of electrochemical methods on Pt-Ru DMFC anode catalysts: The effect of Ru addition, Int. J. Hydrogen Energy. 38 (2013) 901–909. https://doi.org/10.1016/j.ijhydene.2012.10.066.

[145] S.S. Munjewar, S.B. Thombre, R.K. Mallick, Approaches to overcome the barrier issues of passive direct methanol fuel cell – Review, Renew. Sustain. Energy Rev. 67 (2017)

1087–1104. https://doi.org/10.1016/j.rser.2016.09.002.

[146] L. Jiang, A. Hsu, D. Chu, R. Chen, Oxygen Reduction Reaction on Carbon Supported Pt and Pd in Alkaline Solutions, J. Electrochem. Soc. 156 (2009) B370. https://doi.org/10.1149/1.3058586.

[147] J.Y. Lee, D.H. Kwak, Y.W. Lee, S. Lee, K.W. Park, Synthesis of cubic PtPd alloy nanoparticles as anode electrocatalysts for methanol and formic acid oxidation reactions, Phys. Chem. Chem. Phys. 17 (2015) 8642–8648. https://doi.org/10.1039/c5cp00892a.

[148] Y. Nie, L. Li, Z. Wei, Recent advancements in Pt and Pt-free catalysts for oxygen reduction reaction, Chem. Soc. Rev. 44 (2015) 2168–2201. https://doi.org/10.1039/c4cs00484a.

[149] S. Barazzouk, M. Lefèvre, J.-P. Dodelet, Oxygen Reduction in PEM Fuel Cells: Fe-Based Electrocatalysts Made with High Surface Area Activated Carbon Supports, J. Electrochem. Soc. 156 (2009) B1466. https://doi.org/10.1149/1.3242293.

[150] X. Ren, Q. Lv, L. Liu, B. Liu, Y. Wang, A. Liu, G. Wu, Current progress of Pt and Pt-based electrocatalysts used for fuel cells, Sustain. Energy Fuels. 4 (2019) 15–30. https://doi.org/10.1039/c9se00460b.

[151] F. Gao, H. Xu, Y. Zhang, J. Wang, C. Wang, Y. Du, Facile construction of pompon-like PtAg alloy catalysts for enhanced ethylene glycol electrooxidation, Int. J. Hydrogen Energy. 43 (2018) 9644–9651. https://doi.org/10.1016/j.ijhydene.2018.04.005.

[152] J.B. Xu, T.S. Zhao, W.W. Yang, S.Y. Shen, Effect of surface composition of Pt-Au alloy cathode catalyst on the performance of direct methanol fuel cells, Int. J. Hydrogen Energy. 35 (2010) 8699–8706. https://doi.org/10.1016/j.ijhydene.2010.05.008.

[153] Y.Y. Feng, G.H. Song, Q. Zhang, H.S. Hu, M.Y. Feng, J.Y. Wang, D.S. Kong, Catalytic performance of non-alloyed bimetallic PtAu electrocatalysts for methanol oxidation reaction, Int. J. Hydrogen Energy. 42 (2017) 30109–30118. https://doi.org/10.1016/j.ijhydene.2017.10.102.

[154] N. Singh, Polypyrrole-based emerging and futuristic hybrid nanocomposites, Springer Berlin Heidelberg, 2022. https://doi.org/10.1007/s00289-021-03840-5.

[155] C.I. Idumah, E.O. Ezeani, I.C. Nwuzor, A review: advancements in conductive polymers nanocomposites, Polym. Technol. Mater. 60 (2021) 756–783. https://doi.org/10.1080/25740881.2020.1850783.

[156] S.H. Choi, A.I. Gopalan, J.H. Ryu, K.P. Lee, Hollow spherical nanocapsules of

poly(pyrrole) as a promising support for Pt/Ru nanoparticles based catalyst, Mater. Chem. Phys. 120 (2010) 18–22. https://doi.org/10.1016/j.matchemphys.2009.11.035.

[157] H.B. Bae, J.H. Ryu, B.S. Byun, S.H. Jung, S.H. Choi, Facile synthesis of novel Pt-Ru@PPy-MWNT electrocatalysts for direct methanol fuel cells, Curr. Appl. Phys. 10 (2010) S44–S50. https://doi.org/10.1016/j.cap.2009.11.039.

[158] A.L. Mohana Reddy, N. Rajalakshmi, S. Ramaprabhu, Cobalt-polypyrrole-multiwalled carbon nanotube catalysts for hydrogen and alcohol fuel cells, Carbon N. Y. 46 (2008) 2–11. https://doi.org/10.1016/j.carbon.2007.10.021.

[159] B. Saner, S.A. Gürsel, Y. Yürüm, Layer-by-layer polypyrrole coated graphite oxide and graphene nanosheets as catalyst support materials for fuel cells, Fullerenes Nanotub. Carbon Nanostructures. 21 (2013) 233–247. https://doi.org/10.1080/1536383X.2011.613536.

[160] K.K. Tintula, S. Pitchumani, P. Sridhar, A.K. Shukla, PEDOT-PSSA as an alternative support for Pt electrodes in PEFCs, Bull. Mater. Sci. 33 (2010) 157–163. https://doi.org/10.1007/s12034-010-0022-z.

[161] K.K. Tintula, A. Jalajakshi, A.K. Sahu, S. Pitchumani, P. Sridhar, A.K. Shukla, Durability of Pt/C and Pt/MC-PEDOT catalysts under simulated start-stop cycles in polymer electrolyte fuel cells, Fuel Cells. 13 (2013) 158–166. https://doi.org/10.1002/fuce.201200158.

[162] E. Daş, A. Bayrakçeken Yurtcan, PEDOT/C Composites used as a Proton Exchange Membrane Fuel Cell Catalyst Support: Role of Carbon Amount, Energy Technol. 5 (2017) 1552–1560. https://doi.org/10.1002/ente.201600779.

[163] R. Rashidi, I. Dincer, G.F. Naterer, P. Berg, Performance evaluation of direct methanol fuel cells for portable applications, J. Power Sources. 187 (2009) 509–516. https://doi.org/10.1016/j.jpowsour.2008.11.044.

[164] T.S. Zhao, R. Chen, W.W. Yang, C. Xu, Small direct methanol fuel cells with passive supply of reactants, J. Power Sources. 191 (2009) 185–202. https://doi.org/10.1016/j.jpowsour.2009.02.033.

[165] B. Bohunicky, S.A. Mousa, Biosensors: The new wave in cancer diagnosis, Nanotechnol. Sci. Appl. 4 (2011) 1–10. https://doi.org/10.2147/NSA.S13465.

[166] P. Martinkova, A. Kostelnik, T. Valek, M. Pohanka, Main streams in the Construction of Biosensors and Their Applications, Int. J. Electrochem. Sci. 12 (2017) 7386–7403. https://doi.org/10.20964/2017.08.02.

[167] I.E. Tothill, Biosensors for cancer markers diagnosis, Semin. Cell Dev. Biol. 20 (2009) 55–62. https://doi.org/10.1016/j.semcdb.2009.01.015.

[168] H. Sharma, R. Mutharasan, Review of biosensors for foodborne pathogens and toxins, Sensors Actuators, B Chem. 183 (2013) 535–549. https://doi.org/10.1016/j.snb.2013.03.137.

[169] L.A.A.N.A. Truta, F.T.C. Moreira, M.G.F. Sales, A dye-sensitized solar cell acting as the electrical reading box of an immunosensor: Application to CEA determination, Biosens. Bioelectron. 107 (2018) 94–102. https://doi.org/10.1016/j.bios.2018.02.011.

[170] A.P.M. Tavares, L.A.A.N.A. Truta, F.T.C. Moreira, L.P.T. Carneiro, M.G.F. Sales, Self-powered and self-signalled autonomous electrochemical biosensor applied to cancinoembryonic antigen determination, Biosens. Bioelectron. 140 (2019) 111320. https://doi.org/10.1016/j.bios.2019.111320.

[171] C.M.R. and A.M.F.R.P. Vânia B. Oliveira, Daniela S. Falcão, Water management in a passive direct methanol fuel cell, Int. J. ENERGY Res. 37 (2012) 991–1001. https://doi.org/10.1002/er.

[172] B.A. Berns, M.F. Torres, V.B. Oliveira, A.M.F.R. Pinto, Performance of passive direct methanol fuel cell: Modelling and experimental studies, U.Porto J. Eng. 1 (2015) 89–103. https://doi.org/10.24840/2183-6493_001.001_0009.

[173] M.G.F. Sales, L. Brandão, Autonomous electrochemical biosensors: A new vision to direct methanol fuel cells, Biosens. Bioelectron. 98 (2017) 428–436. https://doi.org/10.1016/j.bios.2017.07.021.

[174] J.Y. Huang, L. Zhao, W. Lei, W. Wen, Y.J. Wang, T. Bao, H.Y. Xiong, X.H. Zhang, S.F. Wang, A high-sensitivity electrochemical aptasensor of carcinoembryonic antigen based on graphene quantum dots-ionic liquid-nafion nanomatrix and DNAzyme-assisted signal amplification strategy, Biosens. Bioelectron. 99 (2018) 28–33. https://doi.org/10.1016/j.bios.2017.07.036.

[175] A.O. Idris, N. Mabuba, O.A. Arotiba, An Exfoliated Graphite-Based Electrochemical Immunosensor on a Dendrimer / Carbon Nanodot Platform for the Detection of Carcinoembryonic Antigen Cancer Biomarker, Biosensors. 9 (2019) 1–16. https://doi.org/10.3390/bios9010039.

[176] R. Al-Swayeh, S. N.Alvi, M. M.Hammami, A validated HPLC method for the determination of ranitidine in human plasma: Application to bioavailability studies, Anal. Chem. An Indian J. 15 (2014) 339–344.

http://www.publicationhosting.org/toc/article.php?id=2730[12/17/2014 5:19:28 PM].

[177] J. Wu, X. Zi, H. Wang, M. Blanco, J.J. Martin, J. Zhang, Diagnostic tools in PEM fuel cell research : Part I Electrochemical techniques, Int. J. Hydrogen Energy. 33 (2008) 1735–1746. https://doi.org/10.1016/j.ijhydene.2008.01.013.

[178] J. Feng, X. Li, H. Cheng, W. Huang, H. Kong, Y. Li, L. Li, A boronate-modified molecularly imprinted polymer labeled with a SERS-tag for use in an antibody-free immunoassay for the carcinoembryonic antigen, Microchim. Acta. 186 (2019) 1–9. https://doi.org/10.1007/s00604-019-3972-x.

[179] R. Li, F. Feng, Z.Z. Chen, Y.F. Bai, F.F. Guo, F.Y. Wu, G. Zhou, Sensitive detection of carcinoembryonic antigen using surface plasmon resonance biosensor with gold nanoparticles signal amplification, Talanta. 140 (2015) 143–149. https://doi.org/10.1016/j.talanta.2015.03.041.

[180] S. Kumar, M. Umar, A. Saifi, S. Kumar, S. Augustine, S. Srivastava, B.D. Malhotra, Electrochemical paper based cancer biosensor using iron oxide nanoparticles decorated PEDOT:PSS, Anal. Chim. Acta. 1056 (2019) 135–145. https://doi.org/10.1016/j.aca.2018.12.053.

[181] J. Han, Y. Li, J. Feng, M. Li, P. Wang, Z. Chen, Y. Dong, A novel sandwich-type immunosensor for detection of carcino-embryonic antigen using silver hybrid multiwalled carbon nanotubes/manganese dioxide, J. Electroanal. Chem. 786 (2017) 112–119. https://doi.org/10.1016/j.jelechem.2017.01.021.

[182] J. Huang, L. Zhao, W. Lei, W. Wen, Y. Wang, T. Bao, H. Xiong, X.-H. Zhang, S.-F. Wang, Biosensors and Bioelectronics A high-sensitivity electrochemical aptasensor of carcinoembryonic antigen based on graphene quantum dots-ionic liquid-na fi on nanomatrix and DNAzyme-assisted signal ampli fi cation strategy, Biosens. Bioelectron. 99 (2018) 28–33. https://doi.org/10.1016/j.bios.2017.07.036.

[183] M.C.C.G. Carneiro, A. Sousa-Castillo, M.A. Correa-Duarte, M.G.F. Sales, Dual biorecognition by combining molecularly-imprinted polymer and antibody in SERS detection. Application to carcinoembryonic antigen, Biosens. Bioelectron. 146 (2019) 111761. https://doi.org/10.1016/j.bios.2019.111761.

[184] Y. Yu, Q. Zhang, J. Buscaglia, C.C. Chang, Y. Liu, Z. Yang, Y. Guo, Y. Wang, K. Levon, M. Rafailovich, Quantitative real-time detection of carcinoembryonic antigen (CEA) from pancreatic cyst fluid using 3-D surface molecular imprinting, Analyst. 141 (2016) 4424–4431. https://doi.org/10.1039/c6an00375c.

[185] J. Qi, B. Li, N. Zhou, X. Wang, D. Deng, L. Luo, L. Chen, The strategy of antibody-free biomarker analysis by in-situ synthesized molecularly imprinted polymers on movable valve paper-based device, Biosens. Bioelectron. 142 (2019) 111533. https://doi.org/10.1016/j.bios.2019.111533.

[186] S. Vigneshvar, C.C. Sudhakumari, B. Senthilkumaran, H. Prakash, Recent advances in biosensor technology for potential applications - an overview, Front. Bioeng. Biotechnol. 4 (2016) 1–9. https://doi.org/10.3389/fbioe.2016.00011.

[187] A.A. Karyakin, Glucose biosensors for clinical and personal use, Electrochem. Commun. 125 (2021) 106973. https://doi.org/10.1016/j.elecom.2021.106973.

[188] L. Su, W. Jia, C. Hou, Y. Lei, Microbial biosensors: A review, Biosens. Bioelectron. 26 (2011) 1788–1799. https://doi.org/10.1016/j.bios.2010.09.005.

[189] H. Yang, M. Zhou, Mengmeng Liu, Weilu Yang, Tingyue Gu, Microbial fuel cells for biosensor applications, Biotechnol. Lett. 37 (2015) 2357–2364. https://doi.org/10.1007/s10529-015-1929-7.

[190] C. Santoro, C. Arbizzani, B. Erable, I. Ieropoulos, Microbial fuel cells: From fundamentals to applications. A review, J. Power Sources. 356 (2017) 225–244. https://doi.org/10.1016/j.jpowsour.2017.03.109.

[191] F.T.C. Moreira, M.G.F. Sale, M. Di Lorenzo, Towards timely Alzheimer diagnosis: A self-powered amperometric biosensor for the neurotransmitter acetylcholine, Biosens. Bioelectron. 87 (2017) 607–614. https://doi.org/10.1016/j.bios.2016.08.104.

[192] M. Grattieri, S.D. Minteer, Self-Powered Biosensors, ACS Sensors. 3 (2018) 44–53. https://doi.org/10.1021/acssensors.7b00818.

[193] L.P.T. Carneiro, N.S. Ferreira, A.P.M. Tavares, A.M.F.R. Pinto, A. Mendes, M.G.F. Sales, A passive direct methanol fuel cell as transducer of an electrochemical sensor, applied to the detection of carcinoembryonic antigen, Biosens. Bioelectron. 175 (2021) 1–9. https://doi.org/10.1016/j.bios.2020.112877.

[194] L.P.T. Carneiro, N.S. Ferreira, A.P.M. Tavares, A.M.F.R. Pinto, A. Mendes, M.G.F. Sales, A passive direct methanol fuel cell as transducer of an electrochemical sensor, applied to the detection of carcinoembryonic antigen, Biosens. Bioelectron. 175 (2021) 1–9. https://doi.org/10.1016/j.bios.2020.112877.

[195] X.L. Zhou, T.S. Zhao, Y.K. Zeng, L. An, L. Wei, A highly permeable and enhanced surface area carbon-cloth electrode for vanadium redox flow batteries, J. Power Sources. 329 (2016) 247–254. https://doi.org/10.1016/j.jpowsour.2016.08.085.

[196] B. Winther-Jensen, D.R. MacFarlane, New generation, metal-free electrocatalysts for fuel cells, solar cells and water splitting, Energy Environ. Sci. 4 (2011) 2790–2798. https://doi.org/10.1039/c0ee00652a.

[197] W.W. Chiu, J. Travaš-Sejdić, R.P. Cooney, G.A. Bowmaker, Studies of dopant effects in poly(3,4-ethylenedioxythiophene) using Raman spectroscopy, J. Raman Spectrosc. 37 (2006) 1354–1361. https://doi.org/10.1002/jrs.1545.

[198] C. Cerezo-Navarrete, Y. Mathieu, M. Puche, C. Morales, P. Concepción, L.M. Martínez-Prieto, A. Corma, Controlling the selectivity of bimetallic platinum-ruthenium nanoparticles supported on N-doped graphene by adjusting their metal composition, Catal. Sci. Technol. 11 (2021) 494–505. https://doi.org/10.1039/d0cy02379e.

[199] Q.H. Yang, P.X. Hou, M. Unno, S. Yamauchi, R. Saito, T. Kyotani, Dual Raman features of double coaxial carbon nanotubes with N-doped and B-doped multiwalls, 5 (2005) 2465–2469. https://doi.org/10.1021/nl051779j.

[200] W.W. Chiu, J. Travaˇ, R.P. Cooney, G.A. Bowmaker, Spectroscopic and conductivity studies of doping in chemically synthesized poly(3,4-ethylenedioxythiophene), Synt. Met. 155 (2005) 80–88. https://doi.org/10.1016/j.synthmet.2005.06.012.

[201] T.H. Kim, J.Y. Yi, C.Y. Jung, E. Jeong, S.C. Yi, Solvent effect on the Nafion agglomerate morphology in the catalyst layer of the proton exchange membrane fuel cells, Int. J. Hydrogen Energy. 42 (2017) 478–485. https://doi.org/10.1016/j.ijhydene.2016.12.015.

[202] M. Niyaz, N. Sawut, R. Jamal, T. Abdiryim, Z. Helil, H. Liu, S. Xie, Y. Song, Preparation of PEDOT-modified double-layered hollow carbon spheres as Pt catalyst support for methanol oxidation, Int. J. Hydrogen Energy. 46 (2021) 31623–31633. https://doi.org/10.1016/j.ijhydene.2021.07.069.

[203] C. Wang, K. Zhang, H. Xu, Y. Du, M.C. Goh, Anchoring gold nanoparticles on poly(3,4-ethylenedioxythiophene) (PEDOT) nanonet as three-dimensional electrocatalysts toward ethanol and 2-propanol oxidation, J. Colloid Interface Sci. 541 (2019) 258–268. https://doi.org/10.1016/j.jcis.2019.01.055.

[204] Y.H. Chan, T.S. Zhao, R. Chen, C. Xu, A self-regulated passive fuel-feed system for passive direct methanol fuel cells, J. Power Sources. 176 (2008) 183–190. https://doi.org/10.1016/j.jpowsour.2007.10.050.

[205] M.S. Alias, S.K. Kamarudin, A.M. Zainoodin, M.S. Masdar, Structural mechanism investigation on methanol crossover and stability of a passive direct methanol fuel cell performance via modified micro-porous layer, Int. J. Energy Res. 45 (2021) 12928–12943.

https://doi.org/10.1002/er.6624.

[206] A. Pavlišič, J. Jovanovič, V.S. šelih, N. Hodnik, S. Hočevar, M. Gaberšček, The influence of chloride impurities on Pt/C fuel cell catalyst corrosion, Chem. Commun. 50 (2014) 3732–3734. https://doi.org/10.1039/c4cc00086b.

[207] J.P. Pereira, D.S. Falcão, V.B. Oliveira, A.M.F.R. Pinto, Performance of a passive direct ethanol fuel cell, J. Power Sources. 256 (2014) 14–19. https://doi.org/10.1016/j.jpowsour.2013.12.036.

[208] K. Elsaid, S. Abdelfatah, A.M. Abdel Elabsir, R.J. Hassiba, Z.K. Ghouri, L. Vechot, Direct alcohol fuel cells: Assessment of the fuel's safety and health aspects, Int. J. Hydrogen Energy. 46 (2021) 30658–30668. https://doi.org/10.1016/j.ijhydene.2020.12.009.

[209] T.J. Leo, M.A. Raso, E. Navarro, E.S. De La Blanca, M. Villanueva, B. Moreno, Response of a direct methanol fuel cell to fuel change, Int. J. Hydrogen Energy. 35 (2010) 11642–11648. https://doi.org/10.1016/j.ijhydene.2010.02.115.

[210] A.M. López-Marzo, A. Merkoçi, Paper-based sensors and assays: A success of the engineering design and the convergence of knowledge areas, Lab Chip. 16 (2016) 3150–3176. https://doi.org/10.1039/c6lc00737f.

[211] S. Marquez, E. Morales-Narváez, Nanoplasmonics in paper-based analytical devices, Front. Bioeng. Biotechnol. 7 (2019) 1–10. https://doi.org/10.3389/fbioe.2019.00069.

[212] A.T. Singh, D. Lantigua, A. Meka, S. Taing, M. Pandher, G. Camci-Unal, Paper-based sensors: Emerging themes and applications, Sensors (Switzerland). 18 (2018) 1–22. https://doi.org/10.3390/s18092838.

[213] M. Gutiérrez-capitán, A. Baldi, C. Fernández-sánchez, Electrochemical paper-based biosensor devices for rapid detection of biomarkers, Sensors (Switzerland). 20 (2020) 1–15. https://doi.org/10.3390/s20040967.

[214] Y. Zhang, L. Zhang, K. Cui, S. Ge, X. Cheng, M. Yan, J. Yu, H. Liu, Flexible electronics based on micro/nanostructured paper, Adv. Mater. 30 (2018) 1–39. https://doi.org/10.1002/adma.201801588.

[215] D. Zhao, Y. Zhu, W. Cheng, W. Chen, Y. Wu, H. Yu, Cellulose-Based Flexible Functional Materials for Emerging Intelligent Electronics, Adv. Mater. 33 (2021) 1–18. https://doi.org/10.1002/adma.202000619.

[216] Z. Nie, F. Deiss, X. Liu, O. Akbulut, G.M. Whitesides, Integration of paper-based microfluidic devices with commercial electrochemical readers, Lab Chip. 10 (2010) 3163–

3169. https://doi.org/10.1039/c0lc00237b.

[217] Y. Xia, J. Si, Z. Li, Fabrication techniques for microfluidic paper-based analytical devices and their applications for biological testing: A review, Biosens. Bioelectron. 77 (2016) 774–789. https://doi.org/10.1016/j.bios.2015.10.032.

[218] J. Mettakoonpitak, K. Boehle, S. Nantaphol, P. Teengam, J.A. Adkins, M. Srisa-Art, C.S. Henry, Electrochemistry on Paper-based Analytical Devices: A Review, Electroanalysis. 28 (2016) 1420–1436. https://doi.org/10.1002/elan.201501143.

[219] M.M. Gong, D. Sinton, Turning the Page: Advancing Paper-Based Microfluidics for Broad Diagnostic Application, Chem. Rev. 117 (2017) 8447–8480. https://doi.org/10.1021/acs.chemrev.7b00024.

[220] T. Ozer, C. McMahon, C.S. Henry, Advances in Paper-Based Analytical Devices, Annu. Rev. Anal. Chem. 13 (2020) 85–109. https://doi.org/10.1146/annurev-anchem-061318-114845.

[221] E. Noviana, C.S. Henry, Simultaneous electrochemical detection in paper-based analytical devices, Curr. Opin. Electrochem. 23 (2020) 1–6. https://doi.org/10.1016/j.coelec.2020.02.013.

[222] S.A. Mousavi Shaegh, N.T. Nguyen, S.H. Chan, Air-breathing microfluidic fuel cell with fuel reservoir, J. Power Sources. 209 (2012) 312–317. https://doi.org/10.1016/j.jpowsour.2012.02.115.

[223] L.L. Shen, G.R. Zhang, T. Venter, M. Biesalski, B.J.M. Etzold, Towards best practices for improving paper-based microfluidic fuel cells, Electrochim. Acta. 298 (2019) 389–399. https://doi.org/10.1016/j.electacta.2018.12.077.

[224] S. Chandra, S. Lal, V.M. Janardhanan, K.C. Sahu, M. Deepa, Ethanol based fuel cell on paper support, J. Power Sources. 396 (2018) 725–733. https://doi.org/10.1016/j.jpowsour.2018.06.068.

[225] I.D.M. De Barcelona, I. Csic, DISPOSABLE HYDROGEN FUEL CELLS FOR POWERING NEXT-GENERATION University of Washington , Department of Bioengineering , Seattle , WA , USA Instituto de Catálisis y Petroleoquímica , ICP (CSIC), Madrid , SPAIN, (2015) 66–69.

[226] Y. Wang, H.Y.H. Kwok, Y. Zhang, W. Pan, H. Zhang, X. Lu, D.Y.C. Leung, A flexible paper-based hydrogen fuel cell for small power applications, Int. J. Hydrogen Energy. 44 (2019) 29680–29691. https://doi.org/10.1016/j.ijhydene.2019.04.066.

[227] J.P. Esquivel, F.J. Del Campo, J.L. Gómez De La Fuente, S. Rojas, N. Sabaté, Microfluidic fuel cells on paper: Meeting the power needs of next generation lateral flow devices, Energy Environ. Sci. 7 (2014) 1744–1749. https://doi.org/10.1039/c3ee44044c.

[228] R.K. Arun, S. Halder, N. Chanda, S. Chakraborty, A paper based self-pumping and self-breathing fuel cell using pencil stroked graphite electrodes, Lab Chip. 14 (2014) 1661–1664. https://doi.org/10.1039/c4lc00029c.

[229] S. Lal, V.M. Janardhanan, M. Deepa, A. Sagar, K.C. Sahu, Low Cost Environmentally Benign Porous Paper Based Fuel Cells for Micro-Nano Systems, J. Electrochem. Soc. 162 (2015) F1402–F1407. https://doi.org/10.1149/2.0251514jes.

[230] F. Achmad, S.K. Kamarudin, W.R.W. Daud, E.H. Majlan, Passive direct methanol fuel cells for portable electronic devices, Appl. Energy. 88 (2011) 1681–1689. https://doi.org/10.1016/j.apenergy.2010.11.012.

[231] T. Wilberforce, A. Alaswad, A. Palumbo, M. Dassisti, A.G. Olabi, Advances in stationary and portable fuel cell applications, Int. J. Hydrogen Energy. 41 (2016) 16509–16522. https://doi.org/10.1016/j.ijhydene.2016.02.057.

[232] E.J. Ryan, E.M. Creagh, Emerging methods in colorectal cancer screening, Br. J. Surg. 105 (2018) e16–e18. https://doi.org/10.1002/bjs.10650.

[233] A.P. Khan, T.M. Rajendiran, B. Ateeq, I.A. Asangani, J.N. Athanikar, A.K. Yocum, R. Mehra, J. Siddiqui, G. Palapattu, J.T. Wei, G. Michailidis, A. Sreekumar, A.M. Chinnaiyan, The role of sarcosine metabolism in prostate cancer progression, Neoplasia (United States). 15 (2013) 491–501. https://doi.org/10.1593/neo.13314.

[234] A. Roy, Y.P. Chen, J.T. Qiu, S. Maikap, Sarcosine Prostate Cancer Biomarker Detection by Controlling Oxygen in NiOxMembrane on Vertical Silicon Nanowires in Electrolyte-Insulator-Nanowire Structure, Anal. Chem. 92 (2020) 8064–8071. https://doi.org/10.1021/acs.analchem.9b04745.

[235] J.N. Tiwari, R.N. Tiwari, G. Singh, K.S. Kim, Recent progress in the development of anode and cathode catalysts for direct methanol fuel cells, Nano Energy. 2 (2013) 553–578. https://doi.org/10.1016/j.nanoen.2013.06.009.

[236] R. Chen, T.S. Zhao, A novel electrode architecture for passive direct methanol fuel cells, Electrochem. Commun. 9 (2007) 718–724. https://doi.org/10.1016/j.elecom.2006.11.004.

[237] Z. Long, L. Gong, Y. Sun, Y. Li, P. Xu, X. Zhang, J. Ge, C. Liu, S. Ma, Z. Jin, In-situ precise electrocatalytic behaviors of Pt/C and PtRu/C for methanol oxidation of DMFCs via the designed micro-MEA, Int. J. Hydrogen Energy. 43 (2018) 12413–12419.

https://doi.org/10.1016/j.ijhydene.2018.05.024.

[238] Y. Zhang, D.P. Wilkinson, F. Taghipour, Performance Analysis of an Air-Breathing Micro-Direct Methanol Fuel Cell with an Extended Anode Region, Fuel Cells. 20 (2020) 634–642. https://doi.org/10.1002/fuce.201900165.

[239] L. Bokobza, J.L. Bruneel, M. Couzi, Raman spectroscopic investigation of carbon-based materials and their composites. Comparison between carbon nanotubes and carbon black, Chem. Phys. Lett. 590 (2013) 153–159. https://doi.org/10.1016/j.cplett.2013.10.071.

[240] M.S. Dresselhaus, A. Jorio, R. Saito, Characterizing graphene, graphite, and carbon nanotubes by Raman spectroscopy, Annu. Rev. Condens. Matter Phys. 1 (2010) 89–108. https://doi.org/10.1146/annurev-conmatphys-070909-103919.

[241] L.P.T. Carneiro, A.M.F.R. Pinto, A. Mendes, M. Goreti, An all-in-one approach for self-powered sensing: A methanol fuel cell modified with a molecularly imprinted polymer for cancer biomarker detection, J. Electroanal. Chem. 906 (2022) 116009. https://doi.org/10.1016/j.jelechem.2022.116009.

[242] M.M. Ghosh S, Das S, Conducting Polymer-Based Nanohybrids for Fuel Cell Application, Polym. 15 (2020) 1–19. doi: 10.3390/polym12122993. PMID: 33333881; PMCID: PMC7765313.

[243] K.K. Tintula, S. Pitchumani, P. Sridhar, A.K. Shukla, A solid-polymer-electrolyte direct methanol fuel cell (DMFC) with Pt-Ru nanoparticles supported onto poly(3,4-ethylenedioxythiophene) and polystyrene sulphonic acid polymer composite as anode, J. Chem. Sci. 122 (2010) 381–389. https://doi.org/10.1007/s12039-010-0043-6.

[244] C.F. Hsu, L. Zhang, H. Peng, J. Travas-Sejdic, P.A. Kilmartin, Free radical scavenging properties of polypyrrole and poly(3,4-ethylenedioxythiophene), Curr. Appl. Phys. 8 (2008) 316–319. https://doi.org/10.1016/j.cap.2007.10.049.

[245] J.M. Lin, Y.L. Su, W.T. Chang, W.Y. Su, S.H. Cheng, Strong adsorption characteristics of a novel overoxidized poly(3,4-ethylenedioxythiophene) film and application for dopamine sensing, Electrochim. Acta. 149 (2014) 65–75. https://doi.org/10.1016/j.electacta.2014.10.030.

[246] M. Wang, L. Zou, J. Liang, X. Wang, D. Zhang, Y. Fang, J. Zhang, F. Xiao, M. Liu, The urinary sarcosine/creatinine ratio is a potential diagnostic and prognostic marker in prostate cancer, Med. Sci. Monit. 24 (2018) 3034–3041. https://doi.org/10.12659/MSM.909949.

[247] M. Mathew, S. Radhakrishnan, A. Vaidyanathan, B. Chakraborty, C.S. Rout, Flexible and

wearable electrochemical biosensors based on two-dimensional materials: Recent developments, Anal. Bioanal. Chem. 413 (2021) 727–762. https://doi.org/10.1007/s00216-020-03002-y.

[248] J. Yoon, H.Y. Cho, M. Shin, H.K. Choi, T. Lee, J.W. Choi, Flexible electrochemical biosensors for healthcare monitoring, J. Mater. Chem. B. 8 (2020) 7303–7318. https://doi.org/10.1039/d0tb01325k.

[249] M. Bariya, Z. Shahpar, H. Park, J. Sun, Y. Jung, W. Gao, H.Y.Y. Nyein, T.S. Liaw, L.C. Tai, Q.P. Ngo, M. Chao, Y. Zhao, M. Hettick, G. Cho, A. Javey, Roll-to-Roll Gravure Printed Electrochemical Sensors for Wearable and Medical Devices, ACS Nano. 12 (2018) 6978–6987. https://doi.org/10.1021/acsnano.8b02505.

[250] M. Zarei, Portable biosensing devices for point-of-care diagnostics: Recent developments and applications, TrAC - Trends Anal. Chem. 91 (2017) 26–41. https://doi.org/10.1016/j.trac.2017.04.001.

[251] S. Choi, Powering point-of-care diagnostic devices, Biotechnol. Adv. 34 (2016) 321–330. https://doi.org/10.1016/j.biotechadv.2015.11.004.

[252] I.A. de Araujo Andreotti, L.O. Orzari, J.R. Camargo, R.C. Faria, L.H. Marcolino-Junior, M.F. Bergamini, A. Gatti, B.C. Janegitz, Disposable and flexible electrochemical sensor made by recyclable material and low cost conductive ink, J. Electroanal. Chem. 840 (2019) 109–116. https://doi.org/10.1016/j.jelechem.2019.03.059.

[253] M.J. Yee, N.M. Mubarak, E.C. Abdullah, M. Khalid, R. Walvekar, R.R. Karri, S. Nizamuddin, A. Numan, Carbon nanomaterials based films for strain sensing application—A review, Nano-Structures and Nano-Objects. 18 (2019) 100312. https://doi.org/10.1016/j.nanoso.2019.100312.

[254] M.D. Steinberg, P. Kassal, I.M. Steinberg, System Architectures in Wearable Electrochemical Sensors, Electroanalysis. 28 (2016) 1149–1169. https://doi.org/10.1002/elan.201600094.

[255] C.W. Foster, J.P. Metters, C.E. Banks, Ultra flexible paper based electrochemical sensors: Effect of mechanical contortion upon electrochemical performance, Electroanalysis. 25 (2013) 2275–2282. https://doi.org/10.1002/elan.201300274.

[256] T. Lin, Y. Xu, A. Zhao, W. He, F. Xiao, Flexible electrochemical sensors integrated with nanomaterials for in situ determination of small molecules in biological samples: A review, Anal. Chim. Acta. 1207 (2022) 339461. https://doi.org/10.1016/j.aca.2022.339461.

[257] B. Liu, D. Du, X. Hua, X.Y. Yu, Y. Lin, Paper-Based Electrochemical Biosensors: From Test Strips to Paper-Based Microfluidics, Electroanalysis. 26 (2014) 1214–1223. https://doi.org/10.1002/elan.201400036.

[258] K. Ratajczak, M. Stobiecka, High-performance modified cellulose paper-based biosensors for medical diagnostics and early cancer screening: A concise review, Carbohydr. Polym. 229 (2020) 115463. https://doi.org/10.1016/j.carbpol.2019.115463.

[259] J.R. Camargo, L.O. Orzari, D.A.G. Araújo, P.R. de Oliveira, C. Kalinke, D.P. Rocha, A. Luiz dos Santos, R.M. Takeuchi, R.A.A. Munoz, J.A. Bonacin, B.C. Janegitz, Development of conductive inks for electrochemical sensors and biosensors, Microchem. J. 164 (2021) 105998. https://doi.org/10.1016/j.microc.2021.105998.

[260] T. Kant, K. Shrivas, V. Ganesan, Y.K. Mahipal, R. Devi, M.K. Deb, R. Shankar, Flexible printed paper electrode with silver nano-ink for electrochemical applications, Microchem. J. 155 (2020) 104687. https://doi.org/10.1016/j.microc.2020.104687.

[261] Liliana P.T. Carneiro, Nadia S. Ferreira, M.G.F. Sales, Polymer-based nano-inks for fuel cells, in: T.A.N. Ram Gupta (Ed.), Smart Multifunct. Nano-Inks Fundam. Emerg. Appl., 1st ed., Elsevier, 2022: pp. 333–350.

[262] A. Thakur, P. Devi, Paper-based flexible devices for energy harvesting, conversion and storage applications: A review, Nano Energy. 94 (2022) 106927. https://doi.org/10.1016/j.nanoen.2022.106927.

[263] M.B. Kulkarni, N.H. Ayachit, T.M. Aminabhavi, Biosensors and Microfluidic Biosensors: From Fabrication to Application, Biosensors. 12 (2022) 1–25. https://doi.org/10.3390/bios12070543.

[264] C. Cheng, J. Zhang, S. Li, Y. Xia, C. Nie, Z. Shi, J.L. Cuellar-Camacho, N. Ma, R. Haag, A Water-Processable and Bioactive Multivalent Graphene Nanoink for Highly Flexible Bioelectronic Films and Nanofibers, Adv. Mater. 30 (2018) 1–11. https://doi.org/10.1002/adma.201705452.

[265] R. Eivazzadeh-Keihan, E. Bahojb Noruzi, E. Chidar, M. Jafari, F. Davoodi, A. Kashtiaray, M. Ghafori Gorab, S. Masoud Hashemi, S. Javanshir, R. Ahangari Cohan, A. Maleki, M. Mahdavi, Applications of carbon-based conductive nanomaterials in biosensors, Chem. Eng. J. 442 (2022) 136183. https://doi.org/10.1016/j.cej.2022.136183.

[266] M.H. Naveen, N.G. Gurudatt, Y.B. Shim, Applications of conducting polymer composites to electrochemical sensors: A review, Appl. Mater. Today. 9 (2017) 419–433. https://doi.org/10.1016/j.apmt.2017.09.001.

[267] L.P.T. Carneiro, A.M.F.R. Pinto, M.G.F. Sales, Development of an innovative flexible paper-based methanol fuel cell (PB-DMFC) sensing platform – Application to sarcosine detection, Chem. Eng. J. 452 (2023) 139563. https://doi.org/10.1016/j.cej.2022.139563.

[268] N.S. Ferreira, L.P.T. Carneiro, C. Viezzer, M.J.T. Almeida, A.C. Marques, A.M.F.R. Pinto, E. Fortunato, M.G.F. Sales, Passive direct methanol fuel cells acting as fully autonomous electrochemical biosensors: Application to sarcosine detection, J. Electroanal. Chem. 922 (2022) 116710. https://doi.org/10.1016/j.jelechem.2022.116710.

[269] M.M. Ahmad, S.K. Kamarudin, W.R.W. Daud, Z. Yaakub, High power passive μDMFC with low catalyst loading for small power generation, Energy Convers. Manag. 51 (2010) 821–825. https://doi.org/10.1016/j.enconman.2009.11.017.

[270] L. Wang, Z. Yuan, F. Wen, Y. Cheng, Y. Zhang, G. Wang, A bipolar passive DMFC stack for portable applications, Energy. 144 (2018) 587–593. https://doi.org/10.1016/j.energy.2017.12.039.

[271] J.C. Zhu, J. Yu, L. Yin, W. Yang, H. Liu, G.F. Wang, L.W. Wang, W. Cai, A flexible micro direct methanol fuel cells array based on FPCB, Energy Convers. Manag. 258 (2022) 115469. https://doi.org/10.1016/j.enconman.2022.115469.

[272] H. Du, M. Zhang, K. Liu, M. Parit, Z. Jiang, X. Zhang, B. Li, C. Si, Conductive PEDOT:PSS/cellulose nanofibril paper electrodes for flexible supercapacitors with superior areal capacitance and cycling stability, Chem. Eng. J. 428 (2022) 131994. https://doi.org/10.1016/j.cej.2021.131994.

[273] W. Wu, H. Zeng, W. Zhang, W. Zhang, H. Jiang, G. Wu, Z. Li, X. Wang, Y. Huang, Z. Lei, Aqueous in-situ electrosynthesis and electrochromic performance of PEDOT:PSS/Reline film, J. Appl. Polym. Sci. 140 (2022) e53211. https://doi.org/10.1002/app.53211.

[274] Y. Qin, G. Li, Y. Gao, L. Zhang, Y.S. Ok, T. An, Persistent free radicals in carbon-based materials on transformation of refractory organic contaminants (ROCs) in water: A critical review, Water Res. 137 (2018) 130–143. https://doi.org/10.1016/j.watres.2018.03.012.

[275] W. Li, J. Chen, J. Zhao, J. Zhang, J. Zhu, Application of ultrasonic irradiation in preparing conducting polymer as active materials for supercapacitor, Mater. Lett. 59 (2005) 800–803. https://doi.org/10.1016/j.matlet.2004.11.024.

[276] A. Et Taouil, F. Lallemand, J.Y. Hihn, J.M. Melot, V. Blondeau-Patissier, B. Lakard, Doping properties of PEDOT films electrosynthesized under high frequency ultrasound irradiation, Ultrason. Sonochem. 18 (2011) 140–148.

https://doi.org/10.1016/j.ultsonch.2010.04.003.

[277] M. Hujjatul Islam, M.T.Y. Paul, O.S. Burheim, B.G. Pollet, Recent developments in the sonoelectrochemical synthesis of nanomaterials, Ultrason. Sonochem. 59 (2019) 104711. https://doi.org/10.1016/j.ultsonch.2019.104711.

[278] P. Sakunpongpitiporn, K. Phasuksom, N. Paradee, A. Sirivat, Facile synthesis of highly conductive PEDOT:PSS: Via surfactant templates, RSC Adv. 9 (2019) 6363–6378. https://doi.org/10.1039/c8ra08801b.

[279] J. Hossain, Q. Liu, T. Miura, K. Kasahara, D. Harada, R. Ishikawa, K. Ueno, H. Shirai, Nafion-modified PEDOT:PSS as a transparent hole-transporting layer for high-performance crystalline-Si/organic heterojunction solar cells with improved light soaking stability, ACS Appl. Mater. Interfaces. 8 (2016) 31926–31934. https://doi.org/10.1021/acsami.6b10272.

[280] M. Lopez-Haro, L. Guétaz, T. Printemps, A. Morin, S. Escribano, P.H. Jouneau, P. Bayle-Guillemaud, F. Chandezon, G. Gebel, Three-dimensional analysis of Nafion layers in fuel cell electrodes, Nat. Commun. 5 (2014) 1–6. https://doi.org/10.1038/ncomms6229.

[281] G.S. Avcioglu, B. Ficicilar, I. Eroglu, Effect of PTFE nanoparticles in catalyst layer with high Pt loading on PEM fuel cell performance, Int. J. Hydrogen Energy. 41 (2016) 10010–10020. https://doi.org/10.1016/j.ijhydene.2016.03.048.

[282] S. Carli, M. Di Lauro, M. Bianchi, M. Murgia, A. De Salvo, M. Prato, L. Fadiga, F. Biscarini, Water-Based PEDOT:Nafion Dispersion for Organic Bioelectronics, ACS Appl. Mater. Interfaces. 12 (2020) 29807–29817. https://doi.org/10.1021/acsami.0c06538.

[283] Y. Li, N. Hong, An efficient hole transport material based on PEDOT dispersed with lignosulfonate: Preparation, characterization and performance in polymer solar cells, J. Mater. Chem. A. 3 (2015) 21537–21544. https://doi.org/10.1039/c5ta05167c.

[284] B. Yu, Z. Liu, C. Ma, J. Sun, W. Liu, F. Zhou, Ionic liquid modified multi-walled carbon nanotubes as lubricant additive, Tribol. Int. 81 (2015) 38–42. https://doi.org/10.1016/j.triboint.2014.07.019.

[285] W. Yujing, Z. Hongxiu, Z. Ao, Z. Leqing, Numerical simulation of methanol crossover in flowing electrolyte-direct methanol fuel cell, J. Power Sources. 519 (2022) 230801. https://doi.org/10.1016/j.jpowsour.2021.230801.

[286] B. Abderrahim, E. Abderrahman, A. Mohamed, T. Fatima, T. Abdesselam, O. Krim, Kinetic Thermal Degradation of Cellulose, Polybutylene Succinate and a Green

Composite: Comparative Study, World J. Environ. Eng. Vol. 3, 2015, Pages 95-110. 3 (2015) 95–110. https://doi.org/10.12691/WJEE-3-4-1.

[287] D. Shi, P. Li, Preparation of PDMS/PVDF Composite Pervaporation Membrane Modified with Hydrophobic TiO2 Nanoparticles for Separating Formaldehyde Solution, Polym. Sci. 2 (2016) 1–7. https://doi.org/10.4172/2471-9935.100012.

[288] L. Rong, Z. Zhu, B. Wang, Z. Mao, H. Xu, L. Zhang, Y. Zhong, X. Sui, Facile fabrication of thiol-modified cellulose sponges for adsorption of Hg2+ from aqueous solutions, Cellulose. 25 (2018) 3025–3035. https://doi.org/10.1007/s10570-018-1758-7.

[289] L.V.L. and A.S.P. Carsten Grabmann, Maureen Mann, Textile Based Electrochromic Cells Prepared with PEDOT: PSS and Gelled Electrolyte, Sensors. 20 (2020) 1–14. https://doi.org/https://doi.org/10.3390/s20195691.